Current generation in photovoltaic cells

Savina Rita Joseph

St. Catherine's College

University of Oxford

A thesis submitted for the degree of

Doctor of Philosophy in Applied Mathematics

Trinity Term 2018

Ackowledgements

To those who led the way, and to those who shall follow..

I am heartily thankful to all those who have supervised, advised and collaborated with me on this project. Firstly, I would like to express my sincere gratitude to my supervisors Prof. Colin Please, Prof. Christopher Breward, Prof. Andreas Münch and Prof. John Ockendon, for their guidance and useful comments throughout the years.

I would also like to thank Dr Giles Richardson and Dr Jamie Foster for sharing their experience on modelling solar cells and Dr James Kirkpatrick for introducing me to electrochemistry. I am also grateful to Prof Henry Snaith, Dr Pablo Docampo and Dr Agnese Abrusci, through their (past or current) affiliation with the Department of Physics, for the data they have so kindly provided and for guiding me through my attempts of making a solar cell of my own.

In the course of this journey, valuable lessons were learnt, but not all from academia.. That said, I could not be more grateful for having such wonderful people, like my parents, my sister and my partner, in my life. They turn every moment into a happy memory.

To all mentioned above, I am deeply indebted.

This work was partially supported by a scholarship from the Engineering and Physical Sciences Research Council (EPSRC) and a scholarship from the A.G. Leventis Foundation. The research was conducted at the Oxford Centre of Collaborative Applied Mathematics (OCCAM), Mathematics Institute of the University of Oxford. OCCAM was formed under the Award No. KUK-C1-013-04, made by King Abdullah University of Science and Technology (KAUST).

Current generation in photovoltaic cells

Savina Rita Joseph
St. Catherine's College
Submitted in completion of the degree Doctor of Philosophy in Applied Mathematics
Trinity Term 2018

Abstract

In this thesis we present an analysis of the operation of a particular type of hybrid photovoltaic device called a solid-state dye-sensitised solar cell. A mathematical model is used to describe the cell's operation, from the moment the photon reaches the surface of the device, until it is collected at the end electrodes.

The invention of the solid-state dye-sensitised solar cells is recent and is part of the greater search for stable, low cost and efficient alternative means of energy generation. As the physical and chemical analysis has progressed in recent years, there is a need to establish a mathematical model to describe their behaviour. This thesis includes such mathematical analysis, based on our current knowledge of semiconductors and opto-electrochemical properties of solid-state material. The effect of these properties and of the geometry of the cell are examined in detail using analytical, but also numerical techniques that allow to circumvent the complexities involved.

In this thesis, we show how conducting electrons can be generated by absorbing photons within an internal dye layer and are then transported via diffusion in the device until they reach the electrodes connecting it to an external electric circuit. While there are several limiting factors in the analysis, including the geometry of the device, the mathematical model appears to agree qualitatively well with available data on the current generation of solid-state dye-sensitised solar cells.

Contents

List of Symbols

Symbol	Description	Value	Units
Constants			
c	speed of light (in vacuum)	299 792 458	$[ms^{-1}]$
$\hbar$	Planck constant	4.135667×10^{-15}	$[eVs]$
k_B	Boltzmann constant	8.617332×10^{-5}	$[eVK^{-1}]$
	or	$1.3806488 \times 10^{-23}$	$[JK^{-1}]$
q	electric charge	$1.60217648 \times 10^{-19}$	$[C]$
Roman Letters			
B	magnetic field		$[Nm^{-1}A^{-1}]$
D_n	electron diffusivity		$[cm^2s^{-1}]$
D_p	hole diffusivity		$[cm^2s^{-1}]$
E	electric field		$[Vm^{-1}]$
E_A	acceptor energy level		$[eV]$
E_C	lowest conduction band energy level		$[eV]$
E_D	donor energy level		$[eV]$
E_F	Fermi energy level		$[eV]$
E_g	energy band gap		$[eV]$
E_{ph}	phonon energy		$[eV]$
E_s	electron energy level		$[eV]$
E_V	highest valence band energy level		$[eV]$
E_ϕ	photon energy		$[eV]$
E_{X_b}	exciton (Coulomb) binding energy		$[eV]$
E_X	exciton energy		$[eV]$

Continued on next page...

... Continued

Symbol	Description	Units
F_n	electron surface current density	$[m^{-2}]$
F_p	hole surface current density	$[m^{-2}]$
G	generation term	$[m^{-2}]$
I	light intensity	$[mol\ cm^{-2}]$
J	surface current flux	$[C\ m^{-2}s^{-1}] = [Am^{-2}]$
J_n	electron surface current flux	$[Am^{-2}]$
J_p	hole surface current flux	$[Am^{-2}]$
n	(volume) density of electrons in the EA conduction band	$[m^{-3}]$
N	(surface) density of neutral dye molecules	$[m^{-2}]$
n_i	intrinsic surface carrier density	$[m^{-2}]$
p	(volume) density of holes in the valence band of the ED	$[m^{-3}]$
P	power (in 2D)	$[Wm^{-2}]$
P_0	(volume) density of available OMO in the ED for holes to occupy	$[m^{-3}]$
R	recombination term	$[cm^{-2}]$
S	fraction of the dye free portion of the EA surface	dimensionless
T	temperature	$[K]$
V	applied voltage	$[eV]$
V_{bi}	work function difference between electrodes	$[eV]$

Greek Letters

α	absorption coefficient	$[cm^{-1}]$
ϵ_n	dielectric constant for the EA for the ssDSSC	$[CV^{-1}m^{-1}]$
ϵ_p	dielectric constant for the ED for the ssDSSC	$[CV^{-1}m^{-1}]$
μ_n	electron mobility	$[cm^2V^{-1}s^{-1}]$
μ_p	hole mobility	$[cm^2V^{-1}s^{-1}]$
ν	photon frequency	$[s^{-1}]$
Π_0	typical electron/hole concentration	$[cm^{-3}]$
σ_A	cross sectional area seen by a photon in a material	$[cm^2]$
τ_R	recombination timescale	$[s]$
ϕ	electrostatic potential	$[eV\ C^{-1}]$

Continued on next page...

. . . Continued

Symbol	Description	Units
χ_n	electron affinity	$[eV]$
χ_p	ionisation potential	$[eV]$
ψ_n, ψ_p	electrochemical potentials for electrons, holes	$[eV]$
ψ_s	wavefunction (of electrons)	dimensionless

Short hand notations

DSSC	dye-sensitised solar cell
EA	Electron Acceptor
ED	Electron Donor
HOMO	Highest Occupied Molecular Orbital
LUMO	Lowest Unoccupied Molecular Orbital
OMO	Occupied Molecular Orbitals
ssDSSC	solid-state dye-sensitised solar cell
UMO	Unoccupied Molecular Orbitals

1

Introduction

The realisation that fossil fuels are finite and release large amounts of CO_2 into the atmosphere, has turned attention to alternative sources of energy. Climate change has also driven research towards sustainable energy technologies, such as solar cells, that help limit environmental pollution and make use of a seemingly endless energy source - in this case, the sun. One important advantage of this technology is also the ability to provide electricity to isolated communities, increasing their quality of life. The renewable energy consumption has increased by 14% in 2016, according to the 2017 review of the world energy by BP [1].

The self-sustainability of solar panels and other financial incentives provided by governments have contributed to the installation of an increasing number of solar cells by leading organisations, but also from individuals. The European Union has also set a target for a 20% contribution towards the total energy consumption to be obtained from renewable energy resources by 2020 [2].

Research on photovoltaics (PV) has rapidly increased in the last few decades concentrating mostly around developing new materials with higher efficiencies and lower

cost of production. Understanding the complex mechanisms that generate current within a solar cell and its optoelectrochemical properties is key to improving the efficiency. The first attempts towards this were done in the 1950s, when the first mathematical models were developed to describe the behaviour of solar cells.

1.1 What is a solar cell?

A solar cell is a laboratory-made device that can generate electrical current when illuminated. There are, in fact, various types of solar cells nowadays, all of which have the same main principle of operation: the photovoltaic effect. In this process, the photons are absorbed by a material and excite the electors to a higher energy state, and by breaking the energy barrier they conduct energy.

The photovoltaic effect was first demonstrated in an experiment by Alexandre-Edmond Becquerel in 1839 [3], where current was detected when a certain configuration of materials was illuminated. The electrons absorb photons which allows them to overcome the energy barrier that holds them bound to the lattice of materials and become free to move within the material. The vacancy left behind in the lattice, once the electron is excited, is conventionally referred to as a *hole*. Having in mind that when the electron reaches a junction between two materials, it will tend to move to the one with lower energy states and release its excess energy. Becquerel configured a device by creating an interface between two materials with different energy states so that the electron could be extracted from one material and flow in the other. Therefore, the configuration of materials in a solar cell were shown to be important in ensuring that the generated electrons transport within the device leading to the generation of electrical current.

1.2 Types of solar cells

Photovoltaics are, typically, categorised in three generations. First generation solar cells are made of two silicon-based (or equivalent) materials joined together at a single junction. These are the conventional cells used today with a maximum conversion efficiency of 25%. The second generation includes thin film photovoltaics, which have a maximum efficiency of around 23% and require a lower cost for manufacture.

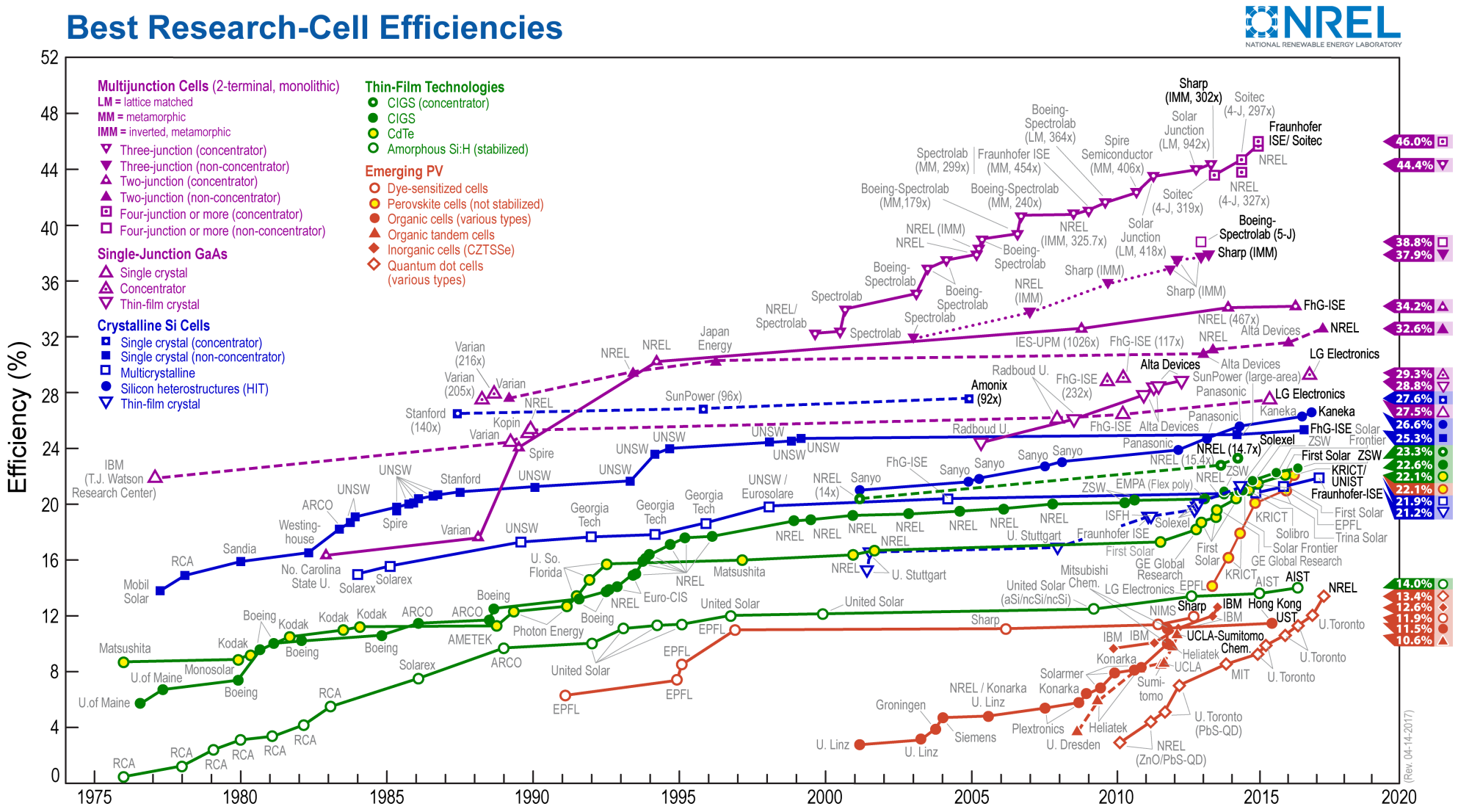

Figure 1.1: Efficiency Chart of solar cells up to date. *This plot is a courtesy of the National Renewable Energy Laboratory, Golden, CO.*

The third generation comprises of all cells that exploit new technological advances. Examples of third generation devices are solar cells with concentrator systems and multi-junction cells that reach efficiencies higher than the theoretical limit of maximum efficiency as proved by Shockley and Queisser [4]. The efficiency of multi-junction solar cells can be drastically increased to 46%. A chart of the efficiencies of all solar cells can be seen in Figure 1.1.

We can also categorise cells based on the type of material they are made of, i.e. inorganic or organic materials or a combination of the two. A short introduction is presented below for each type of cells.

1.2.1 Inorganic solar cells

The first *single junction* silicon solar cell was patented by Russel Ohl at the Bell Laboratories under the name “Light-sensitive electric device" [5]. Most commercial cells are made from silicon either by growing a single crystal, which has the best conducting properties and efficiency, or by putting together smaller silicon crystals or using amorphous silicon. The latter is easier and cheaper to manufacture. Among other materials used for this type of cells are germanium and gallium arsenide.

As shown in Figure 1.2, a single junction cell consists of two regions of silicon-based materials: the *n-region* (negatively charged region) is a *doped* silicon layer, in which impurities have been introduced, leading to the presence of an increased number of electrons, and the *p-region* (positively charged region) is another doped silicon layer with a reduced number of electrons. When these two materials are built together, the charge carriers that have been excited by absorbing energy will diffuse towards the region of lower concentration. Thus in a small region near the junction, called the *depletion region*, electrons concentrate in the p-region and holes in the n-region. This allows for the creation of a built-in potential difference imposing a force, which aids in the movement of charges in the opposite direction to diffusion. During this processes, electrons may remain free and transport to the end of the device, where they enter the electrodes and hence the outer circuit, or they may release energy and fill in a hole, i.e. *recombine* with a hole. When the device is illuminated, the excited electrons diffuse from the n-region to the p-region, overcoming the drift forces at the interface, thus creating electricity.

However efficient silicon solar cells may be, there is an important drawback that limits their use: the cost of production. The need for lower cost, has lead to the use of materials which require less processing time and effort in manufacture.

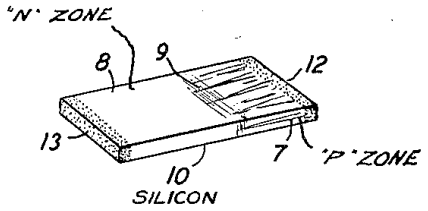

Figure 1.2: Drawing from the original documents of Ohl [5].

1.2.2 Organic solar cells

Organic materials are used in the manufacture of solar cells due to their attractive low cost of production. The idea to use polymers instead of silicon was first introduced in 1990 by Burroughes *et al* [6]. Although cheaper, the degradation of organic materials under UV illumination is an important disadvantage. Currently, the highest lab efficiency of such cells is around 12% (see Figure 1.1).

Purely organic solar cells are made up of two interconnected organic semiconducting materials, each with different chemical properties. The two regions are called the *acceptor region* and the *donor region* depending on whether electrons are 'accepted by' or 'donated from' that region, respectively. The different chemical and optical properties of organic materials, however, imply different generation and recombination mechanisms compared with the silicon cells.

Photons are only absorbed by the donor region creating electron-hole pairs, called *excitons*. The energy required to remove an electron from an atom or molecule, referred to as the *binding energy*, is typically stronger in organic material [7], so free electrons and holes are not considered to be generated instantly. In fact, the binding energy can only be overcome at the donor/acceptor interface, where the electrochemical properties of the device will allow for the dissociation of the excitons. In particular, the dissociation occurs when the electron moves into the acceptor region leaving the hole in the donor region. By drift and diffusion, the charges are then transported to the electrodes.

1.2.3 Hybrid solar cells

A recent hybrid technology is that of dye-sensitized solar cells introduced in 1991 by O'Regan *et al* [8]. The idea of this type of solar cell is innovative in the sense that the device consists of three layers of different materials, all with different electrochemical properties, thus demonstrating different charge generation, recombination and transport mechanisms.

A schematic configuration of a dye-sensitised solar cell is shown in Figure 1.3. On top of the bottom electrode (anode) there is a compact flat layer of metal oxide and, on top of that, a mesoporous layer of the same material. The compact and mesoporous metal oxide layer is known as the *electron acceptor (EA) region*. The surface of the metal oxide is covered with a monolayer of dye. The remaining space is filled with a liquid electrolyte, which we refer to as the *electron donor (ED) region*, and sealed with the second electrode (cathode). The sun hits the cell from the ED side (i.e. from the top of Figure 1.3).

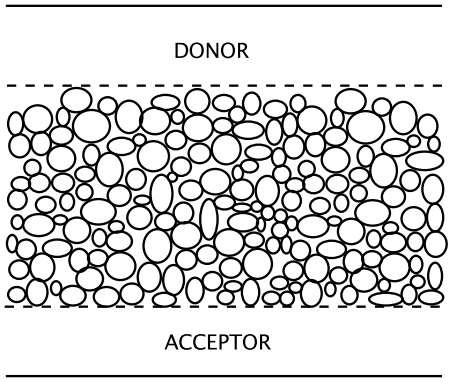

Figure 1.3: Schematic representation of the general structure of a dye-sensitised solar cell. The electron donor may be liquid (electrolyte), gel or solid (polymer).

When a photon hits the cell, the energy is absorbed by the dye which generates excitons with a large binding energy. As an exciton reaches the dye/EA interface, the electrochemical properties of the EA and the dye favour the dissociation of the electrons (from the excitons) and transport them towards the anode. The positively charged ions that remain in the dye recombine with electrons from the ED at the dye/ED interface to regenerate the neutral molecules of the dye.

The energy band structure in materials contains a range of energy levels where no energy states for electrons exist, referred to as the *energy band gap*. The available

energy states of electrons are separated by the band gap into the *valence* states and the *conduction* states (an electron occupies the higher energy conduction states when it is excited). For organic materials, this band gap is large enough to prohibit the generation and recombination in the bulk to the EA and ED regions. Thus, generation and recombination occurs in the dye layer and charge transport in the bulk of the EA and ED regions.

Liquid dye-sensitised cells have reached efficiencies of 12% but, under high temperatures, the liquid electrolyte will dilate and cause leakage. Thus, to overcome this hurdle, researchers have turned to alternative materials in order to replace the electrolyte by a gel solution or even a solid-state material as suggested in Wang *et al* [9] and Bach *et al* [10], respectively. The latter type of cells is commonly referred to as solid state dye-sensitised solar cells (ssDSSC).

While ssDSSCs have a thin layer of dye at the donor/acceptor interface, another type of hybrid solar cells involve a thick slab of perovskite sandwiched between the donor and the acceptor materials. Perovskite is an organic-lead halide compound known for its light absorbing properties. These devices were introduce in 2012 and currently demonstrate efficiency of up to around 22% (see Figure 1.1) [11, 12, 13, 14, 15]. The perovskite layer is responsible for the generation of free charges that flow through the EA and ED regions and into the external circuit. This type of cells has attracted a lot of attention because of its combination of good efficiency and low cost. The efficiency is seen improving, as researchers understand the operating mechanisms and are able to optimise the configuration leading to better and more sustainable performance [16, 17, 18]. It has been reported that better performance is achieved by doping the donor and acceptor regions for these types of cells [19, 20], as well as with better coverage of the EA surface with perovskite [21].

1.3 Objectives

All solar cells operate under the principles of the photovoltaic effect. However, the optoelectrochemical mechanisms that lead to the generation of current depend greatly on the materials and their configuration in a solar cell.

In this thesis, we will focus on hybrid solar cells, and in particular on ssDSSCs.

Our aim is to construct a mathematical model that describes the operation of such cells, from the moment photons reach the surface until the electrons generated are collected at the ends of the device. In particular, we intend to characterise devices via the relation between the applied voltage and the current that is extracted when the cell is either in the dark or illuminated.

1.4 Outline of Thesis

In this thesis, we separate the analysis of the operation of the ssDSSC into two problems: (i) the generation of electrical current and (ii) the transport of current within the ssDSSC. The thesis is then structured in two main Parts, one for each problem.

In Part I, which comprises four chapters, we examine the diode-like behaviour of the ssDSSC in dark conditions. In Chapter 2 we lay out the background theory behind the selection of the materials based on their electrochemical and physical properties. We then employ the theory to derive a mathematical model for the transport of current in Chapter 3. In the following two Chapters, 4 and 5, we apply and solve the model for different geometries of the cell; in particular, we examine a cells made up of a bilayer arrangement of different semiconductors in Chapter 4 and a cell with a more complex (nanostructured) interface between the two layers in Chapter 5.

Part II is also made up of four chapters and describes the behaviour of the device when illuminated. In Chapter 6 we discuss the opto-electrochemical theory of materials that drives the absorption of photons to generate electrons. The model for current generation is explained in Chapter 7 and is later applied and solved in the case of a bilayer cell (Chapter 8) and in the case of a nanostructured cell (Chapter 9).

The final chapter, Chapter 10, summarises our results and lays out a field of possible further development of the research.

Note that all constants and variables used throughout the thesis are available for reference in the *List of Symbols* and that the numerical schemes used in chapters 4 and 5 are presented in the Appendices at the end of the thesis.

1.5 Statement of Originality

This is to certify that to the best of my knowledge, the content of this thesis is my own work. This thesis has not been submitted for any degree or other purposes. I certify that the intellectual content of this thesis is the product of my own work and that all the assistance received in preparing this thesis and sources have been acknowledged.

Part I

The diode

2

Physical background

The theories of Max Planck[22], which state that photons and electrons have a wave-particle duality behaviour and are quantised quantities, form the basis of understanding the operation of a solar cell.

Measured photons' wavelengths lie between $O(1)$ nm and $O(10^3)$ nm [23, 24] and reach the earth's surface with certain *solar irradiance* $[Wm^{-2}]$, i.e. power per unit area. In Figure 2.1, we show schematically the *spectral irradiance*, which is the solar irradiance per wavelength (of the photons) $[Wm^{-2}nm^{-1}]$. One may observe that a vast amount of power can be harvested from photons in the visible light range (i.e. for wavelengths between 400-700 nm).

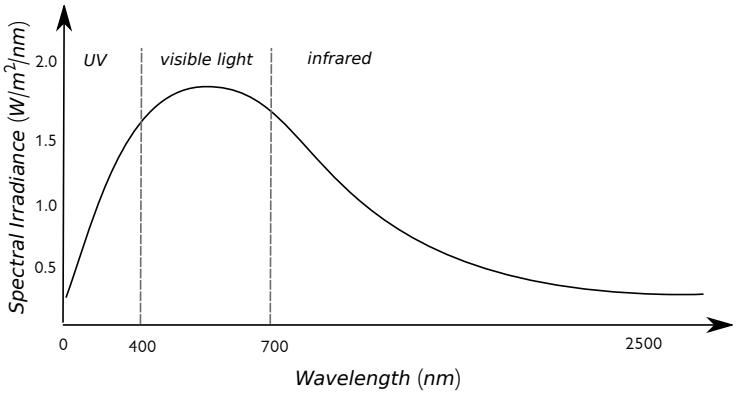

Figure 2.1: Spectral irradiance against the wavelengths of photons. [23, 24]

Similarly, electrons behave like electromagnetic waves and can be found possessing different energies depending on their distance from the core of their atom and the atom's structure. They can be found lying at energy levels, E_s $[eV]$, which are the eigenvalues of the time-independent *Schrödinger equation* [25]

$$-\frac{\hbar^2}{2m}\frac{d^2\psi_{\mathbf{s}}}{d\mathbf{x}^2} + V_s\psi_s = E_s\psi_s, \tag{2.1}$$

where ψ_s is the wavefunction of the electron, $\hbar$ is Planck's constant and m is the particle's mass. $V_s\psi_s$ and $\frac{\hbar^2}{2m}\frac{d^2\psi_{\mathbf{s}}}{d\mathbf{x}^2}$ represent the potential and kinetic energies that act on the wave function. E_s can be interpreted as the total energy of the standing state which the electron may occupy. In general, the solution shows that the energy levels for electrons are packed together in bands of *allowed* and *forbidden* energy levels which the particle may or may not occupy, respectively. The lowest allowed energy band is called the *valence band* and the next higher allowed energy band is called the *conduction band*. Between these two bands is a set of energy levels in which electrons cannot reside, i.e. the band gap, of size E_g $[eV]$.

A *conductor* has very small band gap making it easy for current to flow. In an insulator, the band gap is significantly larger and no external energy can provide the required energy to overcome the gap, so that any flux of electrons is essentially prohibited. A *semiconductor* lies somewhere in between. When an electron absorbs external energy, e.g. in the form of photons, it can be excited from the valence band to the conduction band. In particular, when photons are absorbed by valence electrons, the latter disassociate from the material's lattice and are free to move around, i.e. conduct electricity. The empty space left behind in the lattice is conventionally

referred to as a *hole*.

The photovoltaic effect, mentioned in Chapter 1, occurs in semiconducting materials. We consider two materials with different energy band structures where the lowest energy level of the conduction band, E_C $[eV]$, and the highest energy level of the valence band, E_V $[eV]$, are at different levels in each material, as shown in Figure 2.2. In equilibrium, an electron occupies an energy state in the valence band. Under illumination, photons are absorbed by electrons that, if they gain the necessary energy (E_g), can jump to the conduction band, leaving a hole in the valence band. This electron-hole pair is referred to as an *exciton*. This process may occur in both the EA and ED. However, when the EA and ED are brought together, electrons will move into the material with the lowest E_C (the *acceptor*), in order to release energy, and holes will move into the material with the highest E_V (the *donor*) where they can move freely and thus conduct electricity. For example, the favourable direction of motion for an electron-hole pair generated in the donor material is shown in Figure 2.2. The in-depth examination of the optical properties of semiconducting materials will be the focus of Part II.

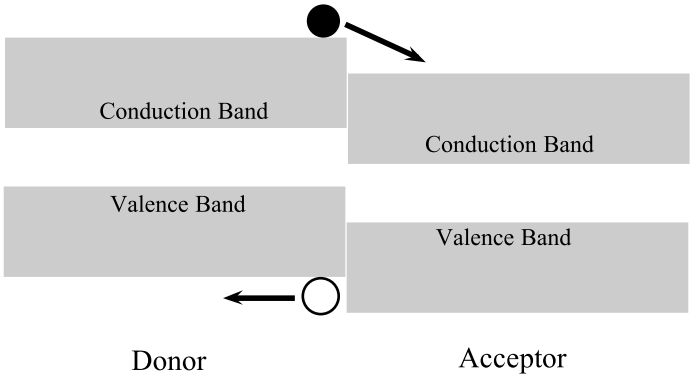

Figure 2.2: Favourable direction of motion of electrons (black node) and holes (white node), due to energy differences, for those generated in the donor region. The vertical axis represents the energy $[eV]$.

Having introduced the main concepts of operation of solar cells, we will first concentrate on the behaviour of a solar cell without the effect of illumination. In this Chapter, we give a brief overview of the theory of electrical conduction in semiconducting material that sets the base for the assumptions for the mathematical model for ssDSSCs.

2.1 Electrochemical properties of materials

When two materials with different chemical properties are in contact, a *redox* reaction may take place. This comprises two processes, namely *oxidation* and *reduction*. Oxidation is the process of losing an electron from a molecule or atom, whereas during reduction an electron is gained.

In order to understand the favourable direction of motion of the electrons, we introduce the notion of the *electrochemical potential*, ψ. This is a measure of the amount of work required to, or produced by, changing the energy state of an ion or electron from a neutral state to a higher or lower energy state. The electrochemical potential is determined by the difference between chemical potential, which is the potential energy released or absorbed by a material during a chemical reaction, and the local *electrostatic potential*, ϕ. The electrostatic potential is the work required to move a positive charge between two points within the electric field without causing the particle to accelerate.

When referring to an oxidation process, the chemical potential is used interchangeably with the term *electron affinity*, which is the energy an electron releases when we (negatively) ionise a neutral atom or molecule, i.e. the energy difference between the zero energy state and the conduction band or the Unoccupied Molecular Orbital (UMO) states[1]. An electron has the tendency to release energy and thus move towards the material with the lowest UMO states.

For the reduction process we usually refer to the *ionisation potential*, which is the energy required to remove an electron from a neutral atom or molecule, i.e. the energy difference between the vacuum and the valence band or the Occupied Molecular Orbital (OMO) states. An electron will tend to move towards the largest ionisation potential, allowing the electron to reduce to an equilibrium state by releasing the excess energy. Schematically, the favourable direction of motion of an electron during the oxidation and reduction processes is shown in Figure 2.3.

[1] A molecular orbital defines the 'allowed' energy states which an electron can occupy in organic materials. Occupied molecular orbitals lie at lower energy levels (corresponding to the valence band for organic materials), whereas the unoccupied molecular orbitals lie at higher energy levels (corresponding to the conduction band for organic materials).

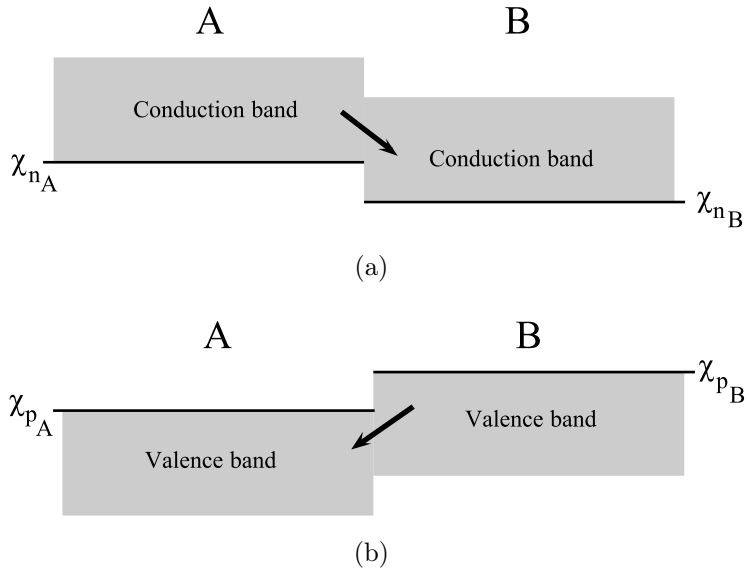

Figure 2.3: The favourable motion of an electron between two materials A and B during (a) oxidation, relative to their electron affinities, χ_n and (b) reduction, relative to their ionisation potentials, χ_p. Note that the direction of motion for a hole or a cation is the opposite of that of an electron. The vertical axis represents the energy.

An example of an electrochemical cell is one that consists of an electrode (anode) accepting electrons from an electrolyte and an electrode (cathode) donating electrons to the electrolyte, the structure of which is shown in Figure 2.4. In this system we have electrochemical reactions taking place; reduction occurs at the cathode/electrolyte interface and oxidation at the electrolyte/anode interface.

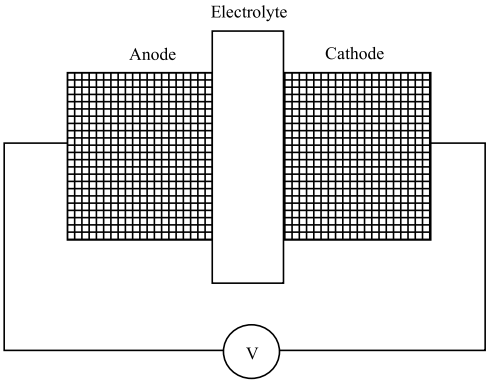

Figure 2.4: An electrochemical cell consisting of an anode, an electrolyte and a cathode. Oxidation and reduction occur at the anode-electrolyte and electrolyte-cathode interfaces, respectively: electrons flow from the electrolyte into the anode and the cathode donates electrons to the electrolyte. This can be connected to an external circuit and a potential difference can be measured across the cell.

A ssDSSC follows the same principles of operation, although in a slightly different configuration, as shown in Figure 2.5. The ssDSSC consists of three main regions, namely the electron acceptor (EA) region, the electron donor (ED) region and a dye monolayer at the interface playing the role that the electrolyte played in the electrochemical cell. The chemical properties of the dye ensure that oxidation and reduction now occur at the EA/dye and ED/dye interfaces, respectively. Anode and cathode electrodes, in contact with the EA and ED ends, respectively, connect the cell to an external circuit.

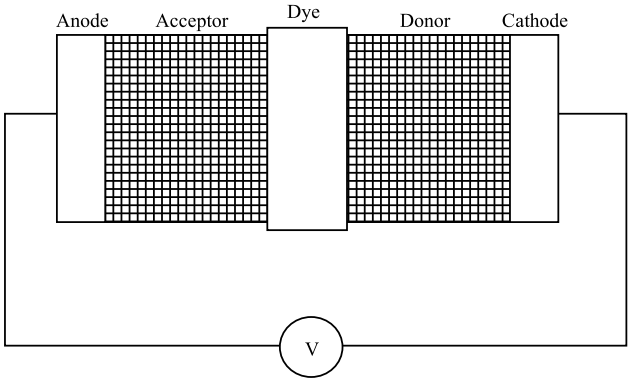

Figure 2.5: Schematic representation of the main parts composing a ssDSSC. These include an anode, an EA layer, a dye monolayer, an ED layer and a cathode. The electrons flow in a directions from the cathode to the donor, then the dye, acceptor and anode. A potential difference can be measured across the cell.

Adding an external potential to the system can help control the redox reactions, by changing the electrochemical potentials. When the applied potential is negative, the energy of electrons increases in the EA and decreases in the ED, leading to reduction and oxidation at the EA/dye and dye/ED interface, opposing the favourable motion of electrons from the ED to the EA. When the applied potential is positive, the chemically-favourable motion of electrons in the cell is assisted.

The ssDSSC has also been called the *photoelectrochemical cell*, as it operates similarly to an electrochemical cell under the necessary lighting conditions.

2.1.1 Configuration of the ssDSSC

In this section we present a more thorough explanation of the charge transport of electrons in a solid state dye-sensitised solar cell (ssDSSC). We further give details of

commonly used materials. A collective list of references on recent developments on this topic can be found in Graetzel [26] and Snaith *et al* [27].

The ssDSSC comprises of a layered configuration of anode/electron acceptor/dye/electron donor/cathode as previously shown in Figure 1.3. Common materials used are (in order): fluorine-doped tin oxide (FTO)/titanium dioxide (TiO_2)/a Ruthenium-based dye (e.g. *Z*907)/ polymer (e.g. spiro-OMeTAD)/silver (Ag). The combination of these materials leads to efficient generation of current. In contrast to the silicon solar cells, generation of excitons in an ssDSSC is limited to the dye layer rather than the whole cell; hence the name of the solar cells. Photons are absorbed in the dye to produce free charges. An in-depth analysis of the generation of free electrons due to illumination will follow in Part II.

The making of a ssDSSC involves several steps [28], and we lay here an example of the possible manufacturing processes. Firstly, a glass substrate is prepared onto which the FTO anode is etched. After the deposition of the anode, a compact layer of TiO_2 is deposited by *spray pyrolysis*. After sintering, the mesoporous TiO_2 layer is deposited via *screen printing*, and then the cells are placed into the dye solution and left overnight. The next step is to *spin coat* the device with a layer of spiro-OMeTAD and, finally, the liquid cathode is deposited on top by a technique known as *evaporation* to form a solid layer. This technique involves the deposition of a liquid solution of the material, which is then heated leading to evaporation of the solution material and leaving the solidified cathode in place.

As the generation of current occurs in the dye layer for these devices, we can separate the process of current generation from the process of charge transport. The interfacial kinetics and the charge transport mechanisms are the topics of the following sections.

2.1.2 Interfacial kinetics

In this section we describe the electrochemical reactions that occur at the interface of the EA and the ED in the absence of dye. We note that the interfacial kinetics between the dye and the outer regions involve the generation of free electrons and holes at the interfaces. This topic will be visited in Part II.

In Figure 2.6, we present a schematic representation of the interfacial kinetics be-

tween the EA and the ED in the absence of dye. The recombination of electrons from the EA with holes in the ED is *direct*, i.e. electrons from the EA release the energy and directly occupy an empty space (hole) in the ED, without occupying any intermediate energy state in-between the initial and final position of the electron. The larger the interface with direct EA and ED contact (i.e. without dye), the greater the loss of generated current. The timescale for recombination has been reported to be on the microsecond scale in [26], [27] and [29].

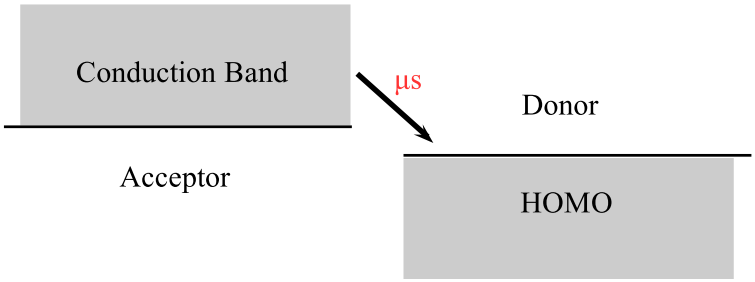

Figure 2.6: Schematic representation of the interfacial kinetics between the (energy levels of the) EA and the ED when in contact. Note that the timescale for direct recombination is $\mu s = O(10^{-6}s)$.

2.1.3 Charge transport

When bias is applied on the device so that electrons are transported in the bulk of the EA and holes in the bulk of the ED towards the electrodes, we refer to the bias as *forward bias* as it allows the generation of current. In this section we give a description of the processes that govern the motion of the particles and the criteria for choosing the materials for the outer regions.

As already mentioned, the TiO_2 (EA) layer typically consists of two regions. At the electrode contact a compact TiO_2 layer of thickness $100 - 200\ nm$ is deposited by spray pyrolysis and at its surface a $2 - 3\ \mu m$ thick mesoporous TiO_2 layer is deposited, usually, by screen printing. The compact TiO_2 layer needs to be made compact and thick enough in order to avoid short-circuiting effects between the ED and the anode. It must also be made thin enough so that any current losses are limited. However, since the dye is responsible for the generation of charges it is important to maximise the surface of the TiO_2 upon which it is deposited. For this, a mesoporous TiO_2 layer is deposited on top of the compact one. Again different thicknesses have been examined, but that of $2 - 3\ \mu m$ is believed to be the optimal

for dye coverage and pore filling by the ED. Details on the manufacture process can be found in Snaith *et al* [27], Docampo *et al* [28], Kavan *et al* [30] and Barbe *et al* [31].

A commonly used material for the ED is spiro-OMeTAD which is applied by spin coating on top of the dyed TiO_2 surface resulting in filling of the pores to approximately 80% and creation of a further (compact) layer on top of thickness 200 nm as measured in Snaith *et al* [27, 32]. Sometimes, lithium salts (Li^+) are added to the spiro-OMeTAD which may increase mobility from 10^{-4} $cm^2V^{-1}s^{-1}$ to as high as 10^{-3} $cm^2V^{-1}s^{-1}$. This addition of lithium is not considered to be doping as suggested by Bach *et al* [10] and Snaith *et al* [33]. This is justified by the colour of the material which does not change once doped (the doping of the material is reflected in the colour absorbed by that material).

The EA, dye and the ED should provide a good band structure in order to allow for electron transfer from the dye to the EA and of holes from the dye into the ED as shown schematically in Figure 2.6. The electron acceptor and donor materials that are used have large band gaps that theoretically can only allow for exciton generation in the ultraviolet limit of the visible solar spectrum. Further, due to the manufacture process of the EA, both the compact and the mesoporous layers have impurities that introduce *trap states* in the band gap as stated in Filipic *et al* [34] and Hagfeldt *et al* [35]. A trap state is an irregularity in the symmetry of the lattice, interpreted as an irregularity in the energy band structure by the introduction of energies states in the band gap that could trap an electron. These do not contribute to the recombination mechanism, but increase conductivity when illuminated by near-UV light as the trap states are filled.

In Figure 2.7 we show the energy bands of the TiO_2 and the spiro-OMeTAD as extracted from Hagfeldt *et al* [35] and Snaith *et al* [27]. The band gap in the TiO_2 has been reported to be 3.2 eV in Tiwava *et al* [36], while it is even larger for the spiro-OMeTAD as suggested in Fox [7]. An explanation of how photons are absorbed by the dye is presented in Part II.

Once electrons and holes are dissociated in the EA and ED, they move due to diffusion and drift, which pull the electron in opposite directions. Diffusion moves electrons towards lower concentration which generates an internal build-in electric field at the

interface due to the local potential differences. The relative permittivity[2] of the TiO_2 is 114 and of the spiro-OMeTAD is approximately 1 as estimated in Feber *et al* [37] and Fox [7], respectively. The mathematical model derived in the next Chapter is based on this principle of operation.

Free electrons are transported in the conduction band of the EA with *mobility*[3] of approximately $10^{-5}\ cm^2V^{-1}s^{-1}$. Holes in the ED hop from one electronic state of the spiro-OMeTAD to the next one until reaching the cathode with mobility of the order of $10^{-4}\ cm^2V^{-1}s^{-1}$ as extracted from Snaith *et al* [27].

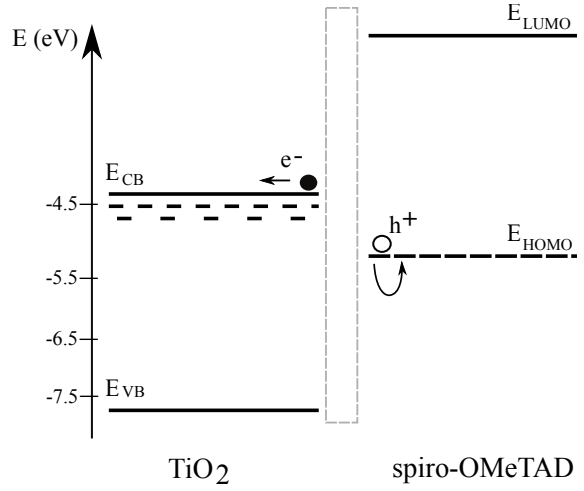

Figure 2.7: Charge transport of electrons in the TiO_2 and of holes in the spiro-OMeTAD. The band gaps in the TiO_2 and the spiro$-$OMeTAD are greater than 3 eV.

In this Chapter we have presented the basic electrochemical principles that underpin the operation of a functional ssDSSC. Both the EA and the ED have wide band gaps so that excitons are only generated in the dye. The electrochemical potential differences between the outer regions virtually prohibit the presence of free electrons in the ED and of holes in the EA. Electrons and holes are transported in the bulk of the EA and ED towards the anode or cathode, respectively. Thus the generation of current, the transport of electrons and the transport of holes can be treated as three spatially separated processes. In the following Chapters we develop the mathematical model for the operation of a ssDSSC in the absence of the dye.

[2]Relative permittivity, ϵ_r,is the ratio of the material's permittivity (or dielectric constant), ϵ to the vacuum permittivity, ϵ_0, i.e. $\epsilon_r = \frac{\epsilon}{\epsilon_0}$ and is dimensionless.

[3]Mobility is a physical quantity describing how quickly an electron can travel in an electric field

3

The model for current transport in an ssDSSC

The invention of the first *p-n* junction silicon solar cell in 1941 by Russel Ohl was pioneering in solid state physics. Shockley[1] was the first to provide an accurate mathematical model for the operation of the p-n junction cell [40]. Shockley assumes a continuum for the free charge carriers, rather than discretising for each particle. This leads to a system of partial differential equations coupled to appropriate boundary conditions arising from the application of an external applied voltage and continuity conditions at the internal junction. A description of the model can be found in Please [41]. This model was the basis for all solar cell models that followed.

In this chapter, we develop a mathematical model for the operation of ssDSSCs. Firstly, we set out the underlying assumptions for the electron and hole transport in the EA and ED regions and the recombination of free charges at the interface. We

[1]In the years that followed two important patents were filed by Shockley: a "Semiconductor amplifier" [38] and a transistor made of semiconducting material [39]. The transistor was made up of an *n-p-n junction* cell which operates under similar principles.

then examine the morphology of the device, before moving on to the derivation of the problem in sections 3.2 and 3.3.

Our model for the EA is based on the work of Penny *et al* [42] for (liquid) DSSCs, in which the interfacial kinetics and charge transport in a (liquid) DSSC are described. This model considers a simplified geometry for the mesoporous TiO_2 layer, in which the TiO_2 molecules are 'organised' in 'columns' of width of the size of the molecules (i.e. $15-20\ nm$ [35]), and allows for doping of the material. Transport in the TiO_2 is achieved by drift and diffusion as described by the Shockley model. No generation or annihilation of electrons occurs in the bulk of the TiO_2 and all electrons are generated by reactions at the dye interface. The EA is considered to be doped, thus a dopant concentration is included in the model along with the concentration of free electrons, and no holes are assumed to exist in the EA. In our model, we assume no holes in the EA, constant mobility both in the dark and in the light, and no dopant concentration in the EA.

Our model for the organic ED layer is based on the work of Richardson *et al* [43] for organic solar cells. The authors derive a model to describe the operation of a bilayer solar cell consisting of two different types of wide band-gap organic semiconducting materials. Light exposure of the organic cell leads to the generation of excitons in the ED which dissociate only at the interface of the two layers. The free charges then enter the outer regions according to the electrochemical properties of the materials, as discussed in the previous Chapter: free electrons move in the EA and holes in the ED. The presence of holes in the EA and of electrons in the ED is found to be insignificant, thus neglected. They argue that transport is governed by drift and diffusion in the bulk of the two layers as described by the Shockley model. In our model, we assume no current generation, no dopant concentration and only the concentration of holes is considered in the ED.

We note that a similar model could also apply on perovskite solar cells [44, 45], with the addition of the perovskite layer between the EA and ED layers.

3.1 Morphology

The choice of morphology of the EA/ED interface plays a significant role in the current generation. The EA/ED interface of the ssDSSC may be manufactured in any of the following ways: (i) as a flat interface with no mesoporous EA layer in-between, as shown in Figure 3.1(a), (ii) as a disordered interface with a mesoporous EA interface, as shown in Figure 3.1(b) or (iii) as a highly ordered nanostructured interface with nanostems, as shown in Figure 3.1(c). Conversion efficiencies for the type (ii) devices reach approximately $5 - 6\%$ [46, 10, 47, 48], while higher efficiencies of up to 10% have been reported for type (iii) devices [49]-[50], as shown in Figure 3.1(c).

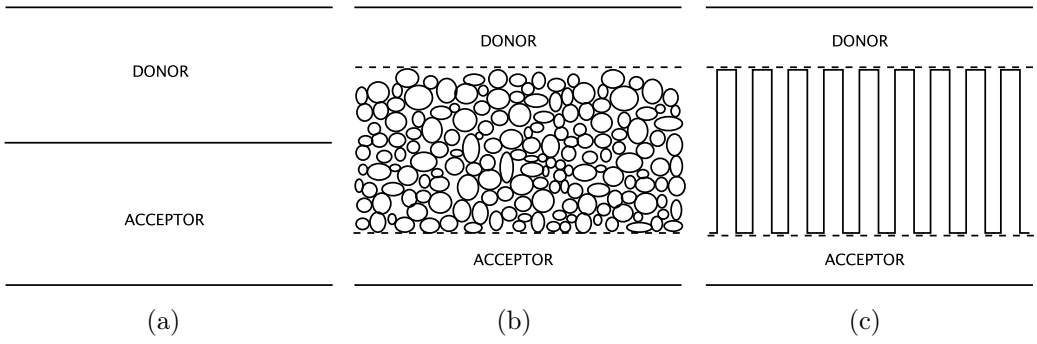

Figure 3.1: Schematic representations of (a) a bilayer cell, (b) a cell with a unordered mesoporous layer and (c) a cell with an ordered array of nanostructured stems. Note: figures are not drawn to scale.

The nanostructures are quasi-one dimensional since the ratio of their length to their width is typically extremely large. As a result, the nanostems have a high surface area-to-volume ratio, which makes them favourable for ssDSSC. A few examples of nanostructured stems include: nanospheres [49], nanospheres with nanosheets on the surface [51], nanorods [52], nanotubes [53]-[54], nanotubes with nanosheets on the surface [55], nanotubes with perpendicularly arranged nanorods on their surface (pine tree-like stems) [56] and nanowires [54, 57, 58, 50]. The width of the nanostem is usually a few nanometers, i.e. of the size of the diameter of the particle of the EA material (e.g. 20 nm for TiO_2 [59]) and the length is of the order of micrometers.

It is still extremely difficult to create full dye coverage of the surface of this acceptor material. As a result, where there is no dye, there may still exist regions of direct acceptor-donor contact. Such direct connection will create regions that allow for recombination of charge carriers: electrons arriving from the acceptor region re-

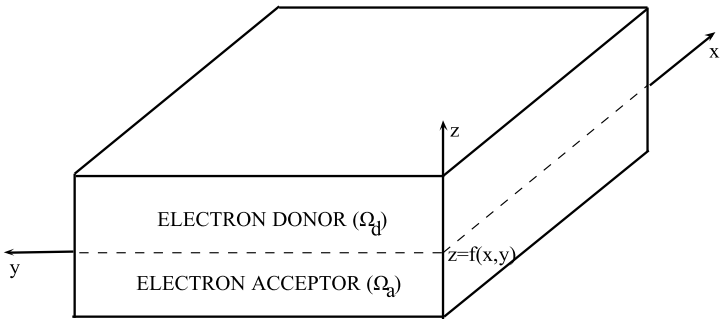

Figure 3.2: A schematic representation of the cell with the coordinate system.

combining with holes arriving from the donor region.

We assume that the dye layer is very narrow so that no charge can be built up in it. Then the limits of the electrostatic potential, $\phi(\mathbf{x})$, which is defined over the whole cell, from either side of the dye interface must be equal.

For a three-dimensional model for the current transport in x, y and z, in the directions shown in Figure 3.2, we may describe the EA/ED interface by the curve

$$z = f(x, y). \tag{3.1}$$

In particular, we consider two cases: (i) a bilayer cell, so that the interface is given by $z =$ constant, and (ii) a cell with periodically arranged nanostems, so that $f(x, y)$ is a periodic hat function. The two geometries are shown in Figures 3.1(a) and (c), respectively. The periodicity in the nanostructured device allows us to model the geometry using a few simple parameters, in particular the separation width between stems, the width and the amplitude of the stems. We let the EA region lie in Ω_a and the ED region in Ω_d. We assume that the EA layer does not allow for short-circuiting between the ED and the anode to occur.

In Part I, we consider that cell in the dark, i.e. we do not examine the effect of illumination, and allow for a variable dye distribution and any resulting direct bi-molecular recombination at the dye-free regions of the interface. We define $S(\mathbf{x})$ as the area fraction of the dye-free portion of the interface in order to describe the dye distribution. Further, we consider a uniform morphology in the y direction, so we may solve the problem in (x, z) only.

For the bilayer cell, we assume that the deposited dye creates a film of thickness

of approximately $1 - 2\ nm$, which is small compared with the lengthscale of the device, thus allowing us to incorporate the dye layer in the model as a line (or point, in the one dimensional simplification of the model). In the case of the nanostructured cell, however, the width of the nanotubes is comparable to the size of the dye thickness, making our assumption less valid. However, we still assume the dye is very thin as this (a) simplifies the analysis considerably and (b) it is reasonable because the current generation process is independent of the charge transport in the bulk of the EA and ED. Further details on the nanostructured cell are given in Chapter 5.

Having set out the main assumptions for our model, we continue with the derivation of the problem. In particular, in the following section we derive the governing equations for our mathematical model for the outer regions: EA and ED. The problem is completed by the imposition of boundary conditions, which are presented in detail in Section 3.3.

3.2 The Bulk Regions

The EA is an inorganic semiconductor and the ED is a semiconducting polymer, both with wide band-gaps, as shown previously in Figure 2.7. For inorganic compounds, we define E_C as the lowest conduction band energy level and E_D as the highest valence band energy level. For organic compounds we call these the lowest unoccupied molecular orbital (LUMO) and the highest occupied molecular orbital (HOMO), respectively, as shown in Figure 2.7.

We assume that the presence of impurities is negligible and we treat both materials as *pure*, i.e. there are no dopants in EA and ED. Based on this assumption we neglect any intermediate energy levels in the band gaps. Thus any generation or recombination in the bulk of the EA and the ED should occur only *directly* from the valence band or OMO to the conduction band or UMO, respectively. However, since the energy band gaps in each of the two regions are large, we do not allow for the generation (and hence recombination) of excitons or free charge carriers due to illumination in the bulk of each material. We note that the addition of lithium atoms as dopants in the ED has demonstrated increased conductivity of the device [60], but we will not be considering this effect in this thesis.

The first governing equation, which holds both in the EA and ED regions, arises from the electrostatic approximation of *Gauss' equation*, which reduces to the *Poisson equation* for the electrostatic potential, ϕ,

$$\nabla \cdot (\epsilon_i \nabla \phi(\mathbf{x})) = q\,(n(\mathbf{x}) - p(\mathbf{x}))\,. \tag{3.2}$$

where q is the electric charge of the election $[C]$ and $n(\mathbf{x})$ and $p(\mathbf{x})$ describe the electron and hole densities $[cm^{-3}]$, respectively. The electric field can be calculated by using $E(\mathbf{x}) = -\nabla\phi(\mathbf{x})$. We assume that each material is uniform so that we may let the dielectric constant[2], $\epsilon_i(\mathbf{x})$, $[CV^{-1}cm^{-1}]$ be

$$\epsilon_i(\mathbf{x}) = \begin{cases} \epsilon_n, & \mathbf{x} \in \Omega_a \\ \epsilon_p, & \mathbf{x} \in \Omega_d, \end{cases} \tag{3.3}$$

where ϵ_n and ϵ_p are the dielectric constants of the EA and ED, respectively. The acceptor and donor regions are described by the volumes Ω_a and Ω_d, respectively.

In order to describe the distribution of the charge carriers, we must first set out some assumptions concerning the generation and recombination of these carriers in the EA and ED. To do so, we define the *electron affinity* by

$$\chi_n(\mathbf{x}) = \begin{cases} \chi_{n-}(= E_{CB}), & \mathbf{x} \in \Omega_a \\ \chi_{n+}(= LUMO), & \mathbf{x} \in \Omega_d \end{cases} \tag{3.4}$$

and the ionisation potential, as defined in Chapter 2, by

$$\chi_p(\mathbf{x}) = \begin{cases} \chi_{p-}(= E_{VB}), & \mathbf{x} \in \Omega_a \\ \chi_{p+}(= HOMO), & \mathbf{x} \in \Omega_d; \end{cases} \tag{3.5}$$

both χ_n and χ_p are measured in electron volts. The jump in electron affinity and the ionisation potential between the outer regions is large so that electrons/holes do not gain immediately the amount of energy required to move into the ED LUMO/EA valence band. The amount of energy needed is approximately equal to that of the band gap size between the outer regions. As discussed earlier, holes move towards the largest ionisation potential, i.e. towards the HOMO of the ED, which happens when the jump in χ_p at the interface is sufficiently large.

[2]The dielectric constant is a measure of how much a material polarizes subject to its chemical composition, thus it may take up a different value in each region of the device.

As the jump in electron affinity and ionisation potential at the interface is large, we assume that only electrons are present in the EA region, where we set $p(\mathbf{x}) = 0$. Similarly, in the ED region we let $n(\mathbf{x}) = 0$. Thus, if we assume no dopants, the Poisson equation becomes

$$\nabla (\epsilon_n \nabla \phi) = qn(\mathbf{x}), \qquad \text{for } \mathbf{x} \in \Omega_a, \tag{3.6}$$

$$\nabla (\epsilon_p \nabla \phi) = -qp(\mathbf{x}), \quad \text{for } \mathbf{x} \in \Omega_d. \tag{3.7}$$

We introduce $\mathbf{F_n}$ and $\mathbf{F_p}$ to denote the current density of electrons and holes respectively, and we define the total current flux, $\mathbf{J}$, to be

$$\mathbf{J}(\mathbf{x}) = \begin{cases} -q\mathbf{F_n}, & \mathbf{x} \in \Omega_a \\ q\mathbf{F_p}, & \mathbf{x} \in \Omega_d \end{cases} \tag{3.8}$$

where we align the positive current density direction for $\mathbf{J}(\mathbf{x})$ in the conventional direction from EA to ED. For our analysis, we consider that the cell operates in steady-state, therefore the conservation of current for each species are

$$\nabla \cdot \mathbf{F_n} = 0, \qquad \text{for } \mathbf{x} \in \Omega_a, \tag{3.9}$$

$$\nabla \cdot \mathbf{F_p} = 0, \qquad \text{for } \mathbf{x} \in \Omega_d, \tag{3.10}$$

where we have assumed no generation or recombination of free charge carriers in the bulk of the materials.

The motion of electrons and holes is driven by diffusion and drift. The drift depends on the electrochemical properties of the materials as discussed in Chapter 2, so we introduce the electrochemical potentials $[eV]$, $\psi_n(\mathbf{x})$ and $\psi_p(\mathbf{x})$, such that

$$\psi_n(\mathbf{x}) = \chi_n - q\phi(\mathbf{x}) \tag{3.11}$$

$$\psi_p(\mathbf{x}) = \chi_p - q\phi(\mathbf{x}), \tag{3.12}$$

and assume the currents are related to the electrochemical potentials and the density of electrons or holes by the drift-diffusion model:

$$\mathbf{F_n} = -\left(\mu_n \frac{n(\mathbf{x})}{q} \nabla \psi_n(\mathbf{x}) + D_n \nabla n(\mathbf{x})\right), \tag{3.13}$$

$$\mathbf{F_p} = -\left(\mu_p \frac{p(x)}{q} \nabla \psi_p(\mathbf{x}) + D_p \nabla p(\mathbf{x})\right), \tag{3.14}$$

where μ_n and μ_p are the mobilities $[cm^2V^{-1}s^{-1}]$ and D_n and D_p the diffusivities $[cm^2s^{-1}]$ of electrons in the EA and of holes in the ED, respectively. We assume that μ_n, μ_p, D_n and D_p are constant in each material.

Both mobility and diffusion of charges depend on material properties, such as scattering by impurities or vibrations (phonons) of the lattice, and are related by

$$\mu_{n,p} = \frac{q}{k_B T} D_{n,p}, \tag{3.15}$$

where k_B is the *Boltzmann constant* $[eVK^{-1}]$ and T the temperature $[K]$, which we assume to be constantt. This is known as the *Einstein relation* and can be derived from satisfying the equilibrium problem, as shown in Fraser [22]. This implies that D_n and D_p are also constant in each material.

In summary, assuming that χ_n is constant in the EA, the governing equations for the EA region, $\mathbf{x} \in \Omega_a$, are

$$\nabla \cdot (\epsilon_n \nabla \phi(\mathbf{x})) = q n(\mathbf{x}), \tag{3.16}$$

$$\nabla \cdot \left(\nabla n(\mathbf{x}) - \frac{q}{k_B T} n(\mathbf{x}) \nabla \phi(\mathbf{x})\right) = 0, \tag{3.17}$$

where the later is the divergence of (3.13). Similarly, we assume that χ_p is constant in the ED so that the governing equations for the ED region, $\mathbf{x} \in \Omega_d$ become

$$\nabla \cdot (\epsilon_p \nabla \phi(\mathbf{x})) = -q p(\mathbf{x}), \tag{3.18}$$

$$\nabla \cdot \left(\nabla p(\mathbf{x}) + \frac{q}{k_B T} p(\mathbf{x}) \nabla \phi(\mathbf{x})\right) = 0, \tag{3.19}$$

where again the latter is the divergence of (3.14).

The problem is completed by imposing relevant conditions at the ends of the de-

vice and the dye interface. We derive the peripheral (boundary) conditions and the interface conditions in the following sections.

3.3 Boundary Conditions

We assume that the anode/EA contact is at $z = -H_1$ and the cathode/ED contact is at $z = H_2$ and that both are Ohmic, i.e. there is neutral charge, reflected by $\nabla^2\phi(\mathbf{x}) = 0$ (see Figure 3.3). At the electrode contacts the boundary conditions must be consistent with the equilibrium conditions. Thus, we take $\hat{\mathbf{F}}_n \cdot \hat{\mathbf{n}} = 0$ in (3.13), with $\hat{n}$ as the outward pointing normal (pointing in the direction from EA to ED), and integrate to get

$$n(\mathbf{x}) = N_0 \exp\left(-\frac{\psi_n(\mathbf{x})}{k_B T}\right), \tag{3.20}$$

where N_0 is the effective density $[cm^{-3}]$ of available (i.e. empty) energy states in the conduction band of the EA for electrons to occupy. For zero applied voltage we let $\phi(x, -H_1) = 0$ to get

$$n(x, -H_1) = N_0 \exp\left(-\frac{\chi_{n-}}{k_B T}\right) \equiv N^-, \text{ say.} \tag{3.21}$$

We impose this condition at the boundary. Similarly, at the cathode contact, we set $\mathbf{F_p} = 0$ and integrate (3.14). If we define the *work function* to be the minimum energy required to remove an electron from a solid, then we define the *built-in* potential, V_{bi}, to be the difference between the work functions of the electrodes at the two ends of the device and impose the condition $\phi = V_{bi}$ at the cathode contact (for zero applied voltage). Thus we derive the following boundary condition for holes

$$p(x, H_2) = P_0 \exp\left(\frac{\chi_{p+} - qV_{bi}}{k_B T}\right) \equiv P^+, \text{ say,} \tag{3.22}$$

where P_0 is the effective density of available OMO in the ED that holes can occupy. The conditions (3.21) and (3.22) must be met when we have no recombination across the cell, thus the relation between N^- and P^+ must be

$$P^+ = \frac{N_0 P_0}{N^-} \exp\left(-\frac{E_g - qV_{bi}}{k_B T}\right), \tag{3.23}$$

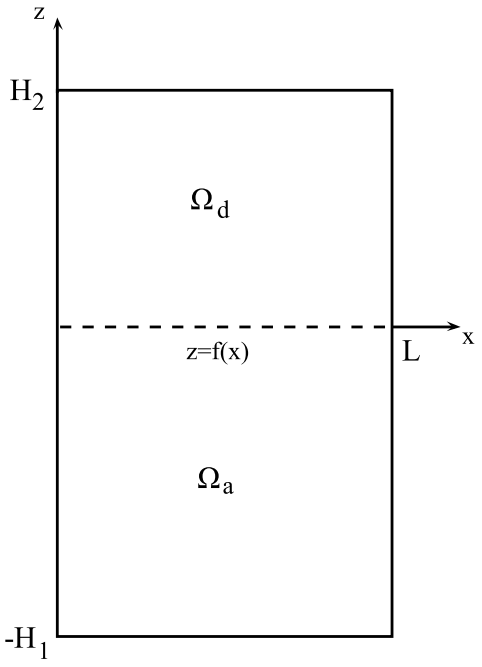

Figure 3.3: A schematic representation of the two dimensional approach of a typical cell with an EA/ED interface at $z = f(x)$. Note: The figure is not drawn to scale.

where $E_g = (\chi_{n-} - \chi_{p+})$ is a *pseudo*-band gap between the EA and ED.

However, the solar cell operates under applied bias via the external circuit. Hence, we define a reference potential to be

$$\phi(x, -H_1) = 0, \tag{3.24}$$

$$\phi(x, H_2) = V + V_{bi}, \tag{3.25}$$

where V is the applied voltage. Without loss of generality, we will set $V_{bi} = 0$ for the remainder of the thesis, although we note that a non-zero built-in voltage would increase the potential barrier needed by the charges to overcome in order to generate current and that this is typically of the order of $0.7 - 0.9\ V$ for this type of solar cells [61].

We assume that the cell has a width of L and set the x-boundaries at $x = 0$ and $x = L$. At these ends we assume that the device is in contact with a glass and,

therefore, no current is transported so we set

$$\frac{\partial \phi}{\partial x}\Big|_{(0,z)} = \frac{\partial \phi}{\partial x}\Big|_{(L,z)} = 0, \tag{3.26}$$

$$\frac{\partial n}{\partial x}\Big|_{(0,z)} = \frac{\partial n}{\partial x}\Big|_{(L,z)} = 0, \tag{3.27}$$

$$\frac{\partial p}{\partial x}\Big|_{(0,z)} = \frac{\partial p}{\partial x}\Big|_{(L,z)} = 0. \tag{3.28}$$

3.4 Interface condition

Given the assumption that, as measured in the z-direction (see Figure 3.2), the dye layer is thin compared to the height of the device, the potential (V) and the electric displacement ($\epsilon_{n,p}\nabla\phi(\mathbf{x})$) are continuous over the EA/ED interface. Thus, we impose

$$[\phi]_{z=f(x)} = 0, \qquad \left[\epsilon_i \frac{\partial \phi}{\partial \hat{n}}\right]_{z=f(x)} = 0, \tag{3.29}$$

where $\hat{n}$ is the outward normal to the interface.

Finally, we have the condition on the electron and hole fluxes at the Ω_a/Ω_d interface

$$\mathbf{F_n} \cdot \hat{\mathbf{n}} = -((1 - S(\mathbf{x}))G - S(\mathbf{x})R(\mathbf{x}), \tag{3.30}$$

$$\mathbf{F_p} \cdot \hat{\mathbf{n}} = (1 - S(\mathbf{x}))G - S(\mathbf{x})R(\mathbf{x}), \tag{3.31}$$

where G and $R(\mathbf{x})$ are the generation and recombination rates, respectively, and $S(\mathbf{x})$ describes the distribution of the dye coverage. Generation occurs only in the presence of dye while recombination occurs in dye-free interfaces. For the remainder of Part I, we will consider $G = 0$. Achieving full dye coverage of the interface is technically challenging, therefore $S < 1$. However, even if $S = 1$, there would still be some recombination, although neglible for the purposes of this analysis.

We restrict the range of values for the applied voltage that we use to explore the system, to exclude extreme behaviours, such as the Zener breakdown[3] in *reverse* bias (the opposite of forward bias). In particular, we concentrate on the regime in which

[3] A Zener breakdown occurs in large reverse bias, when the electric field enables electrons to tunnel from the valence to the conduction band allowing for current to flow in the opposite direction.

the cell operates, i.e. the forward bias regime ($0 < V$).

To derive an expression for the recombination rate, we consider the *short circuit* limit of the cell in the dark, i.e. when $\mathbf{F_n} = \mathbf{F_p} = 0$, so that the electron and hole densities on either side of the dye layer are found from (3.17), (3.19) and the boundary conditions (3.21) and (3.22) to be

$$n(\mathbf{x}) = N_0 \exp\left(-\frac{(\chi_{n-} - q\phi(\mathbf{x}))}{k_B T}\right) \tag{3.32}$$

$$p(\mathbf{x}) = P_0 \exp\left(\frac{\chi_{p+} - q\phi(\mathbf{x})}{k_B T}\right). \tag{3.33}$$

Then, at the interface between the two regions we have that

$$n_i p_i = N_0 P_0 \exp\left(-\frac{E_g}{k_B T}\right) \equiv \Pi_0^2, \quad \text{say,} \tag{3.34}$$

where n_i and p_i are the values of $n(x, f(x))$ and $p(x, f(x))$ at the interface, respectively. When the cell is in equilibrium, i.e. unbiased and in the dark, there must be no recombination in the cell and relation (3.34) holds. However, when voltage is applied, or the cell is illuminated, free charge carriers are generated which will tend to recombine (in order to restore the equilibrium). The excess generated carriers are given by $n(\mathbf{x})p(\mathbf{x}) - \Pi_0^2$, thus the recombination rate is proportional to this term, and inversely proportional to a recombination timescale, τ_R $[s]$, and the cross sectional area for electron capture by a hole in the ED, σ $[cm^2]$. Therefore, the recombination rate can be written as

$$R(\mathbf{x}) = \frac{n(\mathbf{x})p(\mathbf{x}) - \Pi_0^2}{\sigma \tau_R N_0 P_0}. \tag{3.35}$$

The recombination is direct (band-to-band, with no intermediate trap states) and the recombination rate has the typical form for *bimolecular recombination*, i.e. when the electron and hole that recombine do not come from the same molecule. We assume direct recombination for simplicity, although we note that it is more likely that recombination follows the Shockley-Read-Hall process, as also used in Richardson *et al* [43], or even a combination of both processes.

On the top ($z = H_2$) and bottom ($z = -H_1$), the cell is in contact with glass, which acts as an insulator. This does not allow for the presence of an electric field and also no charges may transport within the insulator. On each of these boundaries, we thus impose

$$\hat{\mathbf{n}} \cdot \nabla \phi(\mathbf{x}) = 0 \tag{3.36}$$

$$\hat{\mathbf{n}} \cdot \nabla n(\mathbf{x}) \cdot = \hat{\mathbf{n}} \cdot \nabla p(\mathbf{x}) = 0 \tag{3.37}$$

where $\hat{\mathbf{n}}$ is the outward pointing normal at each surface. In this case $\hat{\mathbf{n}} \cdot \nabla = \pm \frac{\partial}{\partial z}$.

3.5 Summary

Having set out our assumptions, we have derived the following mathematical problems for the electrostatic potential and the distribution of electrons and holes in the device. In the EA we solve

$$\nabla \cdot (\epsilon_n \nabla \phi(\mathbf{x})) = q n(\mathbf{x}), \tag{3.38}$$

$$\nabla n(\mathbf{x}) - \frac{q}{k_B T} n(\mathbf{x}) \nabla \phi(\mathbf{x}) = -\frac{\mathbf{F_n}}{D_n}, \tag{3.39}$$

and in the ED we solve

$$\nabla \cdot (\epsilon_p \nabla \phi(\mathbf{x})) = -q p(\mathbf{x}), \tag{3.40}$$

$$\nabla p(\mathbf{x}) + \frac{q}{k_B T} p(\mathbf{x}) \nabla \phi(\mathbf{x}) = -\frac{\mathbf{F_p}}{D_p}. \tag{3.41}$$

The boundary conditions at $z = H - 1$ are

$$\phi(x, -H_1) = 0, \tag{3.42}$$

$$n(x, -H_1) = N^-, \tag{3.43}$$

and at $z = H_2$

$$\phi(x, H_2) = V, \tag{3.44}$$

$$p(x, H_2) = P^+, \tag{3.45}$$

while we have assumed the absence of electrons n the ED regions and of holes in the EA region.

The boundary conditions at the x-boundaries are

$$\frac{\partial \phi}{\partial x}\Big|_{(0,z)} = \frac{\partial \phi}{\partial x}\Big|_{(L,z)} = 0, \tag{3.46}$$

$$\frac{\partial n}{\partial x}\Big|_{(0,z)} = \frac{\partial n}{\partial x}\Big|_{(L,z)} = 0, \tag{3.47}$$

$$\frac{\partial p}{\partial x}\Big|_{(0,z)} = \frac{\partial p}{\partial x}\Big|_{(L,z)} = 0. \tag{3.48}$$

At the EA/ED interface, we ensure continuity by imposing

$$[\phi]_{z=f(x)} = 0, \qquad \left[\epsilon_i \frac{\partial \phi}{\partial \hat{n}}\right]_{z=f(x)} = 0, \tag{3.49}$$

and set the electron flux to be proportional to the recombination rate below, by assuming no generation of current cause by illumination:

$$\mathbf{F_n} \cdot \hat{\mathbf{n}} = S(\mathbf{x}) \frac{n(\mathbf{x})p(\mathbf{x}) - \Pi_0^2}{\sigma \tau_R N_0 P_0}, \tag{3.50}$$

$$\mathbf{F_p} \cdot \hat{\mathbf{n}} = -S(\mathbf{x}) \frac{n(\mathbf{x})p(\mathbf{x}) - \Pi_0^2}{\sigma \tau_R N_0 P_0}. \tag{3.51}$$

In this Chapter, we have derived our mathematical model for charge transport in the outer regions and interface recombination of electrons and holes. In the following Chapters we apply this model on the bilayer and the nanostructured cells. In each case, we rescale the problem to allow for the identification of the key dimensionless parameters.

4

The bilayer cell

In this chapter we apply the model for the ssDSSC to a cell with a planar interface, as illustrated in Figure 3.1(a), in the case where $G = 0$. As a first step, we reduce the model given in (3.38)-(3.51), using symmetry, to a one dimensional problem in z, assuming uniformity in all other directions. We will rescale the model in order to allow for easier computations and identify, in this way, the key dimensionless parameters of the problem. We will solve for the exact solution, but also use asymptotic approximations to explore certain regimes of the operation of the cell. In the final parts of the Chapter, we will explore the two dimensional problem, by assuming various dye distribution scenarios.

4.1 The one-dimensional approximation

For the one dimensional approximation, we fix the EA/ED interface at $z = 0$ and seek to solve the model in the EA, described by the domain $\Omega_a = \{z \in [-H_1, 0]\}$, and in the ED, described by the domain $\Omega_d = \{z \in [0, H_2]\}$, as shown in Figure 4.1. We consider that the applied voltage, V, is known and seek to solve for the current fluxes,

F_n and F_p. We assume that the physical parameters (ϵ_i, $'mu_i$, D_i) are constant in each of the EA and ED layers.

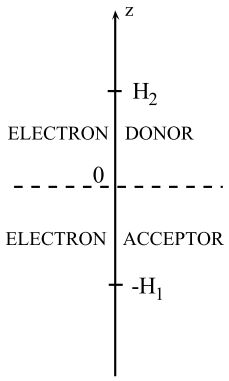

Figure 4.1: A schematic representation of the one dimensional approach of a bilayer cell. Note: The figure is not drawn to scale.

We also shift our reference potentials by $-\frac{V}{2}$ so that the boundary conditions for ϕ read

$$\phi|_{z=-H_1} = -\frac{V}{2} \qquad \phi|_{z=H_2} = \frac{V}{2} \tag{4.1}$$

and $\phi|_{z=0} = 0$.

The governing equations in the EA region are

$$(\epsilon_n \phi_z)_z = qn, \tag{4.2}$$

$$n_z - \frac{qn}{k_B T}\phi_z = -\frac{F_n}{D_n}, \tag{4.3}$$

where $(U)_z = \frac{dU}{dz}$ and F_n is a constant from (3.9). The governing equations in the ED region are

$$(\epsilon_p \phi_z)_z = -qp, \tag{4.4}$$

$$p_z + \frac{qp}{k_B T}\phi_z = -\frac{F_p}{D_p}, \tag{4.5}$$

where F_p is constant from (3.10).

Table 4.1: Definition of non-dimensional variables.

Dimensional variables	Normalised as	Value	Reference
τ	τ_R	$10^{-5} - 10^{-6}\ s$	[27]
z	$H_1 \times \hat{z}$	$1 \times 10^{-7}\ m$	[27]
(n, p)	$\Pi_0 \times (\hat{n}, \hat{p})$	$10^{19} - 10^{22}\ cm^{-3}$	[62]
(F_n, F_p)	$\frac{D_n \Pi_0}{H_1} \times (\hat{F}_n, \hat{F}_p)$	$2.58 \times 10^{16}\ cm^{-2}C^{-1}$	[10]
(ϕ, V)	$\frac{k_B T}{q} \times (\hat{\phi}, \hat{V})$	$0.0259\ V$	[43]

The relevant boundary conditions are

$$n(-H_1) = N^-, \quad \phi(-H_1) = -\frac{V}{2}, \tag{4.6}$$

$$p(H_2) = P^+, \quad \phi(H_2) = \frac{V}{2}, \tag{4.7}$$

and the interface conditions, with $S(z) = S$, are:

$$F_n(0^-) = SR, \tag{4.8}$$

$$F_p(0^+) = -SR, \tag{4.9}$$

with

$$R = \frac{n(0^-)p(0^+) - \Pi_0^2}{\sigma \tau_R N_0 P_0}. \tag{4.10}$$

At the interface we also have

$$\phi(0) = 0 \quad \text{and} \quad \epsilon_n \phi(0^-) = \epsilon_p \phi(0^+). \tag{4.11}$$

We nondimensionalise the problem using the scalings in 4.1. We choose to rescale both outer regions by the size of the parameters in the EA region.

We rescale the system (4.2)-(4.2) for the EA problem and get $\hat{F}_n = \frac{F_n H_1}{D_n \Pi_0}$, which is the non-dimensionalised electron current flux. By dropping the hats, the problem reads

$$\frac{d^2\phi}{dz^2} = \Lambda n, \tag{4.12}$$

$$F_n = -\left(\frac{dn}{dz} - n\frac{d\phi}{dz}\right), \tag{4.13}$$

where $\Lambda = q^2 H_1^2 \frac{\Pi_0}{k_B T \epsilon_n}$, which is the square of ratio of the thickness of the EA layer

to the Debye length. The boundary conditions reduce to

$$\phi(-1) = -\frac{V}{2}, \qquad n(-1) = \frac{N^-}{\Pi_0} \equiv \hat{N}^-, \tag{4.14}$$

$$F_n(0^-) = -\delta SR, \qquad \phi(0) = 0, \tag{4.15}$$

with $\delta = \frac{H_1}{\sigma\tau_R D_n N_0 P_0}$ being the recombination coefficient and $R = np - 1$.

Similarly, we rescale the system (4.4)-(4.5) for the ED problem and get $\hat{F}_p = \frac{F_p H_1}{\Pi_0 D_n}$, which is the non-dimensionalised hole current flux. By dropping the hats, the problem reduces to

$$\frac{d^2\phi}{dz^2} = -\frac{\Lambda}{\hat{\epsilon}_p} p, \tag{4.16}$$

$$F_p = -\hat{D}_p \left(\frac{dp}{dz} + p\frac{d\phi}{dz} \right), \tag{4.17}$$

where $\hat{D}_p = \frac{D_p}{D_n}$ and $\hat{\epsilon}_p = \frac{\epsilon_p}{\epsilon_n}$. The boundary conditions reduce to

$$\phi(m) = \frac{V}{2}, \qquad p(m) = \frac{P^+}{\Pi_0} \equiv \hat{P}^+, \tag{4.18}$$

$$F_p(0^+) = -\delta SR \qquad \phi(0) = 0, \tag{4.19}$$

with $m = \frac{H_2}{H_1}$. The final two conditions on the electric potential are reduced to their one-dimensional equivalent:

$$[\phi]_{z=0} = 0, \qquad \left[\hat{\epsilon}_i \frac{\partial\phi}{\partial z} \right]_{z=0} = 0, \tag{4.20}$$

where

$$\hat{\epsilon}_i = \begin{cases} 1 & -1 \le z < 0 \\ \hat{\epsilon}_p & 0 < z \le m. \end{cases} \tag{4.21}$$

All dimensionless parameters appearing in (4.12)-(4.20) along with their approximate size, are listed in Table 4.2.

We, further, set $m = 1$, $\hat{D}_p = \hat{\epsilon}_p = 1$ and $\hat{N}^- = \hat{P}^+ = 1$. Then n, p and the electric field, E, are symmetric and ϕ is antisymmetric across $z = 0$. This allows us to solve only for one of the two regions and then use symmetry (or antisymmetry) to

Table 4.2: The dimensionless parameters

Dimensionless Parameter	Equals	Size
m	$\frac{H_2}{H_1}$	$\sim O(10^1)$
$\hat{\epsilon}_p$	$\frac{\epsilon_p}{\epsilon_n}$	$\sim O(10^{-2})$
$\hat{D}_p$	$\frac{D_p}{D_n}$	$\sim O(10^{-1})$
Λ	$q^2 H_1^2 \frac{\Pi_0}{k_B T \epsilon_n}$	$\sim O(1)$
δ	$\frac{H_1}{\sigma \tau_R D_n N_0 P_0}$	$\sim O(10^{-4})$

find the behaviour of the (corresponding) variable in the other region, i.e.

$$n(z) = p(-z) \qquad \phi(-z) = -\phi(z). \tag{4.22}$$

As the applied voltage increases, a large built-up of electric field at the interface drives the operation of the cell. This allows us to use an asymptotic approach to understand it more in depth.

4.2 Cell with symmetric parameters

In this section we present the one dimensional solution for a cell with symmetric properties. In particular, we solve for the electron acceptor problem; the solution to the electron donor problem by using the (anti-) symmetry properties described in (4.22). Analytical and numerical results are presented in the analysis that follows.

We substitute for n from (4.12) into (4.13), which gives

$$-\Lambda F_n = \phi_{zzz} - \phi_{zz}\phi_z \tag{4.23}$$

with boundary conditions

$$\phi = -\frac{V}{2}, \quad \phi_{zz} = \Lambda, \quad \text{at} \;\; z = -1 \tag{4.24}$$

$$\phi = 0, \quad F_n = \delta S \left(\frac{\phi_{zz}^2}{\Lambda^2} - 1 \right) \quad \text{at} \;\; z = 0. \tag{4.25}$$

The expression for the latter, was derived by substituting for n and p from (4.12) and (4.16).

4.2.1 Exact Solution

An exact solution can be found for the problem (4.23)-(4.25), as follows. By integrating (4.23) once, we get the *Riccati* equation

$$\phi_{zz} - \frac{\phi_z^2}{2} = -\Lambda F_n z + constant, \tag{4.26}$$

and then use the transformation $\psi = \exp\left(-\frac{\phi}{2}\right)$ to reduce (4.26) to the *Airy* equation

$$\psi_{zz} - \frac{F_n \Lambda}{2}(z + C_1)\,\psi = 0 \tag{4.27}$$

where C_1 is an arbitrary constant. If we let $\chi = \left(\frac{F_n\Lambda}{2}\right)^{\frac{1}{3}}$ and $\omega = \left(\frac{F_n\Lambda}{2}\right)^{\frac{1}{3}} C_1$, the solution is then [1]

$$\phi = -2\log\left[\frac{\left(e^{\frac{V}{4}}\,\mathrm{Bi}(\omega) - \mathrm{Bi}(\omega-\chi)\right)\mathrm{Ai}(\omega+\chi z) - \left(e^{\frac{V}{4}}\,\mathrm{Ai}(\omega) - \mathrm{Ai}(\omega-\chi)\right)\mathrm{Bi}(\omega+\chi z)}{\mathrm{Ai}(\omega-\chi)\,\mathrm{Bi}(\omega) - \mathrm{Ai}(\omega)\,\mathrm{Bi}(\omega-\chi)}\right] \tag{4.28}$$

where χ and ω can be obtained by solving the transcendental equations, for a given V:

$$\Lambda = 2\chi^2\left[\left(\frac{\mathrm{Bi}(\omega)\,\mathrm{Ai}'(\omega-\chi) - \mathrm{Ai}(\omega)\,\mathrm{Bi}'(\omega-\chi) + \frac{e^{-\frac{V}{4}}}{\pi}}{\mathrm{Bi}(\omega)\,\mathrm{Ai}(\omega-\chi) - \mathrm{Ai}(\omega)\,\mathrm{Bi}(\omega-\chi)}\right)^2 - (\omega-\chi)\right] \tag{4.29}$$

$$2\chi^3 = \delta S\Lambda\left[\frac{4\chi^4}{\Lambda^2}\left(\left(\frac{\mathrm{Ai}(\omega-\chi)\,\mathrm{Bi}'(\omega) - \mathrm{Bi}(\omega-\chi)\,\mathrm{Ai}'(\omega) - \frac{e^{\frac{V}{4}}}{\pi}}{\mathrm{Bi}(\omega)\,\mathrm{Ai}(\omega-\chi) - \mathrm{Ai}(\omega)\,\mathrm{Bi}(\omega-\chi)}\right)^2 - \omega\right)^2 - 1\right], \tag{4.30}$$

which are obtained by using (4.28) into the boundary relations (4.24) and (4.25). By solving (4.29) and (4.30) we produce current density-voltage curves, as shown in Figure 4.2. We observe that the voltage increases as the current density increases. Of particular interest is that a smaller δ requires a larger voltage to overcome the recombination at the interface and produce current. A small δ implies either a lower recombination rate wither through slower recombination timescale or through a large number of available free charge carriers for recombination. Figure 4.2 shows that

[1] We have made use of the identity: $\mathrm{Ai}(y)\,\mathrm{Bi}'(y) - \mathrm{Ai}'(y)\,\mathrm{Bi}(y) = \frac{1}{\pi}$

at low voltages the solar cell behaves as a diode, with an exponential relationship between the current density and the voltage, while at larger voltages the cell behaves as an Ohmic resistor with a linear relationship between F_n and V.

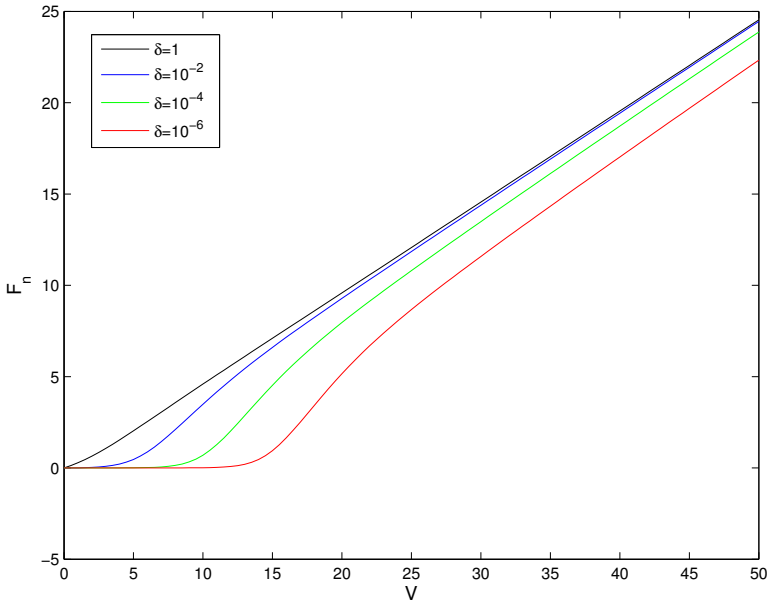

Figure 4.2: Current density against the applied voltage as given by the exact solution for various values of δ [Parameters: $S = 0.5,\ \Lambda = 1$]

In Figure 4.3 we present the exact solutions for the electrostatic potential and the electron concentration in the EA region under increasing forward bias ($V > 0$). The increasing slope of the electrostatic potential near the interface at $z = 0$, as δ decreases, as shown in Figure 4.3(a), indicates that drift, represented by $(\phi_{zz}\phi_z)$ in (4.23), increases through the build-up of concentration near the interface. The corresponding concentration of electrons is shown in Figure 4.3(b). For larger values of applied potential, V, these behaviours are exaggerated as shown in Figures 4.3(c) for ϕ and 4.3(d) for n. As V increases and $\delta \to 0$, we observe a boundary layer forming in the distribution of ϕ near the interface.

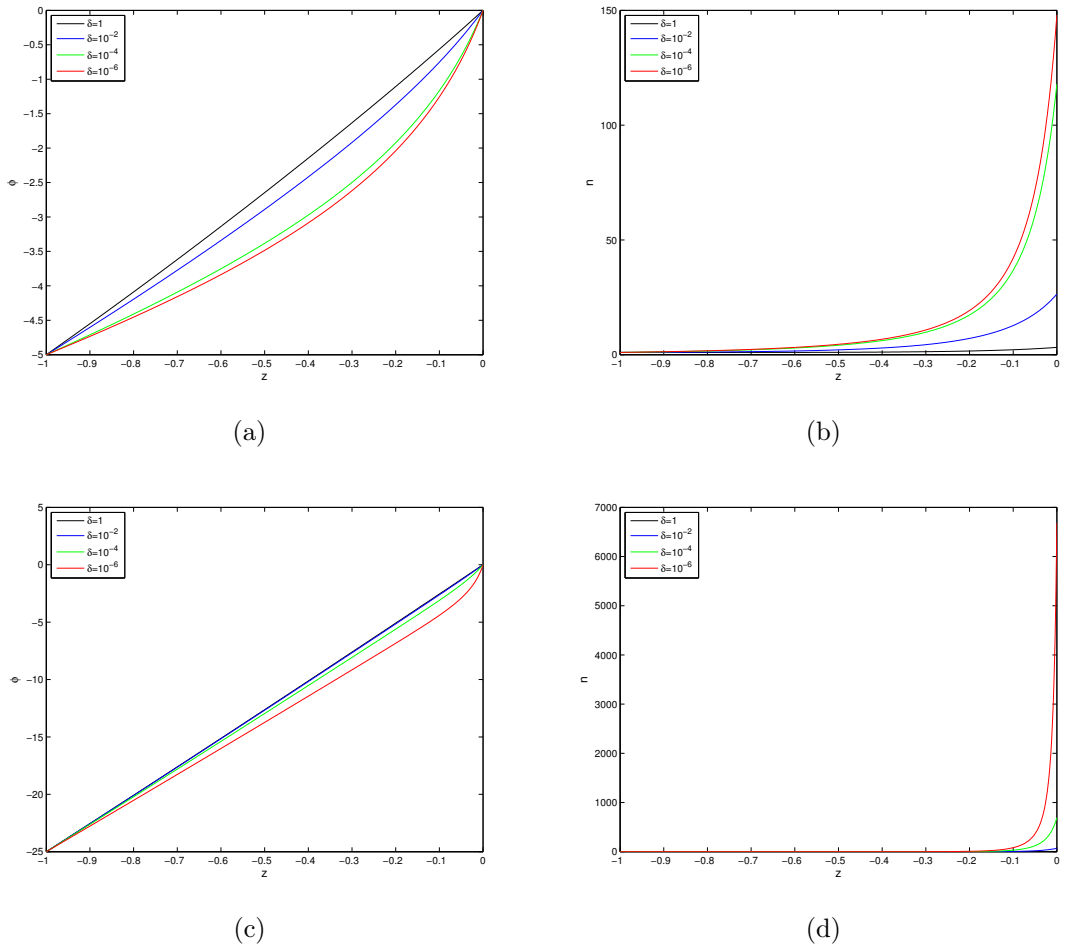

Figure 4.3: Exact solution for V=10 for (a) ϕ and (b) n and for V=50 for (c) ϕ and (d) n. [Parameters: $S = 0.5,\ \Lambda = 1$]

While the problem has an exact solution for the simple case we are considering here, it is worth exploring a solution to the more general problem which would be valid as we consider less assumptions. In what follows we consider the formation of a boundary layer when $0 < \delta \ll 1$, which allows us to generate asymptotic solutions for a large range of values for the applied voltage.

4.2.2 Asymptotic Analysis

The exact solution suggests that, by increasing the applied voltage, V, a boundary layer forms near the interface ($z = 0$), in the solution of the electrostatic potential. We, therefore, identify three current/voltage regimes: (i) where drift and diffusion counterbalance each other ('small current regime'), (ii) where drift dominates ('large

current regime') in the bulk of the outer regions and (iii) a transitional regime between the two ('intermediate regime'). The exploration of these regimes using asymptotic methods in the limit $\delta \to 0$ for the various sizes of V is now presented.

4.2.2.1 Small Current Regime

As $\delta \to 0$, given V and all other parameters and variables to be of $O(1)$, the current is small, i.e. $F_n = O(\delta)$, by (4.25). Under this assumption we assume the asymptotic expansions

$$F_n \approx \delta F_{n1} + ... \tag{4.31}$$

$$\phi \approx \phi_0 + \delta\phi_1 + ... \tag{4.32}$$

$$n \approx n_0 + \delta n_1 + ... \tag{4.33}$$

By putting these into (4.23)-(4.25), and balancing terms by the order of powers of δ, we obtain

$$O(1): \quad \phi_{0zzz} - \phi_{0z}\phi_{0zz} = 0 \tag{4.34}$$

$$O(\delta): \quad \phi_{1zzz} - \phi_{0z}\phi_{1zz} - \phi_{1z}\phi_{0zz} = -\Lambda F_{n1} \tag{4.35}$$

with

$$\phi_0(-1) = -\frac{V}{2}, \quad \phi_1(-1) = 0, \quad \phi_{0zz}(-1) = \Lambda, \quad \phi_{1zz}(-1) = 0 \tag{4.36}$$

$$\phi_0(0) = 0, \quad \phi_1(0) = 0, \quad F_{n1} = S\left(\frac{\phi_{0zz}^2(0)}{\Lambda^2} - 1\right) \tag{4.37}$$

We divide (4.34) through by ϕ_{0zz} ($\phi_{0zz} \neq 0$, as that would imply the absence of electrons) and integrate once to get $\log(\phi_{zz}) - \phi_0 = constant$. We apply the boundary conditions for ϕ_0 in (4.36) to get

$$\phi_{0zz} = \Lambda \exp\left(\phi_0 + \frac{V}{2}\right) \tag{4.38}$$

which can be used in (4.37)c to give the small current approximation for the current density:

$$F_n = \delta S\left(e^V - 1\right). \tag{4.39}$$

In forward bias (i.e. when $F_n > 0$ or equivalently $V > 0$) the current increases rapidly. In reverse bias ($V < 0$), only a small current flows due to the electrochemical properties of the cell (as explained in Chapter 2), which restrict the flow of current in the opposite direction by inreasing the energy barrier at the EA/ED interface. In particular, in reverse bias, the current generation saturates at $F_n = -\delta S$. Similarly to a diode, the ssDSSC allows for current to pass through easily only in one direction, while restricting it in the other.

Now, to obtain an analytic approximate solution for ϕ we return to the leading-order problem and solve for ϕ. We integrate (4.34) once to get

$$\phi_{0zz} - \frac{\phi_{0z}^2}{2} = A_0 \tag{4.40}$$

and then use the transformation $\phi_0 = -2\log(\psi)$ so that we may write (4.40) as

$$\psi_{zz} + \frac{A_0}{2}\psi = 0. \tag{4.41}$$

Depending on the sign of A_0 we may write the solution in the following ways.
(i) For $A_0 = 0$ we may write

$$\phi_0 = -2\log\left(\left(1 - e^{\frac{V}{4}}\right)z + 1\right) \tag{4.42}$$

where, by applying the boundary conditions (4.36) the following relation must be satisfied

$$\Lambda = 2\left(e^{-\frac{V}{4}} - 1\right)^2. \tag{4.43}$$

(ii) For $A_0 < 0$, we let $A_0 = -2\omega^2$ and, by imposing (4.36) and (4.37), we get

$$\phi_0 = -2\log\left[\frac{\sinh(\omega(z+1)) - e^{-\frac{V}{4}}\sinh(\omega z)}{\sinh(\omega)}\right], \tag{4.44}$$

where (4.36)c requires that

$$\Lambda e^{\frac{V}{2}}\left(\cosh(2\omega) - 1\right) = 4\omega^2\left(1 + e^{\frac{V}{2}} - 2e^{\frac{V}{4}}\cosh(\omega)\right). \tag{4.45}$$

(iii) For $A_0 > 0$, we let $A_0 = 2\omega^2$ and , by imposing (4.36) and (4.37), we get

$$\phi_0 = -2\log\left[\frac{\sin(\omega(z+1)) - e^{-\frac{V}{4}}\sin(\omega z)}{\sin(\omega)}\right], \tag{4.46}$$

where (4.36)c requires that

$$\Lambda e^{\frac{V}{2}}\left(1-\cos(2\omega)\right) = 4\omega^2\left(1 + e^{\frac{V}{2}} - 2e^{\frac{V}{4}}\cos(\omega)\right). \tag{4.47}$$

The asymptotic solution for ϕ_0 in the small current regime can thus be expressed in the forms of (4.42), (4.44) or (4.46), depending on the sign of A_0 (or the value of V given the conditions (4.43), (4.45) and (4.47)). In Figure 4.4 we show a comparison between the exact solution (4.28)-(4.30) and the asymptotic in the small current regime for forward bias. This approximation fails when $V \sim O\left(\log\left(\frac{1}{\delta}\right)\right)$, or equivalently when $F_n \sim O(1)$, since (4.39) no longer balances. This suggests the subsequent regime which we term as the intermediate current regime and analyse in the next section.

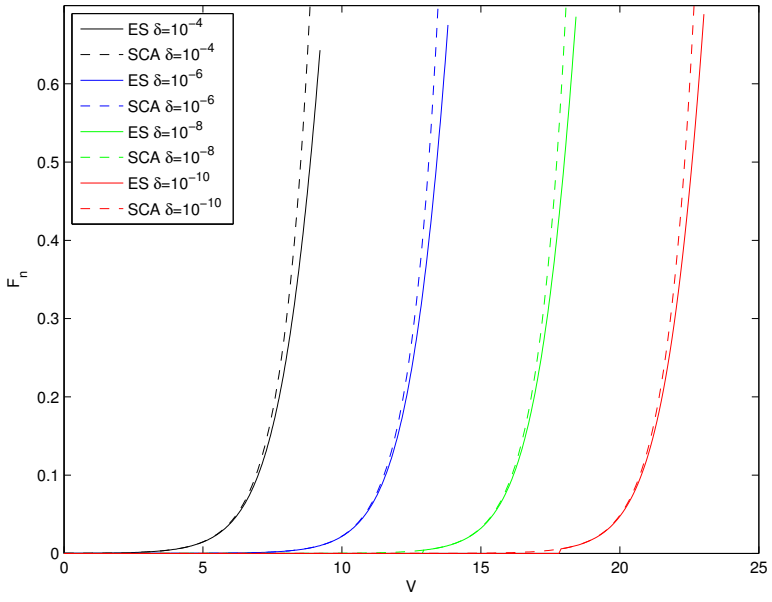

Figure 4.4: Current density against voltage plotted using the exact solution (ES; solid line) and the small current approximation (SCA; broken line) for the range V$=\left[0, \log\left(\frac{1}{\delta}\right)\right]$ for varying values of δ. [Parameters: $S = 1,\ \Lambda = 1$]

4.2.2.2 Intermediate current approximation

As we increase the applied voltage for small values of δ, a rapid change in the potential near the dye interface is apparent as depicted in Figure 4.3, which the small current approximation (SCA) can no longer predict. As suggested by the plots in Figure 4.3, we assume the presence of a boundary layer in the vicinity of $z = 0$ (inner solution) in the solution for ϕ and n, in which drift and siffusion balance, as opposed to the bulk regions (i.e. away from $z = 0$) where drift dominates.

Outer Solution

As discussed earlier, the small current approximation fails when (4.39) no longer balances, i.e. when $V = O(\log(\delta^{-1}))$. Thus, we introduce $\epsilon^{-1} = \log\left(\frac{1}{\delta}\right)$ and the asymptotic expansions

$$\phi = \epsilon^{-1}\Phi^{(o)} = \epsilon^{-1}\Phi_0^{(o)} + \Phi_1^{(o)} + \epsilon\Phi_2^{(o)} + ... \tag{4.48}$$

$$V = \epsilon^{-1}V_0 + V_1 + \epsilon V_2 + ... \tag{4.49}$$

where the superscript $^{(o)}$ is used to indicate the solution away from $z = 0$, referred to as the *outer* solution. We allow $F_n \sim O(1)$ and seek to find the solution given V. The problem (4.23)-(4.25) reduces to:

$$O\left(\log^2(\delta^{-1})\right): \quad \Phi_{0z}^{(o)}\Phi_{0zz}^{(o)} = 0 \tag{4.50}$$

$$O\left(\log(\delta^{-1})\right): \quad \Phi_{0zzz}^{(o)} - \Phi_{0z}^{(o)}\Phi_{1zz}^{(o)} - \Phi_{1z}^{(o)}\Phi_{0zz}^{(o)} - 0 \tag{4.51}$$

$$O(1): \quad \Phi_{1zzz}^{(o)} - \Phi_{1z}^{(o)}\Phi_{1zz}^{(o)} - \Phi_{0z}^{(o)}\Phi_{2zz}^{(o)} - \Phi_{2z}^{(o)}\Phi_{0zz}^{(o)} = -\Lambda F_n, \tag{4.52}$$

with boundary conditions for the two leading-order terms, for which we will be solving, to be

$$\Phi_0^{(o)}(-1) = -\frac{V_0}{2}, \quad \Phi_1^{(o)}(-1) = -\frac{V_1}{2}, \quad \Phi_{0zz}^{(o)}(-1) = 0, \quad \Phi_{1zz}^{(o)}(-1) = \Lambda. \tag{4.53}$$

If we assume that $\Phi_{0z}^{(o)} \neq 0$, we must have that $\Phi_{0zz}^{(o)} = 0$. This implies that $\Phi_{1zz}^{(o)} = 0$ from (4.51), which contradicts the boundary condition (4.53)d. Thus $\Phi_{0z}^{(o)} = 0$ which, together with (4.53)a, gives

$$\Phi_0^{(o)} = -\frac{V_0}{2}. \tag{4.54}$$

The $O(1)$ problem gives the general solution for $\Phi_1^{(o)}$ to be

$$\Phi_1^{(o)} = -2\log\left(\alpha\,\mathrm{Ai}(\omega+\chi z)+\beta\,\mathrm{Bi}(\omega+\chi z)\right), \tag{4.55}$$

where ω is an arbitrary constant and $\chi = \left(\frac{\Lambda F_n}{2}\right)^{\frac{1}{3}}$ is known. The values for the unknown parameters α and β are found by matching with the inner solution.

Inner Solution

To find the width of the boundary layer near the interface at $z = 0$ we use (4.25)b to define the inner variable, which we find to be

$$z = \delta^{\frac{1}{4}}\zeta \tag{4.56}$$

and we let

$$\Phi^{(i)} = \epsilon^{-1}\Phi^{(o)}, \tag{4.57}$$

where the superscript $^{(i)}$ is used to indicate the solution near the interface at $z = 0$, or, else, the *inner* solution. Then the leading-order inner problem for $\Phi^{(i)}$ reads

$$\Phi^{(i)}_{\zeta\zeta\zeta} - \Phi^{(i)}_{\zeta\zeta}\Phi^{(i)}_{\zeta} = 0, \tag{4.58}$$

which must satisfy the boundary conditions

$$\Phi^{(i)}(0) = 0, \quad \Phi^{(i)}_{\zeta\zeta}(0) = \Lambda\sqrt{\frac{F_n}{S}}. \tag{4.59}$$

In order for matching to be possible, we find that we must choose the following form of the solution

$$\Phi^{(i)} = -2\log\left(1-\left(\frac{\Lambda}{2}\right)^{\frac{1}{2}}\left|\frac{F_n}{S}\right|^{\frac{1}{4}}\zeta\right), \tag{4.60}$$

which satisfies (4.58) and (4.59). We note that there are no unknown parameters in (4.60).

Matching

We use the Van Dyke matching principle to get a composite solution that is valid

in both the inner and outer region. Following the Van Dyke notation, we use mto to denote the mth-order term of the outer asymptotic expansion (in the outer variable) and qti to denote the qth-order term of the inner asymptotic expansion (in the inner variable). The principle requires that the q-term inner expansion of the m-term outer expansion matches with the m-term of the q-term inner expansion, or that $qti(mto) = mto(qti)$.

Outer Solution:

$$1ti(1to) = \epsilon^{-1}\Phi_0^{(o)} = -\epsilon^{-1}\frac{V_0}{2} \tag{4.61}$$

$$(2to) = \epsilon^{-1}\Phi_0^{(o)+}\Phi_1^{(o)} = -\epsilon^{-1}\frac{V_0}{2} - 2\log\left(\alpha\,\mathrm{Ai}(\omega+\chi z) + \beta\,\mathrm{Bi}(\omega+\chi z)\right) \tag{4.62}$$

$$i(2to) = -\epsilon^{-1}\frac{V_0}{2} - 2\log\left(\alpha\,\mathrm{Ai}(\omega+\chi\delta^{\frac{1}{4}}\zeta) + \beta\,\mathrm{Bi}(\omega+\chi\delta^{\frac{1}{4}}\zeta)\right) \tag{4.63}$$

$$\approx -\epsilon^{-1}\frac{V_0}{2} - 2\log\left(\alpha\,\mathrm{Ai}(\omega) + \beta\,\mathrm{Bi}(\omega) + \left(\alpha\,\mathrm{Ai}'(\omega) + \beta\,\mathrm{Bi}'(\omega)\right)\chi\delta^{\frac{1}{4}}\zeta + ...\right) \tag{4.64}$$

$$2ti(2to) = -\epsilon^{-1}\frac{V_0}{2} - 2\log\left(\alpha\,\mathrm{Ai}(\omega) + \beta\,\mathrm{Bi}(\omega) + \left(\alpha\,\mathrm{Ai}_z(\omega) + \beta\,\mathrm{Bi}_z(\omega)\right)\chi z + ...\right) \tag{4.65}$$

Inner Solution:

$$(1ti) = \Phi^{(i)} = -2\log\left(1 - \left(\frac{\Lambda}{2}\right)^{\frac{1}{2}}\left(\frac{F_n}{S}\right)^{\frac{1}{4}}\zeta\right), \tag{4.66}$$

$$o(1ti) = -2\log\left(1 - \left(\frac{\Lambda}{2}\right)^{\frac{1}{2}}\left(\frac{F_n}{S}\right)^{\frac{1}{4}}\delta^{-\frac{1}{4}}z\right) \tag{4.67}$$

$$= -2\log\left(\delta^{-\frac{1}{4}}\left(\delta^{\frac{1}{4}} - \left(\frac{\Lambda}{2}\right)^{\frac{1}{2}}\left(\frac{F_n}{S}\right)^{\frac{1}{4}}z\right)\right) \tag{4.68}$$

$$= -\frac{\epsilon^{-1}}{2} - 2\log\left(\delta^{\frac{1}{4}} - \left(\frac{\Lambda}{2}\right)^{\frac{1}{2}}\left(\frac{F_n}{S}\right)^{\frac{1}{4}}z\right) \tag{4.69}$$

$$1to(1ti) = -\frac{\epsilon^{-1}}{2} \tag{4.70}$$

$$2to(2ti) = -\frac{\epsilon^{-1}}{2} - 2\log\left(-\left(\frac{\Lambda}{2}\right)^{\frac{1}{2}}\left(\frac{F_n}{S}\right)^{\frac{1}{4}} z\right). \tag{4.71}$$

Matching $1ti(1to) = 1to(1ti)$ gives

$$\Phi_0^{(o)} = -\frac{1}{2} \quad \text{and} \quad V_0 = 1. \tag{4.72}$$

Matching $2ti(2to) = 2to(2ti)$ gives

$$\alpha\,\mathrm{Ai}(\omega) + \beta\,\mathrm{Bi}(\omega) = 0, \tag{4.73}$$

$$(\alpha\,\mathrm{Ai}'(\omega) + \beta\,\mathrm{Bi}'(\omega))\,\chi = -\left(\frac{\Lambda}{2}\right)^{\frac{1}{2}}\left(\frac{F_n}{S}\right)^{\frac{1}{4}}. \tag{4.74}$$

Using (4.73) and (4.74) we solve to find

$$\Phi_1^{(o)} = -\log\left(\left|\frac{F_n}{S}\right|^{\frac{1}{2}}\frac{\Lambda}{2}\right) - 2\log\left|\frac{\pi}{\chi}\left(\mathrm{Ai}(\omega)\,\mathrm{Bi}(\omega+\chi z) - \mathrm{Bi}(\omega)\,\mathrm{Ai}(\omega+\chi z)\right)\right|, \tag{4.75}$$

by using the identity: $\mathrm{Ai}(y)\,\mathrm{Bi}'(y) - \mathrm{Ai}'(y)\,\mathrm{Bi}(y) = \frac{1}{\pi}$. To find the remaining unknowns, i.e. ω and F_n, given V, we use the boundary conditions (4.24) and (4.25) which give us that

$$-\frac{V_1}{2} = -\log\left(\left|\frac{F_n}{S}\right|^{\frac{1}{2}}\frac{\Lambda}{2}\right) - 2\log\left|\frac{\pi}{\chi}\left(\mathrm{Ai}(\omega)\,\mathrm{Bi}(\omega-\chi) - \mathrm{Bi}(\omega)\,\mathrm{Ai}(\omega-\chi)\right)\right| \tag{4.76}$$

$$\Lambda = -2\chi^2(\omega-\chi) + 2\chi^2\left(\frac{\mathrm{Ai}(\omega)\,\mathrm{Bi}_z(\omega-\chi) - \mathrm{Bi}(\omega)\,\mathrm{Ai}_z(\omega-\chi)}{\mathrm{Ai}(\omega)\,\mathrm{Bi}(\omega-\chi) - \mathrm{Bi}(\omega)\,\mathrm{Ai}(\omega-\chi)}\right)^2. \tag{4.77}$$

The composite solution valid everywhere can be written as

$$\phi^{(c)} = \epsilon^{-1}\Phi_0^{(o)} + \Phi_1^{(o)} + \Phi^{(i)} - \underbrace{\left\{-\frac{\epsilon^{-1}}{2} - 2\log\left(-\left(\frac{\Lambda}{2}\right)^{\frac{1}{2}}\left(\frac{F_n}{S}\right)^{\frac{1}{4}} z\right)\right\}}_{\text{common part}}. \tag{4.78}$$

We observe that (4.76) is valid for when $V_1 = O(\epsilon^{-1})$ and $F_n = O(1)$, as anticipated. Sample plots of the intermediate current approximation are displayed in Figure 4.5 for

various (small) values of δ. The approximation fits well in the regime and indicating the point of failure to be when V and F_n become order . Next we shall consider the large current approximation.

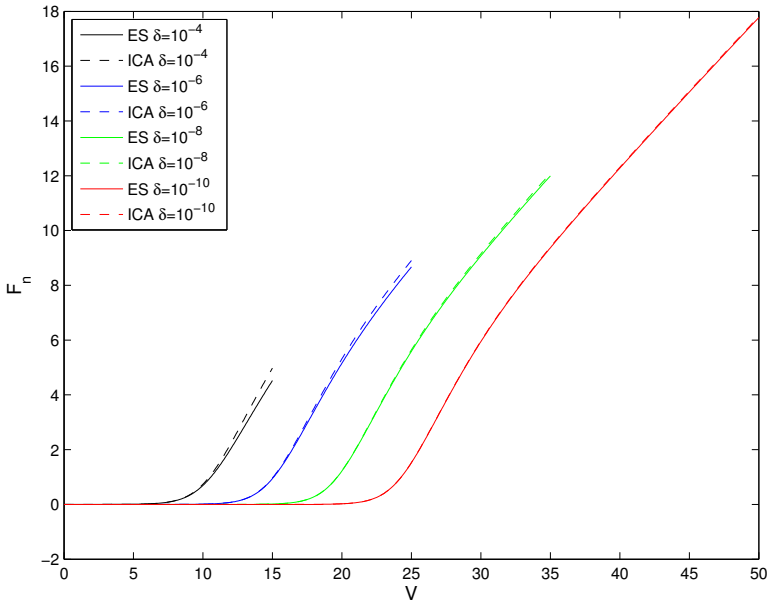

Figure 4.5: Current density against voltage with the exact solution (ES; solid line) and the intermediate current approximation (ICA; broken line) for V=$O\left[\log\left(\frac{1}{\delta}\right)\right]$ for varying values of δ. [Parameters: $S = 1,\ \Lambda = 1$]

In our analysis of the intermediate current regime, we have observed that drift and diffusion balance in the inner layer at a quas-equilibrium state, while all terms balance in the outer region. Therefore, we have found two separate solutions for the region near and the region away from the interface at $z = 0$ and used Van Dyke's matching principles to find a universal solution. The solution is valid when $V = O(\epsilon^{-1})$ and $F_n = O(1)$. However, when F_n increases to $O\left(\epsilon^{-1}\right)$, V_1 is no longer of the same order. Thus the asymptotic approximation for V fails when[2] $V_1 = O\left(\log\left(\epsilon^{-1}\right)\right)$, which hints at the asymptotic expansion for the large current approximation for the voltage.

[2]We note $\log\left(\epsilon^{-1}\right) \gg \log\left(\frac{1}{\delta}\right) \gg \delta$.

4.2.2.3 Large current approximation

In the large current regime we have deduced that our parameters, V and F_n, are of size $O(\epsilon^{-1})$. Thus we rescale $F_n = \epsilon^{-1}\hat{F}_n$ in the original problem to get

$$\phi_{zzz} - \phi_z\phi_{zz} = -\epsilon^{-1}\Lambda\hat{F}_n, \tag{4.79}$$

with boundary conditions

$$\phi(-1) = -\frac{V}{2}, \qquad \phi_{zz}(-1) = \Lambda, \tag{4.80}$$

$$\phi(0) = 0, \qquad \epsilon^{-1}\hat{F}_n = \delta S\left(\frac{\phi_{zz}^2(0)}{\Lambda^2} - 1\right). \tag{4.81}$$

As with the intermediate current regime, we assume the presence of a boundary layer at the interface and scale ϕ for the three regions that are needed in this case to describe the solution: (i) the outer region, (ii) a small intermediate region and (iii) a smaller inner region.

Inner Solution

In the inner region, near $z = 0$, the scaling for the spatial parameter is found by balancing $\epsilon^{-1}\hat{F}_n$ with $\delta\phi_{zz}^2(0)$ in (4.81)b. Thus, we introduce the new variable

$$z = (\delta\epsilon)^{\frac{1}{4}}\,\bar{\zeta}, \tag{4.82}$$

as in the intermediate current asymptotics. We define $\Phi^{(i)}$ to be the solution in the inner layer substitute into (4.79)-(4.81) to get

$$\Phi^{(i)}_{\bar{\zeta}\bar{\zeta}\bar{\zeta}} - \Phi^{(i)}_{\bar{\zeta}}\Phi^{i}_{\zeta\zeta} = -\delta^{\frac{3}{4}}\epsilon^{-\frac{1}{4}}\Lambda\hat{F}_n, \tag{4.83}$$

and the boundary conditions

$$\Phi^{i}(0) = 0, \qquad \hat{F}_n = \frac{S}{\Lambda^2}\Phi^{(i)2}_{\bar{\zeta}\bar{\zeta}}(0) - \delta\epsilon S. \tag{4.84}$$

Similarly to the intermediate current regime's inner solution, we find the solution to be

$$\Phi^{(i)} = -2\log\left(1 - \left(\frac{\Lambda}{2}\right)^{\frac{1}{2}} \left|\frac{\hat{F}_n}{S}\right|^{\frac{1}{4}} \bar{\zeta}\right). \tag{4.85}$$

For matching purposes it is helpful to expand (4.85) in $\bar{\zeta} = (\delta\epsilon)^{-\frac{1}{4}} z$:

$$\Phi^{(i)} = -2\log\left(1 - \left(\frac{\Lambda}{2}\right)^{\frac{1}{2}} \left|\frac{\hat{F}_n}{S}\right|^{\frac{1}{4}} (\delta\epsilon)^{-\frac{1}{4}} z\right) \tag{4.86}$$

$$= -2\log\left((\delta\epsilon)^{-\frac{1}{4}}\right) - 2\log\left(-\left(\frac{\Lambda}{2}\right)^{\frac{1}{2}} \left|\frac{\hat{F}_n}{S}\right|^{\frac{1}{4}} z + (\delta\epsilon)^{\frac{1}{4}}\right) \tag{4.87}$$

$$\approx \frac{1}{2}\epsilon^{-1} - \frac{1}{2}\log\left(\epsilon^{-1}\right) - 2\log\left(-\left(\frac{\Lambda}{2}\right)^{\frac{1}{2}} \left|\frac{\hat{F}_n}{S}\right|^{\frac{1}{4}} z\right), \tag{4.88}$$

as $\delta \to 0$.

Outer Solution

We then look at the outer solution, which will lead to the consideration of an intermediate layer for facilitating the matching with the inner solution (4.85). Motivated by the order of ϕ at $z = -1$, as seen in (4.81), we assume the expansions:

$$\phi^{(o)} \approx \epsilon^{-1}\Phi_0^{(o)} + \log\left(\epsilon^{-1}\right)\Phi_1^{(o)} + \Phi_2^{(o)} + ..., \tag{4.89}$$

$$V \approx \epsilon^{-1}V_0 + \log\left(\epsilon^{-1}\right)V_1 + V_2 + ... \tag{4.90}$$

Substituting into (4.79), we find that

$$\begin{aligned} &\epsilon^{-1}\Phi_{0zzz}^{(o)} + \log\left(\epsilon^{-1}\right)\Phi_{1zzz}^{(o)} + \Phi_{2zzz}^{(o)} - \\ &\left(\epsilon^{-1}\Phi_{0z}^{(o)} + \log\left(\epsilon^{-1}\right)\Phi_{1z}^{(o)} + \Phi_{2z}^{(o)}\right)\left(\epsilon^{-1}\Phi_{0zz}^{(o)} + \log\left(\epsilon^{-1}\right)\Phi_{1zz}^{(o)} + \Phi_{2zz}^{(o)}\right) \\ &= -\epsilon^{-1}\Lambda\hat{F}_n \end{aligned} \tag{4.91}$$

with

$$\Phi^{(o)}(-1) = \epsilon^{-1}\Phi_0^{(o)}(-1) + \log\left(\epsilon^{-1}\right)\Phi_1^{(o)}(-1) + \Phi_2^{(o)}(-1) \tag{4.92}$$
$$= -\epsilon^{-1}\frac{V_0}{2} - \log\left(\epsilon^{-1}\right)\frac{V_1}{2} - \frac{V_2}{2}$$
$$\Phi_{0zz}^{(o)}(-1) = 0, \quad \Phi_{1zz}^{(o)} = 0, \quad \Phi_{2zz}^{(o)} = \Lambda \tag{4.93}$$

Equating orders of δ we get the following problems for the leading-order terms of $\Phi^{(o)}$ to be as follows. The problem for $\Phi_0^{(o)}$ reduces to

$$\Phi_{0z}^{(o)}\Phi_{0zz}^{(o)} = 0, \tag{4.94}$$
$$\text{with} \quad \Phi_0^{(o)}(-1) = -\frac{V_0}{2}, \quad \Phi_{0zz}^{(o)}(-1) = 0. \tag{4.95}$$

The problem for $\Phi_1^{(o)}$ reduces to

$$\Phi_{0z}^{(o)}\Phi_{1zz}^{(o)} + \Phi_{1z}^{(o)}\Phi_{0zz}^{(o)} = 0 \tag{4.96}$$
$$\Phi_{1z}^{(o)}\Phi_{1zz}^{(o)} = 0, \tag{4.97}$$
$$\text{with} \quad \Phi_1^{(o)}(-1) = -\frac{V_1}{2}, \quad \Phi_{1zz}^{(o)}(-1) = 0. \tag{4.98}$$

The problem for $\Phi_2^{(o)}$ reduces to

$$\Phi_{0zzz}^{(o)} - \Phi_{0z}^{(o)}\Phi_{2zz}^{(o)} - \Phi_{2z}^{(o)}\Phi_{0zz}^{(o)} = -\Lambda|\hat{F}_n| \tag{4.99}$$
$$\Phi_{1zzz}^{(o)} - \Phi_{1z}^{(o)}\Phi_{2zz}^{(o)} - \Phi_{2z}^{(o)}\Phi_{1zz}^{(o)} = 0 \tag{4.100}$$
$$\Phi_{2zzz}^{(o)} - \Phi_{2zz}^{(o)}\Phi_{2z}^{(o)} = 0 \tag{4.101}$$
$$\text{with} \quad \Phi_2^{(o)}(-1) = -\frac{V_2}{2}, \quad \Phi_{2zz}^{(o)}(-1) = \Lambda. \tag{4.102}$$

The solution for $\Phi_0^{(o)}$ is found by solving (4.94)-(4.95) to be

$$\Phi_0^{(o)} = A_0(z+1) - \frac{V_0}{2}, \tag{4.103}$$

where A_0 is an arbitrary constant. The solution for $\Phi_1^{(o)}$ is found by solving (4.96)-(4.98) to be

$$\Phi_1^{(o)} = -\frac{V_1}{2} + B_0 z, \tag{4.104}$$

for some arbitrary constant B_0. Lastly, the general solution for $\Phi_2^{(o)}$ is found by solving (4.99)-(4.100) to be

$$\Phi_{2zz}^{(o)} = -\frac{\Lambda|\hat{F}_n|}{A_0}, \tag{4.105}$$

and gives that $B_0 = 0$. The equation (4.105) must satisfy the boundary condition (4.95) at $z = -1$. Thus, $A_0 = -|\hat{F}_n|$ and the solution reads

$$\Phi_2^{(o)} = \Lambda\left(z^2 - 1\right) + A_2(z+1) - \frac{V_2}{2}. \tag{4.106}$$

Then the full outer solution reads

$$\phi^{(o)} \approx -\epsilon^{-1}\left(|F_n|(z+1) - \frac{V_0}{2}\right) - \log\left(\epsilon^{-1}\right)\left(\frac{V_1}{2}\right) + \frac{\Lambda}{2}\left(z^2+1\right) + A_2(z+1) - \frac{V_2}{2} + ... \tag{4.107}$$

The values for V_0, V_1, V_2 and A_2 are to be found by matching with the inner solution.

Matching inner and outer solutions

Using the Van Dyke notation for expansions of the inner and outer solutions, as described earlier, we must balance

$$-\frac{1}{2} = |\hat{F}_n| - \frac{V_0}{2}, \tag{4.108}$$

$$-\frac{1}{2} = -\frac{V_1}{2}, \tag{4.109}$$

$$-\log\left(-\left(\frac{\Lambda}{2}\right)^{\frac{1}{2}}\left|\frac{\hat{F}_n}{S}\right|^{\frac{1}{4}} z\right) = A_2 - \frac{\Lambda}{2} - \frac{V_2}{2}. \tag{4.110}$$

We note that (4.110) can not be satisfied and thus we introduce an intermediate layer for matching purposes.

Inner Intermediate Layer

We now consider an intermediate variable between $z = O(1)$ and $\bar{\zeta} = (\delta\epsilon)^{-\frac{1}{4}}$. We

introduce the intermediate scaling

$$z = \epsilon^{\frac{1}{2}}\eta \tag{4.111}$$

for the inner intermediate (ii) layer. To find the expansion for $\phi^{(ii)}$ we expand the inner solution with our new variable, i.e. letting $\bar{\zeta} = \delta^{-\frac{1}{4}}\epsilon^{\frac{1}{4}}\eta$

$$\phi^{(i)} = -2\log\left(1 - \left(\frac{\Lambda}{2}\right)^{\frac{1}{2}}\left|\frac{F_n}{S}\right|^{\frac{1}{4}}\bar{\zeta}\right) \tag{4.112}$$

$$= -2\log\left(\delta^{-\frac{1}{4}}\epsilon^{\frac{1}{4}}\right) - 2\log\left(-\left(\frac{\Lambda}{2}\right)^{\frac{1}{2}}\left|\frac{F_n}{S}\right|^{\frac{1}{4}}\eta + \delta^{\frac{1}{4}}\epsilon^{-\frac{1}{4}}\right) \tag{4.113}$$

$$\approx \frac{\epsilon^{-1}}{2} - \frac{\log\left(\epsilon^{-1}\right)}{2} - 2\log\left(-\left(\frac{\Lambda}{2}\right)^{\frac{1}{2}}\left|\frac{F_n}{S}\right|^{\frac{1}{4}}\eta\right) + ... \tag{4.114}$$

Thus, we let the expansion for the intermediate inner solution be

$$\phi^{(ii)} \approx \frac{\epsilon^{-1}}{2} - \frac{\log\left(\epsilon^{-1}\right)}{2} + \Phi_2^{(ii)} + ... \tag{4.115}$$

Using the scaling (4.111) and the expansion (4.115) in (4.79), the problem for $\Phi_2^{(ii)}$ then reads

$$\Phi_{2\eta\eta\eta}^{(ii)} - \Phi_{2\eta}^{(ii)}\Phi_{2\eta\eta}^{(ii)} = 0 \tag{4.116}$$

with matching conditions

$$\phi^{(ii)} \to \phi^{(i)} \quad \text{as} \quad \eta \to 0 \tag{4.117}$$

$$\phi^{(ii)} \to \phi^{(o)} \quad \text{as} \quad \eta \to -\infty. \tag{4.118}$$

We take the general solution to be of the form[3]

$$\Phi_2^{(ii)} = a_2 - 2\log\left(\sinh(b_2\eta)\right), \tag{4.120}$$

where the constants a_2 and b_2 are to be found by matching.

[3]If we take the general solution to be of the form

$$\Phi_2^{(ii)} = -2\log\left(a_2\sinh(b_2\eta + c_2)\right) \sim -2\log\left(a_2c_2 + a_2b_2\eta\right) + ... \quad \text{as} \quad \eta \to 0 \tag{4.119}$$

we get that $c_2 = 0$ by matching with the inner solution.

Matching with the inner solution

As $\eta \to 0$ we can expand (4.120) as

$$\Phi_2^{(ii)} \sim a_2 - 2\log\left(b_2\eta\right), \tag{4.121}$$

which will be used to match the intermediate inner solution with the inner solution. This gives

$$a_2 = 2\log\left(b_2\right) - 2\log\left(-\left(\frac{\Lambda}{2}\right)^{\frac{1}{2}}\left|\frac{\hat{F}_n}{S}\right|^{\frac{1}{4}}\right) \tag{4.122}$$

resulting in

$$\phi^{(ii)} \approx \frac{\epsilon^{-1}}{2} + \frac{\log\left(\epsilon^{-1}\right)}{2} + 2\log\left(b_2\right) - 2\log\left(-\left(\frac{\Lambda}{2}\right)^{\frac{1}{2}}\left|\frac{\hat{F}_n}{S}\right|^{\frac{1}{4}}\right). \tag{4.123}$$

Matching with the outer solution

As $\eta \to -\infty$ we can expand (4.120) as

$$\Phi_2^{(ii)} \sim -2b_2\eta \tag{4.124}$$

which will be used to match the intermediate inner solution with the outer solution, giving

$$\Phi_0^{(o)} = \epsilon^{-1}\left(|\hat{F}_n|x + |\hat{F}_n| + \frac{V_0}{2}\right) \tag{4.125}$$

$$= \epsilon^{-1}\left(|\hat{F}_n|z + \frac{V_0}{2}\right) + |\hat{F}_n|\eta. \tag{4.126}$$

Thus $b_2 = -\frac{|\hat{F}_n|}{2}$ and

$$\phi^{(ii)} \sim \frac{\epsilon^{-1}}{2} + \frac{\log\left(\epsilon^{-1}\right)}{2} + 2\log\left(-\frac{|\hat{F}_n|}{2}\right) - 2\log\left(-\left(\frac{\Lambda}{2}\right)^{\frac{1}{2}}\left|\frac{\hat{F}_n}{S}\right|^{\frac{1}{4}}\right) + ... \tag{4.127}$$

Also, we extract that $|\hat{F}_n| + \frac{V_0}{2} = -\frac{1}{2}$. By matching the following terms we obtain

that $V_1 = -1$. Then,

$$V \sim \epsilon^{-1} V_0 + \log\left(\epsilon^{-1}\right) V_1 + ... \tag{4.128}$$

$$\sim \epsilon^{-1}\left(1 - 2|\hat{F}_n|\right) - \log\left(\epsilon^{-1}\right). \tag{4.129}$$

Using $F_n = \epsilon^{-1}\hat{F}_n$, we obtain the current density-voltage relation to be:

$$F_n \sim \frac{V}{2} - \frac{\epsilon^{-1}}{2} - \frac{\log\left(\epsilon^{-1}\right)}{2} + ... \tag{4.130}$$

In Figure 4.6 we show the large current approximation (LCA) in comparison with the exact solution, but also the SCA and ICA to show the various regimes of validity for each.

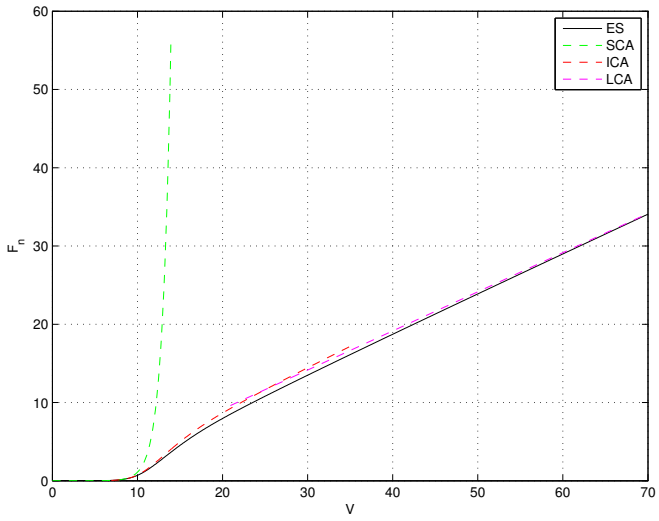

Figure 4.6: Current density against voltage with the exact solution (ES) and the approximation solutions obtained via the SCA, ICA and LCA. [Parameters: $\delta = 10^{-4}$, $S = 0.5$, $\Lambda = 1$]

In this section we have presented asymptotic solutions for the one dimensional problem for the current transport in an ssDSSC. While an exact solution was shown to be established for a symmetric cell with certain parameters (e.g. $\epsilon_{n,p}$, $D_{n,p}$) taken as unity, the asymptotics allow us to explore the problem in more detail and ican act as a benchmark for more complicated problems. In summary, the asymptotic analysis verifies that the behavior of the cell at lower voltage is diode-like and at higher voltages it behaves as a resistor.

4.3 Non-symmetric cell

In this section we present the solution for the cell in the non-symmetric scenario. The numerical scheme used to obtain the results is given in Appendix I.

The distribution of electrons and holes and the electrostatic potential are found by solving the following two systems: (i) for the EA region (4.13)-(4.12) subject to the boundary conditions (4.14), and (ii) for the ED region (4.17)-(4.16) subject to the boundary condition (4.18). These two regions are coupled together using the interface conditions (4.15), (4.19) and (4.20). We use our numerical scheme to investigate the effect of several key dimensionless parameters on the behaviour of the cell.

In what follows, we vary the key parameters of the problem: the dielectric ratio, $\hat{\epsilon}_p$, and the diffusivity ratio, $\hat{D}_p$. We retain the assumption that $m = 1$. We measure the efficiency of the cell in order to examine the performance of the cell under these variations. We define the overall efficiency of the cell by the maximum power output, P_{max},

$$P_{max} = maximum(JV), \tag{4.131}$$

for $J = -F_n$, which is a key measure of performance for solar cells.

4.3.1 Varying $\hat{\epsilon}_p$

We are interested in the effect that different dielectric ratios, $\hat{\epsilon}_p = \frac{\epsilon_p}{\epsilon_n}$, have on the performance and the internal dynamics of the cell. The dielectric constant describes how much the material polarizes in response to an electric field, i.e. how much the electric field pushes/pulls on the charges in the medium. In Figure 4.7 we show the behaviour of the electrostatic potential, ϕ, the electric field, E, and the free charge carriers in each region, n and p, when the dielectric constant of the ED is much lower than that of the EA material. In Figure 4.7, we show the results for $\hat{\epsilon}_p = 0.01$ while varying V.

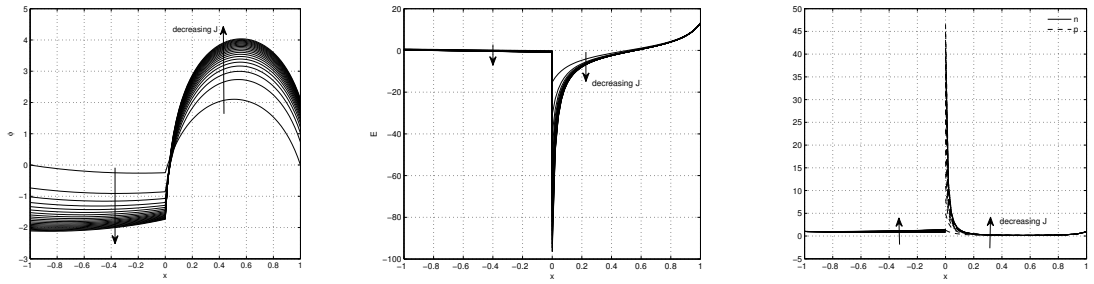

(a) (b) (c)

Figure 4.7: Plots with $\hat{\epsilon}_p = 0.01$ for (a) the electrostatic potential, (b) the electric field and (c) the electron (in the EA region, i.e. $-1 \leq z \leq 0$) and hole (in the ED region, i.e. $0 \leq z \leq 1$) densities for decreasing J from 0 to -10^{-3} in increments of 0.5×10^{-4}. [Parameters: $\delta = 10^{-4}$, $\hat{D}_p = 1$, $S = 0.15$, $\Lambda = 1$]

The result of a lower dielectric constant in the ED region is a higher electric field near the interface in the ED region. The large change in the electric field across the interface as shown in Figure 4.7(b) suggests the existence of a boundary layer. This, consequently, leads to a non-zero electrostatic potential at the interface as shown in Figure 4.7(a). Physically, this large electric field in the ED region near the interface produces a significantly larger drift force on the holes (rather than in the bulk) resulting in a higher concentration of holes at the interface.

In order to use the efficiency metric given by (4.131), we allow for a monochromatic constant illumination by setting $G = 1$ and vary the dielectric ratio $\hat{\epsilon}_p = 1,\ 0.1$ and 0.01. When $\hat{\epsilon}_p = 0.001$, we get a shallower $J - V$ curve than when $\hat{\epsilon}_p = 1$, implying a lower power output. In fact, we show this clearly by plotting the maximum power output for a cell when varying the dielectric ratio in Figure 4.8(b). This graph suggests that a higher dielectric ratio would result in a more efficient cell, because larger potential difference is required to be applied at the electrode contacts to drive the free charge carriers (due to the short screening of the electric field in the ED region near the interface). However, we should note that a smaller dielectric constant for a material would also imply a larger band gap and exciton binding energy in that material, which is not captured by this model.

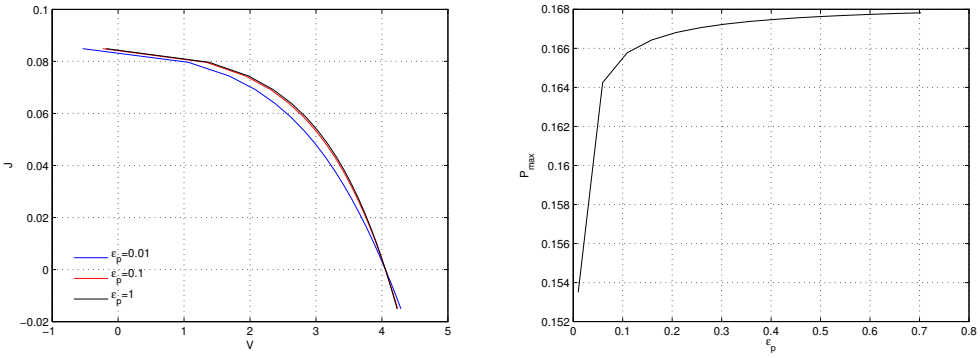

(a) (b)

Figure 4.8: (a) Shows the $J-V$ curves for a cell under low monochromatic illumination for $\hat{\epsilon}_p = 0.01,\ 0.1$ and 1. (b) Shows the maximum power output by varying $\hat{\epsilon}_p$. [Parameters: $\delta = 0.01$, $\hat{D}_p = 1$, $S = 0.15$, $\Lambda = 1$]

4.3.2 Varying $\hat{D}_p$

It is generally the case with ssDSSCs that the diffusivity of electrons in the ED region is higher than that of holes in the EA region (recall Chapter 2). Overall, if $\hat{D}_p = \frac{D_p}{D_n} > 1$, we observe a larger electric field in the EA compared to the ED and ϕ is no longer symmetric. In fact, the potential drop at the interface is no longer a half of the applied voltage V as shown in Figure 4.9(b). In fact, if V_1 is the value of ϕ at the interface, then $V - (V_1 + \frac{V}{2})$ is the potential drop across the ED and $V_1 + \frac{V}{2}$ is the potential drop across the EA. Physically, a higher diffusivity of holes in the ED reduces the drift in that region (as the diffusion current opposes the electric current) resulting in a lower potential drop.

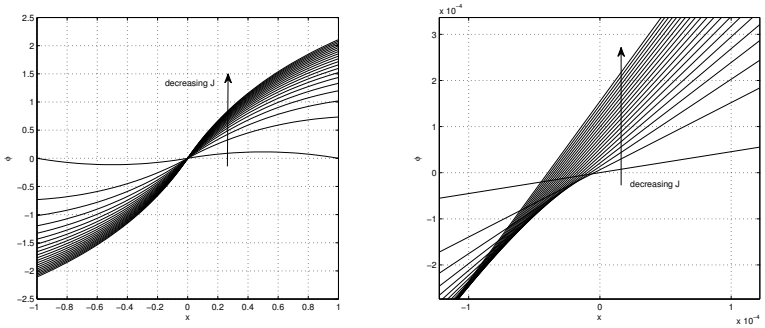

(a) (b)

Figure 4.9: Plots for a cell with $\hat{D}_p = 10$ in the dark for (a) the electrostatic potential with (b) a zoom in the EA/ED interface when decreasing J from 0 to -10^{-3} in increments of 0.5×10^{-4}. [Parameters: $\delta = 10^{-4}$, $\hat{\epsilon}_p = 1$, $S = 0.15$, $\Lambda = 1$]

In Figure 4.10(a), we show a comparison between the $J - V$ curves for cells under illumination with diffusivity ratios $\hat{D}_p = 0.1,\ 1$ and 10, where the latter produces a larger power output. Figure 4.10(b) shows the overall power output resulting from varying the diffusivity ratio, which is greater with larger $\hat{D}_p$.

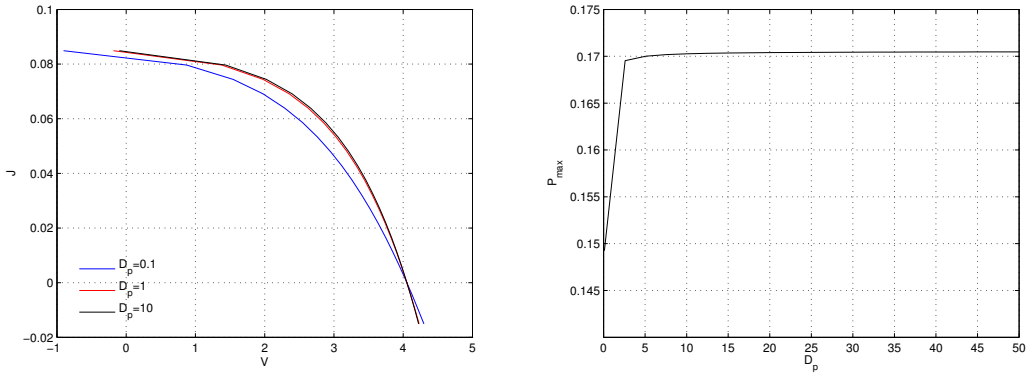

(a) (b)

Figure 4.10: (a) Shows the $J - V$ curves for the cases $\hat{D}_p = 0.1,\ 1,\ 10$ for a cell in the dark. (b) Shows the maximum power output by varying $\hat{D}_p$. [Parameters: $\delta = 0.01$, $\hat{\epsilon}_p = 1$, $S = 0.15$, $\Lambda = 1$, $G = 1$]

4.3.3 Summary

In this Section, we have solved (4.13)-(4.20) for the electrostatic potential, ϕ, and the distribution of electrons, n. The solution to this current transport problem in the

ssDSSC was done both analytically and numerically, with the results tested against each other. Initially, we have made several assumptions on the geometry of the device and the physical properties of the materials used, to make the solution symmetric across the EA/ED interface. At later stages, we have examined the effect of several key parameters, except for the effect of the distribution of the dye, S, as this is the topic of the following section. We considered a larger dielectric and diffusivity ratio between the ED and the EA which is shown to lead to larger current generation. In general, we were able to show that the behaviour of an ssDSSC resembles that of a diode, i.e. allowing current to travel in one direction only.

4.4 Dye Distribution

In this section, we examine the effect on the cell's performance by the distribution of dye at the interface. As discussed earlier, dye is not evenly distributed and does not cover all of the surface of the electron acceptor. Thus, it is worth understanding how this impacts the generation of current. In order to incorporate this into our model, we return to the two dimensional model as presented in Chapter 3.

We consider the two dimensional problem (3.38)-(3.41) in z and x as shown in Figure 3.2 with boundary conditions (3.42)-(3.51). We define the electron acceptor region to lie in $\Omega_a \equiv \{-H_1 < z < 0\} \cup \{0 < x < L\}$ and the electron donor region in $\Omega_d \equiv \{0 < z < H_2\} \cup \{0 < x < L\}$, as shown in Figure 4.11.

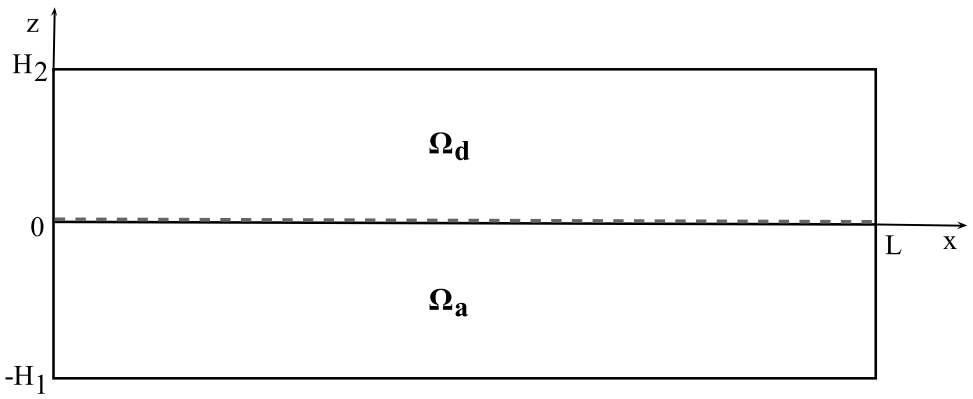

Figure 4.11: A schematic representation of the domain and the interface morphology for a bilayer cell in two dimensions.

We describe the flat interface by the curve $z = 0$ as earlier. In this case, however, we

allow for variable dye distribution. In particular, we assume that the dye is deposited as simply-connected segments and lies at the interface between Ω_a and Ω_d. We will refer to these segments as 'blobs'. We assume a periodic distribution of dye blobs so that the dye coverage can be described by a periodic function $S_d(x)$ along $z = 0$. In order to define this formally we introduce the *rectangle function*[4], Π_α[5], as

$$\Pi_\alpha(x) = \begin{cases} 1, & |x| \leq \frac{1}{2}, \\ 0, & |x| > \frac{1}{2}. \end{cases} \tag{4.132}$$

If we define the width of the blobs as ω and the inter-blob gap as g (see Figure 4.12), then

$$S_d(x) = \sum_{k=0}^{\frac{L}{2d}} \Pi_\alpha \left(\frac{x - (\frac{\omega}{2} + kd)}{\omega} \right), \tag{4.133}$$

where $d = g + w$ is the repeated period and $\frac{L}{2d}$ is the number of blobs, N_b, we are allowing.

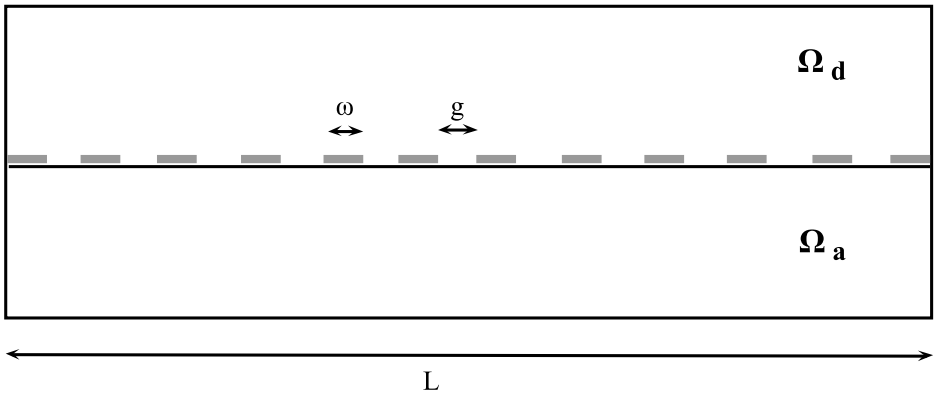

Figure 4.12: A schematic representation of the dye blobs distributed at evenly spaced segments along the interface of the electron acceptor and donor. This image is a zoomed from Figure 4.11.

4.4.1 Nondimensionalisation

In order to understand the relative sizes of the variables of the problem (3.38)-(3.51), it is important to scale them with the physical parameters. We scale the spatial

[4]Not to be confused with the notation Π_0 which stands for the typical carrier concentration.
[5]We note that we could use a periodic step function here as well.

variables with the two lengthscales of the device, namely H_1 and L, as appropriate, and the remaining variables with

$$z = H_1\hat{z}, \quad x = L\hat{x}, \quad \phi - \frac{V}{2} = \frac{k_B T}{q}\hat{\phi}, \quad n = \Pi_0\hat{n}, \quad p = \Pi_0\hat{p}, \quad \mathbf{F}_n = \frac{D_n\Pi_0}{H_1}\hat{\mathbf{F}}_n. \tag{4.134}$$

We substitute the scalings (4.134) in the original problem and for simplicity of notation in the following work we drop the hat denoting dimensionless variables. Avoiding the calculations, as they are similar to those in Section 4.1, we reduce to the nondimensional problem

$$\phi_{zz} + \varepsilon^2\phi_{xx} = \begin{cases} \Lambda n, & \mathbf{x} \in \Omega_a, \\ -\frac{\Lambda}{\hat{\epsilon}_p}p, & \mathbf{x} \in \Omega_d, \end{cases} \tag{4.135}$$

$$(n\phi_z - n_z)_z + \varepsilon^2(n\phi_x - n_x)_x = 0, \quad \mathbf{x} \in \Omega_a, \tag{4.136}$$

$$(p\phi_z + p_z)_z + \varepsilon^2(p\phi_x + p_x)_x = 0, \quad \mathbf{x} \in \Omega_d, \tag{4.137}$$

with boundary conditions

$$n(-1, x) = \hat{N}^-, \qquad \phi(-1, x) = -\frac{\hat{V}}{2}, \tag{4.138}$$

$$p(m, x) = \hat{P}^+, \qquad \phi(m, x) = \frac{\hat{V}}{2}, \tag{4.139}$$

$$\phi_x(z, 0) = n_x(z, 0) = p_x(z, 0) = 0, \tag{4.140}$$

$$\phi_x(z, 1) = n_x(z, 1) = p_x(z, 1) = 0 \tag{4.141}$$

and interface conditions

$$[\phi] = 0, \tag{4.142}$$

$$[\epsilon_i\phi_x] = 0, \tag{4.143}$$

$$[F_{n_1}] = -[F_{p_1}\frac{D_p}{D_n}] = -\delta(1 - S_d(x))\left(n(0, x)p(0, x) - 1\right), \tag{4.144}$$

where [..] denotes the jump across the interface from $z = 0^-$ to 0^+ and

$$F_{n1} = n\phi_z - n_z, \quad F_{p1} = -(p\phi_z + p_z), \tag{4.145}$$

$$\epsilon_i = \begin{cases} 1, & \mathbf{x} \in \Omega_a \\ \hat{\epsilon}_p, & \mathbf{x} \in \Omega_d \end{cases}, \tag{4.146}$$

$$S_d(x) = \sum_{k=0}^{N_b} \Pi_\alpha \left(\frac{x - (\frac{\hat{\omega}}{2} + k\hat{d})}{\hat{\omega}} \right). \tag{4.147}$$

The dimensionless parameters are defined by

$$\hat{\omega} = \frac{\omega}{L}, \quad \hat{d} = \frac{d}{L}, \quad \hat{V} = \frac{qV}{k_B T} \tag{4.148}$$

$$m = \frac{H_1}{H_2}, \quad \hat{N}^- = \frac{N^-}{\Pi_0}, \quad \hat{P}^+ = \frac{P^+}{\Pi_0}, \quad \hat{\epsilon}_p = \frac{\epsilon_p}{\epsilon_n},$$
$$\varepsilon = \frac{H_1}{L}, \quad \Lambda = \frac{q^2 \Pi_0 H_1^2}{\epsilon_n k_B T} = \frac{H_1^2}{\lambda^2}, \quad \delta = \frac{H_1 \Pi_0}{\sigma \tau_R D_n N_0 P_0}. \tag{4.149}$$

We estimate the size of these parameters is estimated based on a typical cell with the electron acceptor made of TiO_2, the electron donor of spiro-OMeTAD and a Ru-based dye as in Chapter 4. The spatial parameters are taken to be $\omega \sim d \approx 10^{-9}\ m$, $H_1 \approx 10^{-6}\ m$ and $L \approx 10^{-2}\ m$ and the remaining parameters, which are related to the properties of the materials used, are as defined in Table 4.1. We briefly note that the value of Π_0 may vary depending on the measuring technique, the size of the material and the manufacture procedure as reported by Sellers *et al.* [62], thus the size of the Debye length, λ, and the recombination coefficient, δ, vary accordingly. In order to get an insight of the operations, we make certain assumptions to simplify the problem (4.135)-(4.144), although we recognise that these may not be the most realistic ones. For this study we take

$$\varepsilon \approx 10^{-4}, \quad \Lambda \approx 1, \quad \delta \approx 1, \quad \hat{\epsilon}_p \approx 1, \tag{4.150}$$

unless otherwise stated. We consider a symmetric cell by assuming $m = 1$, $\hat{\epsilon}_p = 1$ and $D_n = D_p$. This allows us to explore solutions which have the symmetry property

$$n(z, x) = p(-z, x) \quad \text{and} \quad \phi(z, x) = -\phi(-z, x). \tag{4.151}$$

Then we need to solve only for the EA region ($-1 \leq z \leq 0$) and use this symmetry to retrieve the solution in the ED region ($0 \leq z \leq 1$)). We also take $N^- = 1$.

We note that some of these conditions can be removed and the analyses can still be undertaken at the expense of very complicated algebraic expressions and lack of simple interpretations. Since the analysis of the effect of a small recombination coefficient was done extensively in Chapter 4, here we will take $\delta = O(1)$ and $\hat{V} = O(1)$ as given, in order to find the current flux, F_n.

4.4.2 Methodology

A key feature of the model (4.135)-(4.144) is that it allows spatial variations in the dye distribution which is examined in this section. To explore the complex problem we use both analytic and numerical techniques to obtain solutions. Before proceeding, we give an explanation of these two approaches.

4.4.2.1 Numerical method

Under the simplification of a symmetric cell, we only solve for the electron acceptor region. We use a finite difference scheme, with centred differences to solve the nondimensional problem given in (4.135)-(4.147). We solve on a uniform grid in $[-1, 0] \times [0, 1]$ with step size h so that the numerical nodes are at (z_j, x_k), where $z_j = -1 + hj$ and $x = hk$, for $j, k = 0, ..., J$, as shown in Figure 4.13. We let $\Phi(z_j, x_k)$ and $N(z_j, x_k)$ be the numerical solutions for ϕ and n at each node, respectively. If we write our variables in vector form as

$$\Phi = \begin{pmatrix} \Phi_{0,0} \\ \Phi_{0,1} \\ \Phi_{0,2} \\ ... \\ \Phi_{0,J} \\ \Phi_{1,0} \\ \Phi_{1,1} \\ ... \\ \Phi_{1,J} \\ ... \\ \Phi_{J,J} \end{pmatrix} \quad \text{and} \quad N = \begin{pmatrix} N_{0,0} \\ N_{0,1} \\ N_{0,2} \\ ... \\ N_{0,J} \\ N_{1,0} \\ N_{1,1} \\ ... \\ N_{1,J} \\ ... \\ N_{J,J} \end{pmatrix}. \tag{4.152}$$

The resulting system of simultaneous equations can be expressed by the following

matrix systems for $\mathbf{\Phi}$ and $\mathbf{N}$

$$A_\phi \mathbf{\Phi}^{[q+1]} = \Lambda \mathbf{N}^{[q]} + \mathbf{b}_\phi, \tag{4.153}$$

$$A_n(\mathbf{\Phi}^{[q+1]}, \mathbf{N}^{[q]})\mathbf{N}^{[q+1]} = \mathbf{b}_n, \tag{4.154}$$

where the vectors $\mathbf{b}_\phi$ and $\mathbf{b}_n$ impose the Dirichlet boundary conditions. The matrices of coefficients A_ϕ and A_n describe numerically the operators acting on ϕ and n as in (4.135) and (4.136), respectively. A_ϕ has constant entries, whereas these in A_n depend on the values of Φ and N. The system is solved iteratively, with q indicating the number of iteration, using a simple Jacobi method. We stop the iteration when a certain tolerance is reached, in particular until the L_2-norm error between the solutions in steps q and $q+1$ is smaller than a given value, tol, i.e.

$$\|\mathbf{\Phi}^{[q+1]} - \mathbf{\Phi}^{[q]}\| < tol \quad \text{and} \quad \|\mathbf{N}^{[q+1]} - \mathbf{N}^{[q]}\| < tol. \tag{4.155}$$

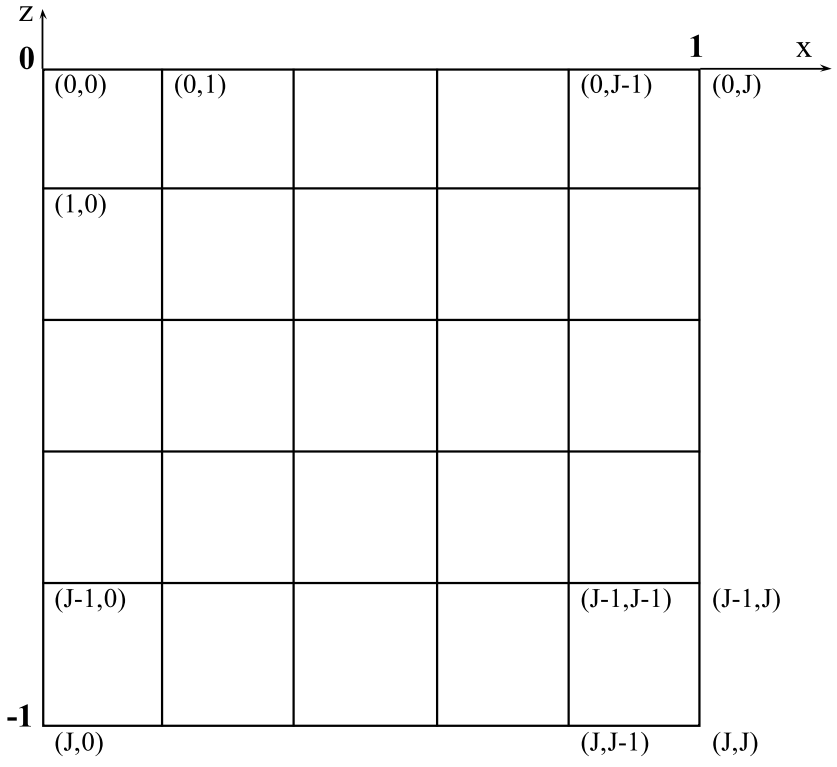

Figure 4.13: The uniform grid used for the numerical scheme.

In our examples, the results yield a good agreement with analytic results as will be demonstrated later on. A more detailed description of the scheme is found in Appendix II.

4.4.2.2 Analytic approach

In certain parameter regimes we may use asymptotic expansions for the variables to find an explicit solution for the leading-order terms. In order to find these we must account for boundary (or inner) regions where the dependent variables change abruptly, and we use the method of matched asymptotic expansions to obtain universal solutions, whenever possible.

In what follows we use both analytic and numerical tools to solve the scaled problem (4.135)-(4.147) for a bilayer cell in two limiting cases. In the first case, we look at the thin film approximation by taking the aspect ratio, ε, to be small, while allowing for only one dye blob ($N_b = 1$) of width $\hat{\omega} = O(1)$ and $\hat{d} = 1$. In the second case, we investigate the effect of a periodic distribution of a large number ($N_b \gg 1$) of dye blobs of width $\hat{\omega} \ll 1$ and $\hat{d} = 2\hat{\omega}$ on the interface, but with the total width of the dye-covered surface adding up to give $N_b\omega = O(1)$.

4.4.3 Thin film approximation

In this section we use numerical and asymptotic tools to study the behaviour of the solution in the limit $\varepsilon \to 0$. This corresponds to the device being very long and thin. For the simplicity of the analysis we assume only one dye blob laying on $0 < x < \hat{\omega} = O(1)$, as shown in Figure 4.14, so that only part of the thin film has dye on it. The difficulty in finding a explicit solution for the full problem is caused by the abrupt change in the behaviour of the solution near $x = \hat{\omega}$. This is suggested by the jump in the boundary condition (4.144) and the dominance of the z-derivatives in (4.135)-(4.136) when $\epsilon \to 0$. We therefore split our analysis into three spatial regions:
- an *outer region*, $\hat{\omega} - x \gg \varepsilon$, in which we expect the variables to follow the behaviour predicted by a one dimensional problem with $S_d(x) = 0$,
- an *outer region*, $x - \hat{\omega} \gg \varepsilon$, in which we expect the variables to follow the behaviour predicted by a one dimensional problem with $S_d(x) = 1$, and
- an *inner region*, $|x - \hat{\omega}| = O(\varepsilon)$, in which we will show that no explicit solution can be found asymptotically.

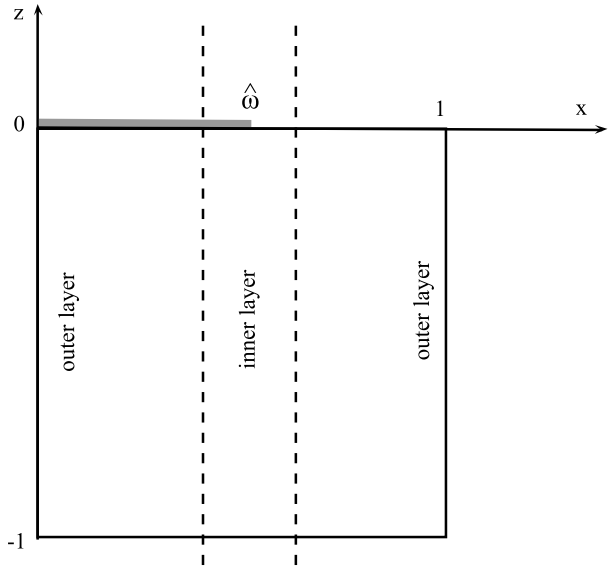

Figure 4.14: The (scaled) domain of interest with $\varepsilon \ll 1$ and $\hat{\omega} = O(1)$. The grey blob represents the dye, where $S_d = 1$.

Outer Solutions

Given V, the solution for the F_n in the two outer regions away from $x = \hat{\omega}$ will be sought simultaneously. Thus, we seek the solutions for $\phi^{(o)}$ and $n^{(o)}$ for the outer problems in $|x - \hat{\omega}| \gg \varepsilon$, using the asymptotic expansions

$$\phi^{(o)}(z, x; \varepsilon) \approx \phi_0^{(o)}(z, x) + \varepsilon^2 \phi_1^{(o)}(z, x) + ... \text{ and} \tag{4.156}$$

$$n^{(o)}(z, x; \varepsilon) \approx n_0^{(o)}(z, x) + \varepsilon^2 n_1^{(o)}(z, x) + ... \ . \tag{4.157}$$

By substituting these into (4.135) and (4.136) we get

$$\phi_{0zz}^{(o)} + \varepsilon^2 \phi_{1zz}^{(o)} + \varepsilon^2 \left(\phi_{0x}^{(o)} + \varepsilon^2 \phi_{1x}^{(o)} \right)_x = \Lambda \left(n_0^{(o)} + \varepsilon^2 n_1^{(o)} \right) + ... \quad \text{and} \tag{4.158}$$

$$\left[\left(n_0^{(o)} + \varepsilon^2 n_1^{(o)} \right) \left(\phi_{0z}^{(o)} + \varepsilon^2 \phi_{1z}^{(o)} \right) - \left(n_{0z}^{(o)} + \varepsilon^2 n_{1z}^{(o)} \right) \right]_z + \varepsilon^2 \left[\left(n_0^{(o)} + \varepsilon^2 n_1^{(o)} \right) \left(\phi_{0x}^{(o)} + \varepsilon^2 \phi_{1x}^{(o)} \right) - \left(n_{0x}^{(o)} + \varepsilon^2 n_{1x}^{(o)} \right) \right]_x + ... = 0, \tag{4.159}$$

respectively. Similarly for the boundary conditions (4.138), (4.140)-(4.141) on $\phi(z, x)$

and $n(z,x)$ we get

$$\phi_0^{(o)}(-1,x) = \frac{\hat{V}}{2}, \quad \phi_1^{(o)}(-1,x) = 0, \tag{4.160}$$

$$n_0^{(o)}(-1,x) = 1, \qquad n_1^{(o)}(-1,x) = 0, \tag{4.161}$$

$$\phi_0^{(o)}(0,x) = 0, \qquad \phi_1^{(o)}(0,x) = 0, \tag{4.162}$$

$$\phi_{0x}^{(o)}(z,0) = n_{0x}^{(o)}(z,0) = 0, \qquad \phi_{1x}^{(o)}(z,0) = n_{1x}^{(o)}(z,0) = 0, \tag{4.163}$$

$$\phi_{0x}^{(o)}(z,1) = n_{0x}^{(o)}(z,1) = 0, \qquad \phi_{1x}^{(o)}(z,1) = n_{1x}^{(o)}(z,1) = 0. \tag{4.164}$$

and

$$F_{n1}(0,x) = \begin{cases} 0, & 0 \le x < \hat{\omega} \quad (S_d = 1), \\ \delta\left(n_0^{(o)2}(0,x) - 1 + 2\varepsilon^2 n_0^{(o)}(0,x) n_1^{(o)}(0,x)\right) + ..., & \hat{\omega} < x \le 1 \quad (S_d = 0) \end{cases} . \tag{4.165}$$

For $0 \le x < \hat{\omega}$ we anticipate the solution to be approximated by the one-dimensional solution with $S - d = 1$ and for $\hat{\omega} < x \le 1$ to be approximated by the same with $S_d = 0$.

Then the leading-order problem reads

$$\phi_{0zz}^{(o)} = \Lambda n_0^{(o)}, \tag{4.166}$$

$$(n_0^{(o)} \phi_{0z}^{(o)} - n_{0z}^{(o)})_z = 0 \tag{4.167}$$

with

$$\phi_0^{(o)}(-1,x) = -\frac{\hat{V}}{2}, \qquad \phi_0^{(o)}(0,x) = 0, \tag{4.168}$$

$$n_0^{(o)}(-1,x) = 1, \qquad F_{n1}(0,x) = \begin{cases} 0, & x < \hat{\omega}, \\ \delta\left(n_0^{(o)2}(0,x) - 1\right), & x > \hat{\omega} \end{cases} , \tag{4.169}$$

$$\phi_{0x}^{(o)}(z,0) = n_{0x}^{(o)}(z,0) = 0, \tag{4.170}$$

$$\phi_{0x}^{(o)}(z,1) = n_{0x}^{(o)}(z,1) = 0. \tag{4.171}$$

The general solution of (4.166)-(4.167) in each outer region is then found to be

$$\phi_0^{(o)}(z,x) = -2\log\left(\alpha\,\mathrm{Ai}(\chi_1 z+\chi_2)+\beta\,\mathrm{Bi}(\chi_1 z+\chi_2)\right), \tag{4.172}$$

$$n_0^{(o)}(z,x) = -\frac{2\chi_1^2}{\Lambda}\left[\chi_1 z+\chi_2-\left(\frac{\alpha\,\mathrm{Ai}'(\chi_1 z+\chi_2)+\beta\,\mathrm{Bi}'(\chi_1 z+\chi_2)}{\alpha\,\mathrm{Ai}(\chi_1 z+\chi_2)+\beta\,\mathrm{Bi}(\chi_1 z+\chi_2)}\right)^2\right] \tag{4.173}$$

with α, β, χ_1 and χ_2 being some arbitrary constants to be found. By imposing the boundary conditions (4.168) and (4.169)a we find

$$\alpha = \frac{e^{\frac{V}{4}}\,\mathrm{Bi}(\chi_2)-\mathrm{Bi}(\chi_2-\chi_1)}{\mathrm{Ai}(\chi_2-\chi_1)\,\mathrm{Bi}(\chi_2)-\mathrm{Ai}(\chi_2)\,\mathrm{Bi}(\chi_2-\chi_1)}, \tag{4.174}$$

$$\beta = \frac{e^{\frac{V}{4}}\,\mathrm{Ai}(\chi_2)-\mathrm{Ai}(\chi_2-\chi_1)}{\mathrm{Ai}(\chi_2-\chi_1)\,\mathrm{Bi}(\chi_2)-\mathrm{Ai}(\chi_2)\,\mathrm{Bi}(\chi_2-\chi_1)}, \tag{4.175}$$

$$\frac{\Lambda}{2\chi_1^2} = \left(\frac{\mathrm{Bi}(\chi_2)\,\mathrm{Ai}'(\chi_2-\chi_1)-\mathrm{Ai}(\chi_2)\,\mathrm{Bi}'(\chi_2-\chi_1)+\frac{e^{-\frac{V}{4}}}{\pi}}{\mathrm{Bi}(\chi_2)\,\mathrm{Ai}(\chi_2-\chi_1)-\mathrm{Ai}(\chi_2)\,\mathrm{Bi}(\chi_2-\chi_1)}\right)^2-(\chi_2-\chi_1), \tag{4.176}$$

where χ_1 and χ_2 depend on the value of $F_{n1}(0,x)$ in each of the outer regions as in (4.169)b. In fact, on $0\le x<\hat{\omega}$, it is necessary to have

$$\frac{2\chi_1^3}{\Lambda}=0. \tag{4.177}$$

In the other outer region, where $\hat{\omega}<x\le 1$, the condition to be satisfied is

$$\frac{2\chi_1^3}{\delta\Lambda} = \frac{4\chi_1^4}{\Lambda^2}\left(\left(\frac{\mathrm{Ai}(\chi_2-\chi_1)\,\mathrm{Bi}'(\chi_2)-\mathrm{Bi}(\chi_2-\chi_1)\,\mathrm{Ai}'(\chi_2)-\frac{e^{\frac{V}{4}}}{\pi}}{\mathrm{Bi}(\chi_2)\,\mathrm{Ai}(\chi_2-\chi_1)-\mathrm{Ai}(\chi_2)\,\mathrm{Bi}(\chi_2-\chi_1)}\right)^2-\chi_2\right)^2-1. \tag{4.178}$$

These are one-dimensional problems in each region, one with generation only and the other with recombination only at the interface, respectively.

Inner Solution

It is now essential to consider how the solution varies between the two outer regions. For the inner region where $|x-\hat{\omega}|=O(\varepsilon)$, we first introduce the inner variable ξ by

taking

$$x = \hat{\omega} + \varepsilon\xi, \quad -\infty < \xi < \infty \tag{4.179}$$

and seek the inner solutions $\phi^{(i)}$ and $n^{(i)}$ using the asymptotic expansions

$$\phi^{(i)}(z,\xi;\varepsilon) \approx \phi_0^{(i)}(x,\xi) + \varepsilon\phi_1^{(i)} + ..., \tag{4.180}$$

$$n^{(i)}(z,\xi;\varepsilon) \approx n_0^{(i)}(x,\xi) + \varepsilon n_1^{(i)} + ... \ . \tag{4.181}$$

By substituting the scaling (4.179) and the expansions (4.180)-(4.181) into (4.135) and (4.136), the leading-order inner problem becomes

$$\phi_{0zz}^{(i)} + \phi_{0\xi\xi}^{(i)} = \Lambda n_0^{(i)}, \tag{4.182}$$

$$\left(n_0^{(i)}\phi_{0z}^{(i)} - n_{0z}^{(i)}\right)_z + \left(n_0^{(i)}\phi_{0\xi}^{(i)} - n_{0\xi}^{(i)}\right)_\xi = 0. \tag{4.183}$$

The solution to this system of equations must satisfy the boundary conditions at $z = 0, -1$, namely

$$\phi^{(i)}(-1,\xi) = -\frac{\hat{V}}{2}, \quad n^{(i)}(-1,\xi) = 1 \tag{4.184}$$

$$\phi^{(i)}(0,\xi) = 0, \quad F_{n1}(0,\xi) = \begin{cases} 0, & \xi < 0 \\ \delta\left(n_0^{(i)2}(0,\xi) - 1\right), & 0 < \xi. \end{cases} \tag{4.185}$$

and the following matching conditions to the outer regions

$$\lim_{\xi\to-\infty} \phi^{(i)} = \lim_{x\to\omega^-} \phi^{(o)}, \quad \lim_{\xi\to\infty} \phi^{(i)} = \lim_{x\to\omega^+} \phi^{(o)}, \tag{4.186}$$

$$\lim_{\xi\to-\infty} n^{(i)} = \lim_{x\to\omega^-} n^{(o)}, \quad \lim_{\xi\to\infty} n^{(i)} = \lim_{x\to\omega^+} n^{(o)}. \tag{4.187}$$

We can extract useful information about the behaviour of the solution even without solving (4.182)-(4.187) analytically.

4.4.3.1 The effective model

We have examined the distribution of the electrostatic potential, ϕ, and the electron concentration, n, in the limit of $\varepsilon \to 0$. The results have shown that the solutions in the outer regions are essentially solutions to one-dimensional problems as given by (4.172)-(4.178). We define $\phi_{0,\,x<\hat{\omega}}^{(o)}$ and $n_{0,\,x<\hat{\omega}}^{(o)}$ to be the solution to (4.172)-(4.176)

with (4.177), and $\phi^{(o)}_{0,\ x>\hat{\omega}}$ and $n^{(o)}_{0,\ x>\hat{\omega}}$ the solution to (4.172)-(4.176) with (4.178), and write

$$\phi(z,x) = \begin{cases} \phi^{(o)}_{0,\ x<\hat{\omega}}(z), & 0 \le x < \hat{\omega}, \\ \phi^{(o)}_{0,\ x>\hat{\omega}}(z), & \hat{\omega} < x \le 1 \end{cases}, \tag{4.188}$$

$$n(z,x) = \begin{cases} n^{(o)}_{0,\ x<\hat{\omega}}(z), & 0 \le x < \hat{\omega}, \\ n^{(o)}_{0,\ x>\hat{\omega}}(z), & \hat{\omega} < x \le 1 \end{cases}, \tag{4.189}$$

as $\varepsilon \to 0$ for $x = O(1)$.

An important result to obtain from this analysis is obtained by integrating (4.185) along x to get the distribution of the current density F_{n1} to be approximated by an effective solution which describes the end current density-voltage relationship

$$F_{n\ \text{eff}} = -\delta(1-S)(n^{(o)2}_{0,x>\hat{\omega}}(0) - 1), \tag{4.190}$$

where $S =< S_d(x) >$ is the average over the interface at $z = 0$ and

$$n^{(o)}_{0,x>\hat{\omega}} = n^{(o)}_0(0, x > \hat{\omega}) \tag{4.191}$$

as described by (4.173) and (4.174)-(4.176) as $S = 0$ for $x > \hat{\omega}$. This indicates that we may approximate the current density-voltage characteristics by only knowing the proportion of the dyed EA surface, S and finding the one-dimensional distribution of electrons, n, as in (4.173). This approximate relation is compared with numerical solutions in the following section.

4.4.3.2 Results and interpretation

We now present the spatial distributions of, ϕ and n, and the current density-voltage characteristics by solving numerically (4.135)-(4.144) with $N_b = 1$, $\hat{\omega} = 0.5$ $\hat{d} = 1$.

The numerically predicted distributions of ϕ and n are presented in Figure 4.15, along with the corresponding contour plots on the left of each distribution plot. In these simulations, we decrease the aspect ratio, ε, gradually, by letting it taking values 1, 0.1 and 0.001. When $\varepsilon \ll 1$ we observe a small jump in ϕ and a large jump in n as we move from $x = \hat{\omega}^-$ to $x = \hat{\omega}^+$. As the aspect ratio becomes smaller, the jumps become more sudden and the inner region thinner, leading to a steeper transition.

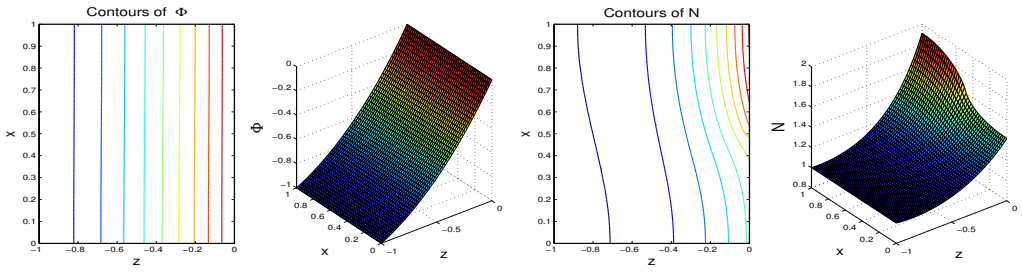

(a)

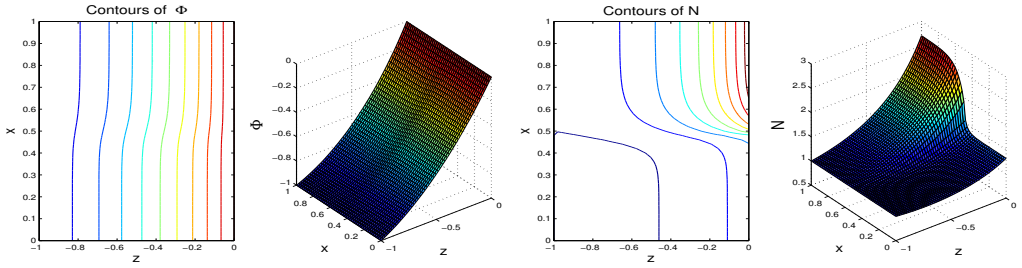

(b)

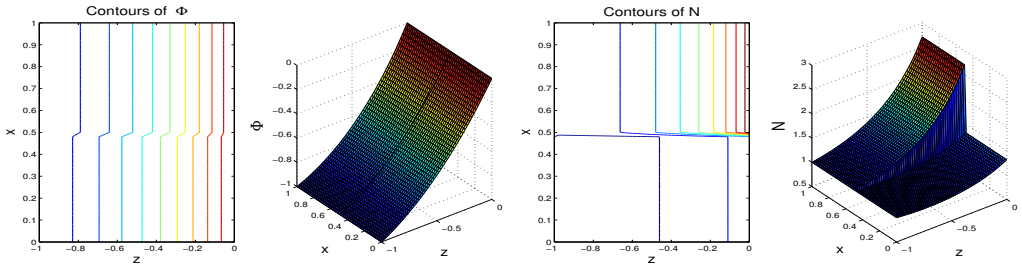

(c)

Figure 4.15: The contour and distribution plots of the numerical solutions, Φ and N, for (a) $\varepsilon = 1$, (b) $\varepsilon = 0.1$ and (c) $\varepsilon = 0.001$. Note: the plots are not shown in the same orientation as earlier Figures in this section. [Parameters: $\Lambda = 1$, $\delta = 1$, $\hat{\omega} = 0.5$, $\hat{d} = 1$, $\hat{V} = 2$, $\hat{\epsilon}_p = \hat{N}^- = \hat{P}^+ = 1$]

In Figure 4.16, we show the numerically predicted current density, F_{n1}, plotted against the applied voltage, $\hat{V}$, in the range $0 < \hat{V} < 5$ for $\varepsilon = 1,\ 0.1$ and 0.001. On the same plot, we show the distribution of $F_{n\ \text{eff}}$ as defined in (4.190). It is clear that as $\varepsilon \to 0$, the solution to the thin film problem tends to $F_{n\ \text{eff}}$, making (4.190) a good approximation to the current-density-voltage relation for a bilayer thin film cell.

In this section we have presented the two-dimensional problem that describes a thin film bilayer device. In the limit of small aspect ratio, we have used asymptotic techniques in order to find an analytic solution to the problem in the outer regions. Even

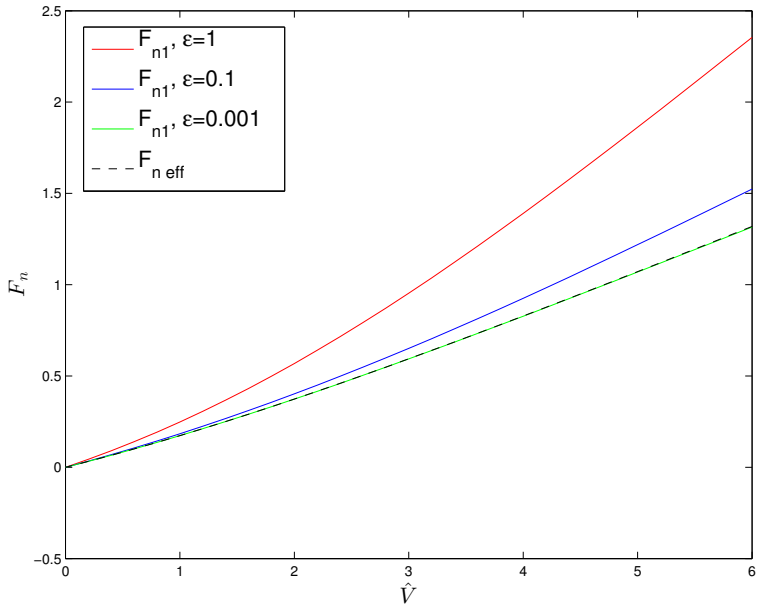

Figure 4.16: Plots of the current density, F_{n1}, against the applied voltage, V, generated numerically for $\varepsilon = 1,\ 0.1$ and 0.001 and of the effective current density $F_{n\ \text{eff}}$ against $\hat{V}$. [Parameters: $\Lambda = 1$, $\delta = 1$, $\hat{\omega} = 0.5$, $\hat{d} = 1$]

though no analytic solution is explicitly found in the inner region, we set up an effective model which appears to agree well with the two dimensional problem. In the effective model, the current density is the average of the solutions to the regions away from $x = \hat{\omega}$. In the following section we examine the case of a bilayer thin film with periodically deposited dye blobs of small width at the interface.

4.4.4 Thin dye blobs approximation

In this section we investigate the behaviour of the cell when the EA surface is covered with multiple non-connected blobs of dye such that the total area covered with dye is comparable to the width of the device, as shown schematically in Figure 4.11. We let the separation width in-between dye blobs, $\hat{g}$, be the same as the width of a blob, $\hat{\omega}$, for simplicity. This allows us to solve the problem for only one repeated block. Here, we investigate the effect of having repeated thin blobs with $\omega \ll 1$, distributed uniformly along the interface.

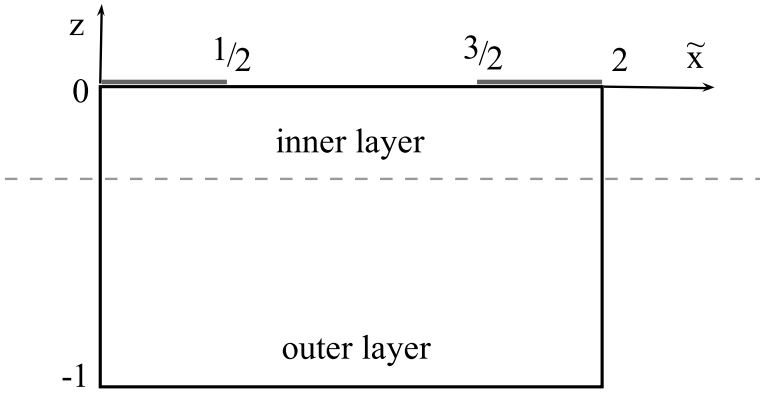

Figure 4.17: The (rescaled) domain of the repeated block for the multiple thin blobs approximation.

We focus in one blob and the nearby gap, as we consider this the repetitive building block. Therefore, we reduce the domain of the EA layer, Ω_a, to $0 \leq x \leq 2\omega$ and $-1 \leq z \leq 0$. The problem we seek to solve is given by (4.135)-(4.137), together with the z-boundary conditions (4.138)-(4.139) and interface conditions (4.142)-(4.144). We replace the x-boundary conditions (4.140)-(4.141) with periodic boundary conditions on ϕ, ϕ_x, n and n_x. We scale the problem as in the previous section, except for x which is scaled by $x = \omega\tilde{x}$, i.e. the width of a dye blob (we retain the new notation to avoid confusion with any previous analysis).

The aspect ratio for this problem is

$$\varepsilon_\omega = \frac{\omega}{H_1} \approx 10^{-3}. \tag{4.192}$$

We seek an approximate solution to the problem in the limit $\varepsilon_\omega \to 0$. This corresponds to a device with repeated dye blobs of small blobs compared to the thickness of the layers. For this analysis we consider two distinguished regions in the device as indicated in Figure 4.17:
- an *outer region* away from the interface, $-1 \leq z \ll 0$, in which we expect the variables to behave according to a one-dimensional problem by taking $S =< S_d(x) >$[6], and
- an *inner region* near the interface, $O(\varepsilon_\omega) = z \leq 0$, in which we expect the variables to take account of the dye distribution.

[6]This can be obtained by $S = \frac{1}{2}\int_0^2 S_d(x)dx$.

After rescaling the EA layer, the domain -in which we seek a solution- reduces to $x \in [0,2]$ and $z \in [-1,0]$, as shown in Figure 4.17. The equations become

$$\varepsilon_\omega^2 \phi_{zz} + \phi_{\tilde{x}\tilde{x}} = \Lambda \varepsilon_\omega^2 n, \tag{4.193}$$

$$\varepsilon_\omega^2 (n\phi_z - n_z)_z + (n\phi_{\tilde{x}} - n_{\tilde{x}})_{\tilde{x}} = 0. \tag{4.194}$$

along with the boundary conditions

$$\phi(z,0) = \phi(z,2), \qquad n(z,0) = n(z,2), \tag{4.195}$$

$$\phi_{\tilde{x}}(z,0) = \phi_{\tilde{x}}(z,2), \quad n_{\tilde{x}}(z,0) = n_x(z,2), \tag{4.196}$$

$$\phi(-1,\tilde{x}) = -\frac{\hat{V}}{2}, \qquad n(-1,\tilde{x}) = 1, \tag{4.197}$$

$$\phi(0,\tilde{x}) = 0, \qquad n(0,\tilde{x})\phi_z(0,\tilde{x}) - n_z(0,\tilde{x}) = \begin{cases} 0, & 0 \le \tilde{x} \le \frac{1}{2} \\ \delta(n^2(0,\tilde{x}) - 1), & \frac{1}{2} < \tilde{x} < \frac{3}{2} \\ 0, & \frac{3}{2} \le \tilde{x} \le 2 \end{cases}, \tag{4.198}$$

where we have considered geometrical symmetry across $\tilde{x} = 1$, as shown in Figure 4.17.

Our aim is to solve (4.193)-(4.198) asymptotically and numerically and compare the results. We will consider V as given and seek the generate current, F_n.

4.4.4.1 Outer Solution

In the region away from the dye interface, we solve (4.193)-(4.194) with (4.195)-(4.197), where $z = O(1)$ and $\tilde{x} = O(1)$. We consider the following asymptotic expansions in the outer region

$$\phi^{(o)}(z,\tilde{x};\varepsilon_\omega) \approx \phi_0^{(o)}(z,\tilde{x}) + \varepsilon_\omega^2 \phi_1^{(o)}(z,\tilde{x}) + ..., \tag{4.199}$$

$$n^{(o)}(z,\tilde{x};\varepsilon_\omega) \approx n_0^{(o)}(z,\tilde{x}) + \varepsilon_\omega^2 n_1^{(o)}(z,\tilde{x}) + ..., \tag{4.200}$$

so that the leading order problem reads

$$\phi_{0\tilde{x}\tilde{x}}^{(o)} = 0, \tag{4.201}$$

$$(n_0^{(o)}\phi_{0\tilde{x}}^{(o)} - n_{0\tilde{x}}^{(o)})_{\tilde{x}} = 0. \tag{4.202}$$

By applying the periodic boundary conditions (4.195)-(4.196), we find that $\phi_0^{(o)} = \phi_0^{(o)}(z)$ and $n_0^{(o)} = n_0^{(o)}(z)$. The $O(\varepsilon_\omega^2)$ order problem reads

$$\phi_{0zz}^{(o)} + \phi_{1\tilde{x}\tilde{x}}^{(o)} = \Lambda n_0^{(o)}, \tag{4.203}$$

$$(n_0^{(o)}\phi_{0z}^{(o)} - n_{0z}^{(o)})_z + (n_1^{(o)}\phi_{0\tilde{x}}^{(o)} + n_0^{(o)}\phi_{1\tilde{x}}^{(o)} - n_{1\tilde{x}}^{(o)})_{\tilde{x}} = 0, \tag{4.204}$$

which, by imposing the periodic boundary conditions [7] again, admits the following system for the leading order terms of the asymptotic expansions

$$\phi_{0zz}^{(o)} = \Lambda n_0^{(o)}, \tag{4.208}$$

$$(n_0^{(o)}\phi_{0z}^{(o)} - n_{0z}^{(o)})_z = 0. \tag{4.209}$$

The variables must satisfy the boundary conditions

$$\phi_0^{(o)}(-1) = -\frac{\hat{V}}{2}, \qquad n_0^{(o)}(-1) = 1. \tag{4.210}$$

This is equivalent to the previous one-dimensional problem and has, as in (4.172)-(4.173), a general solution of the form

$$\phi_0^{(o)}(z) = -2\log\left(\alpha\,\mathrm{Ai}(\chi_1 + \chi_2 z) + \beta\,\mathrm{Bi}(\chi_1 + \chi_2 z)\right), \tag{4.211}$$

$$n_0^{(o)}(z) = -\frac{2\chi_2^2}{\Lambda}\left[\chi_1 + \chi_2 z - \left(\frac{\alpha\,\mathrm{Ai}'(\chi_1 + \chi_2 z) + \beta\,\mathrm{Bi}'(\chi_1 + \chi_2 z)}{\alpha\,\mathrm{Ai}(\chi_1 + \chi_2 z) + \beta\,\mathrm{Bi}(\chi_1 + \chi_2 z)}\right)^2\right], \tag{4.212}$$

where the unknown parameters, $\alpha = \alpha(x), \beta = \beta(x),\ \chi_1 = \chi_1(x)$ and $\chi_2 = \chi_2(x)$, are found by imposing the boundary conditions at $z = -1$, and the matching conditions

[7] If we impose periodicity for $\phi_{1\tilde{x}}^{(o)}$ and $\phi_1^{(o)}$ on the left hand side of (4.203) we get the result in (4.208) as follows:

$$\int_0^2 \phi_{zz}^{(o)} d\tilde{x} + \int_0^2 \phi_{1\tilde{x}\tilde{x}} d\tilde{x} = \Lambda \int_0^2 n_0^{(o)} d\tilde{x} \tag{4.205}$$

$$2\phi_{0zz}^{(o)} + \left[\phi_{1\tilde{x}}^{(o)}\right]_0^2 = 2\Lambda n_0^{(o)} \tag{4.206}$$

which, using $\phi_{1\tilde{x}}^{(o)} = 0$ at $\tilde{x} = 0, 2$, gives

$$\phi_{0zz}^{(o)} = \Lambda n_0^{(o)}. \tag{4.207}$$

Similarly, imposing periodicity for $n_{1\tilde{x}}^{(o)}$ and $n_1^{(o)}$ in (4.204) gives (4.209).

with the inner layer as $z \to 0$. The boundary conditions (4.210)a and (4.210)b give

$$(\alpha\,\mathrm{Ai}(\chi_1-\chi_2)+\beta\,\mathrm{Bi}(\chi_1-\chi_2)) = e^{\frac{V}{4}}, \tag{4.213}$$

$$-\frac{2\chi_2^2}{\Lambda}\left[\chi_1-\chi_2-\left(\frac{\alpha\,\mathrm{Ai}'(\chi_1-\chi_2)+\beta\,\mathrm{Bi}'(\chi_1-\chi_2)}{\alpha\,\mathrm{Ai}(\chi_1-\chi_2)+\beta\,\mathrm{Bi}(\chi_1-\chi_2)}\right)^2\right] = 1. \tag{4.214}$$

4.4.4.2 Inner Solution

In this region, we introduce an inner variable by scaling z with the small parameter of the problem, ε_ω, by introducing the inner variable, η, as

$$z = \varepsilon_\omega \eta. \tag{4.215}$$

We define the solutions in the inner region as $\phi^{(i)}$ and $n^{(i)}$ and the problem becomes

$$\phi^{(i)}_{\eta\eta} + \phi^{(i)}_{\tilde{x}\tilde{x}} = \Lambda\varepsilon_\omega^2 n^{(i)}, \tag{4.216}$$

$$(n^{(i)}\phi^{(i)}_\eta - n^{(i)}_\eta)_\eta + (n^{(i)}\phi^{(i)}_{\tilde{x}} - n^{(i)}_{\tilde{x}})_{\tilde{x}} = 0, \tag{4.217}$$

along with the boundary conditions in $z = 0$:

$$\phi^{(i)}(0,\tilde{x}) = 0, \tag{4.218}$$

$$n^{(i)}(0,\tilde{x})\phi^{(i)}_\eta(0,x) - n^{(i)}_\eta(0,\tilde{x}) = \varepsilon_\omega F_{n1}(\tilde{x}) = \begin{cases} 0, & 0 \le x \le \frac{1}{2} \\ \varepsilon_\omega\delta(n^{(i)2}(0,\tilde{x})-1), & \frac{1}{2} < \tilde{x} < \frac{3}{2} \\ 0 & \frac{3}{2} \le \tilde{x} \le 2 \end{cases}, \tag{4.219}$$

and the periodic boundary conditions

$$\phi^{(i)}(\eta,0) = \phi^{(i)}(\eta,2), \qquad n^{(i)}(\eta,0) = n^{(i)}(\eta,2), \tag{4.220}$$

$$\phi^{(i)}_{\tilde{x}}(\eta,0) = \phi^{(i)}_{\tilde{x}}(\eta,2), \qquad n^{(i)}_{\tilde{x}}(\eta,0) = n^{(i)}_{\tilde{x}}(\eta,2). \tag{4.221}$$

The solutions must also match with the outer solution, $\phi^{(o)}$ and $n^{(o)}$, as $\eta \Rightarrow \infty$. We expand our variables as

$$\phi^{(i)}(\eta,\tilde{x};\varepsilon_\omega) \approx \phi^{(i)}_0(\eta,\tilde{x}) + \varepsilon_\omega\phi^{(i)}_1(\eta,\tilde{x}) + \varepsilon_\omega^2\phi^{(i)}_2(\eta,\tilde{x}) + ..., \tag{4.222}$$

$$n^{(i)}(\eta,\tilde{x};\varepsilon_\omega) \approx n^{(i)}_0(\eta,\tilde{x}) + \varepsilon_\omega n^{(i)}_1(\eta,\tilde{x}) + \varepsilon_\omega^2 n^{(i)}_2(\eta,\tilde{x}) + ... \tag{4.223}$$

and substitute into (4.216)-(4.217). Then, the $O(1)$ problem reads

$$\phi^{(i)}_{0\eta\eta} + \phi^{(i)}_{0\tilde{x}\tilde{x}} = 0, \tag{4.224}$$
$$n^{(i)}_{0\eta\eta} + n^{(i)}_{0\tilde{x}\tilde{x}} = n^{(o)}_{0\eta}\phi^{(o)}_{0\eta} + n^{(o)}_{0\tilde{x}}\phi^{(o)}_{0\tilde{x}}, \tag{4.225}$$

with the boundary conditions (4.218)-(4.221) reducing to

$$\phi^{(i)}_0(\eta, 0) = \phi^{(i)}_0(\eta, 2), \qquad n^{(i)}_0(\eta, 0) = n^{(i)}_0(\eta, 2), \tag{4.226}$$
$$\phi^{(i)}_{0\tilde{x}}(\eta, 0) = \phi^{(i)}_{0\tilde{x}}(\eta, 2), \qquad n^{(i)}_{0\tilde{x}}(\eta, 0) = n^{(i)}_{0\tilde{x}}(\eta, 2), \tag{4.227}$$
$$\phi^{(i)}_0(0, \tilde{x}) = 0, \qquad n^{(i)}_{0\eta}(0, \tilde{x}) = 0. \tag{4.228}$$

along with the matching conditions that require that $\phi^{(o)}_0$ and $n^{(o)}_0$ are bounded as $\eta \to \infty$. The solution is found to be

$$\phi^{(i)}_0 = 0 \ \text{ and } \ n^{(i)}_0 = A, \tag{4.229}$$

where A is an arbitrary constant. The $O(\varepsilon_\omega)$ problem reads

$$\phi^{(i)}_{1\eta\eta} + \phi^{(i)}_{1\tilde{x}\tilde{x}} = 0, \tag{4.230}$$
$$n^{(i)}_{1\eta\eta} + n^{(i)}_{1\tilde{x}\tilde{x}} = 0, \tag{4.231}$$

where we have used the solution for $\phi^{(o)}_0$ and $n^{(o)}_0$ in (4.229) with (4.230) to eliminate extra terms in (4.231). The boundary conditions are

$$\phi^{(i)}_1(\eta, 0) = \phi^{(i)}_1(\eta, 2), \qquad n^{(i)}_1(\eta, 0) = n^{(i)}_1(\eta, 2), \tag{4.232}$$
$$\phi^{(i)}_{1\tilde{x}}(\eta, 0) = \phi^{(i)}_{1\tilde{x}}(\eta, 2), \qquad n^{(i)}_{1\tilde{x}}(\eta, 0) = n^{(i)}_{1\tilde{x}}(\eta, 2), \tag{4.233}$$
$$\phi^{(i)}_1(0, \tilde{x}) = 0, \quad n^{(i)}_0\phi^{(i)}_{1\eta} - n^{(i)}_{1\eta}(0, \tilde{x}) = F_{n1}(\tilde{x}). \tag{4.234}$$

along with matching conditions that require that $\phi^{(o)}_1$ and $n^{(o)}_1$ grow at most linearly as $\eta \to \infty$ The solution to this problem is found to be

$$\phi^{(i)}_1 = A_1\eta \tag{4.235}$$
$$n^{(i)}_1 = C_1\eta + q_0 + \sum_{m=1}^{\infty} q_m e^{m\pi\eta}\cos\left(m\pi(x-1)\right). \tag{4.236}$$

By imposing (4.234)b, we find

$$q_m = \left(-\frac{2}{(m\pi)^2} (\delta(n_0^{(i)2} - 1) \right) \quad \text{and} \tag{4.237}$$

$$n_0^{(i)} A_1 - C_1 = \frac{1}{2}(+\delta(n_0^{(i)2}(0, \tilde{x}) - 1). \tag{4.238}$$

We then require the solution for next order term of $\phi^{(i)}$, so we turn to the $O(\varepsilon_\omega^2)$ problem for $\phi_2^{(i)}$, which is

$$\phi_{2\eta\eta}^{(i)} + \phi_{2\tilde{x}\tilde{x}}^{(i)} = \Lambda n_0^{(i)}, \tag{4.239}$$

with

$$\phi_2^{(i)}(\eta, 0) = \phi_2^{(i)}(\eta, 2), \qquad \phi_{2\tilde{x}}^{(i)}(\eta, 0) = \phi_{2\tilde{x}}^{(i)}(\eta, 2), \tag{4.240}$$

$$\phi_2^{(i)}(0, \tilde{x}) = 0. \tag{4.241}$$

and $\phi_2^{(o)}$ growing at most linearly as $\eta \to 0$. This gives

$$\phi_2^{(i)} = \Lambda n_0^{(i)} \frac{\eta^2}{2} + A_2 \eta. \tag{4.242}$$

We do not attempt to solve for $n_2^{(i)}$ as we find it is not necessary for the matching at this order. The remaining parameters are then found by matching with the outer solution, as follows.

Matching

For simplicity of the notation in the following analysis, we define

$$f(z) = \alpha \, \mathrm{Ai}(\chi_1 + \chi_2 z) + \beta \, \mathrm{Bi}(\chi_1 + \chi_2 z). \tag{4.243}$$

We re-write the outer solution for ϕ in terms of (4.243) and the inner variable, η, and

expand for $\varepsilon_\omega \ll 1$ so that

$$i(1.t.o.) = \phi_0^{(o)} = -2\log(f(\varepsilon_\omega \eta)) \tag{4.244}$$

$$= \underbrace{\underbrace{\underbrace{-2\log(f(0))}_{1.t.i.(1.t.o)} - 2\frac{f'(0)}{f(0)}\eta\varepsilon_\omega}_{2.t.i.(1.t.o.)} - \left(\frac{f''(0)}{f(0)} - \left(\frac{f'(0)}{f(0)}\right)^2\right)\eta^2\varepsilon_\omega^2 + \ldots}_{3.t.i.(1.t.o.)} . \tag{4.245}$$

Then the inner solution, $\phi^{(i)}$, expanded in terms of the outer variable z and re-written in the inner variable η, gives

$$\phi^{(i)} \sim \underbrace{\underbrace{\underbrace{0}_{1.t.o.(1.t.i.)} + A_1\eta\varepsilon_\omega}_{1.t.o.(2.t.i.)} + \left(A_2\eta + \Lambda n_0^{(i)}\frac{\eta^2}{2}\right)\varepsilon_\omega^2 + O(\varepsilon_\omega^3)}_{1.t.o.(3.t.i.)} \tag{4.246}$$

Then, by Van Dyke's matching principle, we have that

$$1.t.i.(1.t.o.) = 1.t.o.(1.t.i.) \quad \Rightarrow f(0) = 1, \tag{4.247}$$

$$2.t.i.(1.t.o.) = 1.t.o.(2.t.i.) \quad \Rightarrow A_1 = -2f'(0), \tag{4.248}$$

$$3.t.i.(1.t.o.) = 1.t.o.(3.t.i.) \quad \Rightarrow A_2 = 0, \quad \Lambda n_0^{(i)} = -2\left(f''(0) - f'(0)^2\right). \tag{4.249}$$

For n, as before, we re-write the outer solution $n^{(o)}$, given by (4.212), in terms of $f(z)$ (as defined in (4.243)), and the inner variable, η, and expand for small ε_ω so that

$$i(1.t.o.) = n_0^{(o)} = -\frac{2}{\Lambda}\left(\frac{f''(\varepsilon_\omega\eta)}{f(\varepsilon_\omega\eta)} - \left(\frac{f'(\varepsilon_\omega\eta)}{f(\varepsilon_\omega\eta)}\right)^2\right) \tag{4.250}$$

$$= -\frac{2}{\Lambda}\left(\frac{f''(0)}{f(0)} - \left(\frac{f'(0)}{f(0)}\right)^2\right) - \frac{2}{\Lambda}\left[\frac{f'''(0)}{f(0)} - \frac{f''(0)f'(0)}{f^2(0)} - 2\left(\frac{f''(0)}{f(0)} - \left(\frac{f'(0)}{f(0)}\right)^2\right)\right]\eta\varepsilon_\omega + O(\varepsilon_\omega^2) \tag{4.251}$$

The inner solution, $n^{(i)}$, expanded in terms of the outer variable z and re-written in

the inner variable η, gives

$$n^{(i)} \sim \underbrace{\underbrace{n_0^{(i)}}_{1.t.o.(1.t.i.)} + (q_0 + C_1\eta)\varepsilon_\omega}_{1.t.o.(2.t.i.)} + O(\varepsilon_\omega^2) \tag{4.252}$$

Then, by Van Dyke's matching principle, we have that

$$1.t.i.(1.t.o.) = 1.t.o.(1.t.i.) \quad \Rightarrow \Lambda n_0^{(i)} = -2\left(f''(0) - f'(0)^2\right), \tag{4.253}$$

$$2.t.i.(1.t.o.) = 1.t.o.(2.t.i.) \quad \Rightarrow q_0 = 0, \quad C_1 = -\frac{2}{\Lambda}\left[f''(0) - f''(0'_f(0) - 2\left(f''(0) - f'(0)^2\right)\right], \tag{4.254}$$

using (4.247) to simplify (4.254). Thus, we may solve the eight equations (4.213), (4.214), (4.238), (4.247)-(4.249), (4.253) and (4.254) to find the value of the eight unknown parameters: χ_1, χ_2, A, C_1, α, β, A_1 and q_m for $m = 1, 2, ...$ The composite (leading order) solution is simply the outer solution given by $\phi^{(o)}$ and $n^{(o)}$, with the parameters satisfying the aforementioned relations. We use this result to write an approximate expression describing the current density-voltage characteristics in the limit $\varepsilon_\omega \to 0$.

4.4.4.3 The effective model

Having found the approximate solutions for the leading order solution of ϕ and n, we observe that the inner problem provides a new boundary condition for the outer problem given by

$$\phi_0^{(o)}(z, \tilde{x}))|_{z\to 0} \to 0 \tag{4.255}$$

$$n_0^{(o)}(z, \tilde{x})|_{z\to 0} \to n_0^{(i)}. \tag{4.256}$$

Then, by integrating (4.238), it follows that

$$\left(n_0^{(o)}\frac{\partial \phi_0^{(o)}}{\partial z} - \frac{\partial n_0^{(o)}}{\partial z}\right)\Big|_{z\to 0} \to \frac{1}{2}\int_0^2 F_{n1}(\tilde{x})d\tilde{x} =< F_{n1}, \tag{4.257}$$

where $< U >$ is the average of U across the dye interface ($z = 0$). Further, by using (4.198)b, we can introduce an effective description of the current density, $F_{n\ eff}$, as

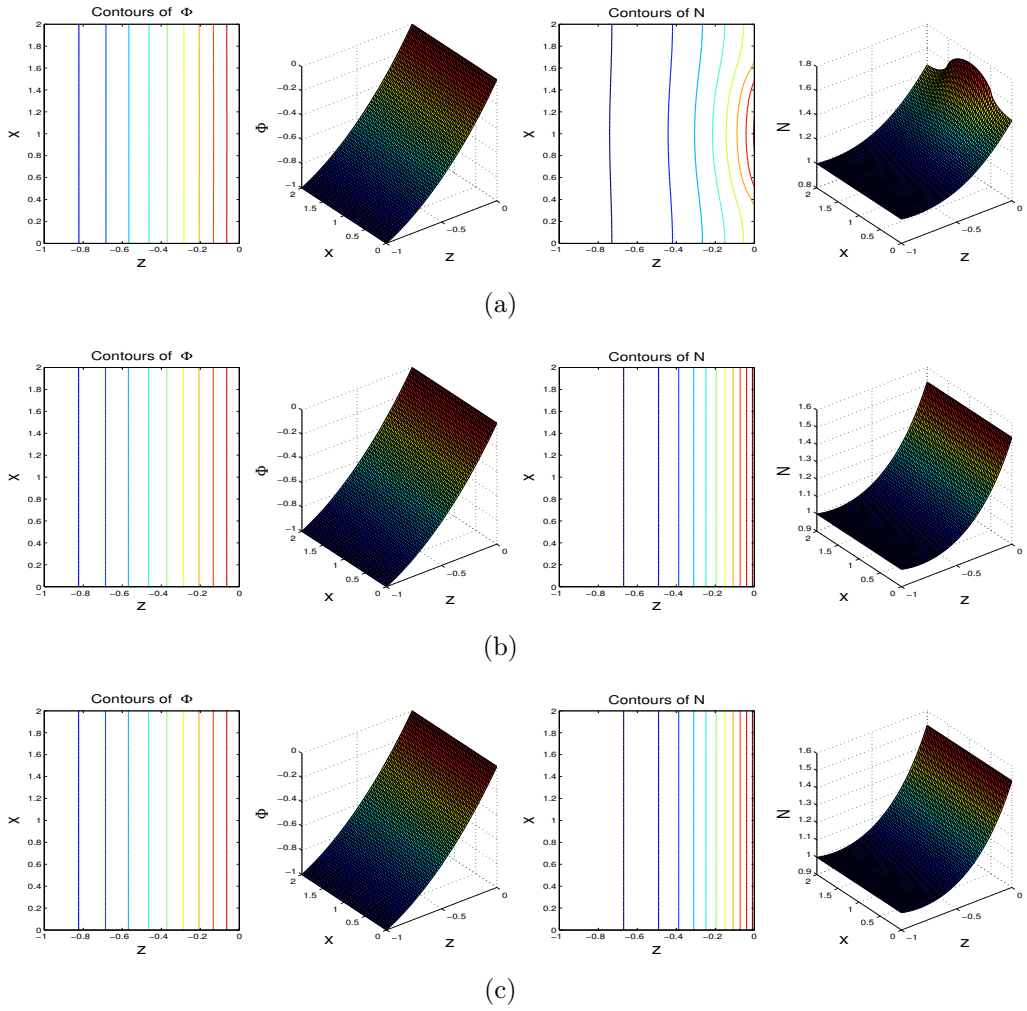

Figure 4.18: The contour and distribution plots of Φ and N - the numerical solutions for ϕ and n, respectively - for (a) $\varepsilon_\omega = 1$, (b) $\varepsilon_\omega = 0.1$ and (c) $\varepsilon_\omega = 0.001$. [Parameters: $\Lambda = 1$, $\delta = 1$, $\hat{V} = 2$]

being the average of the current calculated along the dye interface, by

$$F_{n\ eff} =< F_{n1}(\tilde{x}) >= -\delta(1-S)\left(n^{(o)2}(0,\tilde{x}) - 1\right), \tag{4.258}$$

as $\varepsilon_\omega \to 0$. We compare the prediction of this relation against numerical results in the following section.

4.4.4.4 Results and interpretation

We present numerical simulations of the distributions of the variables, ϕ and n, and also the current density-voltage characteristics using the thin dye blobs prob-

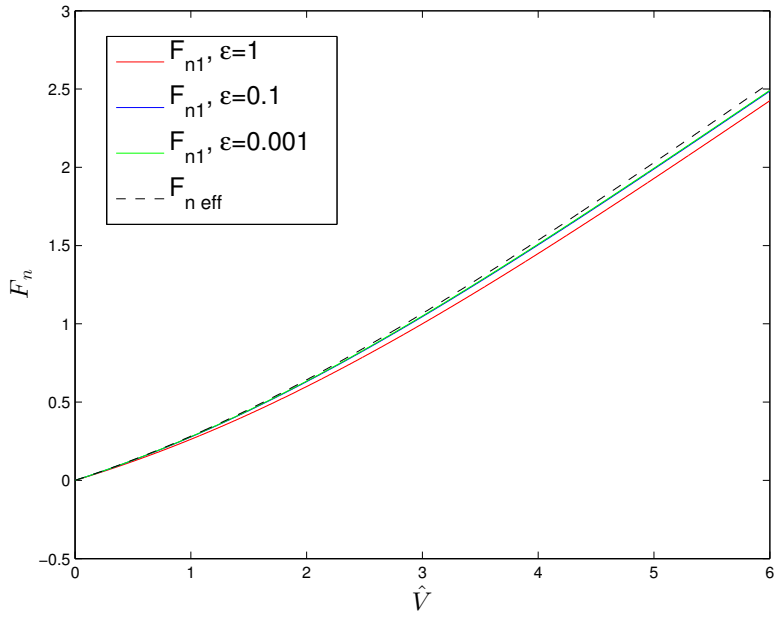

Figure 4.19: Plots of the current density, F_{n1}, against the applied voltage, $\hat{V}$, generated numerically for $\varepsilon_\omega = 1,\ 0.1$ and 0.001 and of the effective current density $F_{n\ \text{eff}}$ against V. [Parameters: $\Lambda = 1$, $\delta = 1$]

lem given by (4.193)-(4.198). We compare the numerical solutions to the effective one-dimensional results in all three cases in the limit of small aspect ratio, ε_ω.

The computed distributions of ϕ and n are shown in Figure 4.18, along with the corresponding contours. In these simulations, we decrease the aspect ratio, ε_ω, gradually, by letting it take values $1,\ 0.1$ and 0.001. We observe that as the aspect ratio becomes smaller, the region in which the variables are affected by the non-uniform dye distribution becomes smaller. This allows for solutions that are quasi-uniform in the x direction in this limit.

In Figure 4.19 we illustrate the current density, F_{n1}, defined in (4.144), against the applied voltage, $\hat{V}$, as calculated numerically for $\varepsilon_\omega = 1,\ 0.1$ and 0.001. On the same plot, we show the distribution of $F_{n\ \text{eff}}$ as defined in (4.258). Therefore, we have shown that for small ε_ω, the numerical solution to the thin dye blobs problem can be approximated by $F_{n\ \text{eff}}$.

Finally, the total current generated is expressed as the sum of current generated over each building block. Therefore, for a cell with $N = \frac{d}{L}$ blobs will have a total

current of:

$$F_{n\ total} = \sum_{q=1}^{N} F_{n\ eff} = -\delta(1-S)\left(n^{(o)2}(0,\tilde{x}) - 1\right). \tag{4.259}$$

In this section we have presented the two-dimensional problem that describes a bilayer device with a non-uniform distribution of dye blobs along the interface. We have, however, imposed the assumption of an ordered dye distribution to simplify the analysis. We have used asymptotic techniques to find an approximate analytic solution of the problem as the aspect ratio gets smaller. The analysis allowed us to find an effective one-dimensional model which agrees well with the two-dimensional original problem. Thus, the solution can be effectively represented by the solution of a one-dimensional problem in z with $S =< S_d(x) >$, i.e. the current generated along the interface can be averaged spatially.

4.5 Data Validation

While this thesis is confined to a theoretical analysis of the operation of ssDSSCs, a team of physicists at the Clarendon Laboratory[8] working on photovoltaic technology, have kindly provided some data for the validation of our model. While common ssDSSCs typically include a mesoporous EA layer with a non-planar interface, the team has provided us with data for a cell with a planar interface. A cell of this simplified structure is not considered efficient, but it is still valuable for the context of this thesis as it helps illustrating the ability of the models to qualitatively predict the current-voltage relationships.

The current density-voltage measurements for the cell have been taken under standard testing conditions (AM1.5 light at 100 $mW\ cm^{-2}$), while on top of the cell a metal mask was placed with an opening for the active layer in order to eliminate edge effects. In Figure 4.20 we show the experimentally obtained current-voltage curves for this cell both in the dark and under illumination for the range of 0 to 0.4 V. The cell is configured as FTO/TiO_2/Dye N102/Spiro-OMEtAD/Silver with no additives

[8]We are indebted to both Dr Pablo Docampo and Dr Agnese Abrusci, former members of the team, for providing us with the data used in this section.

in the outer regions. The current is measured across the two ends as voltage increases from $0V$ to $1V$. The efficiency of the cell is experimentally calculated to be $\sim 0.002\%$.

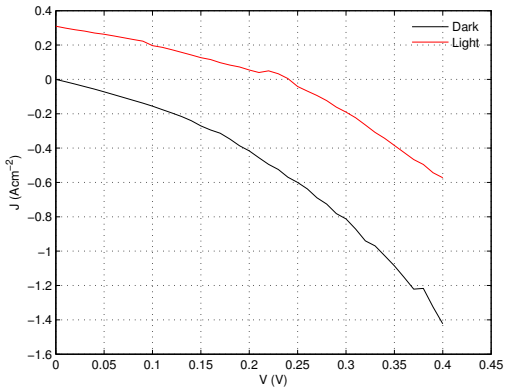

Figure 4.20: Plot of the the experimental data for the current density, J described by (3.8), against the applied voltage, V, measured from zero (0V) to forward bias (0.4V), for the dark and illuminated cell from data extracted from a FTO/TiO_2/Dye (Z907)/spiro−OMeTAD/Ag cell. Note: The red curve is not to be fitted, but only presented here for the interest of the reader.

The maximum power output is reached within the range of $0-0.25V$, thus we choose to test our model against the range $0-0.5V$ only. Following our deduction that solutions converge to a one-dimensional model, we fit the one-dimensional exact solution to the data provided to allow for faster computation. Consistent with the Chapter, we demonstrate the fitting for a cell in the dark. To fit the model to the data, we allow for the variability of the parameters $\alpha = \delta S$, $\beta = \Lambda$ and γ, such that $\hat{V} = \gamma\tilde{V}$ and use a MatLab embedded function for *least squares* regression in order to fit the model to the available data. For comparability, we have rescaled the experimental values of the voltage by $V_{thermal} = 0.0026V$ and of the current by $J_d = 0.04Am^{-2}$. As shown in Figure 4.21, the solution to our model qualitatively agrees with the experimental data. The resulting parameter values were obtained to be $\alpha = 0.1071$, $\beta = 0.9912$ and $\gamma = 8.1689$, which appear to lie close to our initial assumptions of $\Lambda = 1$, $0 < S < 1$ and $\delta \ll 1$.

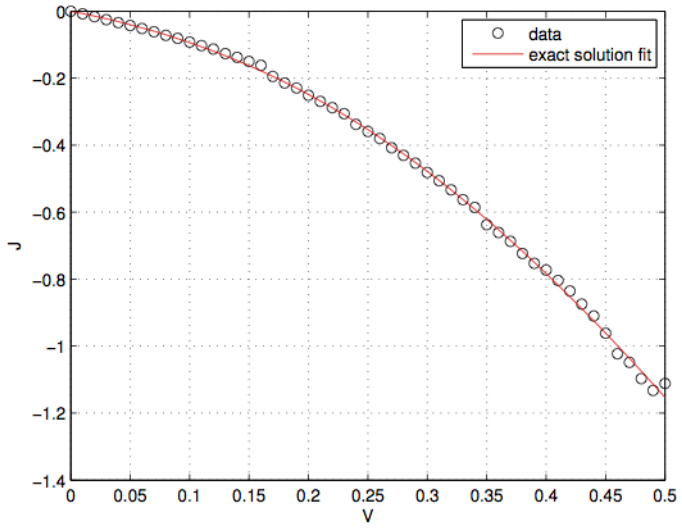

Figure 4.21: Fitting the exact one dimensional solution to the experimental data for a ssDSSC in the dark with two fitting parameters.

We note that the resistance of the contacts and the impurities of the device were not accounted for in this data validation exercise. Given this, the exact solution described by (4.28)-(4.30) agrees qualitatively well with the experimental data. However, the experimental data represent an ideality factor which is larger than unity, implying that the recombination process is not purely in the form of direct recombination and that other forms of recombination should be taken into consideration for model enhancement, as suggested earlier in the earlier chapters of this thesis as well.

4.6 Summary

In this Chapter we have analysed the current transport in a bilayer cell in the dark. Starting from the simplest one-dimensional symmetric scenario and ending with the two-dimensional case with variable dye distribution, we have demonstrated the predictive capabilities of the mathematical model by validating our results against experimental data.

Under the one-dimensional approximation, in Sections 4.1, 4.2 and 4.3, we examined the transport of carriers under varying applied bias. We have shown that, as the voltage increases, the resulting electric field at the interface controls the transport of current. We have identified two regimes of operation: (i) the quasi-equilibrium state,

where drift and diffusion balance and are both significantly larger than the current and, (ii) the drift-dominant state (which includes both the intermediate and large current approximations). The exact solution was calculated and compared with the asymptotic results for each regime to demonstrate validity.

In Section 4.4, we examined the effect of the dye distribution at a planar interface using a two-dimensional approach. We have used a simplification, by allowing a uniform distribution of dye which proved useful in understanding the effect of the ratios of the lengthscales of the device. In particular, we have considered the following two cases:
(i) a bilayer device with a small length-to-width ratio, namely $\varepsilon = \frac{H_1}{L} \ll 1$, and
(ii) a bilayer device with a small blob thickness-to-device length ratio, namely $\varepsilon_\omega = \frac{\omega}{H_1} \ll 1$.
We simplified the problems by allowing the cell to be symmetric and taking the dye distribution to have a periodic distribution in order to avoid unnecessary complexity. Thus, we have only considered the half-device, and, in particular, the EA region. We have used analytic techniques to simplify the models by finding an effective one-dimensional models that agree well with the numerically computed electrostatic potential and the electron concentration distributions.

In particular, it is found that for case (i), the current density-voltage curve can be approximated by an effective model given by (4.190) in the limit of $\varepsilon \to 0$. If we allow for a dye blob to cover an $O(1)$ portion of the interface, it can be shown that away from the end of the blob, on either side, the solution can be approximated by an appropriate one dimensional model with different boundary conditions at the interface: one with dye and another without dye, as $\varepsilon \to 0$. The current density-voltage curve is then taken to be the average of these two solutions. Under scenario (ii), i.e. for repeated thin dye blobs, the effect of the dye distribution is found to be significant only in a small layer near the interface with width of the order of ε_ω. An effective one-dimensional model was found as $\varepsilon_\omega \to 0$ with interface spatially averaged by taking $S =< S_d >$, as given in (4.258). In comparison of the two results, it can be observed (see Figures 4.16 and4.19) that the current generated in case (ii) is larger suggesting that a device is more efficient when the dye blobs are periodically and evenly distributed along a bilayer interface.

In the following Chapter we consider a nonplanar interface where the electron ac-

ceptor penetrates the donor region in the form of thin nanostems in a highly ordered arrangement.

5

The nanostructured cell

In this Chapter we examine the effects of the interfacial geometry for a nanostructured cell. In particular, we revisit the case where we have an ordered array of nanostructured stems, as shown in Figure 3.1(c). We employ both numerical and, whenever possible, analytic techniques to solve for the distribution of the electrostatic potential, ϕ, and the electron and hole densities, n and p, respectively, and generate the current density-voltage characteristics.

5.1 Morphology

The nanostructures are quasi-one dimensional, since the ratio of their length to their width is typically extremely large (see Figure 3.1(c)). As a result, they have a high surface area-to-volume ratio, which makes them favourable for ssDSSC. A few examples of nanostructured stems include: nanospheres [49], nanospheres with nanosheets on the surface [51], nanorods [52], nanotubes [53, 54], nanotubes with nanosheets on the surface [55], nanotubes with perpendicularly arranged nanorods on their surface (pine tree-like stems) [56] and nanowires [54, 57, 58, 50]. The width of the nanostem

is usually a few nanometers, i.e. of the size of the diameter of the particle of the EA material (e.g. 20 nm for TiO_2 [59]) and the length is of the order of microns. However, it is still extremely difficult to reach full dye coverage of the surface of the acceptor material, and thus there may be regions of direct acceptor-donor contact which allow for recombination of charge carriers: electrons arriving from the acceptor region recombining with holes arriving from the donor region. We assume the device to be modelled by the two-dimensional problem (3.16)-(3.19), (3.21),(3.22), (3.24),(3.25), (3.36) and (3.37) in z and x. We describe the interface by the curve

$$z = f(x). \tag{5.1}$$

We consider a cell with periodically arranged nanostems (which could be nanotubes, nanowires or nanorods), so that $f(x)$ is a periodic step function, as shown in Figure 3.1(c). We consider the case where the width of the stem, ω, is equal to the separation width between stems, g, which allows us to incorporate fewer parameters in designing the interface. Therefore, we only need to consider the width and length of the stem, ω, and the periodicity.

The complexity of this problem lies in the two-dimensional interface, when preparing the numerical scheme, requires careful consideration on the nodes along the interface. In this study, we solve the problem on the full domain, i.e. including both the EA and ED regions, which makes it more challenging analytically than in Chapter 4. To simplify the analysis we make further assumptions. The central idea behind these simplifications is to concentrate on investigating the effect of a structured interface.

We assume that the stems are placed in parallel and follow a periodic pattern so that the EA and ED regions each form a simply-connected region. We take the width of the stem to be equal to the diameter of the particles of the EA material. For TiO_2 this is approximately 20 nm, which allows to fit roughly 5×10^5 stems in a device of a total thickness of a few centimeters. We consider only one block of the repeated pattern, as shown in Figure 5.1. We use the parameters a, b, c and d to describe the interface. The mathematical model we are addressing remains unchanged, as given in (3.38)-(3.41) with the z boundary conditions (3.42)-(3.45) and the interface conditions (3.49)-(3.51). The x-boundary conditions at the x-boundaries, (3.46)-(3.48),

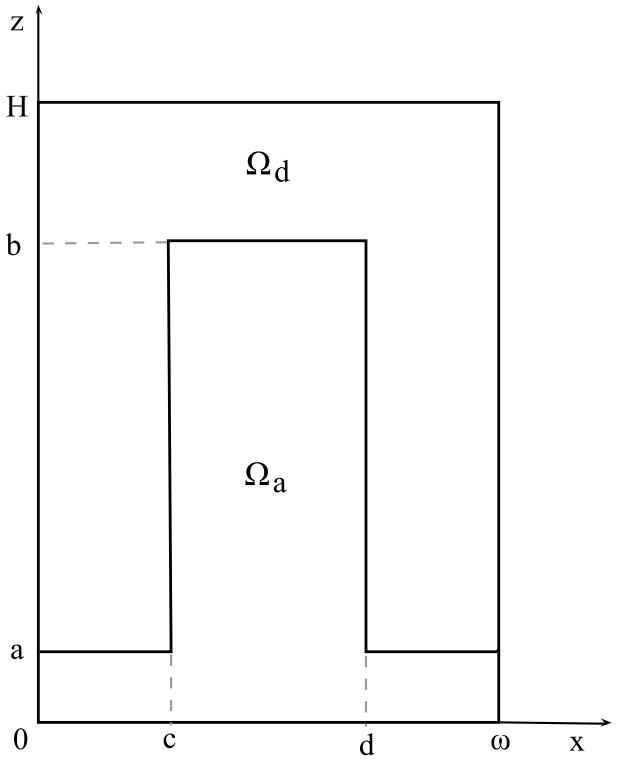

Figure 5.1: A block of the repeated pattern for the structured mixed layer. We take $a = c = \frac{1}{4\omega}$ and $b = d = \frac{3}{4\omega}$, unless otherwise stated. Note: The figure is not drawn to scale ($H \sim 1\mu m$, $\omega \sim 20nm$.

are replaced by the periodic conditions

$$\phi(z,0) = \phi(z,\omega),\ \phi_x(z,0) = \phi_x(z,\omega), \tag{5.2}$$

$$n(z,0) = n(z,\omega),\ n_x(z,0) = n_x(z,\omega), \quad \text{in } \Omega_a, \tag{5.3}$$

$$p(z,0) = p(z,\omega),\ \ p_x(z,0) = p_x(z,\omega), \quad \text{in } \Omega_d, \tag{5.4}$$

and the jump of the current fluxes at the interface is replaced by

$$[\mathbf{F}_n \cdot \hat{\mathbf{n}}] = -[\mathbf{F}_p \cdot \hat{\mathbf{n}}] = -(1 - S_d(z,x)) \left(\frac{np - \Pi_0^2}{\sigma \tau_R N_0 P_0} \right), \tag{5.5}$$

where [..] denotes the jump across the interface, from the EA to the ED, and $\hat{\mathbf{n}}$ is the outward normal to the acceptor surface[1] along the EA-ED interface.

[1]We note that the corner points represent singularity points in our model.

5.1.1 Nondimensionalisation

We scale all variables as in Section 4.1, except for the electrostatic potential and the spatial variables where we use $\phi = \frac{k_B T}{q}\hat{\phi}$, $z = H\hat{z}$ and $x = \omega\hat{x}$. Here, we let $H \approx 10^{-6}m$ be the height of the cell, as shown in Figure 5.1, and $\frac{\omega}{2} \approx 10^{-8}m$ is the width of the nanotubes. We drop the hats for ease of notation, so that the scaled problem reads

$$\varepsilon_\omega^2\phi_{zz} + \phi_{xx} = \begin{cases} \varepsilon_\omega^2\Lambda n, & \mathbf{x} \in \Omega_a \\ -\varepsilon_\omega^2 \frac{\Lambda}{\hat{\epsilon}_p} p, & \mathbf{x} \in \Omega_d \end{cases}, \tag{5.6}$$

$$\varepsilon_\omega^2(n\phi_z - n_z)_z + (n\phi_x - n_x)_x = 0, \quad \mathbf{x} \in \Omega_a, \tag{5.7}$$

$$\varepsilon_\omega^2(p\phi_z + p_z)_z + (p\phi_x + p_x)_x = 0, \quad \mathbf{x} \in \Omega_d, \tag{5.8}$$

where $\varepsilon_\omega = \frac{\omega}{H}$, while $\hat{\epsilon}_p = \frac{\epsilon_p}{\epsilon_n}$, $\hat{D}_p = \frac{D_p}{D_n}$, $\Lambda = q^2H^2\frac{\Pi_0}{k_BT\epsilon_n}$ and $\delta = \frac{H}{\sigma\tau_R D_n N_0 P_0}$. The domains Ω_a and Ω_d are now the scaled domains for the EA and ED regions, respectively. The scaled boundary conditions are

$$\phi(0,x) = 0, \quad n(0,x) = \hat{N}^-, \quad p(0,x) = 0, \tag{5.9}$$

$$\phi(1,x) = \hat{V}, \quad n(1,x) = 0, \quad p(1,x) = \hat{P}^+, \tag{5.10}$$

$$\phi(z,0) = \phi(z,1), \quad \phi_x(z,0) = \phi_x(z,1), \tag{5.11}$$

$$n(z,0) = n(z,1), \quad n_x(z,0) = n_x(z,1), \tag{5.12}$$

$$p(z,0) = p(z,1), \quad p_x(z,0) = p_x(z,1). \tag{5.13}$$

On the interface we have the following jump conditions

$$[\phi] = 0, \tag{5.14}$$

$$[\epsilon_i\nabla_\omega\phi \cdot \hat{\mathbf{n}}] = 0, \tag{5.15}$$

$$[\mathbf{F}_n \cdot \hat{\mathbf{n}}] = -[\mathbf{F}_p \cdot \hat{\mathbf{n}}] = -\delta(1 - S_d(z,x))(np - 1), \tag{5.16}$$

where

$$\mathbf{F}_n = n\nabla_\omega\phi - \nabla_\omega n, \quad \mathbf{F}_p = -\left(p\nabla_\omega\phi + \nabla_\omega p\right) \tag{5.17}$$

The scaled gradient operator is then defined as $\nabla_\omega = \left(\varepsilon_\omega\frac{\partial}{\partial z}, \frac{\partial}{\partial x}\right)$. The dimensionless parameters of the problem are as given in (4.149) with sizes as given in (4.150), except

for the aspect ratio that now is

$$\varepsilon_\omega = \frac{\omega}{H} \approx 10^{-2}. \tag{5.18}$$

5.1.2 Simplifications

In order to understand how the device operates in the limit $\varepsilon_\omega \to 0$, we consider a simplified example of the problem to which an analytic solution can be found. In particular, we impose symmetry on the cell by letting $\hat{\epsilon}_p = 1$, $\hat{N}^- = 1$ and $\hat{P}^+ = 1$. We assume that the nanostem starts well away from the anode and ends well away from the cathode, in order to avoid short-circuiting of the system, i.e. $0 < a = O(1)$ and $0 < 1 - b = O(1)$. We consider the case where δ is small and, in particular, we assume $\delta = \varepsilon_\omega \delta_0$ with $\delta_0 = O(1)$. We also assume that $\hat{V} = O(1)$.

We further assume that the width of the nanotube is equal to the total width of the gap between nanotubes, i.e. $d - c = \frac{1}{2}$, and also that the thickness of the acceptor region is equal to the width of the donor region, i.e. $b - a = \frac{1}{2}$.

We are only considering idealised cases of the cell with a nonplanar interface where there is no dye coating on the interface.

5.2 Methodology

We analyse the problem in (5.6)-(5.16) using both numerical and analytic techniques and solve the problem in the full domain, including both the EA and ED region.

5.2.1 Numerical method

We solve the problem using a uniform grid in $[0, 1] \times [0, 1]$ with step size h so that the numerical nodes are at (z_j, x_k), where $z_j = hj$ and $x = hk$, for $j, k = 0, ..., J$, as shown in Figure 5.2. We let $\Phi_{j,k} = \Phi(z_j, x_k)$, $N_{j,k} = N(z_j, x_k)$ and $P_{j,k} = P(z_j, x_k)$ be the numerical approximations for ϕ, n and p at each node, respectively.

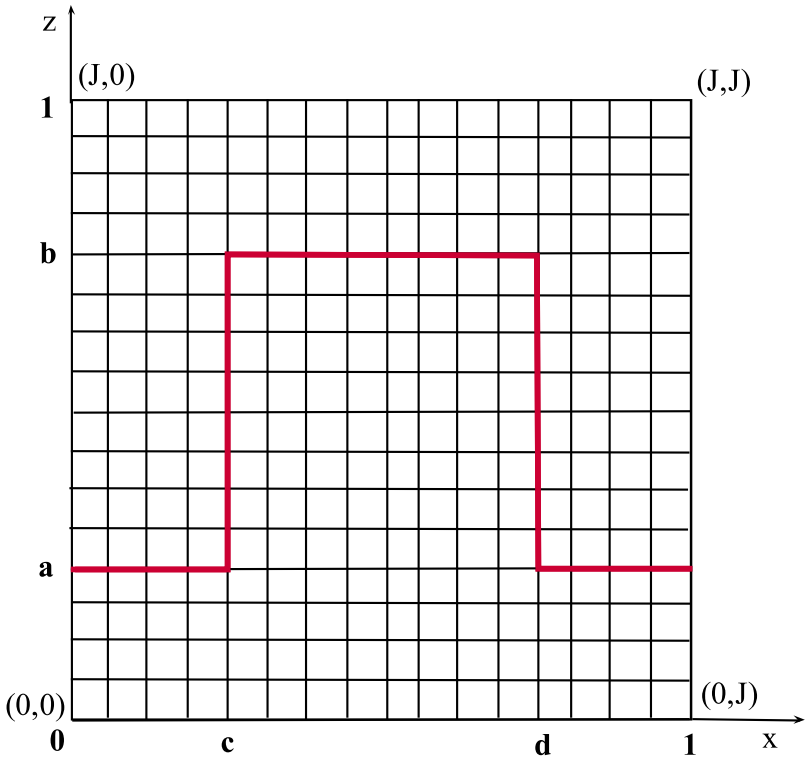

Figure 5.2: The numerical domain for one stem.

We initially used a second-order centred difference scheme as in Chapter 4, but this failed due to the discontinuity of the dependent variables at the interface. In order to overcome this obstacle, we use the method of finite volumes [63]. We note that the finite elements numerical method could be used in this analysis, as it has been demonstrated for the case of an organic solar cell with a sinusoidal interface [64].

By writing the variables in vector form $\mathbf{\Phi}$, $\mathbf{N}$ and $\mathbf{P}$, as in Chapter 4, we may write the problem as a system of three vector equations with nonlinear matrix coefficients, i.e.

$$A_\phi \mathbf{\Phi}^{[q+1]} = \mathbf{c}_\phi(\mathbf{N}^{[q]}, \mathbf{P}^{[q]}) + \mathbf{b}_\phi, \tag{5.19}$$

$$A_n(\mathbf{\Phi}^{[q+1]}, \mathbf{N}^{[q]}, \mathbf{P}^{[q]})\mathbf{N}^{[q+1]} = \mathbf{b}_n, \tag{5.20}$$

$$A_p(\mathbf{\Phi}^{[q+1]}, \mathbf{N}^{[q+1]}, \mathbf{P}^{[q]})\mathbf{P}^{[q+1]} = \mathbf{b}_p. \tag{5.21}$$

Here, $\mathbf{c}_\phi$, $\mathbf{b}_\phi$, $\mathbf{b}_n$ and $\mathbf{b}_p$ are vectors with constant entries used to impose the boundary conditions as they appear on the right hand side of the problem in (5.6)-(5.8). A_ϕ, A_n and A_p are matrices of coefficients describing the operators acting on ϕ, n and

p, respectively, as given by the left hand side of the equations in (5.6)-(5.8). A_n and A_p depend on the values of Φ, N and P. The vector $\mathbf{c}_\phi$ describes the right hand side of (5.6). This nonlinear algebraic system was solved iteratively, as suggested by the iteration index q, using a simple Jacobi method. We stop the iteration when the following three conditions are satisfied

$$\|\mathbf{\Phi}^{[q+1]} - \mathbf{\Phi}^{[q]}\| < tol, \quad \|\mathbf{N}^{[q+1]} - \mathbf{N}^{[q]}\| < tol, \quad \|\mathbf{P}^{[q+1]} - \mathbf{P}^{[q]}\| < tol, \tag{5.22}$$

for a particular value of tol. A detailed description of the scheme is given in Appendix III.

5.2.2 Analytic approach

We consider a long and thin stem so that $\varepsilon_\omega \ll 1$ and reduce to an easier example for which we can find an analytical solution according to the simplifications stated earlier. We solve the problem separately in three main regions, as shown in Figure (5.3):
I : the compact EA region, in $0 \leq z < a$, where we seek a solution for ϕ and n only,
II : the compact ED region, in $b < z \leq 1$, where we seek a solution for ϕ and p only, and
III : the mixed layer, in $a \leq z \leq b$, where we seek a solution for ϕ, n and p.
Having obtained general solutions for each region we join them together using continuity or jump conditions. We note that a similar analysis to this is done in Richardson *et al* [64] for an organic solar cell. We use asymptotic expansions to approximate the solution in the limit of $\varepsilon_\omega \to 0$ and find the behaviour of the leading-order terms. Under the simplifications stated earlier, the leading-order problem in essentially the same as solving for a cell with no dye ($S_d(z,x) = 0$) and hence represents quasi-equilibrium, where we find that $\mathbf{F_n} = \mathbf{F_p} = \mathbf{0}$.

We define the electrostatic potential in each regions I, II and III as $\phi^{(I)}$, $\phi^{(II)}$ and $\phi^{(III)}$, respectively. We use the same superscript notation for n and p for each region. We assume the following asymptotic expansions for each dependent variable

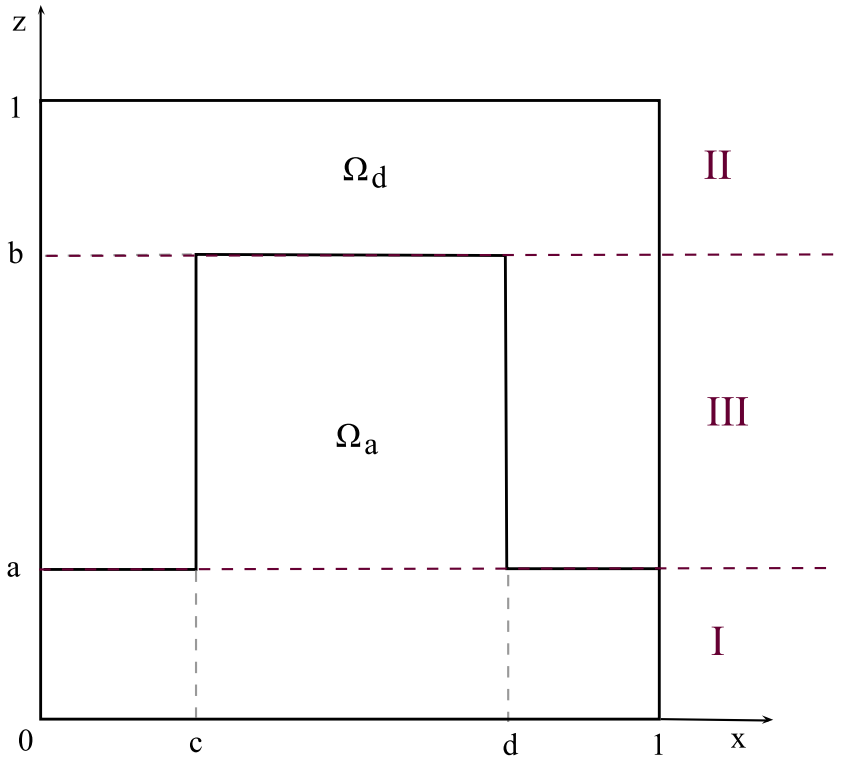

Figure 5.3: The various regions in the (dimensionless) domain.

in each of the regions I, II, and III:

$$\phi^{I,II,III} \sim \phi_0^{I,II,III} + \varepsilon_\omega \phi_1^{I,II,III} + O(\varepsilon_\omega^2), \tag{5.23}$$

$$n^{I,II,III} \sim n_0^{I,II,III} + \varepsilon_\omega n_1^{I,II,III} + O(\varepsilon_\omega^2), \tag{5.24}$$

$$p^{I,II,III} \sim p_0^{I,II,III} + \varepsilon_\omega p_1^{I,II,III} + O(\varepsilon_\omega^2), \tag{5.25}$$

and seek the solution for the leading order terms in each region separately. We start with the compact regions I and II and then match at the interface with the mixed region III.

5.2.2.1 For region II:

We first consider the ED region and, in particular, region II and seek a solution for ϕ and p away from the interface $z = b$. We substitute (5.23)-(5.25) in the nondimen-

sional problem (5.6)-(5.16) to obtain

$$\varepsilon_\omega^2\phi_{0zz}^{(II)} + \left(\phi_{0xx}^{(II)} + \varepsilon_\omega\phi_{1xx}^{(II)} + \varepsilon_\omega^2\phi_{2xx}^{(II)}\right) = -\varepsilon_\omega^2\frac{\Lambda}{\hat{\epsilon}_p}p_0^{(II)} + ... \tag{5.26}$$

$$\varepsilon_\omega^2(p_0^{(II)}\phi_{0z} + p_{0z}^{(II)})_z + \Big[\left(p_0^{(II)} + \varepsilon_\omega p_1^{(II)} + \varepsilon_\omega^2 p_2^{(II)}\right)\left(\phi_{0x}^{(II)} + \varepsilon_\omega\phi_{1x}^{(II)} + \varepsilon_\omega^2\phi_{2x}^{(II)}\right) + (p_{0x}^{(II)} + \varepsilon_\omega p_{1x}^{(II)} + \varepsilon_\omega^2 p_{2x}^{(II)})\Big]_x + ... = 0. \tag{5.27}$$

The corresponding boundary conditions[2] are

$$p_0^{(II)}(1,x) = \hat{P}^+, \quad p_{1,2}^{(II)}(1,x) = 0, \tag{5.28}$$

$$\phi_0^{(II)}(1,x) = \hat{V}, \quad \phi_{1,2}^{(II)}(1,x) = 0, \tag{5.29}$$

$$\phi_{0,1,2}^{(II)}(z,0) = \phi_{0,1,2}^{(II)}(z,1), \quad \phi_{0,1,2x}^{(II)}(z,0) = \phi_{0,1,2x}^{(II)}(z,1), \tag{5.30}$$

$$p_{0,1,2}^{(II)}(z,0) = p_{0,1,2}^{(II)}(z,1), \quad p_{0,1,2x}^{(II)} = p_{0,1,2x}^{(II)}(z,1). \tag{5.31}$$

Along the II-III interface, on $c \le x \le d$, we have the following conditions

$$\phi_0^{(I)}(b,x) + \varepsilon_\omega\phi_1^{(I)}(b,x) = \phi_0^{(II)}(b,x) + \varepsilon_\omega\phi_1^{(II)}(b,x), \tag{5.32}$$

$$\phi_{0z}^{(I)}(b,x) + \varepsilon_\omega\phi_{1z}^{(I)}(b,x) = \phi_{0z}^{(II)}(b,x) + \varepsilon_\omega\phi_{1z}^{(II)}(b,x), \tag{5.33}$$

$$(p_0 + \varepsilon_\omega p_1+)\left(\phi_{0z} + \varepsilon_\omega\phi_{1z}\right) + \left(p_{0z} + \varepsilon_\omega p_{1z}\right)|_{z=b} = -\varepsilon_\omega\delta_0(n_0p_0 - 1))|_{z=b} + ... \ . \tag{5.34}$$

On $0 \le x \le c$ and $d \le x \le 1$, the solutions must be continuous, i.e.

$$\phi_0^{(II)}(b,x) + \varepsilon_\omega\phi_1^{(II)}(b,x) = \phi_0^{(III)}(b,x) + \varepsilon_\omega\phi_1^{(III)}(b,x), \tag{5.35}$$

$$\phi_{0z}^{(II)}(b,x) + \varepsilon_\omega\phi_{1z}^{(II)}(b,x) = \phi_{0z}^{(III)}(b,x) + \varepsilon_\omega\phi_{1z}^{(III)}(b,x), \tag{5.36}$$

$$p_0^{(II)}(b,x) + \varepsilon_\omega p_1^{(II)}(b,x) = p_0^{(III)}(b,x) + \varepsilon_\omega p_1^{(III)}(b,x). \tag{5.37}$$

We then seek a solution to the leading-order problem. As in Section 4.4, $\phi_0^{(II)} = \phi_0^{(II)}(z)$ and $p_0^{(II)} = p_0^{(II)}(z)$, and we use the $O(\varepsilon_\omega^2)$ problem to find the following system of ordinary differential equations for $\phi_0^{(II)}$ and $p_0^{(II)}$

$$\left(p_0^{(II)}\phi_{0z}^{(II)} + p_{0z}^{(II)}\right)_z = 0, \tag{5.38}$$

$$\frac{\Lambda}{\hat{\epsilon}_p}p_0^{(II)} + \phi_{0zz}^{(II)} = 0. \tag{5.39}$$

[2]We note that $\phi_{0,1,2}^{II}(z,0) = \phi_{0,1,2}^{II}(z,1)$ means $\phi_0^{II}(z,0) = \phi_0^{II}(z,1)$, $\phi_1^{II}(z,0) = \phi_1^{II}(z,1)$ and $\phi_2^{II}(z,0) = \phi_2^{II}(z,1)$. The same applies to any such subscript notation.

The variables must satisfy the boundary conditions

$$\phi_0^{(II)}(1) = \hat{V}, \quad p_0^{(II)}(1) = \hat{P}^+ \tag{5.40}$$

and the x-boundary conditions given by (5.11)-(5.13).

By integrating (5.38) and applying the leading-order version of (5.34), we find that

$$p_0^{(II)}\phi_{0z}^{(II)} + p_{0z}^{(II)} = 0, \tag{5.41}$$

which we can integrate and use (5.40) to find that

$$p_0^{(II)} = \hat{P}^+ \exp\left(\hat{V} - \phi_0^{(II)}\right). \tag{5.42}$$

We may then write a single equation for $\phi_0^{(II)}$ as follows

$$\phi_{0zz}^{(II)} + \frac{\left(\phi_{0z}^{(II)}\right)^2}{2} = 2\hat{a}_0 \tag{5.43}$$

where $\hat{a}_0$ is a constant. The solution can then be written, depending on the sign of $\hat{a}_0$, in either of the following forms:

$$(i) \text{ if } \hat{a}_0 > 0: \quad \phi_0^{(II)} = \hat{V} + 2\log\left(\frac{\sinh(a_0 z + b_0)}{\sinh(a_0 + b_0)}\right), \quad a_0 = \sqrt{\hat{a}_0}, \tag{5.44}$$

$$\text{with} \quad 2a_0^2 = \frac{\Lambda\hat{P}^+}{\hat{\epsilon}_p}\sinh^2(a_0 + b_0)$$

$$(ii) \text{ if } \hat{a}_0 < 0: \quad \phi_0^{(II)} = \hat{V} + 2\log\left(\frac{\sin(a_0 z + b_0)}{\sin(a_0 + b_0)}\right), \quad a_0 = \sqrt{-\hat{a}_0}, \tag{5.45}$$

$$\text{with} \quad 2a_0^2 = \frac{\Lambda\hat{P}^+}{\hat{\epsilon}_p}\sin^2(a_0 + b_0),$$

$$(iii) \text{ if } \hat{a}_0 = 0: \quad \phi_0^{(II)} = 2\log\left(b_0(z-1) + e^{\frac{\hat{V}}{2}}\right), \tag{5.46}$$

$$\text{with} \quad 2b_0^2 = \frac{e^{\hat{V}}\Lambda\hat{P}^+}{\hat{\epsilon}_p},$$

having imposed the boundary conditions (5.40).

5.2.3 For region I:

Similarly to region II, it is found that the solution for region I , away from the interface $z = a$, can be written in either of the two following forms, depending on the sign of the arbitrary constant $\hat{\alpha}_0$:

$$(i) \text{ if } \hat{\alpha}_0 < 0: \quad \phi_0^{(I)} = 2\log\left(\frac{\sinh(\alpha_0 z + \beta_0)}{\sinh(\alpha_0)}\right), \quad \alpha_0 = \sqrt{-\hat{\alpha}_0}, \tag{5.47}$$

$$\text{with } \; 2\alpha_0^2 = \Lambda \hat{N}^- \sinh^2(\alpha_0 + \beta_0)$$

$$(ii) \text{ if } \hat{\alpha}_0 > 0: \quad \phi_0^{(I)} = 2\log\left(\frac{\sin(\alpha_0 z + \beta_0)}{\sin(\alpha_0)}\right), \quad \alpha_0 = \sqrt{\hat{\alpha}_0}, \tag{5.48}$$

$$\text{with } \; 2\alpha_0^2 = \Lambda \hat{N}^- \sin^2(\alpha_0 + \beta_0),$$

$$(iii) \text{ if } \hat{\alpha}_0 = 0: \quad \phi_0^{(I)} = 2\log\left(\beta_0(z+1)\right), \tag{5.49}$$

$$\text{with } \; 2\beta^2 = \Lambda \hat{N}^-.$$

5.2.4 For region III:

Again, we substitute the asymptotic expansions (5.23)-(5.25) in the problem (5.6)-(5.16) for the mixed layer. As before, the leading-order problems away from the interface give that

$$\phi_0^{(III)} = \phi_0^{(III)}(z, x), \tag{5.50}$$

$$n_0^{(III)} = n_0^{(III)}(z, x), \tag{5.51}$$

$$p_0^{(III)} = p_0^{(III)}(z, x), \tag{5.52}$$

and we proceed to the $O(\varepsilon_\omega^2)$ problem to find that

$$\phi_{2xx}^{(III)} = \begin{cases} \Lambda n_0^{(III)} - \phi_{0zz}^{(III)} & \text{in } c < x < d \\ -\frac{\Lambda}{\epsilon_p} p_0^{(III)} - \phi_{0zz}^{(III)} & \text{in } 0 < x < c \text{ and } d < x < 1. \end{cases} \tag{5.53}$$

The boundary conditions are

$$\phi_0^{(I)}(a,x) = \phi_0^{(III)}(a,x), \quad \phi_{0z}^{(I)}(a,x) = \phi_{0z}^{(III)}(a,x), \quad n_0^{(I)}(a,x) = n_0^{(III)}(a,x), \tag{5.54}$$

$$\phi_0^{(II)}(b,x) = \phi_0^{(III)}(b,x), \quad \phi_{0z}^{(II)}(b,x) = \phi_{0z}^{(III)}(b,x), \quad p_0^{(II)}(b,x) = p_0^{(III)}(b,x), \tag{5.55}$$

$$\phi_0^{(III)}(z,0) = \phi_0^{(III)}(z,1), \quad n_0^{(III)}(z,0) = n_0^{(III)}(z,1), \quad p_0^{(III)}(z,0) = p_0^{(III)}(z,1), \tag{5.56}$$

$$\phi_{0x}^{(III)}(z,0) = \phi_{0x}^{(III)}(z,1), \quad n_{0x}^{(III)}(z,0) = n_{0x}^{(III)}(z,1), \quad p_{0x}^{(III)}(z,0) = p_{0x}^{(III)}(z,1), \tag{5.57}$$

$$\left[\phi_0^{(III)}\right]_{x=c,d} = 0, \tag{5.58}$$

$$\left[\epsilon_i \nabla_\omega \phi_0 \cdot \hat{\mathbf{n}}\right]_{x=c,d} = 0. \tag{5.59}$$

Further, along the interfaces

- $x = c$, $a \le z \le b$
- $x = d$, $a \le z \le b$
- $z = a$, $0 \le x \le c$ and $d \le x \le 1$
- $z = b$, $c \le x \le d$

the solution must satisfy

$$\left[\mathbf{F}_n \cdot \hat{\mathbf{n}}\right] = -\left[\mathbf{F}_p \cdot \hat{\mathbf{n}}\right] = -\delta\left(1 - S_d(z,x)\right)\left(n(z,x)p(z,x) - 1\right). \tag{5.60}$$

Then, we integrate (5.53) over $0 \le x \le 1$ to get

$$\int_0^1 \left(\epsilon_p \phi_{2x}^{(III)}\right)_x dx = 0$$

$$\Rightarrow \int_0^c \hat{\epsilon}_p \left(-\frac{\Lambda}{\hat{\epsilon}_p} p^{(III)} - \phi_{0zz}^{(III)}\right) dx + \int_c^d \left(\Lambda n^{(III)} - \phi_{0zz}^{(III)}\right) dx + \int_0^1 \hat{\epsilon}_p \left(-\frac{\Lambda}{\hat{\epsilon}_p} p^{(III)} - \phi_{0zz}^{(III)}\right) dx = 0.$$

By imposing the periodic boundary conditions (5.56)-(5.57) to get

$$(1 + \epsilon_p)\phi_{0zz}^{(III)} = \Lambda n_0^{(III)} - \Lambda p_0^{(III)}. \tag{5.61}$$

For p we have

$$p_0^{(III)}\phi_{2xx}^{(III)} + p_{2xx}^{(III)} = -\left(p_{0z}^{(III)}\phi_{0z}^{(III)} + p_0^{(III)}\phi_{0zz}^{(III)} + p_{0zz}^{(III)}\right) \tag{5.62}$$

which, similarly, gives[3]

$$(p_0^{(III)}\phi_{0z}^{(III)} + p_{0z}^{(III)})_z = 0. \tag{5.65}$$

Then, by the interface condition $[p_0^{(III)}\phi_{0z}^{(III)} + p_{0z}^{(III)}]|_{z=b} = 0$ we obtain that

$$p_0^{(III)} = P^+ \exp(\hat{V} - \phi_0^{(III)}), \tag{5.66}$$

where we have imposed the matching condition (5.55). Similarly for $n_0^{(III)}$ we obtain that

$$n_0^{(III)} = N^- \exp(\phi_0^{(III)}), \tag{5.67}$$

by the matching condition (5.54). Then, by substituting (5.66) and (5.67) in (5.61) we get

$$\phi_{0zz}^{(III)} = \frac{\Lambda}{(1+\hat{\epsilon}_p)}\left(N^- \exp\left(\phi_0^{(III)}\right) - P^+ \exp\left(\hat{V} - \phi_0^{(III)}\right)\right). \tag{5.68}$$

Although the solution to the above can be written in terms of Jacobi amplitude functions, we will not analyse this analytically further due to its complexity. Going forward (5.68) is computed numerically.

In what follows, we solve (5.68) numerically together with the solutions for regions I and II by imposing the matching conditions, for the special case $\hat{\epsilon}_p = 1$, at the interfaces $z = a$ and $z = b$, namely (5.54)a,b and (5.55)a,b. Since the analysis in the mixed layer is completed numerically we can not specify beforehand when the solution takes the form of (i), (ii) or (iii) as defined in (5.44)-(5.46) and (5.47)-(5.49). It is worth

[3]We integrate (5.62) for x over $[0,1]$ to get

$$\int_0^1 (p_0\phi_{2xx} + p_{2xx})dx = \int_0^c (p_0\phi_{2xx} + p_{2xx})dx + \int_d^1 (p_0\phi_{2xx} + p_{2xx})dx \tag{5.63}$$

$$= [(p_0\phi_{2x} + p_{2x})dx]|_{x=c} - [(p_0\phi_{2x} + p_{2x})dx]|_{x=0} + [(p_0\phi_{2x} + p_{2x})dx]|_{x=1} - [(p_0\phi_{2x} + p_{2x})dx]|_{x=d} = 0 \tag{5.64}$$

and impose the interface condition $[p_0\phi_{2x} + p_{2x}]_{x=c,d} = 0$ and the periodic boundary conditions on the x-boundaries to obtain the result.

noting that in the special case of shrinking the mixed layer to a planar interface (i.e. setting $a = b$) we can show that form (i), as defined in (5.47) and (5.44), is appropriate when $\Lambda > 8\left(\exp(-\frac{\hat{V}}{4} - 1)\right)^2$. Form (ii), as defined in (5.48) and (5.45), is found to be appropriate when $\Lambda < 8\left(\exp(-\frac{\hat{V}}{4} - 1)\right)^2$ and, finally, form (iii), as defined in (5.49) and (5.46), is more appropriate when $\Lambda = 8\left(\exp(-\frac{\hat{V}}{4} - 1)\right)^2$. The system of equations is well determined, i.e has the same number of variables as equations and the appropriate number of boundary conditions, and is solved simultaneously for all regions in order to find values of the various arbitrary constants. In the following discussion we present a comparison between the full numerical solutions and analytic results with numerically computed constants.

5.2.5 Results and interpretation

In this section we compare the distribution of ϕ and n as well as the current density-voltage relation, produced by the full numerical results with the analytical results in the case when $\varepsilon_\omega \ll 1$ and $\delta = O(\varepsilon_\omega)$.

The leading-order analytic solution for $\phi_0(z)$, is given by (5.47)-(**??**) in region I, (5.44)-(5.46) in region II and (**??**). We compare this with the numerical solution averaged over x, denoted by $\Phi_a(z)$, in Figure 5.4(a). In addition, we plot the error between the two solutions, defined as

$$\text{error}_\phi = |\phi_0(z) - \Phi_a(z)|, \tag{5.69}$$

which is approximately of $O(\varepsilon_\omega)$, in Figure 5.4(b). There is excellent agreement between the numerical and analytic solutions, thus suggesting that our approximation is valid. We do not present current density-voltage curves in our comparison with the analytic solution as in the leading-order approximation $\mathbf{F_n} = \mathbf{F_p} = 0$ (recall that essentially $\delta = 0$ in the leading-order problem).

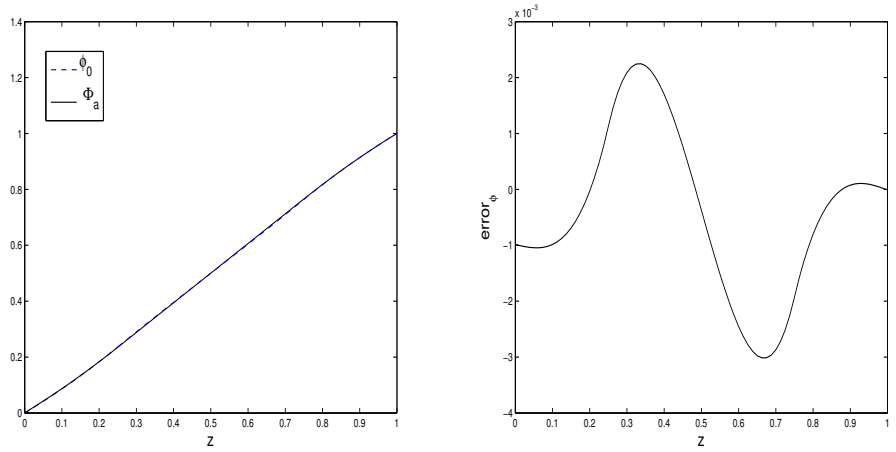

(a) (b)

Figure 5.4: (a) The profile of Φ_a and of ϕ_0 and (b) the error_ϕ averaged over x. [Parameters: $\delta = 0$, $\hat{V} = 1$, $\Lambda = 1$, $\hat{N}^- = 1$, $\hat{P}^+ = 1$, $\hat{\epsilon}_p = 1$, $S_d(z, x) = 0$, $a, c = \frac{1}{4}$, $b, d = \frac{3}{4}$, $\varepsilon = 0.1$]

We further note that when $\delta = O(1)$, we can still obtain an analytic solution, where the solution in the outer regions (I and II) take the form of Airy functions as in Section 4.1, and the derivation is similar to the exact solution of the one-dimensional problem found in Chapter 4. The algebra becomes more complicated in the mixed layer (III), so we have chosen not to include this here. Instead, we present results obtained numerically in what follows.

In Figure 5.5 we show the distribution profile for the dependent variables at a constant voltage as we decrease the aspect ratio ε_ω from 1 to 0.01. The numerical solution verifies that the dependent variables become independent of x as $\varepsilon_\omega \to 0$.

The current density, F, is calculated numerically using the expression in (5.16). This is plotted against the applied voltage, V, for the aforementioned values of ε_ω in Figure 5.6. In Figure 5.6(a) we have let $a = b$, so that the interface is planar, and in Figure 5.6(b) we let $a,\ c = \frac{\omega}{4}$ and $b,\ d = \frac{3\omega}{4}$. In both cases, it is shown that the slope of the curve decreases as ε_ω decreases. This agrees with the physical expectation that, as we increase the surface area between EA and ED, we increase the recombination, thus reducing the available charge carriers and, hence, the current.

We have, so far, considered only idealised cases of the cell with a structured non-planar interface where there is no dye coating on the interface. In addition, we have

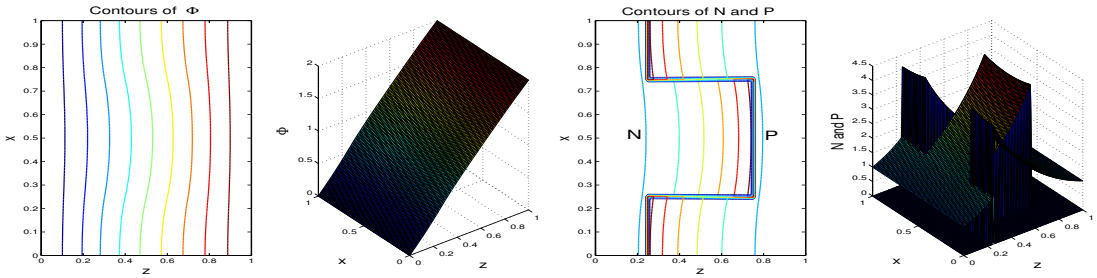

(a)

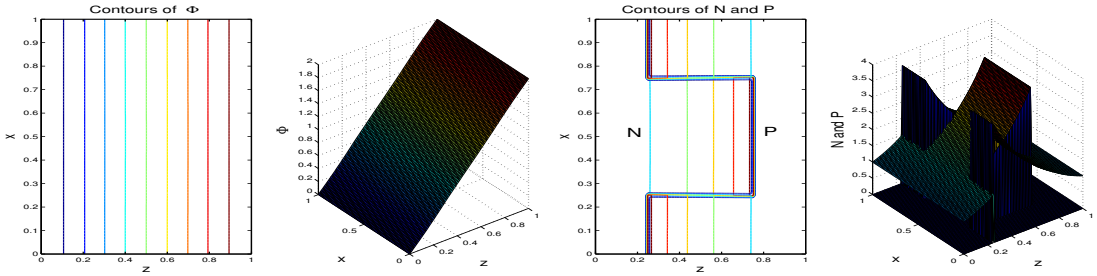

(b)

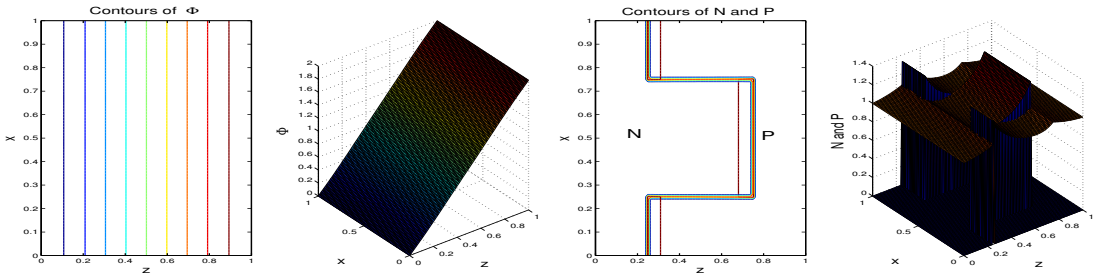

(c)

Figure 5.5: The profiles of Φ, N and P for (a) $\varepsilon_\omega = 1$, (b) $\varepsilon_\omega = 0.1$ and (c) $\varepsilon_\omega = 0.01$. [Parameters: $\delta = 0.01$, $V = 2$, $\Lambda = 1$, $\hat{N}^- = 1$, $\hat{P}^+ = 1$, $\hat{\epsilon}_p = 1$, $\hat{G} = 0$, $S_d(z,x) = 0$, $a, c = \frac{1}{4}$, $b, d = \frac{3}{4}$]

not examined the effect of varying most of the parameters of the problem, such as the Debye length, the ratio of ED-to-EA dielectric constants, and the recombination rate coefficient. The effect of varying the latter has been extensively studied in Chapter 4, so we do not examine this further here to avoid repetition. In the following Section, we use our numerical scheme to explore the effect of the Debye length and the dielectric constant on the current density-voltage curves.

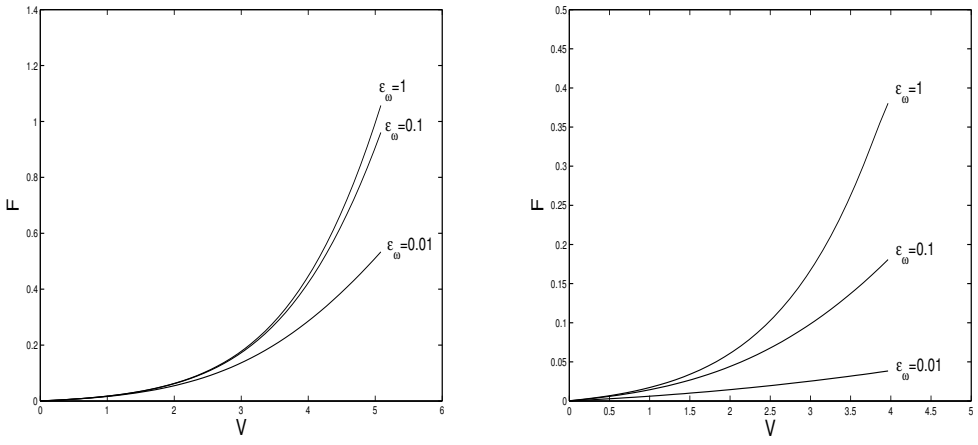

(a) (b)

Figure 5.6: The current density-voltage curves as simulated numerically for decreasing value of the aspect ratio $\varepsilon_\omega = 1,\ 0.1,\ 0.01$ for (a) a planar interface $a = b$ and (b) for a non-planar interface with $a,\ c = 0.25$ and $b,\ d = 0.75$. The colouring indicates the size of the variables, with warner (e.g. red) colours indicating the higher value of the variables. [Parameters: $\delta = 10^{-2}$, $\Lambda = 1$, $\hat{N}^- = 1$, $\hat{P}^+ = 1$, $\hat{\epsilon}_p = 1$, $\hat{G} = 0$, $S_d(z, x) = 0$]

5.2.5.1 Effect of varying the electric field screening length

We, first, explore the influence of varying the screening length of the electric field, by varying either the Debye length (via Λ) or the ratio of the dielectric constants (via $\hat{\epsilon}_p$). By increasing Λ, we are essentially decreasing the length over which the electric field can push/pull on the charges. A similar effect is observed when we increase $\hat{\epsilon}_p$ in the ED region. This results in a higher electric field near the interface, as shown in Figure 5.7, so that charge carriers are concentrated near the interface. Further, we show the current density-voltage curves in Figure 5.8. We see that, by increasing Λ or decreasing $\hat{\epsilon}_p$, we may decrease the power consumption[4] and, hence, increase the efficiency of the cell.

[4]Recall that the power output can be found by multiplying the current with the voltage.

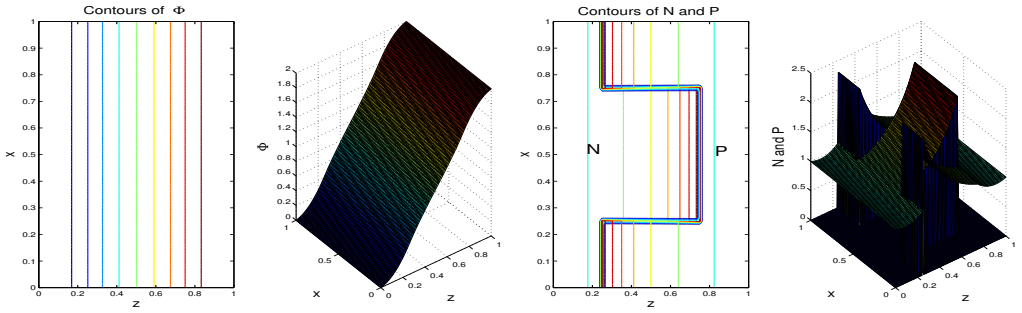

(a)

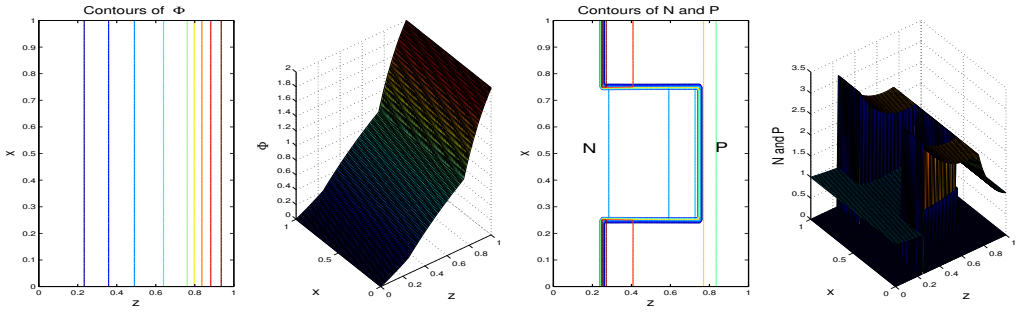

(b)

Figure 5.7: The contour and distribution plots of Φ, N and P for (a) $\Lambda = 10$ and $\hat{\epsilon}_p = 1$ and (b) $\hat{\epsilon}_p = 0.1$ and $\Lambda = 1$. [Parameters: $\varepsilon_\omega = 0.01$, $\delta = 0.01$, $\hat{V} = 1$, $\hat{N}^- = 1$, $\hat{P}^+ = 1$, $S_d(z, x) = 0$, $a,\ c = 0.25$, $b,\ d = 0.75$]

5.2.6 Summary

In this Chapter, we have examined the case where the cell has a periodic, structured, mixed layer with long and thin nanostems of EA material penetrating the ED region. We considered the problem in only one of the repeated blocks. The nondimensionalisation of the two dimensional model gave rise to the ratio, ε_ω, which was the width of the nanostem to the length of the device and we considered the case where this ratio was small. Having made further assumptions about the symmetry of the device, we have been able to find a solution that has insignificant x variation (at leading order in ε_ω) and could be approximated analytically using asymptotic expansions. We assumed that the recombination rate was small and the cell was in the dark. For further analysis of this problem, we have developed a numerical scheme that solves the problem in the one stem and the surrounding region. The complexity of the interface is overcome by using the finite volume method, which allows the variables to be discontinuous at certain points.

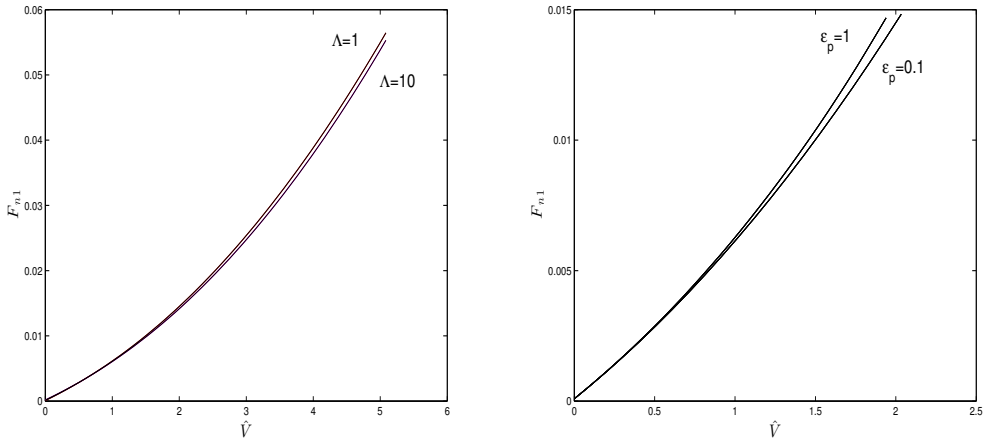

(a) (b)

Figure 5.8: The current density-voltage curves (a) for $\Lambda = 1,\ 10$ and $\hat{\epsilon}_p = 1$, (b) for $\hat{\epsilon}_p = 1,\ 0.1$ and $\Lambda = 1$. [Parameters: $\varepsilon_\omega = 0.01$, $\delta = 0.01$, $\Lambda = 1$, $\hat{N}^- = 1$, $\hat{P}^+ = 1$, $S_d(z,x) = 0$, $a,\ c = 0.25$,$b,\ d = 0.75$]

The results of the asymptotic analysis have been shown to have good agreement with the corresponding numerical results. Further, we have presented a discussion on the effect of varying the Debye length and dielectric constants. The examples have been interpreted physically in order to understand the mechanisms that are involved. In varying Λ we changed the solution symmetrically in both the acceptor and donor regions, whereas increasing $\hat{\epsilon}_p$ increased the hole concentration near the interface, whilst decreases relatively that of electrons. We have shown that, when Λ is increased or $\hat{\epsilon}_p$ is decreased, the recombination at the interface increases, resulting in lower power consumption for a cell in the dark.

Part II

The solar cell

6

Physical background and model

In this Part of the thesis we examine the effect of illumination on the solar cell. We derive a model that describes the absorption of photons by electrons in the device, converting solar energy to electrical energy. We start by exploring the underlying mechanisms, before stating the mathematical problem. We analyse the model both in the bilayer and the nanostructured cell.

In this Chapter we present the theoretical background that is required to understand the absorption of photons by the device leading on to the derivation of the model. The drivers for absorption are the interfacial kinetics between the various materials comprising the solar cell and their optical properties.

6.1 Physical background

6.1.1 Interfacial Kinetics

As mentioned in earlier Chapters, electrochemical reactions drive the generation of free charge carriers at the interface between the dye and the outer regions. These carriers are a result of photon absorption by the dye and reactions at the dye layer.

The main function of the dye in an ssDSSC is to generate excitons and dissociate these into free charges at the dye interface. Thus, the dye must be chosen under two constraints: (i) its energy band structure must agree well with those of the EA and the ED, i.e. allow for the favourable charge carrier transfer from the dye into the EA and ED as explained in Parti I, and (ii) it must absorb as large a range of the light spectrum as possible. Different ruthenium (Ru)-based complexes have been examined for the role of the dye sensitiser, and a comparison between their absorbances can be found in Sahin *et al* [65] and Fredin *et al* [66]. For example, we give the absorbance (per wavelength) of two commonly used dye complexes, called CS9 and Z907, in Figure 6.1. Sahin *et all* [65] have measured that the maximum absorption for these two dyes is achieved within photons in the visible light spectrum of $400 - 800\ nm$, and that there are two peaks at approximately $370\ nm$ and $520\ nm$.

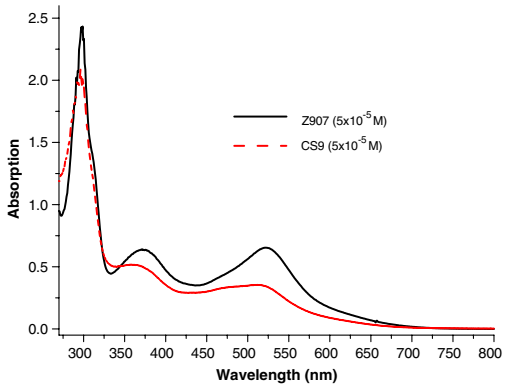

Figure 6.1: The absorption spectra of the dyes CS9 and Z907. Graph taken from Sahin *et al* [65].

It is also important that the dye covers as much of the surface of the EA as possible, in order to minimise direct recombination between electrons in the EA and holes in the ED. In practice, the coverage depends on the fluid mechanics of the production

process along with the chemistry of the dye adsorption; modelling these processes was the scope of this thesis.

In Figure 6.2 we show a schematic representation of the interfacial kinetics between the dye and the outer regions, i.e. the EA and ED regions. Excitons that are generated by photon absorption in the dye have a large binding energy ($\gg k_B T$) that does not allow for dissociation into free charges by the photon (or phonon) energy alone. The generation of excitons occurs on the femtosecond timescale. An exciton then dissociates at the dye/EA interface where the electron is injected into the EA; this occurs on a femto- to picosecond timescale, leaving a positively charged ion (cation) in the dye. A neutral dye molecule is regenerated at the dye/ED interface where an electron is donated from the ED to a positively charged ion and this occurs on the pico- to nanosecond timescale. The timescales of these processes have been measured experimentally as described in [26], [27] and [29]. These are the favourable processes for the generation of free charges. The faster these processes occur, the larger the output current will be.

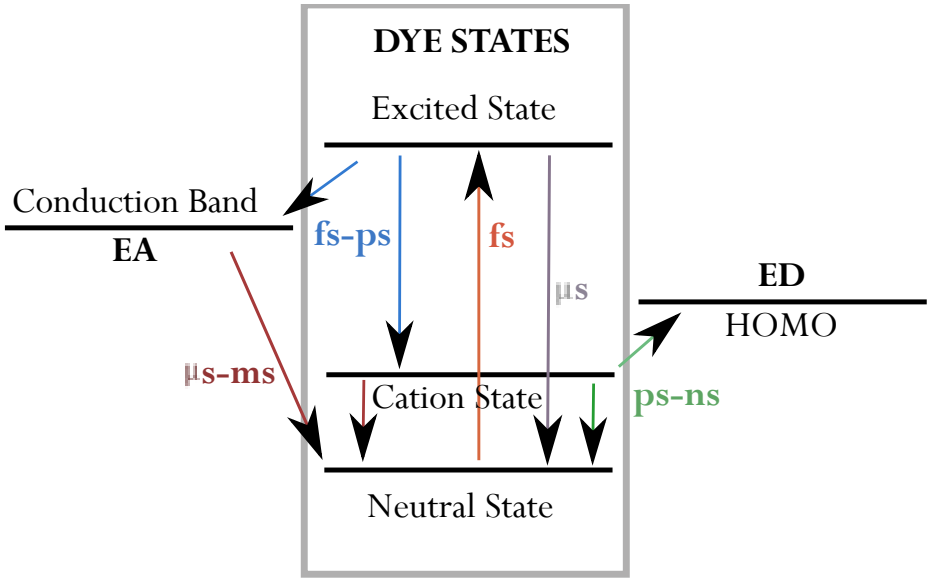

Figure 6.2: Schematic representation of the interfacial kinetics between the (energy levels of the) EA and the ED in the presence of dye as discussed in [26], [27] and [29]. Note that the timescales of each process are shown, where fs=femtoseconds (10^{-15} s), ps=picoseconds (10^{-12} s), ns=nanoseconds (10^{-9} s), μs= microseconds (10^{-6} s), ms=milliseconds (10^{-3} s). [27]

In addition to the direct recombination of free charge carriers between the outer regions (electrons from the EA and holes from the ED), as discussed in the previous

part of the thesis, there is another important charge-loss mechanism in this system. This mechanism involves recombination within the dye. An exciton generated in the dye has a lifetime expectancy of approximately a few microseconds before annihilating (i.e. the electron and hole comprising the exciton recombine), if it doesn't reach the dye/EA contact. Apart from the electron and hole injection into the outer regions, it is also important for the dye to have the appropriate optical properties that help absorb the photons.

6.1.2 Physical properties of materials

In this section we explain how electron-hole pairs, known as *excitons*, are formed, and present the theoretical background for the photon absorption by materials.

A beam of light in a homogeneous medium follows a straight line when there are no obstacles, i.e. *propagates*, or is forced to change its path, i.e. *scatters*, when in contact with obstacles. When a photon, the energy wave, reaches the surface of another medium, part of the energy continues to propagate in the second medium with a different speed and direction, which is known as *refraction*, while another part is *reflected* back into the first medium. Materials may also absorb the photon according to their optical properties. A photon that propagates in a medium is characterised by the *refractive index*, which is a dimensionless parameters of the ratio of the speed the photon reaches in the medium to the speed in vacuum.

An important concept that describes the optical response of a material is its energy band gap. The material's vibration, described by the concept of *phonon*, could provide the energy necessary for electrons to overcome the energy band gap. A phonon is accepted as a wave packet of energy that leads to quantum mechanical oscillation of a compact lattice. A phonon carries (thermal) energy, E_{ph}, given by

$$E_{ph} = k_B T \tag{6.1}$$

and is vibrating. The interaction of phonons with photons may cause scattering of particles within a material, especially at higher temperatures. Given that $k_B = 8.62 \times 10^{-5}\ eVK^{-1}$, E_{ph} is approximately $0.025\ eV$ at room temperature ($T = 300\ K$). Even though there is no strict separation line between conductors and semiconductors, it is common to consider materials as semiconductors whenever their band gap

exceeds the order of $O(E_{ph})$. Similarly, it is difficult to distinguish between semiconductors and insulators, but commonly insulators have band gaps of the order $\gg O(E_{ph})$.

A metal can conduct electricity easily since its band gap is less than E_{ph}, so that energy absorption from phonons alone can cause conduction. For semiconductors, electrons are bound from the atom at the lower energy states lying in the valence band with (possibly) only few electrons in the low levels of the conduction band [67]. Electrons must be free in order to conduct, thus electrons must be promoted by energy absorption to the conduction band, which must be at least the size of the energy band gap. For insulators, virtually no electrons are found in the conduction band and a (larger) amount of energy is required to promote them from the valence to the conduction band.

For a material with a small band gap, such as silicon, a photon may be absorbed to excite a neutral atom and produce a free electron and a hole. Formally, energy absorption creates an electron-hole pair separated both spatially and energetically, called an *exciton*. For semiconductors with small band gaps (usually between $1 - 3\ eV$), electron-hole pairs are bound with some binding energy E_{X_b}. These are called *Wannier-Mott excitons* and the distance between the charges is of the order of several atoms. The typical binding energy is around $0.01\ eV$ ($< E_{ph}$) as given in Fox [7]. Since this is less than the thermal energy, these excitons are not stable and hence we consider them to move freely within the material. For larger band gap materials, i.e. wide band gap semiconductors (including organic semiconductors) and insulators[1], the electron-hole pair is tightly bound typically with $E_{X_b} \sim 0.1 - 1\ eV$ and with distance between the electron and the hole to be of the order of an atom-/molecule. These are known as *Frenkel excitons* and move by hopping from one atom/molecule to the next one.

The energy of an exciton, E_X, is given by

$$E_X = E_g - E_{X_b}, \tag{6.2}$$

where E_g is the band gap size of the material. The tightly bound exciton requires additional energy in order for the electron and hole to dissociate. This is usually

[1]Usually insulators have band gap energy larger than $4\ eV$ as explained in Sze [67].

provided by the electrochemical differences between the material and the adjacent environment as explained in Chapter 2.

The energy required to excite the electron can be obtained by photon absorption. In fact, if the energy of the photon, E_ϕ, is greater than E_X, excitons will form. Solar photons usually have wavelengths larger than 300 nm or, equivalently, energy up to 4 eV. It is important that the band gap of the absorbing material in the solar cell allows for maximum absorption of the visible light spectrum (see Figure 6.3).

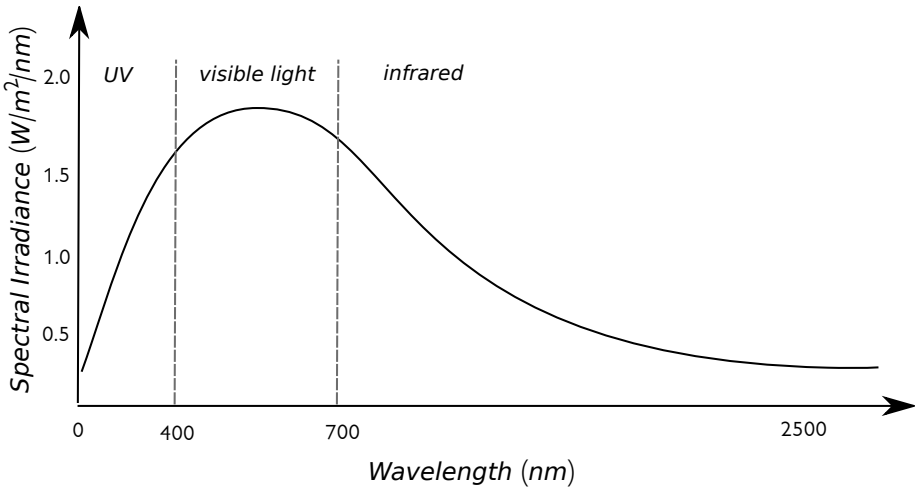

Figure 6.3: Spectral irradiance.

The rate with which photons are absorbed by a material is described by the Beer-Lambert Law, which will be discussed in the next Section. The rate of absorption is associated with the rate of free electron generation in a ssDSSC.

6.2 The model

Here, we establish a mathematical model for the light absorption mechanism in an ssDSSC and use this to derive the generation rate of free electrons in the cell. First, we revisit the main physical properties of the materials involved and explain why the model does not have symmetry features, in contrast with the model for current transport in Chapter 4.

In Part I, we set the generation rate in the problem to zero. In Part II, we write down a model for the electromagnetic field in an absorbing medium. The behaviour

of solutions of this model are examined primarily numerically in order to allow for the inclusion of the non-trivial geometry of the device.

The composition of the cell was set out in Chapter 2. However, for the analysis of the propagation of light within any system we need to know also the optical properties of the material. In particular, the refractive index, κ, is essential in measuring the refraction and absorption in a medium. If κ is real, the medium is not absorbing, and only allows for refraction at its surfaces for any light entering. However, if $\kappa = \kappa_R + i\kappa_I$, then any electric field, $\tilde{\mathbf{E}}$ generated in a medium by the absorption of photons, and under no other force applied, is given by

$$\tilde{\mathbf{E}} \sim \exp\left(-\frac{2\pi\nu\kappa_I}{c}\mathbf{x}\right), \tag{6.3}$$

where ν $[s^{-1}]$ is the frequency of the incident light wave and c $[ms^{-1}]$ is the speed of light in vacuum, as derived in Fox [7]. The light intensity[2], $\mathbf{I}$ Wm^{-2}, is proportional to the square of the electric field. The generation rate expresses the amount of photons absorbed by the material, and is therefore measured as the negative rate of change in light intensity in the field, a relation known as the *Beer-Lambert law*. For the one dimensional case, the Beer-Lambert law is given by

$$G = -\frac{d\mathbf{I}}{dl} \sim -\exp\left(-\frac{4\pi\nu\kappa_I}{c}l\right) = -\exp\left(-\alpha_{dye}l\right), \tag{6.4}$$

where l is the distance travelled within the material and α_{dye} is called the absorption coefficient $[cm^{-1}]$. The generation rate, i.e. the absorption, depends on the thickness and the absorption coefficient of a material.

TiO_2 and the dye agent are light absorbing semiconducting media, whereas light absorption in the spiro-OMeTAD is negligible. The estimated refractive index of the electron acceptor and donor and the dye are given in Table 6.1. The refractive index varies with the wavelength of light, thus we choose to present our analysis using only the information obtained with a wavelength of 521 nm, as this is the peak absorbance for the Ruthenium-based dye Z907 suggested in Wegner [68].

[2]Light intensity is measured in $Watts$ per m^2.

Table 6.1: The physical constants for light of wavelength 521 nm (green light)

Material	Refractive Index	Extinction Coefficient	Source
TiO_2	2.85	0	Tang *et al* [69]
spiro−OMeTAD	1.75	0	Chen *et al* [70]
Z_{907}	1.9	1.84×10^{-2}	Wegner *et al* [68]

We assume that the solar cell is comprised of a piecewise-homogeneous medium of absorbing/non-absorbing materials. We derive our mathematical model based on Maxwell's equations in three dimensions and then we reduce to one and two dimensions as necessary for our analysis. A schematic of the device we will consider is shown in Figure 6.4.

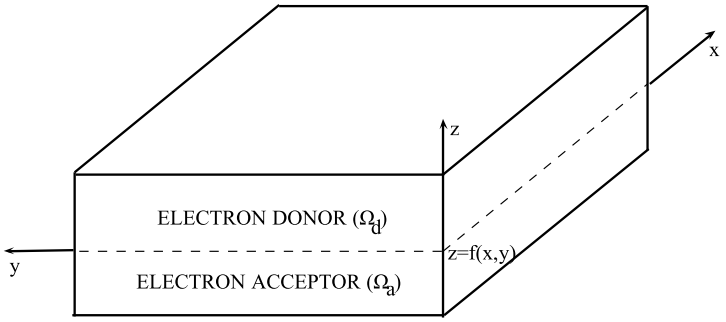

Figure 6.4: A schematic representation of the cell in three dimensions, for an interface described by $z = f(x, y)$.

6.2.1 The governing equations

We consider the cell to have volume, Υ and surface area $\partial\Upsilon$. The electromagnetic field of light in the material, is described by the electric and magnetic field intensities, **E** and **H**, respectively, through Maxwell's equations [71] as follows:

$$\nabla \times \mathbf{H} - \frac{\partial \mathbf{D}}{\partial t} = \sigma(\mathbf{x})\mathbf{E}, \tag{6.5}$$

$$\nabla \times \mathbf{E} + \frac{\partial \mathbf{B}}{\partial t} = 0, \tag{6.6}$$

$$\nabla \cdot \mathbf{D} = \frac{\rho(\mathbf{x}, t)}{\epsilon_0}, \tag{6.7}$$

$$\nabla \cdot \mathbf{B} = 0, \tag{6.8}$$

where, $\sigma(\mathbf{x})$ is the conductivity $[AV^{-1}]$ and $\rho(\mathbf{x}, t)$ is the volume electric charge density $[Cm^{-3}]$.

The electric displacement, $\mathbf{D}$ $[Vm^{-1}]$, and the magnetic induction, $\mathbf{B}$ $[Am^{-1}]$, are related to the electric and magnetic field intensities via the constitutive relations

$$\mathbf{D} = \epsilon(\mathbf{x})\mathbf{E}, \quad \text{and} \tag{6.9}$$

$$\mathbf{B} = \mu(\mathbf{x})\mathbf{H}, \tag{6.10}$$

respectively, where $\epsilon(\mathbf{x})$ is the permittivity $[CV^{-1}m^{-1}]$ and $\mu(\mathbf{x})$ is the permeability $[VsA^{-1}m^{-1}]$. The permittivity, permeability and conductivity are assumed to be piecewise constant functions, i.e. constant in each material of the ssDSSC.

By assuming that the permittivity and conductivity, we take the divergence of (6.5) and use (6.7) to write the charge conservation equation

$$\frac{\partial \rho(\mathbf{x}, t)}{\partial t} + \frac{\rho(\mathbf{x}, t)}{\epsilon_i} = 0, \tag{6.11}$$

for each homogeneous layer i. This solves into

$$\rho(\mathbf{x}, t) = \rho_0(\mathbf{x}) \exp\left(-\frac{t}{\epsilon_i} t\right), \tag{6.12}$$

where $\rho_0(\mathbf{x})$ describes the initial volume charge distribution. We assume $\rho = 0$, as there is negligible amount of charges in semiconductors [72, 73, 74, 75], and $\nabla \cdot \mathbf{D} = 0$.

The system (6.5)-(6.8) may be reduced to the Helmholtz equation by undertaking a series of manipulations. First, we take the time derivative of (6.5) and use (6.9) to obtain

$$\nabla \times \frac{\partial \mathbf{H}}{\partial t} - \epsilon_i \mu_i \frac{\partial^2 \mathbf{E}}{\partial t^2} = \mu_i \frac{\partial \mathbf{E}}{\partial t} \tag{6.13}$$

We then use (6.10) to substitute for $\mathbf{H}$ in (6.6) to convert $\mathbf{B}$ into $\mathbf{E}$, to get

$$\nabla \times (\nabla \times \mathbf{E}) + \mu_i \frac{\partial E}{\partial t} + \mu_i \epsilon_i \frac{\partial^2 E}{\partial t^2} = 0. \tag{6.14}$$

By using the identity $\nabla\times(\nabla\times\mathbf{E}) = \nabla(\nabla\cdot\mathbf{E}) - \nabla^2\mathbf{E}$ and according to our assumption that $\rho = 0$, we take $\nabla\cdot\mathbf{D} = 0$, so that we get

$$-\nabla^2\mathbf{E} + \mu_i\epsilon_i\frac{\partial^2\mathbf{E}}{\partial t^2} = -\mu_i\frac{\partial\mathbf{E}}{\partial t}, \tag{6.15}$$

for each homogeneous layer i of a piecewise homogeneous medium.

Now, for a monochromatic light with frequency ν, we assume a time-harmonic solution of the form

$$\mathbf{E}(\mathbf{x}, t) = \hat{\mathbf{E}}(\mathbf{x})\exp(-i\nu t), \tag{6.16}$$

where $\hat{\mathbf{E}}$ is a time-independent coefficient. Using this ansantz leads to the Helmholtz equation

$$\nabla^2\hat{\mathbf{E}} + k_i^2\hat{\mathbf{E}} = 0, \tag{6.17}$$

where $k_i^2 = \frac{\nu^2}{c^2}\kappa_i^2 = \frac{\nu^2\mu_i}{c^2}(\epsilon_i + i\nu\sigma)$ is the square of the wavenumber associated with the material throughout which the light passes. This is proportional to the square of the complex refractive index.

A similar Helmholtz equation to (6.17) holds for the magnetic vector, $\hat{\mathbf{H}}$. From equation (6.6) it is implied that there the relation

$$\hat{\mathbf{H}} = -\frac{i}{\mu_i\nu}\nabla\times\hat{\mathbf{E}} \tag{6.18}$$

holds. We, thus, restrict to solving only for the electric field. In the following section we present the boundary and initial conditions which complete the problem.

6.2.2 The Boundary Conditions

We complete the problem by assigning the appropriate conditions at the interfaces and the boundaries. In this section, we start by presenting the conditions at the interface between the materials of the device and then at the boundaries of the entire device, which we will refer to as *peripheral conditions* here.

6.2.2.1 Interface conditions

In this section, we first derive the interface conditions for the electric and magnetic field intensities, namely **E** and **H**, which apply to the interfaces between donor/acceptor, donor/dye and acceptor/dye.

The physical parameters (permittivity and permeability) of the problem are assumed to be constant in each material. We will briefly describe the derivation of the boundary conditions and their meaning, but we refer the reader to Born and Wolf [71] for further details.

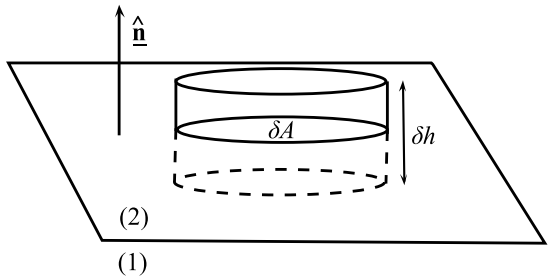

Figure 6.5: Tangential boundary.

At the interface between two different materials, we introduce the normal to the surface, $\hat{\mathbf{n}}$, with direction from material (1) to material (2) as shown in Figure 6.5. We consider a small ellipse on this surface with radius r and cross-sectional area δA and allow this to extend into a cylinder of material (1) in direction $-\hat{\mathbf{n}}$ and height $\frac{\delta h}{2}$ and of material (2) in direction $\hat{\mathbf{n}}$ and height $\frac{\delta h}{2}$, as shown in Figure 6.5. We let this cylinder have arbitrary volume Υ and integrate (6.7) in this space to get

$$\int_{\Upsilon} \nabla \cdot (\epsilon(\mathbf{x})\mathbf{E}) d\Upsilon = \int_{\partial\Upsilon} (\epsilon(\mathbf{x})\mathbf{E}) \cdot \hat{\mathbf{n}} dS = 0, \tag{6.19}$$

using the divergence theorem and assuming that $\rho = 0$ at the surface, as well. Then, the integration in (6.19) around the surface of the cylinder gives

$$-\epsilon_1 \mathbf{E}_1 \cdot \hat{\mathbf{n}} \delta A + \epsilon_2 \mathbf{E}_2 \cdot \hat{\mathbf{n}} \delta A + 2\pi r \delta h \left(\frac{\epsilon_1 \mathbf{E_1} + \epsilon_2 \mathbf{E_2}}{2} \right) = 0, \tag{6.20}$$

where the subscript indicates the side of the surface on which we calculate. By letting

$\delta h \to 0$, the last term vanishes, giving

$$[\epsilon(\mathbf{x})\mathbf{E} \cdot \hat{\mathbf{n}}] = 0, \tag{6.21}$$

where [.] denotes the jump across the interface. This is the tangential boundary condition for the electric field. We can perform a similar analysis on (6.8) to find

$$[\mu(\mathbf{x})\mathbf{H} \cdot \hat{\mathbf{n}}] = 0, \tag{6.22}$$

which is the jump for the magnetic vector. Using (6.6), we obtain the tangential jump of the curl of the electric field to be

$$[\hat{\mathbf{n}} \cdot (\nabla \times \mathbf{E})] = 0. \tag{6.23}$$

Next, we look at the normal boundary condition. Again, we use a transition plane, described by an area A enclosed by the circuit with perimeter δA, as shown in Figure 6.6. We introduce the direction vector $\hat{\mathbf{b}}$ to be perpendicular to the normal $\hat{\mathbf{n}}$ and the tangential $\hat{\mathbf{t}}$ vectors to the surface S. W

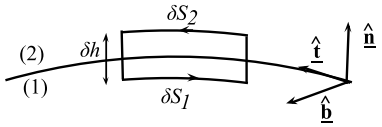

Figure 6.6: Normal boundary.

Then, by using Stokes' theorem on (6.6) in this plane, we get

$$\int_A (\nabla \times \mathbf{E}) \cdot \hat{\mathbf{b}} dS = \oint_{\partial A} \mathbf{E} \cdot d\mathbf{r} = -\frac{1}{c} \int_A \frac{\partial \mathbf{B}}{\partial t} \cdot \hat{\mathbf{b}} dS. \tag{6.24}$$

This says that the induced electric field in a closed circuit equals the negative change of the magnetic field in time in the volume enclosed by the closed circuit. Upon integrating the electric field around the boundary of the area and the time derivative of the magnetic vector throughout the area, we find

$$-\mathbf{E}_1 \cdot \hat{\mathbf{t}} \delta S_1 + \mathbf{E}_2 \cdot \hat{\mathbf{t}} \delta S_2 = -\frac{\partial \mathbf{B}}{\partial t} \cdot \hat{\mathbf{b}} \delta S \delta h, \tag{6.25}$$

where the terms arising from the ends parallel to $\hat{\mathbf{n}}$ cancel each other out. Using

$\hat{\mathbf{t}} = \hat{\mathbf{b}} \times \hat{\mathbf{n}}$ as $\delta h \to 0$, we reduce (6.25) to

$$(\mathbf{E}_2 - \mathbf{E}_1) \cdot \hat{\mathbf{t}} = (\mathbf{E}_2 - \mathbf{E}_1) \cdot (\hat{\mathbf{b}} \times \hat{\mathbf{n}}) = 0, \tag{6.26}$$

since . Using the identity $\mathbf{A} \cdot (\mathbf{B} \times C) = \mathbf{B} \cdot (\mathbf{C} \times \mathbf{A})$, we find that across the interface

$$[\hat{\mathbf{n}} \times \mathbf{E}] = 0. \tag{6.27}$$

In a similar manner, we apply Stoke's on (6.5) and follow the same steps as above to obtain

$$[\hat{\mathbf{n}} \times \mathbf{H}] = \frac{4\pi}{c} \lim_{\delta h \to 0} \int_A \sigma(\mathbf{x}) \mathbf{E} dS = 0, \tag{6.28}$$

which can be approximated by zero as the surface charges are assumed to be negligible. Using (6.18), we obtain

$$\left[\hat{\mathbf{n}} \times \left(\frac{1}{\mu(\mathbf{x})} \nabla \times \mathbf{E}\right)\right] = 0. \tag{6.29}$$

The transmission conditions (6.21) and (6.23) indicate that the system (6.17) does not decouple for the electric and magnetic field intensities. Thus we need to solve for the coupled problem in order to find the solution for these two variables.

6.2.2.2 Peripheral conditions

In this section we determine the boundary conditions on the surface of the entire device. We will continue with a two dimensional analysis by considering the same geometries for the cell as described in Part I, namely: (i) the bilayer cell, as schematically presented in Figure 3.1(a), with the dye interface at $z = 0$, and (ii) the nanostructured cell, as shown in Figure 3.1(c), with the dye interface located at $z = f(x)$.

The incident wave

The device is, typically, illuminated from the electron acceptor side with photons hitting the EA with an incident angle θ_1. This conventionally measures the angle between the direction of light propagation and the normal to the surface as shown in

Figure 6.7. According to Snell's law [71, 76], if θ_1 is the external incident angle and θ_2 the internal incident angle after refraction at the interface of two materials, then these are related by

$$\Re\{\kappa_1\}\sin(\theta_1) = \Re\{\kappa_2\}\sin(\theta_2)\,, \tag{6.30}$$

where $\Re\{\kappa_1\}$ and $\Re\{\kappa_2\}$ are the real parts of the refractive indices for materials (1) and (2), respectively. We restrict $-\frac{\pi}{2} < \theta_2 < \frac{\pi}{2}$ in order to avoid total reflection. Thus we restrict our incident angle to

$$-\sin^{-1}\left(\frac{\Re\{\kappa_2\}}{\Re\{\kappa_1\}}\right) \leq \theta_1 \leq \sin^{-1}\left(\frac{\Re\{\kappa_2\}}{\Re\{\kappa_1\}}\right). \tag{6.31}$$

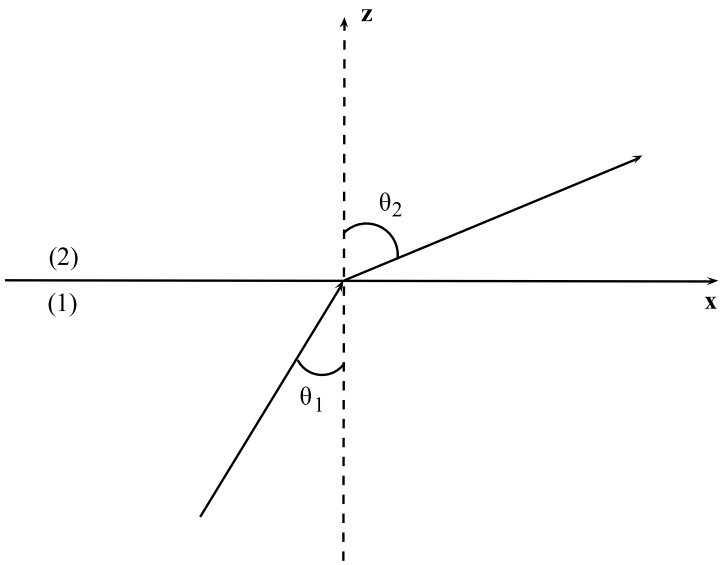

Figure 6.7: Schematic representation of refraction between two different materials, as described by Snell's law.

We will assume that light propagates as a two-dimensional plane wave with direction $\hat{\mathbf{s}} = (\cos\theta_1, \sin\theta_1)^T$, for some angle θ_1, from air into the electron acceptor. For a uniform, linearly polarized plane wave, i.e. with the components of the electric field varying with the same phase and amplitude, we may assume that the incident electric field takes the form

$$\mathbf{E} = \Re\left\{E_0\mathbf{p}\exp\left\{i\Re\{\kappa_1\}\hat{\mathbf{s}}\cdot\hat{\mathbf{x}} - i\nu t\right\}\right\}, \tag{6.32}$$

where E_0 is the wave magnitude, $\hat{\mathbf{p}} = (\sin\alpha, \cos\alpha)$ is the direction of the electric field $\mathbf{E}$ (for some angle α) and κ_1 is the wave vector in material (1), in this case light travels from the air (material 1) into the electron acceptor (material 2). As the direction of light propagation is perpendicular to the electric field, the relation between the angles α and θ_1 must satisfy

$$\hat{\mathbf{s}} \cdot \hat{\mathbf{p}} = \cos\alpha \sin\theta_1 + \cos\theta_1 \sin\alpha = \sin(\alpha + \theta_1) = 0. \tag{6.33}$$

Thus, $\alpha = \pi - \theta_1$ and $\mathbf{p} = (\sin\theta_1, -\cos\theta_1)$ and the incident wave at the air/electron acceptor interface can be written as

$$\mathbf{E}_{incident} = \Re\left\{E_0 \mathbf{p} \exp\left\{i\kappa_1 \left(x\sin(\theta_1) + z\cos(\theta_1)\right)\right\}\right\}. \tag{6.34}$$

In our analysis, we will consider that the light enters the device only from one surface, by letting $\theta_1 = 0$. Then, (6.34) reduces to

$$\mathbf{E}_{incident} = \Re\left\{E_0 \mathbf{p} \exp\left\{i\kappa_1 z\right\}\right\}, \tag{6.35}$$

with $\mathbf{p} = (0, -1)$ at $z = -H_1$.

The radiation condition

At the remaining outer surfaces of the device we assume that no light enters, but only exits, as shown in Figure 6.8. At the electron donor end, we do not allow for any light to enter, thus we use the radiation condition[3] [76]

$$\frac{\partial \mathbf{E}}{\partial z} - ik_{ED_R}\mathbf{E} = 0, \tag{6.36}$$

at $z = H_2$, where k_{ED} is the wave number in the ED region.

[3] This condition can be retrieved by using the wave properties of the electric field components (**??**) and writing the solution of Helmholtz equation (6.17) for the electric field as the sum of an ingoing and outgoing wave. For more details, the reader is directed to *Sommerfeld* [76].

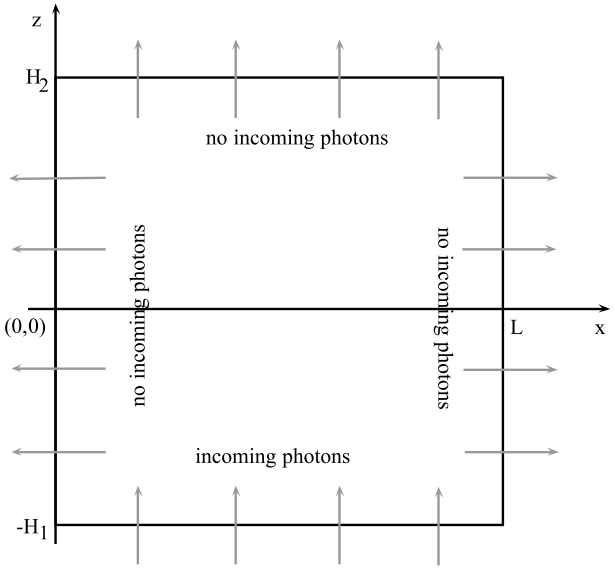

Figure 6.8: Schematic representation of the permissible radiation at boundaries: photons insert the device from the electron acceptor side, while they are not allowed to exit the device through any other surface for $\theta_1 = 0$.

Similarly, by assuming that no energy enters the device from the surfaces $x = 0$ and $x = L$ (see Figure 6.8), we impose the radiation condition

$$(\hat{\mathbf{n}} \cdot \nabla)\, \mathbf{E} - ik_i \mathbf{E} = 0, \tag{6.37}$$

where $\hat{\mathbf{n}}$ is the outward pointing normal to the corresponding surface.

If we assume that the device's structure follows a periodic pattern either as a bilayer with multiple blobs of dye at the interface of the EA/ED or as a structured nanostem arrangement at the interface, we may replace (6.37) with the periodic conditions

$$\mathbf{E}(0, z, t) = \mathbf{E}(\omega, z, t) \tag{6.38}$$

$$\frac{\partial \mathbf{E}}{\partial x}(0, z, t) = \frac{\partial \mathbf{E}}{\partial x}(\omega, z, t), \tag{6.39}$$

on the x-boundaries, where $x = 0$ and $x = \omega$ define the ends of one period of the pattern, as represented in Figure **??** in Chapter 5. This will allow us to consider only one block of the repeated pattern.

For our analytical purposes, we need only to examine the time-independent problem of the light propagation and absorption in the device. This suffices in order to

complete the model for a ssDSSC. The scope of the following section is defining the generation of current in the dye.

6.2.3 Current generation

We use Maxwell's equations to find an expression for the light intensity, i.e. the number of photons going through a surface. We start by subtracting the dot product of $\mathbf{H}$ with (6.6) from the dot product of $\mathbf{E}$ with (6.5) to get

$$\mathbf{E}\cdot(\nabla\times\mathbf{H})-\mathbf{H}\cdot(\nabla\times\mathbf{E})=\sigma(\mathbf{x})\mathbf{E}\cdot\mathbf{E}+\left(\mathbf{E}\cdot\frac{\partial\mathbf{D}}{\partial t}+\mathbf{H}\cdot\frac{\partial\mathbf{B}}{\partial t}\right) \tag{6.40}$$

Using a vector identity on the left hand side and multiplying through by $\frac{c}{4\pi}$, we may reduce (6.40) to the energy law of an electromagnetic field

$$\nabla\cdot(\mathbf{E}\times\mathbf{H})+\sigma(\mathbf{x})\mathbf{E}^2+\frac{1}{2}\left(\epsilon(\mathbf{x})\frac{\partial\mathbf{E}^2}{\partial t}+\mu(\mathbf{x})\frac{\partial\mathbf{H}^2}{\partial t}\right)=0. \tag{6.41}$$

Equation (6.41) represents the balance of energy in the electromagnetic wave. In particular, the first term represents the change in power as represented by the Poynting vector ($\mathbf{S}=\mathbf{E}\times\mathbf{H}$) $[Wm^{-2}]$ and the second term is the Joule heat (the resistive dissipation energy). The final two terms indicate the electric and magnetic energies, respectively.

In what follows we seek a time-independent expression for the generation rate, which is in fact the average of the left hand side of (6.45), i.e.

$$G=\Re\left\{\int_{\partial V}<\mathbf{E}\times\mathbf{H}>\cdot\hat{\mathbf{n}}dA\right\}. \tag{6.42}$$

To facilitate the algebra that follows, we rewrite (6.53) and (6.54) into

$$\mathbf{E}(\mathbf{x},t)=\Re\left(\hat{\mathbf{E}}(\mathbf{x})e^{-i\nu t}\right)=\frac{1}{2}\left(\hat{\mathbf{E}}(\mathbf{x})e^{-i\nu t}+\hat{\mathbf{E}}^*(\mathbf{x})e^{i\nu t}\right), \tag{6.43}$$

$$\mathbf{H}(\mathbf{x},t)=\Re\left(\hat{\mathbf{H}}(\mathbf{x})e^{-i\nu t}\right)=\frac{1}{2}\left(\hat{\mathbf{H}}(\mathbf{x})e^{-i\nu t}+\hat{\mathbf{H}}^*(\mathbf{x})e^{i\nu t}\right), \tag{6.44}$$

where $[.]^*$ represents the complex conjugate of the relevant variable.

To find the energy in the volume of interest, say Υ, we substitute (6.43) and (6.44)

into (6.41) and integrate over the volume Υ, to get

$$\int_{\partial\Upsilon} (\hat{\mathbf{E}} \times \hat{\mathbf{H}}) \cdot \hat{\mathbf{n}} dA = -\int_{\Upsilon} \sigma(\mathbf{x}) \hat{\mathbf{E}}^2 d\Upsilon - \frac{1}{2} \int_{\Upsilon} \left(\epsilon(\mathbf{x}) \hat{\mathbf{E}} + \mu(\mathbf{x}) \hat{\mathbf{H}} \right) d\Upsilon \tag{6.45}$$

We define the fundamental period of the electric field $\mathbf{E}$ as $T = \frac{2\pi}{\nu}$. It is more valuable to estimate the value of the Poynting vector over an appreciable amount of time, where the effect of the electromagnetic field can be observed, say $T' \gg T$. If we, then, take the time average of the Poynting vector over some period $2T'$, the left hand side of (6.45) will give the generation rate, i.e. the flux of photons through the total surface of our domain of interest. The light intensity, which is a measure of the power per unit volume/area, is the magnitude of the time-averaged Poynting vector, i.e. $I = | < \mathbf{S} > | = | < \mathbf{E} \times \mathbf{H} > |$. Then, the power lost within the volume of interest is equivalent to the amount of photons which are absorbed by the material by turning electrons into excitons. This is the current generation rate within a material.

Then, we may evaluate the time-averaged Poynting vector as follows:

$$< \mathbf{E} \times \mathbf{H} > = \frac{1}{2T'} \int_{-T'}^{T'} \mathbf{E} \times \mathbf{H} dt \tag{6.46}$$

$$= \frac{1}{8T'} \int_{-T'}^{T'} \left(\hat{\mathbf{E}} \times \hat{\mathbf{H}} e^{-2i\nu t} + \hat{\mathbf{E}}^* \times \hat{\mathbf{H}} + \hat{\mathbf{E}} \times \hat{\mathbf{H}}^* + \hat{\mathbf{E}}^* \times \hat{\mathbf{H}}^* e^{2i\nu t} \right) dt \tag{6.47}$$

$$= \left(-\frac{1}{16\nu T'} [e^{-2i\nu t}]_{T'}^{T'} \hat{\mathbf{E}} \times \hat{\mathbf{H}} + \hat{\mathbf{E}}^* \times \hat{\mathbf{H}} + \hat{\mathbf{E}} \times \hat{\mathbf{H}}^* + \frac{1}{4\nu T'} [e^{2i\nu t}]_{T'}^{T'} \hat{\mathbf{E}}^* \times \hat{\mathbf{H}}^* \right) \tag{6.48}$$

$$\approx \frac{1}{4} \left(\hat{\mathbf{E}}^* \times \hat{\mathbf{H}} + \hat{\mathbf{E}} \times \hat{\mathbf{H}}^* \right) \tag{6.49}$$

$$= \frac{1}{2} \Re \left(\hat{\mathbf{E}}^* \times \hat{\mathbf{H}} \right), \tag{6.50}$$

where we have used the fact that $\frac{1}{4\nu T'} = \frac{T}{8\pi T'} \ll 1$. We apply the ansantz (6.43)-(6.44) into (6.6) to get

$$\hat{\mathbf{H}} = -\frac{i}{\mu_i \nu} \nabla \times \hat{\mathbf{E}}, \tag{6.51}$$

which we then use in (6.50) to obtain the generation rate in terms only of the electric field:

$$G = G_0 \Re \left\{ \int_{\partial \Upsilon} \frac{2i}{\nu \mu} \left(\hat{\mathbf{E}}^* \times (\nabla \times \hat{\mathbf{E}}) \right) \cdot \hat{\mathbf{n}} dA \right\}. \tag{6.52}$$

Here, G_0 is the inverse of the photon energy, E_{photon}. Therefore, the generation rate, G, equals the photon flux $G = \frac{S}{E_{photon}}$ which has the same units, $[m^{-2}s^{-1}]$, as the current density in Part I.

6.2.4 The time-independent model: summary

Here, we summarise the problem, comprising the governing equations and the associated interface and peripheral conditions. However, we limit our interest to the time-independent solution, which we achieve by applying the following ansatzes

$$\mathbf{E} = \Re \left(\hat{\mathbf{E}}(\mathbf{x}) \exp \{-i\nu t\} \right) \tag{6.53}$$

$$\mathbf{H} = \Re \left(\hat{\mathbf{H}}(\mathbf{x}) \exp \{-i\nu_H t\} \right), \tag{6.54}$$

into the equations and boundary conditions derived earlier. By avoiding the presentation of the relevant algebra, we present the full problem below. For Ω_a and Ω_d being the domain representing the electron acceptor and electron donor regions, respectively, and $z = f(x)$ the interface between the two, we may write out the following time-independent problem:

$$\nabla^2 \hat{\mathbf{E}} + k_i^2 \hat{\mathbf{E}} = 0, \tag{6.55}$$

with the accompanying interface conditions on $z = f(x)$

$$\left[\epsilon_i \hat{\mathbf{E}} \cdot \hat{\mathbf{n}} \right] = 0 \tag{6.56}$$

$$\left[\hat{\mathbf{n}} \times \hat{\mathbf{E}} \right] = 0 \tag{6.57}$$

$$\left[\hat{\mathbf{n}} \cdot (\nabla \times \hat{\mathbf{E}}) \right] = 0 \tag{6.58}$$

$$\left[\hat{\mathbf{n}} \times \left(\frac{1}{\mu_i} \nabla \times \hat{\mathbf{E}} \right) \right] = 0, \tag{6.59}$$

with $\hat{\mathbf{E}}_s$ indicating the electric field measured on the interface, while the incident wave is represented by

$$\hat{\mathbf{E}} = \Re\left\{E_0 \mathbf{p} \exp\left(\kappa_{air} z\right)\right\}, \tag{6.60}$$

at the air/compact EA interface ($z = -H_1$), and the restriction on the outgoing wave on the remaining three surfaces, i.e. $z = H_2,\ x = 0$, and $x = L$, is given by

$$\left(\hat{\mathbf{n}} \cdot \nabla\right) \hat{\mathbf{E}} - i k_i \hat{\mathbf{E}} = 0. \tag{6.61}$$

In the remaining of the thesis we examine the model as given by (6.55)-(6.61) in one and two dimensional spaces. However, while this model helps understand the distribution of light within the involved materials, it is important to establish a relationship between the light absorption and the current generation in our domain of interest. The scope of the following section is defining the generation of current in the dye.

In the following Chapters we approximate the light absorption by the generation rate described by

$$G = G_0 \Re\left\{\int_{\partial\Upsilon} \frac{2ic}{\nu\mu}\left(\hat{\mathbf{E}}^* \times \left(\nabla \times \hat{\mathbf{E}}\right)\right) \cdot \hat{\mathbf{n}} dA\right\}. \tag{6.62}$$

in the dye layer. The generation rate combined with the current transport model derived in Part I, complete the model of the operation of the ssDSSC.

7

The bilayer cell

In this Chapter, we show how the light absorption problem described in the previous Chapter can be used to calculate the generation rate for various scenarios, including two for the bilayer cell, as in Chapter 4. The scenarios are: (i) the thin film cell with a blob of dye covering half of the EA/dye interface, i.e. $0 \leq x \leq \omega$ (recall Section 4.4.3) and (ii) the thin blob approximation where the interface is covered periodically with dye blobs of width $\hat{\omega} \ll 1$ (recall Section 4.4.4). For our analysis, we also retain all assumptions on symmetry and material properties as posed in Part I.

7.1 The thin film approximation

In this section, we study the thin film approximation both in one and two dimensions. Our analysis involves numerical, rather than analytical, solutions, except for the calculation of the one-dimensional exact solution.

7.1.1 The one-dimensional approximation

For the one dimensional problem (as in Section 4.1) we consider the geometrical simplifications as shown in Figure 7.1, whereby we divide the cell into the three regions: (i) the electron acceptor region described by $\Omega_{EA} = \{-H_1 \leq z \leq -u\}$, with $u \ll 1$, (ii) the electron donor region $\Omega_{ED} = \{\epsilon \leq z \leq H_2\}$ and (iii) the dye region $-u \leq z \leq u$. For the purposes of our analysis in Part II, we consider $u \ll 1$ to be infinitesimally small compared to the size of the outer region, namely $|H_2|$ and $|H_1|$. However, we allow for some thickness in this layer, in order to evaluate the generation rate in the dye layer.

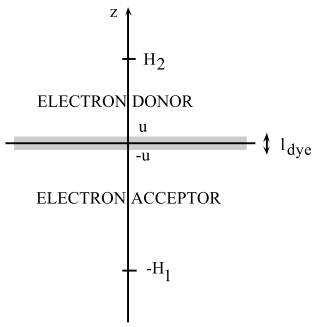

Figure 7.1: A schematic representation of the one dimensional approach of a bilayer cell. The dye layer length is represented by $l_{dye} = 2u \ll |H_1|$.

The time-independent model (6.53)-(6.61) then reduces to

$$\frac{d^2\hat{E}}{dz^2} + k^2(z)\hat{E} = 0, \tag{7.1}$$

with a perpendicularly incident light wave on the dye at $z = -H_1$ described by

$$\hat{E} = \Re\left\{\hat{E}_0 \exp(-iH_1\kappa_{air})\right\}, \tag{7.2}$$

and the outgoing wave condition at $z = H_1$

$$\frac{d\hat{E}}{dz} - ik_{ED}\hat{E} = 0. \tag{7.3}$$

The interface conditions at $z = -u$ and $z = u$ are

$$\left[\epsilon_i\hat{E}\right] = 0. \tag{7.4}$$

We rescale the problem by $z = H_1\hat{z}$ and $\hat{E} = \hat{E}_0\bar{\hat{E}}$. We also set $H_1 = H_2 = 1$ for symmetry and, thus, $u \ll 1$. By dropping the barss, the rescaled problem is given by

$$\frac{d^2\hat{E}}{dz^2} + k^2(z)\hat{E} = 0, \tag{7.5}$$

with

$$\hat{E}(-1) = \Re\left\{\exp(-i\kappa_{air})\right\}, \tag{7.6}$$

$$\frac{d\hat{E}}{dz}(1) - ik_{ED}\hat{E}(1) = 0 \tag{7.7}$$

$$\left[\epsilon_i\hat{E}\right] = 0 \quad \text{at} \quad z = -u, u. \tag{7.8}$$

The general form of solution to (7.5)-(7.8) is

$$\hat{E}(z) = \alpha\exp(-ik(z)z) + \beta\exp(ik(z)z). \tag{7.9}$$

Upon the application of the boundary conditions (7.2) and (7.3) and by assuring continuity at the interface of the regions, we find the solution to be:

$$\hat{E} = \begin{cases} \exp(ik_{EA}z), & -1 \le z < -u \\ \frac{\epsilon_n}{\epsilon_{dye}}\exp(-ik_{EA}u)\exp(ik_{dye}(z+u)) & -u \le z \le u \\ \frac{\epsilon_{dye}}{\epsilon_p}\exp(-iu(k_{EA}-2k_{dye}))\exp(ik_{ED}(z-u)) & u < z \le 1, \end{cases} \tag{7.10}$$

as shown in Figure 7.2. The electric field of the electromagnetic wave (i.e. light) is oscillating along z, while the wavenumber defines the wavelength in each material. The periodicity of the electric field is $\frac{2\pi}{k_i}$ in each region i.

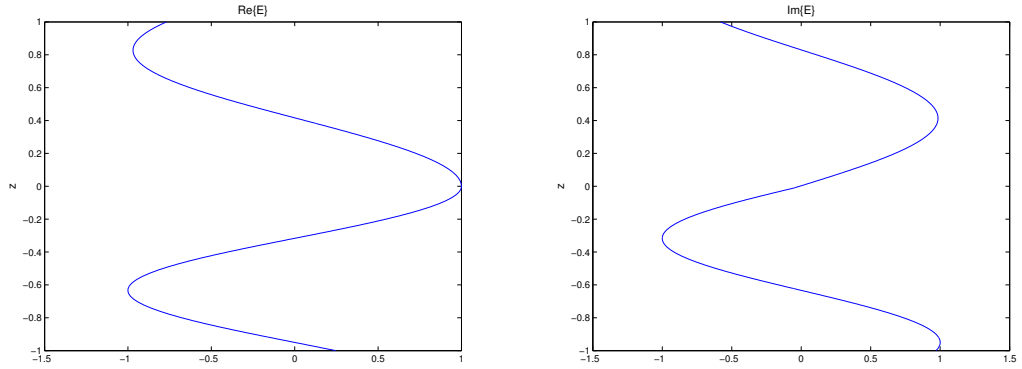

(a) (b)

Figure 7.2: The plot shows the real and imaginary parts of the electric field as given in (7.10). Parameters: the refractive indices are given in Table 7.1, $\epsilon_n = \epsilon_{dye} = \epsilon_p = 1$, $u = 0.01$.

We then calculate the generation rate in the dye region, as the change in light intensity, I, in the dye. In the one-dimensional case, we approach the problem by considering the change in light intensity in the dye ($-u \leq z \leq u$)) and using the light intensity as measured at the end of the dye region ($z = u$) as the generation rate. According to the Beer-Lambert law, as discussed in the previous Chapter, the change in light intensity satisfies [71]

$$\frac{dI}{dz} = -\frac{2\pi c \Im(k_{dye})}{\nu} I, \tag{7.11}$$

where λ is the wavelength of the light. The solution to (7.11) can be found by integrating over $-u \leq z \leq u$ to get

$$I = I_0 \exp\left(-i\frac{4\pi \Im(\kappa_{dye})u}{\nu}\right), \tag{7.12}$$

with I_0 being the amount of initial power of photons entering the medium (at $z = -u$)[1]. Then the generation rate is found to be the real part of light intensity at

$$G = G_0 \cos\left(\frac{4\pi \Im(\kappa_{dye})u}{\nu}\right). \tag{7.13}$$

We then use the expression obtained in (7.13) to rescale the generation rate with $G = G_0\hat{G}$.

[1]In this case, I_0 depends on the absorbance occurring in the EA region, where a similar expression to (7.12) holds. However, since there is limited absorbance in the EA region, we may approximate $I_0 = I_{z=-1}$, with $I_{z=-1}$ the light intensity measured at the surface of the EA.

As the dye layer is thin relative to the length of the cell, the generation rate in the one dimensional approximation is a constant. The generation rate depends on the wavelength of the incident light and the optical absorption properties of the materials in place.

We now consider the current transport problem for the constant generation rate. Similarly to Chapter 4, we only solve for the rescaled symmetric bilayer cell problem (as defined in section 4.2) and present the results only for the electron acceptor region. The electrostatic potential satisfies

$$-\Lambda F_n = \phi_{zzz} - \phi_{zz}\phi_z, \tag{7.14}$$

while we modify the boundary conditions to include the generation term

$$\phi(-1) = -\frac{V}{2}, \qquad \phi_{zz}(-1) = \Lambda \tag{7.15}$$

$$\phi(0) = 0, \qquad F_n = \delta S\left(\frac{\phi_{zz}^2}{\Lambda^2} - 1\right) - (1-S)\hat{G}. \tag{7.16}$$

To avoid repetition and tedious algebra, we present only the final form of the solution.

The solution to the problem (7.14)-(7.16) can be found by following the same steps as in Section 4.2.1, so that

$$\phi = -2\log\left[\frac{\left(e^{\frac{V}{4}}\operatorname{Bi}(\omega) - \operatorname{Bi}(\omega-\chi)\right)\operatorname{Ai}(\omega+\chi z) - \left(e^{\frac{V}{4}}\operatorname{Ai}(\omega) - \operatorname{Ai}(\omega-\chi)\right)\operatorname{Bi}(\omega+\chi z)}{\operatorname{Ai}(\omega-\chi)\operatorname{Bi}(\omega) - \operatorname{Ai}(\omega)\operatorname{Bi}(\omega-\chi)}\right] \tag{7.17}$$

where ω and χ can be found by solving the equations

$$\Lambda = 2\chi^2\left[\left(\frac{\operatorname{Bi}(\omega)\operatorname{Ai}'(\omega-\chi) - \operatorname{Ai}(\omega)\operatorname{Bi}'(\omega-\chi) + \frac{e^{-\frac{V}{4}}}{\pi}}{\operatorname{Bi}(\omega)\operatorname{Ai}(\omega-\chi) - \operatorname{Ai}(\omega)\operatorname{Bi}(\omega-\chi)}\right)^2 - (\omega-\chi)\right] \tag{7.18}$$

$$\frac{2\chi^3}{\Lambda} = \delta S\left[\frac{4\chi^4}{\Lambda^2}\left(\left(\frac{\operatorname{Ai}(\omega-\chi)\operatorname{Bi}'(\omega) - \operatorname{Bi}(\omega-\chi)\operatorname{Ai}'(\omega) - \frac{e^{\frac{V}{4}}}{\pi}}{\operatorname{Bi}(\omega)\operatorname{Ai}(\omega-\chi) - \operatorname{Ai}(\omega)\operatorname{Bi}(\omega-\chi)}\right)^2 - \omega\right)^2 - 1\right] - (1-S)\hat{G} \tag{7.19}$$

with $\chi = \left(\frac{F_n \Lambda}{2}\right)^{\frac{1}{3}}$ and $\omega = \left(\frac{F_n \Lambda}{2}\right)^{\frac{1}{3}} C_1$ as earlier.

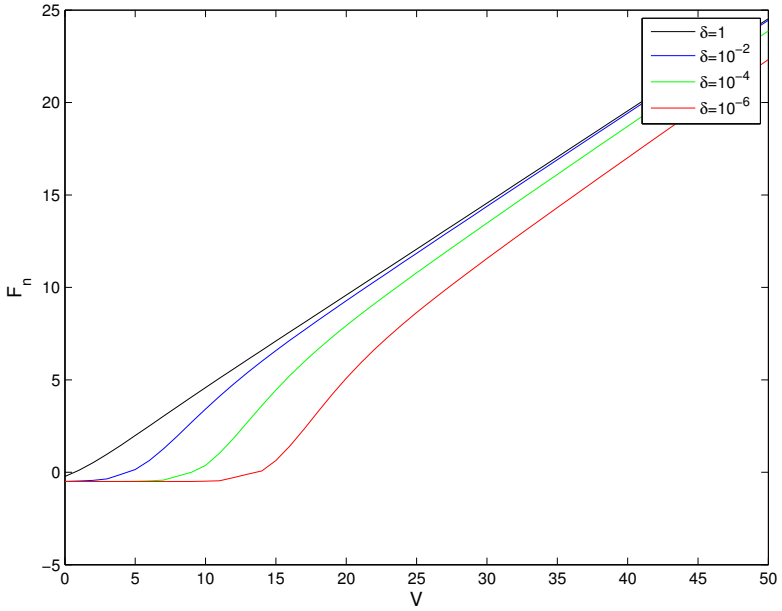

Figure 7.3: Current density against the applied voltage as given by the exact solution [Parameters: $S = 0.5$, $\Lambda = 1$, $G = 1$]

In Figure 7.3 we present current-voltage curves as obtained from the exact solution (7.17)-(7.19). We observe that, compared with Figure 4.2, the curves are shifted downwards due to current generation. An important measure used to describe solar cells, is the generated power (i.e. the voltage times the current density). For a cell under forward bias, the maximum power is obtained between the short circuit current density and the open circuit voltage. As illumination increases (i.e. as G increases) the output power is larger, while other factors can help increase this value, such as the recombination coefficient, the mobility of carriers etc.

The interested reader is directed to Foster *et al* [77] for an analysis of the asymptotic approximation of the full current voltage range shown in Figure 7.3. In what follows we consider the two dimensional approximation for the thin film bilayer problem.

7.1.2 The two-dimensional approximation

In this Section we consider the two dimensional version of the light absorption problem, which we can use as an input to the current transport problem of Chapter 4. The simplified geometry under consideration is demonstrated in Figure 7.4, whereby we have divided the cell into the three regions: (i) the electron acceptor region Ω_{EA}, (ii) the electron donor region Ω_{ED} and (iii) the dye region Ω_{dye}. We assume that the dye has length $\frac{L}{2}$, so that it doesn't extend all the way across the cell.

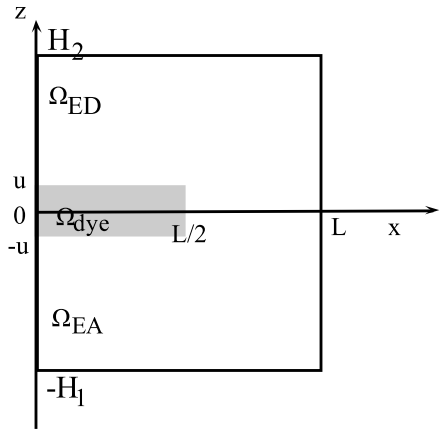

Figure 7.4: A schematic representation of the two dimensional geometrical consideration for a bilayer cell. The dye is represented by the grey region, where $u \ll 1$.

Solving the two dimensional problem for the bilayer cell, or even more complicated geometries, requires cumbersome algebraic calculations. Thus, from this point onwards we utilise only numerical techniques for the approximation of the solution to the two dimensional problem for the generation rate

$$G = -\Re\left\{\int_{\Omega_{dye}} \frac{2c}{i\nu\mu}\left(\hat{\mathbf{E}}^* \times \left(\nabla \times \hat{\mathbf{E}}\right)\right) \cdot \hat{\mathbf{n}} dA\right\}. \tag{7.20}$$

This requires the numerical solution of the electric field across the domain as described by the equation

$$\nabla^2\hat{\mathbf{E}} + k^2(\mathbf{x})\hat{\mathbf{E}} = 0, \tag{7.21}$$

with the interface conditions on $z = -u$ and $z = u$ for $0 \leq x \leq \frac{L}{2}$ and $z = 0$ for

$\frac{L}{2} \leq x \leq L$

$$[\epsilon(\mathbf{x})\hat{\mathbf{E}} \cdot \hat{\mathbf{n}}] = 0 \tag{7.22}$$

$$\left[\hat{\mathbf{n}} \times \left(\frac{1}{\mu(\mathbf{x})}\nabla \times \hat{\mathbf{E}}\right)\right] = \frac{4i\nu\pi}{c^2}\sigma(\mathbf{x})\hat{\mathbf{E}}_s, \tag{7.23}$$

$$\left[\hat{\mathbf{n}} \cdot \left(\nabla \times \hat{\mathbf{E}}\right)\right] = 0 \tag{7.24}$$

$$\left[\hat{\mathbf{n}} \times \hat{\mathbf{E}}\right] = 0. \tag{7.25}$$

In the z-direction we impose the initial condition on the surface where the light is incoming ($z = -H_1$)

$$\hat{\mathbf{E}}_0 = \Re\left\{\mathbf{p}\hat{E}_0 \exp\left\{-ik_{EA}H_1\right\}\right\} \tag{7.26}$$

with $\mathbf{p} = (0, 1)^T$ and the Sommerfeld radiation condition on the other surfaces

$$\left.\frac{\partial\hat{\mathbf{E}}}{\partial z}\right|_{z=H_2} - ik_{ED_R}\hat{\mathbf{E}} = 0, \qquad \left.\frac{\partial\hat{\mathbf{E}}}{\partial \mathbf{x}}\right|_{x=0,L} - ik_i\hat{\mathbf{E}} = 0. \tag{7.27}$$

Nondimensionalisation

As earlier, for the thin film cell, $\frac{H_1}{L} = \varepsilon \ll 1$ and the length of the dye in the x-direction, $\omega = \frac{L}{2} = O(1)$, as shown in Figure 7.4. By applying the rescalings $x = L\bar{x}$, $\hat{w} = L\omega$, $z = H_1\bar{z}$ and $\hat{\mathbf{E}} = E_0\tilde{\mathbf{E}}$ the problem, by dropping the bars and tildes, is reduced to

$$\varepsilon^2\hat{\mathbf{E}}_{xx} + \hat{\mathbf{E}}_{zz} + k_\omega^2(\mathbf{x})\hat{\mathbf{E}} = 0, \tag{7.28}$$

where $k_\omega(\mathbf{x}) = H_1^2 k(\mathbf{x})$. We estimate that $k_\omega \approx 10^{-1} - 1$ for the wavelength of interest, but we note that the value of this parameter may range given the spectrum range. We allow our numerical solution to take variable values for this parameter, but in our presentation of sample results in section we use $k_\omega = O(1)$. For the purposes of our analysis, we take the length of the dye layer to be infinitely thin, with $\frac{u}{H_1} \ll \frac{H_1}{L} \ll 1$ and we introduce the rescaled angle $\hat{\theta}$, which corresponds to $\tan(\hat{\theta}) = \frac{H_1}{L}\tan(\theta)$, i.e. $\hat{\theta} = 0$, since $\frac{H_1}{L} \to 0$. We restrict the angle of the incoming light wave at $z = -1$ with $0 < \hat{\theta}_1 \leq \arcsin\left(\frac{\kappa_{R\_ED}}{\kappa_{air}}\arctan(\varepsilon)\right)$.

It is worth mentioning here that, if the wavelength of light hitting the cell was signif-

icantly smaller than the lengthscale of the cell, then we would be able to use simpler mathematics to approximate the solution. In particular, light of small wavelength could be described by linear optical rays in a larger scale homogeneous material. This idealised model of discrete rays, however, can not be used here since the wavelength and the scale of the problem are similar.

The interface boundary conditions are rescaled in a similar manner, so that ∇ is replaced with $\bar{\nabla} = \left(\frac{1}{L}\frac{\partial}{\partial x}, \frac{1}{H_1}\frac{\partial}{\partial z}\right)$. The z-direction boundary conditions are reduced to

$$\hat{\mathbf{E}}(x,-1) = \Re\left\{\exp\left\{H_1 \cos\left(\arctan\left(\varepsilon x\right)\right)\right\}\right\} \tag{7.29}$$

$$\frac{\partial \hat{\mathbf{E}}(x,1)}{\partial z} - iH_1 k_{ED}\hat{\mathbf{E}}(x,1) = 0. \tag{7.30}$$

For simplicity of our calculations we let $\theta = 0$ so that the light reaches the surface of the cell perpendicularly. As $\varepsilon \to 0$, we use the approximation $\hat{\theta} = 0$. Finally, the x-direction conditions reduce to

$$\left.\frac{\partial \hat{\mathbf{E}}}{\partial \hat{\mathbf{x}}}\right|_{\hat{x}=0,1} - iLk_m\hat{\mathbf{E}} = 0. \tag{7.31}$$

The interface conditions, also reduced to

$$\left[\epsilon(\mathbf{x})\hat{\mathbf{E}}\cdot\hat{\mathbf{n}}\right] = 0 \tag{7.32}$$

$$\left[\hat{\mathbf{n}}\times\left(\frac{1}{\mu(\mathbf{x})}\bar{\nabla}\times\hat{\mathbf{E}}\right)\right] = \frac{4i\nu\pi}{c^2}\sigma(\mathbf{x})\hat{\mathbf{E}}_s, \tag{7.33}$$

$$\left[\hat{\mathbf{n}}\cdot\left(\bar{\nabla}\times\hat{E}\right)\right] = 0 \tag{7.34}$$

$$\left[\hat{\mathbf{n}}\times\hat{\mathbf{E}}\right] = 0. \tag{7.35}$$

The generation rate is then calculated as

$$\bar{G} = \frac{G}{G_0} = -\Re\left\{i\int_{\hat{\Omega}_{dye}}\hat{\mathbf{E}}^*\times\left(\bar{\nabla}\times\hat{\mathbf{E}}\right)dA\right\}, \tag{7.36}$$

with $\hat{\Omega}_{dye}$ representing the scaled dye region and $G_0 = \frac{cE_0}{\nu\mu}$.

In the next section we present the results from the numerical scheme utilised to solve the non-dimensional problem.

Numerical Approximation

We employ a numerical scheme to calculate the electric field by solving the Helmholtz equation (7.7) with the relevant boundary conditions over the area of interest. The numerical code produces the distribution of the electric field throughout the whole cell under illumination, allowing the user to vary the parameters: κ_i, k_i, ε, H_1, H_2, L, δ, V, $\hat{\epsilon}_p$, $\hat{N}^-$ and $\hat{P}^+$. The electric field can then be used for the evaluation of the generation rate, by integrating (7.36) numerically. The scheme employes the *finite volume method* as previously used in Chapter 4. We do not provide any detailed analysis of this scheme, as the steps involved in defining the scheme are the same as those described in Appendix III.

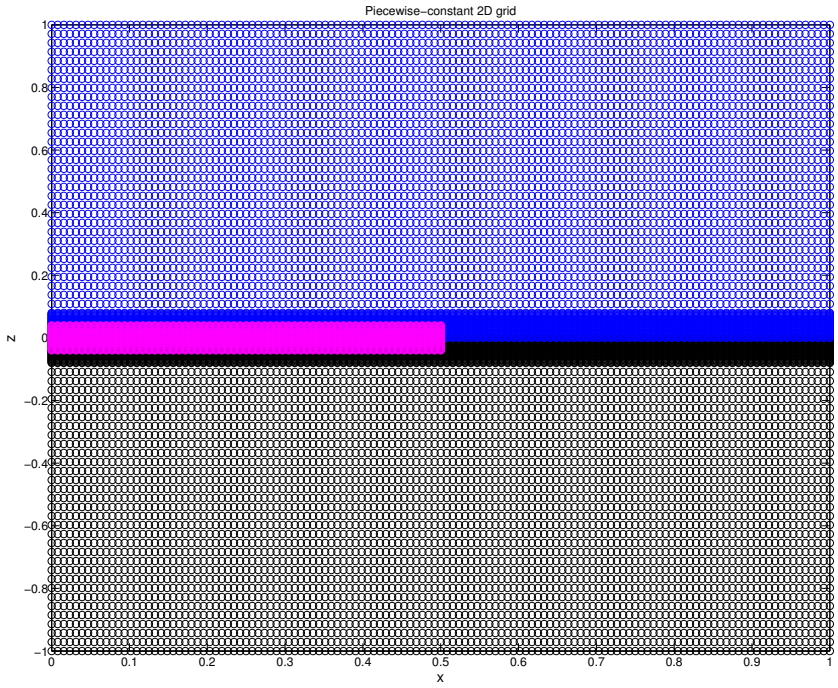

Figure 7.5: The piecewise uniform grid for $[0,1]\times[-1,1]$, for the bilayer case with a dye blob covering the half of the EA/ED interface. The grid is colour coded to discriminate into the three regions: (i) the electron acceptor region is shown with black nodes, (ii) the electron donor is shown with blue nodes and (iii) the dye region is shown with magenta nodes. We have used a piecewise uniform grid, where we have a denser grid near the ED/EA interface as illustrated by the denser nodes.

The space between $x \in [0,1]$ and $z \in [-1,1]$, is discretised into a piecewise-uniform grid as shown in Figure 7.5. The grid is defined by nodes at the points (x_i, z_j), where

$i, j = 0, ..., J$. We let $h_{xi} = x_i - x_{i-1}$ and $h_{zj} = z_j - z_{j-1}$ define the grid step sizes in the x and z directions, respectively. We then let $E_{i,k}$ be the numerical solution for the electric field E at the node (x_i, z_j). In Figure 7.5, we show a sample grid where there is a blob of dye covering the interface only halfway. The colouring in the figure, shows the different materials: black for electron acceptor, blue for electron donor and red for the dye. As shown in Figure 7.5 through the higher number of nodes near the interface, we define a finer grid near the EA/ED interface to accommodate for the numerical solution in the dye monolayer.

The finite volume method reduces to the centred finite differences method in the bulk regions of the electron acceptor and donor. In Figure 7.6 we show the refractive index, $\kappa(\mathbf{x})$, in the full domain, as this is laid out in Table 6.1. As discussed earlier, the imaginary part of the refractive index is proportional to the absorbance of the material, and, therefore, the imaginary parts of κ_{EA} and κ_{ED} are small.

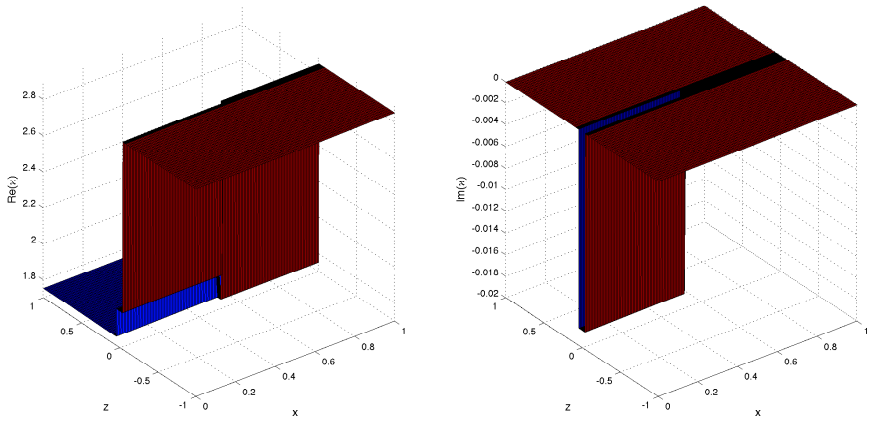

Figure 7.6: Real and imaginary parts of the refractive index for the various materials in the domain of interest. We have taken the imaginary parts of the refractive indices for the electron acceptor and donor to be small compared to that of the dye.

Based on the material properties of the cell, we may then solve the problem for the electric field described by (7.7)-(7.31) to obtain the distribution shown in Figure 7.7. In Figure 7.7(a) and (b) we show the real and imaginary parts of the x-component of the electric field, respectively. We observe jumps at the interfaces between the dye and the outer regions at $x = 0$ and $-1 \leq z < 0$ and between the outer regions at $x = 0$ and $0 < z \leq 1$. While the geometry of our device is chosen to be symmetrical, the outcome is not symmetrical, owing to the refraction of light at the interfaces, as

can be observed by the colouring on the images.

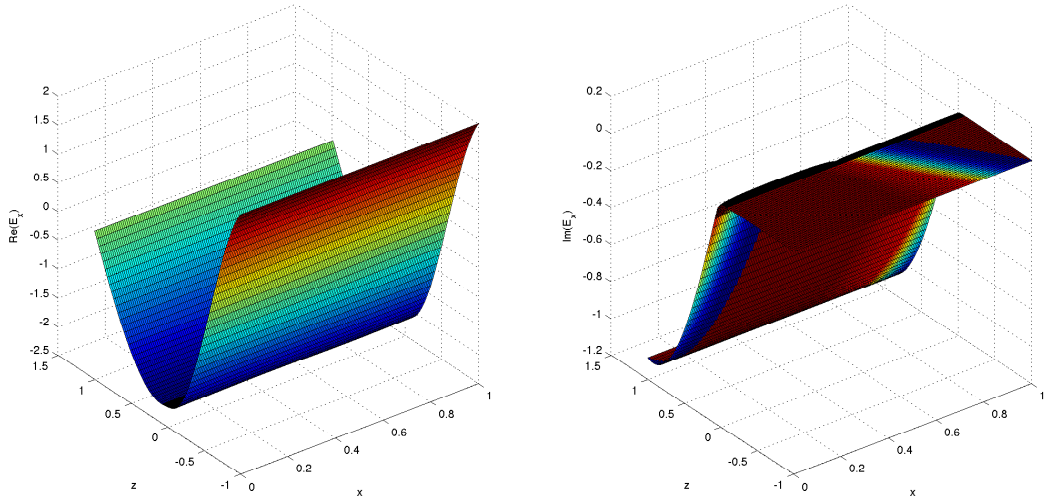

(a)

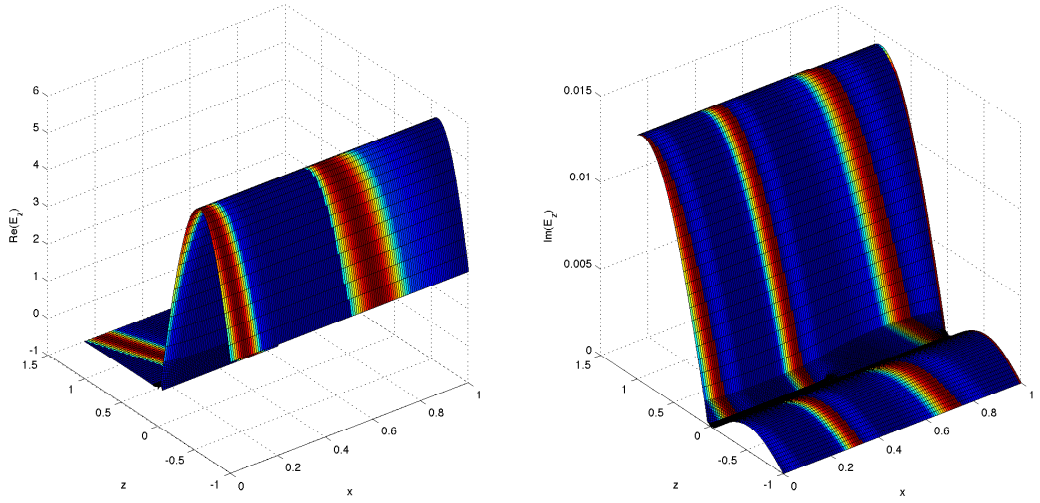

(b)

Figure 7.7: Real and imaginary parts of the electric field components (a) E_x and (b) E_z for a thin film bilayer cell in two dimensional computed numerically [Parameters: κ as defined in Table 6.1, $\varepsilon = 0.1$, $\hat{E}_0 = 1$]

The generation rate is then calculated numerically as described in (7.36), which we then use as a linear approximation to the generation term in the current transport problem. We solve the latter for the EA region only, following our assumption on symmetry on the geometry of the device as we previously did in Part I. The relation

between the current density and voltage for the bilayer thin film cell under illumination is shown in Figure 7.8. Comparing these results to those shown in Figure 4.16 for a cell in the dark, we observe that under illumination the F_n-V curve shift parallel to the V axis as the generation rate increases.

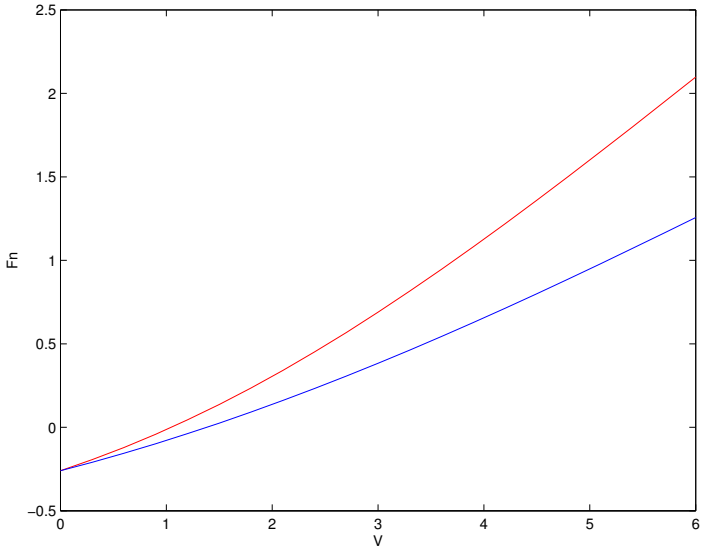

Figure 7.8: The current voltage curve for $\delta = 10^{-2}$ (red curve) and 10^{-4} (blue curve) using the generation rate as calculated via the Helmholtz equation earlier. [Parameters: $\hat{\theta} = 0$, $\mathbf{E_0} = (1, 1)$]

In the following section we present the results for an illuminated cell in the thin dye blobs approximation, which is the final scenario we examine for bilayer cells.

7.2 Thin dye blobs approximation

In this section, we study the generation rate for the "thin dye blobs approximation" as described in Chapter 4, where blobs are positioned in a periodical fashion, so that the blobs' thickness and inter-gap distance is the same. The geometry under consideration is shown schematically in Figure 7.9, where we show the three regions for this case, namely the electron acceptor region Ω_{EA}, the electron donor region Ω_{ED} and the dye region Ω_{dye}. Assuming that each blob of dye has width of ω and an inter-gap width of ω, we show only one block of the repeated structure of the cell.

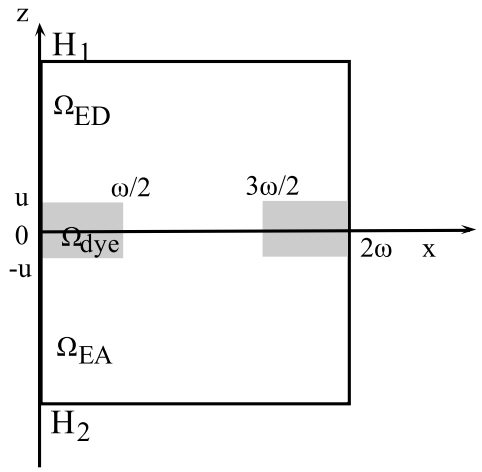

Figure 7.9: A schematic representation of the two dimensional geometrical consideration for the thin dye blob bilayer cell scenario. The dye is represented by the grey region, where $u \ll 1$ and is symmetrical at $x = \omega$.

The thickness of the each blob is small compared to the size of the cell so that $\frac{\omega}{H_1} = \epsilon_\omega \ll 1$ and overall dye coverage of the EA/ED interface is $O(1)$. For this scenario, we solve only for one block of this periodic pattern. The wavelength of maximum absorbance by the Z_{907} dye, is also significantly larger than the thickness of the dye, which is only a few nanometers.

In our analysis we consider only one blob of dye, thus restricting our domain from $0 \leq x \leq L$ to $0 \leq x \leq 2\omega$ and hence use the periodic conditions

$$\hat{\mathbf{E}}(0, z) = \hat{\mathbf{E}}(\omega, z) \tag{7.37}$$

$$\frac{\partial \hat{\mathbf{E}}}{\partial x}(0, z) = \frac{\partial \hat{\mathbf{E}}}{\partial x}(\omega, z), \tag{7.38}$$

on the sides of our domain.

Nondimensionalisation

By applying the rescalings $x = \omega\bar{x}$, $z = H_1\bar{z}$ and $\hat{\mathbf{E}} = E_0\bar{\hat{\mathbf{E}}}$ the problem, by dropping any rescaling notation for the variables, is reduced to

$$\hat{\mathbf{E}}_{xx} + \varepsilon_\omega^2 \hat{\mathbf{E}}_{zz} + \bar{k}_\omega^2(\mathbf{x})\hat{\mathbf{E}} = 0, \tag{7.39}$$

where $\bar{k}_\omega(\mathbf{x}) \sim \omega k(\mathbf{x})$. We estimate that $\bar{k}_\omega = 1 - 10^1$ for the wavelength of interest, but, as in the previous section, we use $\bar{k}_\omega = O(1)$.

The interface boundary conditions are rescaled similarly, so that the differential operator ∇ is replaced with $\bar{\nabla} = \left(\frac{1}{\omega}\frac{\partial}{\partial x}, \frac{1}{H_1}\frac{\partial}{\partial z}\right)$. The z-direction boundary condition for $0 \leq x \leq \frac{1}{2}$ and $\frac{3}{2} \leq x \leq 2$ on $z = 0$ is

$$\hat{\mathbf{E}}_0 = \Re\left\{\mathbf{p}\hat{E}\left\{i\kappa_{EA}H_1\hat{z}\cos\left(\arctan\left(-\varepsilon_\omega\hat{x}\right)\right)\right\}\right\}, \tag{7.40}$$

with $\mathbf{p} = (0,1)^T$. On $z = 1$ we impose the radiation condition, as earlier, namely

$$\frac{\partial\hat{\mathbf{E}}}{\partial\hat{z}} - iH_1k_{ED}\hat{\mathbf{E}} = 0. \tag{7.41}$$

For simplicity of our calculations we let $\hat{E}_0 = 1$ and the initial condition to be light coming in at an angle $\theta = 0$. The generation rate is then calculated as

$$\bar{G} = \Re\left\{i\int_{\hat{\Omega}_{dye}}\hat{\mathbf{E}}\times\left(\hat{\nabla}\times\hat{\mathbf{E}}\right)dA\right\}, \tag{7.42}$$

with $\hat{\Omega}_{dye}$ representing the scaled dye region.

In the next section we present the results from the numerical scheme utilised to solve the non dimensional problem.

Numerical Approximation

For the solution of the problem described by (7.39)-(**??**) we use the numerical technique described in Section 8.1.2, adjusting for the different lengthscales and boundary conditions. We allow for a dye distribution as in Section 4.4.4, where

$$S_d(x) = \begin{cases} 1 & 0 \leq x \leq \frac{1}{2} \\ 0 & \frac{1}{2} < x < \frac{3}{2} \\ 1 & \frac{3}{2} \leq x \leq 2 \end{cases} \tag{7.43}$$

The space between $[0,2]\times[0,1]$ is discretised into a piecewise uniform grid as shown in Figure 7.10. The grid is denser near the ED/EA interface to facilitate a faster convergence of the numerical method to the solution, based on the abrupt changes of

material characteristics there. We allow the dye layer to have finite thickness much smaller than ω.

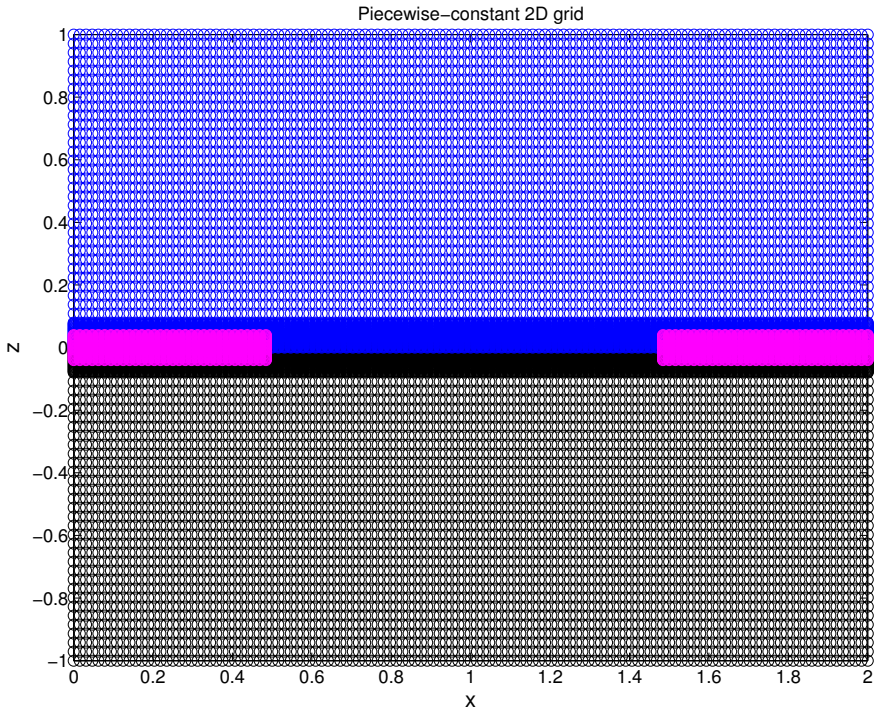

Figure 7.10: The piecewise uniform grid for the rescaled space $[0, 2] \times [-1, 1]$, for one block of periodically distributed dye on the interface for a bilayer cell. The grid is colour coded to differentiate between the three regions: (i) the electron acceptor region is shown with black nodes, (ii) the electron donor region is shown with blue nodes and (iii) the dye region is shown with magenta nodes. We have used a piecewise grid, where we have a denser grid near the interfaces.

In Figure 7.11 we show the refractive index, $\kappa(\mathbf{x})$, in the space of interest and as defined in Table 6.1.

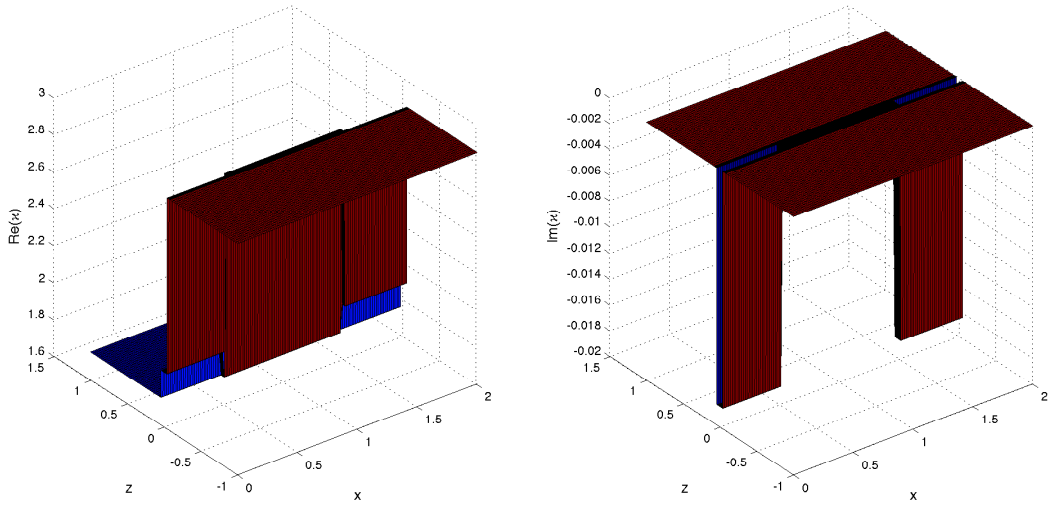

Figure 7.11: Real and imaginary parts of the refractive index for the various materials in the domain of interest. The extinction coefficient of the electron donor and acceptor are small compared to that of the dye.

This assumption is used as an input to the Helmholtz equation for the calculation of the electric field. The electric filed of the electromagnetic wave propagating through the device is shown in Figure 7.12, in a breakdown of its spatial components, $\hat{E}_x$ and $\hat{E}_z$. In the results presented here we use $\varepsilon_\omega = 0.1$, showing the change of both amplitude and periodicity of the wave in each of the electron acceptor, donor and dye regions. The periodicity of the electric field is approximately $\frac{2\pi}{\omega k_i}$ in each region i, away from the interface $z = 0$, as shown in Figure 7.12. Along the interface, we observe an $O(1)$ oscillation in the x direction[2]. The periodicity in x can be seen as $x \to 0$, so that all terms in (7.10) balance. The wavelength of the electric field in the x-direction, along $z = 0$, depends on the size of ε_ω. As $\varepsilon \to 0$, the wavelength is smaller.

[2]In order to see this, we may use the method of *separation of variables*, i.e. by writing $E_m(z,x) = Z(z)X(x)$, for $m = 1, 2$ indicating the spatial components of the electric field in z and x, to solve (7.10). The general solution would then be

$$E_m(z,x) = \sum_{q=1}^{\infty} \left(A_q e^{qz} + B_q e^{-qz}\right) \left(C_q \sin \sqrt{q^2 + \left(\frac{k_\omega}{\varepsilon_\omega}\right)^2}\, x + D_q \cos \sqrt{q^2 + \left(\frac{k_\omega}{\varepsilon_\omega}\right)^2}\, x\right), \qquad (7.44)$$

for arbitrary constants A_q, B_q, C_q and D_q.

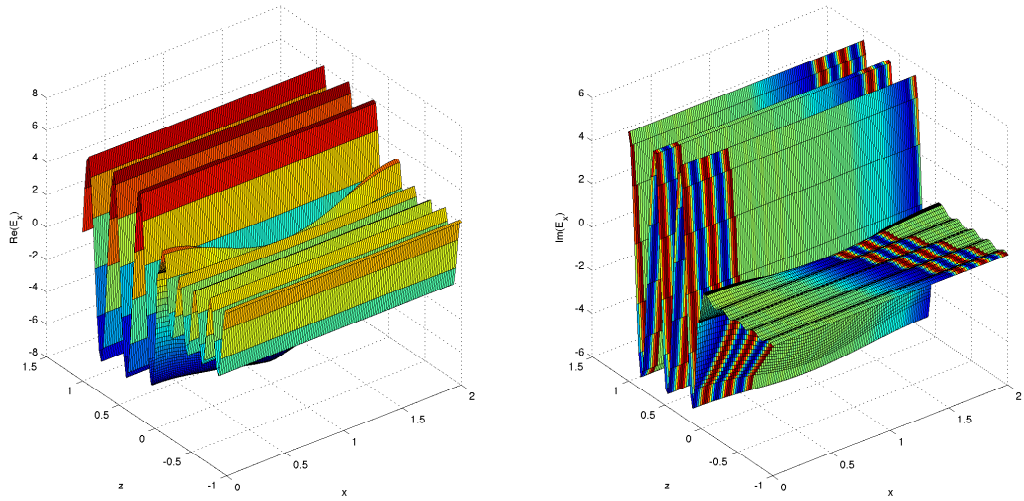

(a)

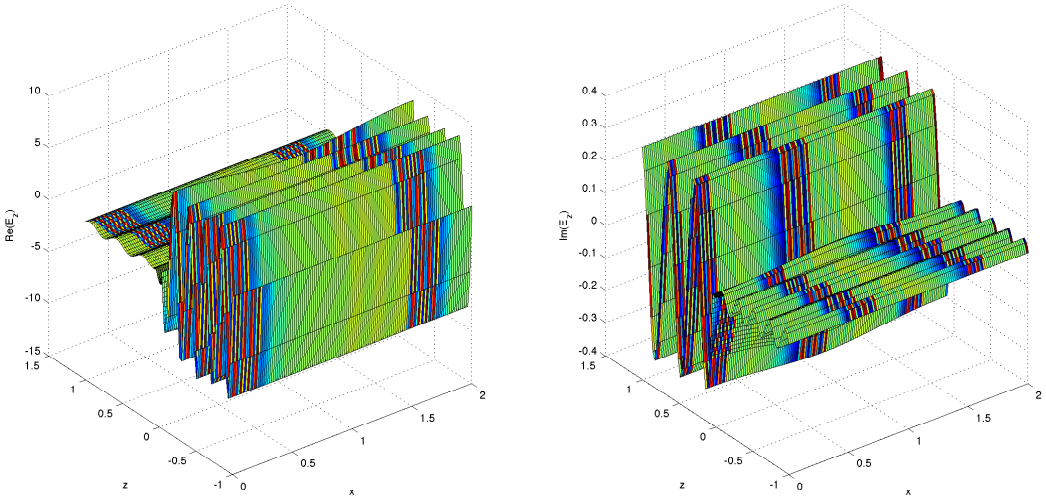

(b)

Figure 7.12: Real and imaginary parts of the electric field components (a) E_x and (b) E_z for a thin blob bilayer cell in two dimensional computed numerically. [Parameters: κ is defined in Table **??**, $L = 1$, $\omega = 1$, $\hat{E}_0 = 1$, $\epsilon_\omega = 0.1$]

The electric field is then used to calculate the generation rate in the dye region using a point-wise approximation on equation (7.36). The numerically approximated numerical solution, is then used as an input to the generation rate into the current-transport model derived in Section 4.4.4 to find the qualitative behaviour of the cell under illumination. The current density-voltage curves for a cell with thin blobs is

shown in Figure 7.13. Under illumination the $F_n - V$ curve shift parallel to the V axis as the generation rate increases, when one compares to Figure 4.19.

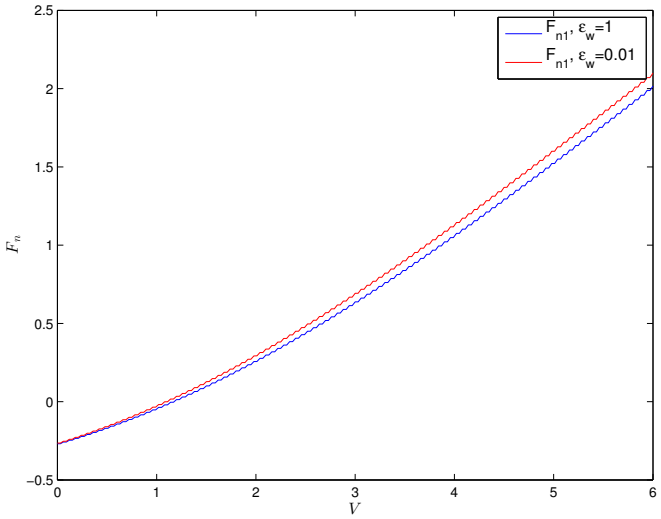

Figure 7.13: The current voltage curve for $\epsilon_\omega = 0.01$ (red curve) and $\epsilon_\omega = 1$ (blue curve), where $\epsilon_\omega = \frac{\omega}{H_1}$. The numerical solution for the generation rate is calculated using equation (7.42). [Parameters: $\hat{\theta} = 0$, $G_0 = 1$, $\delta = 1$]

7.3 Summary

In this Chapter we have shown how a light absorption model can be used to calculate the current generation function for a bilayer cell under illumination. In particular, we have considered the two cases:
(i) thin film approximation with $\epsilon = \frac{H_1}{L} \ll 1$, and
(ii) thin dye blob approximation, with $\epsilon_\omega = \frac{\omega}{H_1} \ll 1$.

The mathematical problem for the generation rate was solved in both cases under the assumption of symmetry and spatial variability of the optical properties of the materials. In both cases, we were able to calculate the electric field across all regions, i.e. EA, ED and dye, following an oscillatory path with periodicity depending on the wavenumber k_i. We further were able to calculate the generation rate along the interface, $z = 0$, by numerically integrating the Poynting vector in the dye.

We have integrated the light absorption and the current transport models to present

the current density-voltage curves for the cell under illumination. The curve is shown to shift, as anticipated, to allow for the increase in generation rate.

In the following Chapter, we will apply the light absorption problem to a nonplanar interfacial morphology as in Chapter 5, where we examine a specific scenario of dye distribution.

8

The nanostructured cell

In this Chapter, we examine the effects of the interfacial geometry for a nanostructured cell. In particular, we revisit the case of a cell with a structured interface with nano-pillars of electron acceptor stemming into the electron donor, as shown in Figure 3.1(c). We will examine only the special scenario, where the walls of the stems are covered with dye only. This choice is made in order to limit the geometrical complexities involved in obtaining a solution. We will employ numerical techniques to find the generation rate along the interface and then solve for the distribution of the electrostatic potential, ϕ, and the electron and hole densities, n and p, respectively, and generate the current density-voltage characteristics.

8.1 Geometrical simplification

For comparability reasons, we retain the morphology set out in Chapter 5 and replicated in Figure 8.1 with the addition of the dye layers under consideration. For the purposes of our analysis, we will consider only one nanostem, as earlier. We will let the dye layer cover the walls of the electron acceptor stems and have a width of $2u$,

with $\frac{2u}{\omega} \ll 1$. We define the domains Ω_a, Ω_d and Ω_{dye} as the domains of the electron acceptor, donor and the dye, respectively (see Figure 8.1). We will define the following interfaces:

- $(\partial\Omega_a/\partial\Omega_d)_a$ as the acceptor/donor interface along $z = a$ and between $0 \leq x \leq c - u$ and $d + u \leq x \leq \omega$
- $(\partial\Omega_a/\partial\Omega_d)_b$ as the acceptor/donor interface along $z = b$ and between $c + u \leq x \leq d - u$
- $(\partial\Omega_{dye}/\partial\Omega_d)_c$ as the dye/donor interface along $x = c - u$ and between $a \leq z \leq b$
- $(\partial\Omega_a/\partial\Omega_{dye})_c$ as the acceptor/dye interface along $x = c + u$ and between $a \leq z \leq b$
- $(\partial\Omega_a/\partial\Omega_{dye})_d$ as the acceptor/dye interface along $x = d - u$ and between $a \leq z \leq b$
- $(\partial\Omega_{dye}/\partial\Omega_d)_d$ as the dye/donor interface along $x = d+u$ and between $a \leq z \leq b$.

We take $a = c = \frac{\omega}{4}$ and $b = d = \frac{3\omega}{4}$ for geometrical symmetry, unless otherwise stated.

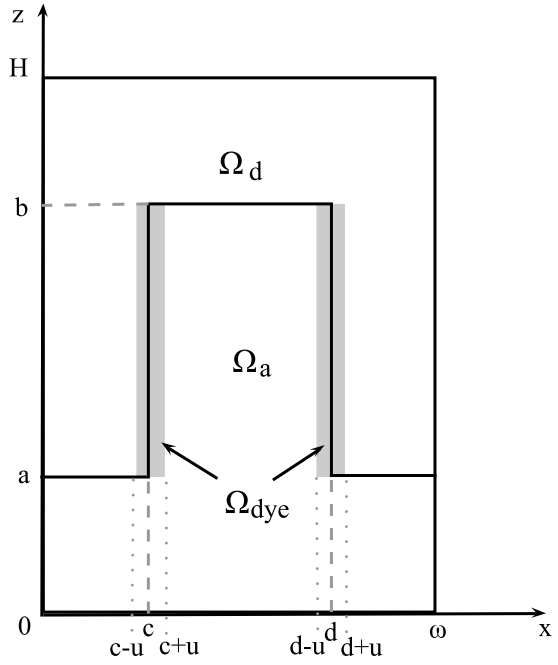

Figure 8.1: A block of the repeated pattern for the nanostructured mixed layer with dye covering the walls of the nano-stem, parallel to the z-axis. Note: Figure is not drawn to scale.

8.1.1 Nondimensionalisation

Following the geometrical simplifications, the next step is to reduce the problem (6.53)-(6.61) by rescaling the spatial and other variables. We use the same scaling as in Chapter 5 and reduce to the same non-dimensional parameters, with the introduction of $\hat{u} = \frac{u}{\omega} \ll 1$, as we consider the dye layer to be significantly thinner than the width of the nanostem. The problem then reduces to

$$\hat{\mathbf{E}}_{\hat{x}\hat{x}} + \varepsilon_\omega^2 \hat{\mathbf{E}}_{\hat{z}\hat{z}} + \hat{k}_{\omega i}^2 \hat{\mathbf{E}} = 0, \tag{8.1}$$

with $\varepsilon_\omega = \frac{\omega}{H}$ and $\hat{k}_{\omega i}^2(\hat{x}, \hat{z}) = H^2 k_i^2$ for each homogeneous region i. The rescaled domains are represented by Ω_a, Ω_d and Ω_{dye} for the EA, ED and dye regions. The interface conditions along the interfaces are reduced to

$$[\epsilon(\mathbf{x})\hat{\mathbf{E}} \cdot \hat{\mathbf{n}}] = 0 \tag{8.2}$$

$$\left[\hat{\mathbf{n}} \times \left(\frac{1}{\mu(\mathbf{x})}\hat{\nabla} \times \hat{\mathbf{E}}\right)\right] = \frac{4i\nu\pi}{c^2}\sigma(\mathbf{x})\hat{\mathbf{E}}_s, \tag{8.3}$$

$$\left[\hat{\mathbf{n}} \cdot \left(\hat{\nabla} \times \hat{\mathbf{E}}\right)\right] = 0 \tag{8.4}$$

$$\left[\hat{\mathbf{n}} \times \hat{\mathbf{E}}\right] = 0. \tag{8.5}$$

Here, we assume a uniform incident wave incident wave at the air/EA interface[1] $z = 0$ given by

$$\hat{\mathbf{E}}_0(0, \hat{x}) = \Re\left\{\mathbf{p}\hat{E}_0\right\}. \tag{8.6}$$

The electrical field of the electromagnetic (EM) radiation should satisfy

$$(\hat{n} \cdot \hat{\nabla})\hat{\mathbf{E}} - ik(\hat{x})\hat{\mathbf{E}} = 0 \tag{8.7}$$

on the surfaces $x = 0$, $x = 1$ and $z = 1$.

The generation rate can then be calculated using

$$\hat{G} = \Re\left\{i\int_{\hat{\Omega}_{dye}} \hat{\mathbf{E}}^* \times \left(\hat{\nabla} \times \hat{\mathbf{E}}\right)\right\}. \tag{8.8}$$

[1]Note that we have used a different domain for this Chapter so that $0 \leq z \leq 1$, instead of $-1 \leq z \leq 1$.

In the next section we present numerical results for the problem (8.1)-(8.7).

8.1.2 Numerical approximation

Possibly the most challenging part of this chapter is determining the fitting dye coverage along the interface of the dye. In order to simplify the numerical solution we have decided to produce results only for the case where the sides of the stems are fully covered, as shown in Figure **??**.

This choice is made in order to show the variation in the generation rate from the base of the stem to its end. We consider the interface between the stems to be dye-free to facilitate our assumption that the dye does not cover the complete surface and also to stress the difficulty of the dye to reach the far most inner part of the cell during its deposition stage. Thus,

$$S_d(\hat{\mathbf{x}}) = \begin{cases} 1 & \hat{\Omega}_{dye} \\ 0 & \hat{\Omega}_a \quad \text{and} \quad \hat{\Omega}_d, \end{cases} \tag{8.9}$$

with a defined as in Figure 5.1.

The space between $\hat{x} \in [0,1]$ and $\hat{z} \in [0,1]$ is discretised into a piecewise uniform grid as shown in Figure 8.2. We use the same colour coding as in Chapter 8 and note that densely packed nodes indicated a finer grid near the interfaces to facilitate the numerical calculations near the jumps. The problem (8.1)-(8.7) is solved numerically using the centred finite differences method.

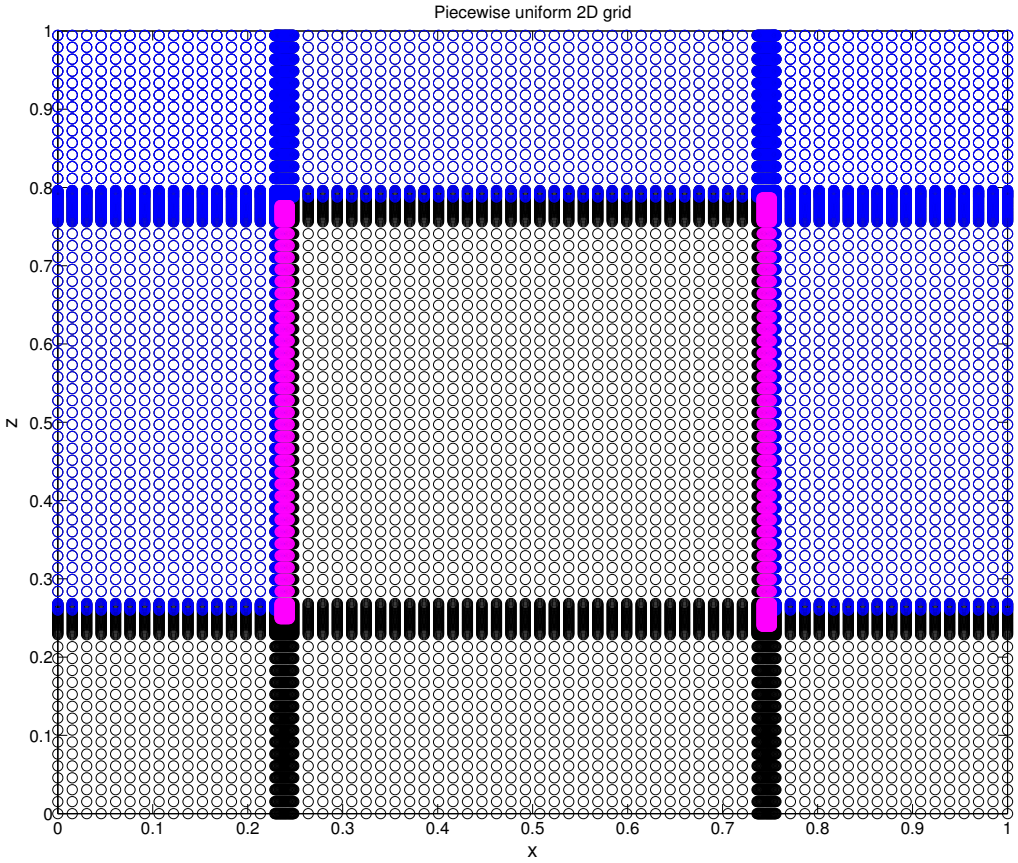

Figure 8.2: The piecewise uniform grid for the rescaled space $[0,1] \times [0,1]$, for one block of periodically positioned nanostems and dye covering only the walls of the nanostems parallel to the z-axis. The grid is colour coded to discriminate into the three regions: (i) the EA region is shown in black nodes, (ii) the ED region is shown with blue nodes and (iii) the dye region is shown with magenta nodes. We have used a piecewise uniform grid, where we have a denser grid near the ED/EA and ED/dye/EA interfaces, as illustrated by the denser nodes. Here, $a,\ c = 0.25$ and $b,\ d = 0.75$.

In Figure 8.3 we show the refractive index, $\kappa(x)$, in the full domain, as laid out in Table 6.1.

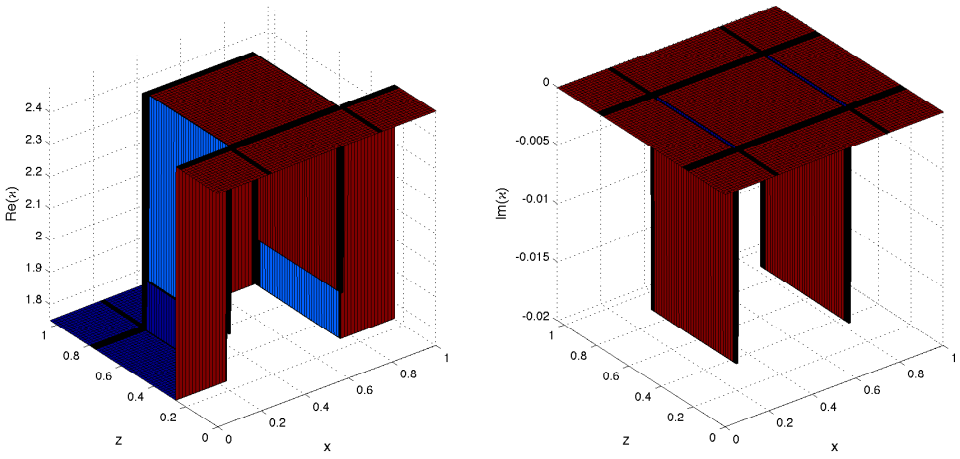

Figure 8.3: Real and imaginary parts of the refractive index, κ, for the nanostructured cell, as defined in Table 6.1. The extinction coefficient of the donor and acceptor are small compared to that of the dye.

$\kappa(\mathbf{x})$ is used as an input to Helmholtz equation for the calculation of the electric field. The electric field of the EM wave is shown in terms of its spatial components in Figure 8.4.

The electric field of EM radiation has a wave-like behaviour, as demonstrated in Figure 8.4. Unlike in previous scenario investigated, here the asymmetry of the problem is becoming more evident due to refraction and absorption in the dyed walls of the nanostem. The generation rate is approximated by the change in the solar irradiance in the dye region which is distributed along the walls, as shown in Figure **??**.

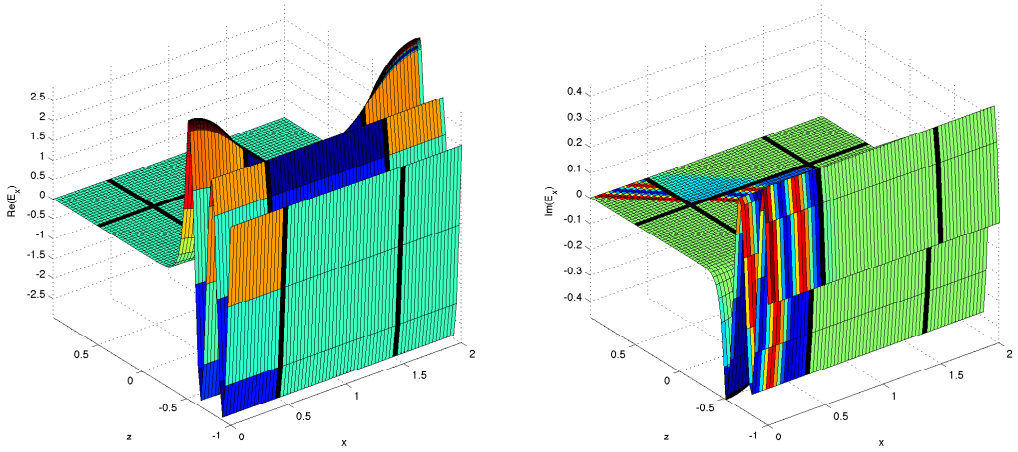

(a)

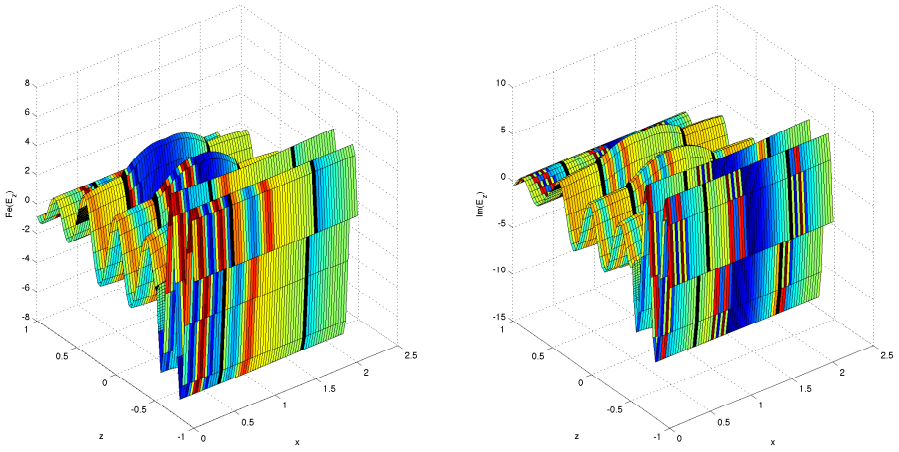

(b)

Figure 8.4: Real and imaginary parts of the electric field components (a) E_x and (b) E_z for a nanostructured cell in two dimensional computed numerically.

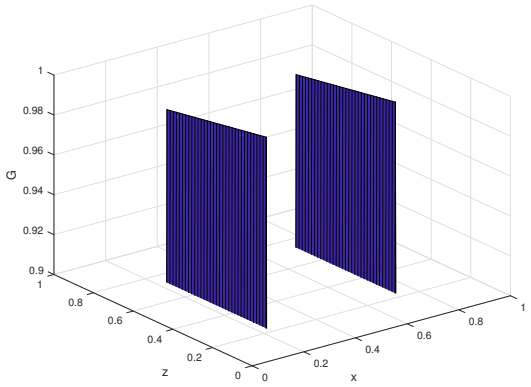

Figure 8.5: The generation rate approximated numerically for a nanostructured ssDSSC.

In Figure 8.6 we show the electric potential, electron and hole distributions, while in Figure 8.7 we present the current density-voltage curve for an illuminated cell. These graphs were generated using the numerical scheme for current transport in a nanostructured cell. Similarly to the previous Chapter, the cell generates current at zero voltage when illuminated.

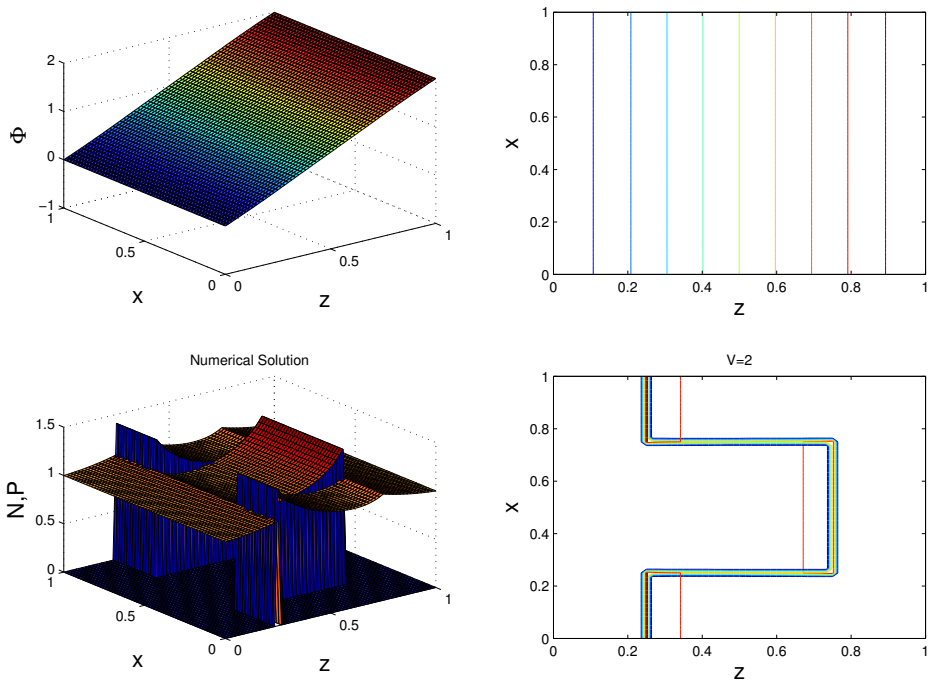

Figure 8.6: The profiles of Φ, N and P for $\epsilon_\omega = 10^{-2}$. [Parameters: $\delta = 0.01, V = 2, \Lambda = 1$]

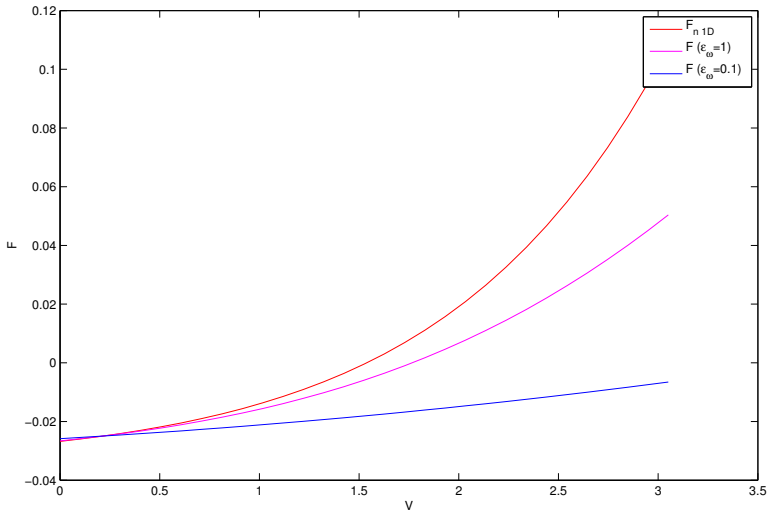

Figure 8.7: The current density-voltage curves as simulated numerically for decreasing value of the aspect ratio $\epsilon_\omega = 1,\ .1,\ 0.01$ for a nanostructured cell. [Parameters: $\delta = 10^{-2},\ \Lambda = 1$]

8.2 Summary

In this Chapter we have shown how the light absorption model applies to a nanostructured cell and how the current generated is transported to the outer electrodes of the device. The current density-voltage curves follow the theory, as at zero voltage the solar cell appears to generate current. The electric field is found to be oscillatory in both spatial directions, as predicted by the electromagnetic theory of light travelling a medium. The generation rate is calculated along the walls of the stem, where the dye lies in a very layer of very small thickness. Using the results from the current generation problem, we used it as an input to the current transport model from Part I.

While the model here is shown to agree qualitatively to the actual problem, one could use the exact parameters to a physical problem to extract more precise estimations to the size of the current generated. One could also remove the assumption of the wavefront of light reaching the surface of the cell perpendicularly, and examine the effect of restrictive light reaching the stems' walls due to shadows from neighbouring stems. This topic would be of interest for optimisation purposes of these devices.

In Part II, we have demonstrated in full numerical extend how light is absorbed in

each of the three scenario we have selected to examine in this thesis and how current is then generated. The results are in accordance with other types of solar cells.

9

Conclusions

In this thesis we have developed a model for an idealised dye-sensitised solar cell. Our aim was to explain the main principles of operation of a solar cell and to understand how each mechanism through a mathematical model. The main focus and novelty of this project lies in explicitly combining the current generation in the dye layer with the transport of current in the EA and ED layers, in the particular case of ssDSSCs. The most important result of the thesis is the thorough description of the current density-voltage characteristic curve, which characterises the response of the ssDSSC given an applied voltage and illumination. The current density-voltage relation for solar cells is useful in examining their efficiency and, therefore, optimising their performance through better manufacturing processes and materials with favorable and enhanced electrochemical properties.

9.1 Summary

Firstly, we described an ssDSSC consisting of an EA region and an ED region, with light-absorbing dye partially covering the interface between the EA and the ED. The

cell generates current through the absorption of photons by the dye molecules, generating excitons. These, later, dissociate as they reach the EA and ED interfaces, due to the electrochemical properties of these materials. The 'free' electrons in the EA region and the 'free' holes in the ED region are transported through a drift-diffusion mechanism to the electrodes. We built two mathematical models to describe: (i) the behavior of the ssDSSC in the dark, when, under the application of biasm current is transported, and (ii) the behavior of the ssDSSC under illumination, when photons are absorbed to generate current. The thesis was structured in two Parts to allow for a more concise and focused analysis of each of the two models.

In our analysis we have assumed that the incident photons reach the surface of the EA perpendicularly, in order to avoid shadowing effects and that the ssDSSC operates in thermodynamic equilibrium and at steady-state conditions. Other assumptions made include limitations on the voltage range examined by not considering the extreme values, which lead to breakdowns of the diode-like current-voltage relation. The removal of these assumptions is not considered to change the qualitative behaviour of an ssDSSC.

In Part I, for the current transport problem, we have assumed that the dye layer is significantly thinner than the thickness of the EA and ED regions, allowing us to write down a model for current transport only in the EA and ED regions. We have assumed that 'free? electrons exist only in the EA and 'free? holes in the ED, as these enter the respective regions from the dye, which is the only region in the cell assumed to generate excitons. We set up a model where the electric current density is driven by drift and diffusion of the 'free? electrons and holes. At the interface between the EA and ED, there either exists a thin layer of dye, or there is direct contact between the EA and ED. At the direct EA/ED contact, electrons and holes recombine, minimising the efficiency of the cell. We assume that the cell is covered with glass at its outermost surfaces, thus restricting the transport of any charge carriers outside of cell.

We have shown that the solution to the charge transport problem for a cell operating in the dark, results in a diode-like behaviour of the cell, i.e. that it allows for the transport of electrical current in one direction, but not the other. We have solved the problem in the special case where the cell is symmetric across the interface both geometrically and in terms of the physical properties of the EA and ED regions, in one dimension. We first nondimensionalised in order to give rise to the key dimen-

sionless parameters. The small parameter of the problem, δ, is the coefficient of the recombination term. We were able to compute an exact analytical solution to the one dimensional model and, also, an asymptotic solution as δ would become very small. We have shown that an ssDSSC has a diode-like relation between the current density and the applied voltage. As $\delta \to 0$, we have shown that as the voltage is very small, drift and diffusion counterbalance each other, allowing for the charge carriers to have in a quasi-equilibrium status; while, as the applied voltage increases, drift dominates, leading to the current density to be linearly related to the applied voltage.

In the one-dimensional case, which we visiter first, we have considered the effect of the various parameters in the problem, such as the dielectric constant and the diffusivity, which are both physical properties of materials, by removing the relevant symmetry assumptions. We have shown that a lower dielectric constant in the ED region (in comparison to the EA) results in a higher built-up of electric field near the EA/ED interface in the ED region, and hence a larger concentration of holes. Similarly, we have examined the effect of a higher diffusivity in the ED region (than in the EA), which results in a larger electric field in the EA, as drift in the ED region is lower. It was verified that the behaviour of the ssDSSC can be qualitatively predicted, through a comparison with available experimental data.

We, then, applied the current transport model to the following two-dimensional scenarios: (i) a thin film with a bilayer interface, with half of the interface covered with dye, (ii) a thin film with a bilayer interface with a periodic dye distribution pattern of small blobs, and (iii) a thin film with a periodic interface of nanostems of small width. In these scenarios, we considered that no electron-hole recombination takes place between the EA and ED regions is allowed through the dye. Each scenario allowed us to test the efficiency of the model through the calculation of the current density response in the application of bias. We nondimensionalised the models in each case, and explored the size of the dimensionless parameters to reduce the models to a one-dimensional version where possible, which we solved analytically under the aforementioned assumptions. We used the solutions to generate current density - voltage curves, which indicated that the cell under forward bias behaves as a diode, i.e. the current density increases exponentially for small voltage, while increasing linearly as voltage increases beyond the threshold value of the order of $\log(\delta^{-1})$. Under negative bias, current saturates at a value proportional to δ, i.e. the recombination coefficient.

For case (i), i.e. the bilayer thin film with the dye covering the EA/ED interface half the way through, we were able to approximate the current density (F_n) - voltage (V) relation by a one-dimensional effective relation. We have rescaled the thin film problem with the lengthscales of the device, i.e. we have scaled z and x with H_1 and L, respectively. As the aspect ratio, $\varepsilon = \frac{H_1}{L}$, is small, we have shown that the current density can be approximated by the sum of the averages in the two regions (the dye covered, $x < \omega$, and the dye-free region, $x > \omega$) of the interface, i.e.

$$F_n \approx F_{n\ eff} = -\delta(1-S)\left(n_0^2|_{x>\omega} - 1\right), \tag{9.1}$$

where S is the portion of the EA/ED interface that is covered with dye and n_0 is the leading-order approximation to the distribution of electrons .

For case (ii), i.e. the bilayer thin film with a periodic thin dye blob distribution, we have assumed that each dye blob covers a length of ω along the EA/ED interface, while the gap between the blobs is of the same size ω. This time, we have rescaled x with the lengthscale of one dye blob and surrounding region, i.e. 2ω, while z was rescaled with H_1. As the aspect ratio, $\varepsilon_\omega = \frac{\omega}{H_1}$, is small, we were able to approximate the two-dimensional solution, we have shown that the current density can be approximated by the average of the current along the interface, i.e.

$$F_n \approx -\delta(1-S)(n_0^2 - 1), \tag{9.2}$$

with n_0 being the leading-order solution away from the interface. The effect of the dye distribution is found to be significant only in a small layer near the interface with width of the order of ε_ω.

For case (iii), we considered a thin film with a structured interface with periodically positioned nano pillars of EA material stemming into the ED. We have solved the corresponding model both analytically and numerically. The F_n-V curve follows the diode-like relation, similarly to the aforementioned cases. We have primarily considered only an idealised case where physical properties of the device are of the same size in the EA and ED region. We have, further, examined the effect of the Debye length, i.e. the screening length of the electric field, by varying Λ (which is proportional to the square of the Debye length), and the dielectric constants ratio, by varying $\hat{\epsilon}_p = \frac{\epsilon_p}{\epsilon_n}$. We have shown that as Λ increases or $\hat{\epsilon}_p$ increases, the result was a higher electric field near the interface, indicated by the higher concentration of

charge carriers near the interface.

In Part II, we derived a mathematical model for light absorption for a partially absorbing device. In particular, we have considered that only the dye absorbs photons and we have assumed a monochromatic light source. This is reflected in the use of the refractive index, κ; if the complex part of κ is non-zero the material is absorbing. We have taken that the generation rate, G, of excitons (we have assumed that all excitons produce one electron which enters the EA region and one hole that enters the ED region) in the dye relates to the change in the photon density in the dye layer. The mathematical model consisted of Maxwell equations for an electromagnetic wave in a semiconducting medium. At the interface between the materials, we have assumed that in the tangential direction of the interface, the electric field, $\mathbf{E}$, is continuous and the jump in the magnetising field, $\mathbf{H}$ equals the surface current. In the normal direction of the interface, we have imposed that the jump in the displacement field, $\mathbf{D}$, equals the surface charge density (which we have assumed to be zero), and that the magnetic field, $\mathbf{B}$, is continuous. We have imposed time-harmonic solutions of the form $\mathbf{E} = \hat{\mathbf{E}}(x)\exp(-i\nu t)$, with ν being the frequency of light. This substitution has reduced the problem to a Helmholtz equation for the electric field, with the wavenumber satisfying $k^2 = \left(\frac{\nu}{c}\kappa\right)^2$. Further, we assumed that photons reach the device perpendicularly from the EA surface and that no photons exit the device from any of the other surfaces. We have manipulated the equations in order to solve for the electric field only, while noting that we can use the relation $\hat{\mathbf{H}} = -\frac{i}{\mu\nu}\nabla \times \hat{\mathbf{E}}$ to find the magnetic field. For the purposes of this analysis, we have allowed the dye region to have a relatively small, but noticeable, thickness, in order to allow for our numerical calculations and solve the model in one- and two-dimensional spaces.

In the one-dimensional case, we have assumed a dye layer of thickness $2u$, centred at the interface ($z = 0$) and rescaled z with the lengthscale of the device H_1 and the electric field by the magnitude of the electric field of the incoming electromagnetic wave. For this case, we computed an analytical solution valid throughout the whole device, showing the oscillatory behaviour of the electric field, with periodicity being inversely proportional to the wavenumber in each material (hence the refractive index). The generation rate was then calculated as the change in light intensity across the dye, i.e. in $-u \leq z \leq u$, giving

$$G \sim \cos\frac{2u}{\nu}\Im(\kappa_{dye}). \tag{9.3}$$

We, then, used the calculated generation rate as an input to the current transport problem from Part I, and examined the impact on the current density-voltage curves. It was shown that current is generated in an ssDSSC under illumination while $V = 0$, as expected by all solar cells.

The mathematical model was then applied to the cases (i)-(iii) visited in Part I, as mentioned earlier. For the bilayer thin films, i.e. cases (i) and (ii), we showed that the generation rate can be approximated by a constant along the interface as the respective aspect ratio becomes small. For the nanostructured cell, i.e. case (iii), the generation rate varies primarily in the z direction only, as the aspect ratio, ε_ω, becomes small. For all cases, current was generated under illumination without the application of bias and the $F_n \sim G$ as $V = 0$.

In concluding the thesis, we believe that the mathematical models derived in this thesis are useful in predicting the behaviour of an ssDSSC and the generated current, given the applied voltage and/or the illumination conditions.

9.2 Future Development

While this thesis is aimed at understanding the mechanisms behind the operation of ssDSSCs, there remains room for further enhancement of the models and the corresponding analysis. It would be worth considering removing the steady-state and thermodynamic equilibrium assumptions, if one is interested in studying the stability of the cells.

We believe that greater interest on the understanding of the operation of the solar cell can be found in varying the parameters already in the model relating to the morphology and the electrochemical properties of the materials. Probably the greatest simplifications that have been made are on the geometry of the cell and on the molecular structure of the materials involved. We have assumed a planar or highly structured EA/ED interface by completely removing the mesoporous EA layer or by organising it into nanostems. Also, we have neglected any impurities of the EA and ED materials and only modelled simple band structures similar to that of silicon, where the energy bands are separated according to the Fermi-Dirac statistics [22]. It is believed that additional energy states would introduce a trapping mechanism which

could be key to describing the behaviour of the system. Depending on whether these states assist in exciton generation in the bulk of the material or limit/enhance the transport of free charges, there are different ways this can be described mathematically. It would also be interesting to identify any electric-field-dependent parameters in our problem, such as the mobility of charges, and incorporate them in the model appropriately.

In real devices, e.g. those described in [78] and [33], additives are introduced into the ED material (as discussed in Chapter 2). In these studies, it has been suggested that the addition of lithium salts does not dope the ED and that it increases the overall efficiency of the device by reducing the recombination rate. It is possible to achieve up to one order of magnitude decrease in recombination time when lithium is increased ten times in concentration [78]. This could be introduced into the model through a refined description of the recombination rate.

The efficiency of the cell may be limited by several mechanisms, not all of which were taken into consideration in our modelling assumptions. Possible loss mechanisms not considered include: photon absorption or scattering by the ED, the anti-reflective glass coating or the cathode design, reducing current generation by the dye. Also, photons of high energy (i.e. of low wavelengths) may be absorbed by the ED generating Frenkel excitons which could, under the appropriate conditions (good mobility and diffusion length) generate additional free charge carriers. It might, also, be the case that the photons are scattered by the cathode or glass coating reducing the intensity of light that reaches the dye.

The assumption on photons reahing the EA surface perpendicularly is a simple way of understanding light absorption by the cell, but it might not be realistic. We see another potential limitation to the generation of current stemming from light hitting the cell at an angle, especially for the case of a cell with a nanostem interface structure, which could restrict the light reaching the end of the nanostems. This could be an optimisation problem.

This is not an exhaustive list of suggested developments of the model presented. As technology keeps evolving, the results in this thesis could help in the understanding of the operation of solar cells and the further enhancement of the cell's configuration.

Part III

Supplementary Material

Appendix I - for Chapter 4

In this appendix we present the numerical scheme used in Section 4.2 to solve (4.13)-(4.12) subject to the boundary condition (4.14) and for the concentration of holes and the electrostatic potential in the ED region, using (4.17)-(4.16) subject to the boundary condition (4.18). These two problems are coupled together at the interface via (4.15), (4.19) and (4.20).

The Numerical Scheme

The numerical technique used is based on the *shooting method* [79]. In particular, we shoot from the EA/electrode contact and aim to satisfy the ED/electrode contact condition on p as given in (4.18). The input parameters are the ratios of diffusion coefficients and dielectric constants, the generation and recombination rates at the interface and the flux. We get V as the output. The code can be summarised in the following steps:

Step 1. We introduce the shooting parameter s such that

$$\frac{d\phi}{dz} = s, \quad \text{at} \quad z = -1. \tag{I.1}$$

Then, given F_n, we solve[1] the EA problem (4.13)-(4.12), subject to the initial conditions for ϕ, ϕ_{zz} as given in (4.14).

Step 2. We use the values of n, ϕ and $\frac{d\phi}{dz}$ at $z = 0^-$ obtained from Step 1 together with the interfacial conditions (4.14) and (4.20) to get ϕ, ϕ_z and p at $z = 0^+$ and (4.17) to get F_p.

[1] We use the method of finite difference.

Step 3. We use the values for ϕ, $\frac{d\phi}{dz}$, p and F_p at $z = 0^+$ found in Step 2 to initiate the solver for the ED problem (4.17)-(4.16).
Step 4. We get the value that was calculated for p at $z = m$ and compare it with $\hat{P}^+$. If the two agree with good accuracy then we stop. If not, we return to Step 1 with an update on the choice of s. For faster convergence we use the *interval bisection method*, by denoting the values for s on each side of the sought value with s_{left} and s_{right} in each iteration. The stopping criterion is

$$|s_{left} - s_{right}| \leq tol, \tag{I.2}$$

where we set the tolerance level to $tol = 10^{-14}$.

If our aim is to obtain the distribution of ϕ, E, n and p for a particular value of F_n, we stop here. If we want to compute the current density-voltage characteristic curve we employ a *bootstrap method* as explained in the final step below.

Step 5. Once the optimal value for s, s_0, is found for a given F_n, we use s_0 as a starting point for the next (nearest) value of F_n and go through steps 1-4 again. We continue to obtain the corresponding range of V for the required domain of F_n.

Verification

To test the tolerance level for the bisection formula as explained in Step 4 above, we let the initial s_{left} and s_{right} in the bisection formula be (for example) -5 and 5, respectively, and update one of the two after each iteration according to the bisection method. When the value of $|s_{left} - s_{right}|$ falls below the tolerance level, tol, we end the iteration. In Figure III, we show the number of steps taken to converge to a value for s that satisfies the tolerance condition (I.2); the number of steps increase as the tolerance level decreases. In Figure **??** we show how a lower tolerance level helps converge to the correct solution for a given value of F_n; in particular, we show that V converges to zero for a very low tolerance level.

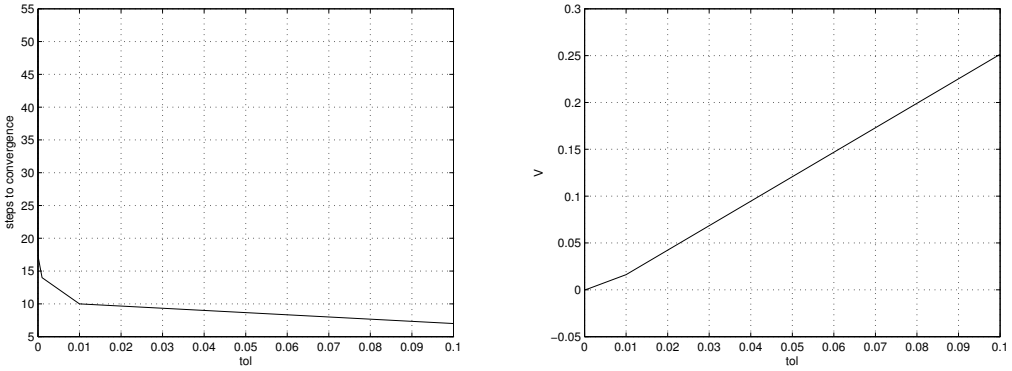

(a) (b)

Figure I.1: (a) Shows the number of steps taken for convergence to the optimal value for s using a bisection formula against the pre-defined tolerance level. (b) Shows the resulting value for V obtained when $J = 0$ against the tolerance applied. {Parameters: $\delta = 10^{-4}$, $\hat{\epsilon}_p = 1$, $\hat{D}_p = 1$, $S = 0.15$, $\Lambda = 1$, $m = 1$, $V_{bi} = 0$, $G = 0$, starting values: $s_{left} = -5$, $s_{right} = 5$}

Appendix II - for Chapter 4

The contents of this appendix are relevant to Section 4.3 and we include a detailed description of the numerical scheme used for solving the bilayer problem.

Numerical Scheme: the thin film approximation

In this section we explain the numerical scheme used to solve the non-dimensional problem given by (4.135)-(4.147) with a dye interface as shown in Figure II.1. The scheme is based on a second order centred finite differences method. The dependent variables are written in vector form and the numerical solution for ϕ and n, expressed as Φ and N, is found by solving two vector systems with nonlinear matrix coefficients. The system is solved iteratively using a simple Jacobi iteration until a certain tolerance is reached. We allow the user to input the values of the various parameters of the problem, namely ε, $\hat{\omega}$, $\hat{g}$, N_b, δ, Λ, $\hat{G}$, $\hat{\epsilon}_p$, $\hat{N}^-$ and $\hat{P}^+$.

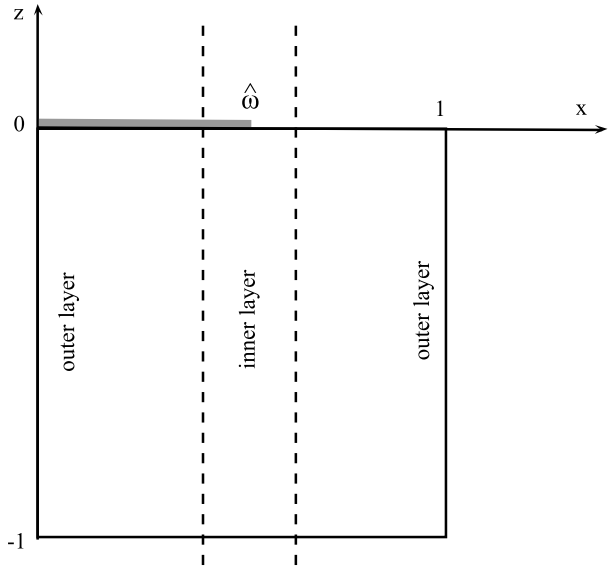

Figure II.1: The (scaled) domain of interest with $\varepsilon \ll 1$ and $\hat{\omega} = O(1)$. The grey blob represents the dye, where $S_d = 1$.

The Grid

The domain for the electron acceptor region is $\{-1 < z < 0, 0 < x < 1\}$. To apply the finite difference scheme we discretise the domain into a uniform grid of J equal steps of width $h = \frac{1}{J}$ as shown in Figure II.2. The problem is solved on the numerical nodes (z_j, x_k), where $z_j = -1 + hj$ and $x_k = hk$ for $j, k = 0, 1, 2, ..., J$. However, in order to apply the boundary conditions, we introduce 'phantom' points lying just outside the boundaries, which are only used in order to obtain the scheme. The variables Φ and

N, are written in vector form as

$$\mathbf{\Phi} = \begin{pmatrix} \Phi_{0,0} \\ \Phi_{0,1} \\ \Phi_{0,2} \\ \dots \\ \Phi_{0,J} \\ \Phi_{1,0} \\ \Phi_{1,1} \\ \dots \\ \Phi_{1,J} \\ \dots \\ \Phi_{J,J} \end{pmatrix} \quad \text{and} \quad \mathbf{N} = \begin{pmatrix} N_{0,0} \\ N_{0,1} \\ N_{0,2} \\ \dots \\ N_{0,J} \\ N_{1,0} \\ N_{1,1} \\ \dots \\ N_{1,J} \\ \dots \\ N_{J,J} \end{pmatrix}. \tag{II.1}$$

Therefore, $\Phi_{j,k}$ and $N_{j,k}$ are the approximation of ϕ and n at the point (z_j, x_k).

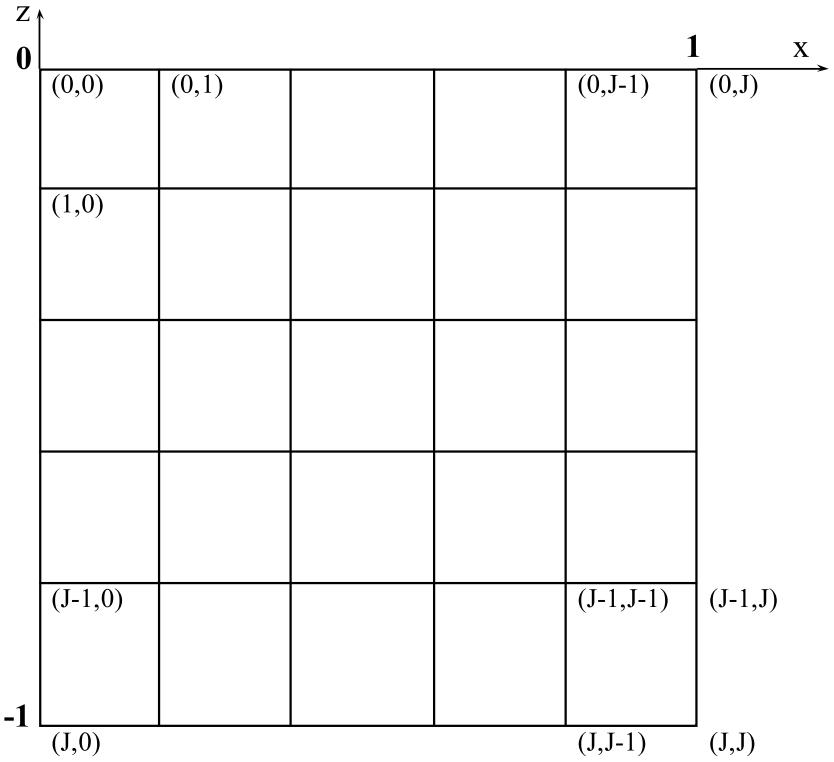

Figure II.2: The uniform grid used for the numerical scheme.

Discretisation

The governing equations are given in (4.135)-(4.136). To discretise these, we let $\Phi_{j,k}$ and $N_{j,k}$ be the numerical solutions for ϕ and n at the point (z_k, x_k), respectively. Then, using a second order centred differences approximation for the discretisation of the derivatives, we obtain, for (4.135),

$$\frac{\Phi^{[q+1]}_{j+1,k} + \Phi^{[q+1]}_{j-1,k} - 2\Phi^{[q+1]}_{j,k}}{h^2} + \varepsilon^2 \left(\frac{\Phi^{[q+1]}_{j,k+1} + \Phi^{[q+1]}_{j,k-1} - 2\Phi^{[q+1]}_{j,k}}{h^2} \right) = \Lambda N^{[q]}_{j,k}, \tag{II.2}$$

for $j, k = 2, ..., J-1$. In (II.2) $q(\geq 1)$ is an indicator of the number of iterations operated for each term. Given an initial guess for Φ, namely $\Phi^{[0]}$, we iterate the scheme so that we reach a desirable level of tolerance, tol, set as

$$||\mathbf{N}^{[q+1]} - \mathbf{N}^{[q]}|| < tol. \tag{II.3}$$

The scheme for ϕ is completed with imposing the boundary conditions at $z = -1, 0$ as

$$\Phi_{1,k} = -\frac{\hat{V}}{2}, \tag{II.4}$$

$$\Phi_{J,k} = 0 \tag{II.5}$$

for $k = 1, ..., J$, and we use the Neumann boundary conditions at $x = 0, 1$ to reduce the discretised equation (II.2) at the boundaries to

$$\frac{\Phi^{[q+1]}_{j+1,1} + \Phi^{[q+1]}_{j-1,1} - 2\Phi^{[q+1]}_{j,1}}{h^2} + \varepsilon^2 \left(\frac{2\Phi^{[q+1]}_{j,2} - 2\Phi^{[q+1]}_{j,1}}{h^2} \right) = \Lambda N^{[q]}_{j,1}, \tag{II.6}$$

$$\frac{\Phi^{[q+1]}_{j+1,J} + \Phi^{[q+1]}_{j-1,J} - \Phi^{[q+1]}_{j,J}}{h^2} + \varepsilon^2 \left(\frac{2\Phi^{[q+1]}_{j,J-1} - 2\Phi^{[q+1]}_{j,J}}{h^2} \right) = \Lambda N^{[q]}_{j,J} \tag{II.7}$$

for $j = 2, ..., J$.

Before discretising n, it is useful to write it as

$$n_z\phi_z + \varepsilon^2 n_x\phi_x + n \underbrace{(\phi_{zz} + \varepsilon^2\phi_{xx})}_{=\Lambda n} - (n_{zz} + \varepsilon^2 n_{xx}) = 0, \tag{II.8}$$

and discretise as follows

$$\left(\frac{\Phi^{[q]}_{j+1,k}-\Phi^{[q]}_{j-1,k}}{4h^2}\right)\left(N^{[q+1]}_{j+1,k}-N^{[q+1]}_{j-1,k}\right)-\left(\frac{N^{[q+1]}_{j+1,k}+N^{[q+1]}_{j-1,k}-2N^{[q+1]}_{j,k}}{h^2}\right)+\Lambda N^{[q]}_{j,k}N^{[q+1]}_{j,k}$$
$$+\varepsilon^2\left(\frac{\Phi^{[q]}_{j,k+1}-\Phi^{[q]}_{j,k-1}}{4h^2}\right)(N^{[q+1]}_{j,k+1}-N^{[q+1]}_{j,k-1})-\varepsilon^2\left(\frac{N^{[q+1]}_{j,k+1}+N^{[q+1]}_{j,k-1}-2N^{[q+1]}_{j,k}}{h^2}\right)=0, \tag{II.9}$$

for $j,k=2,...,J-1$. We impose the Dirichlet boundary condition at $z=-1$ as

$$N_{0,k}=\hat{N}^- \tag{II.10}$$

for $k=0,...J$, and we use the Neumann boundary conditions at $x=0,1$ to reduce (II.9) to the following equations at the boundaries

$$\left(\frac{\Phi^{[q]}_{j+1,1}-\Phi^{[q]}_{j-1,1}}{4h^2}\right)\left(N^{[q+1]}_{j+1,1}-N^{[q+1]}_{j-1,1}\right)-\left(\frac{N^{[q+1]}_{j+1,1}+N^{[q+1]}_{j-1,1}-2N^{[q+1]}_{j,1}}{h^2}\right)$$
$$+\Lambda N^{[q]}_{j,1}N^{[q+1]}_{j,1}-\varepsilon^2\left(\frac{2N^{[q+1]}_{j,2}-2N^{[q+1]}_{j,1}}{h^2}\right)=0, \tag{II.11}$$
$$\left(\frac{\Phi^{[q]}_{j+1,J}-\Phi^{[q]}_{j-1,J}}{4h^2}\right)\left(N^{[q+1]}_{j+1,J}-N^{[q+1]}_{j-1,J}\right)-\left(\frac{N^{[q+1]}_{j+1,J}+N^{[q+1]}_{j-1,J}-2N^{[q+1]}_{j,J}}{h^2}\right)$$
$$+\Lambda N^{[q]}_{j,J}N^{[q+1]}_{j,J}-\varepsilon^2\left(\frac{2N^{[q+1]}_{j,J-1}-2N^{[q+1]}_{j,J}}{h^2}\right)=0, \tag{II.12}$$

for $j=2,...,J-1$.

We are left with discretising

$$n\phi_z-n_z=S_d(x)\hat{G}-\delta(1-S_d(x))(n^2-1)|_{z=0}. \tag{II.13}$$

To find the scheme on these boundary nodes, we use the governing equations for ϕ and n together with the boundary condition, as explained below. We introduce 'phantom' nodes by extending the grid by adding the point $z_{J+1}=-1+(J+1)h$.

Thus, (II.8) at the boundary nodes becomes

$$\left(\frac{\Phi^{[q]}_{J+1,k}-\Phi^{[q]}_{J-1,k}}{4h^2}\right)\left(N^{[q+1]}_{J+1,k}-N^{[q+1]}_{J-1,k}\right)-\left(\frac{N^{[q+1]}_{J+1,k}+N^{[q+1]}_{J-1,k}-2N^{[q+1]}_{J,k}}{h^2}\right)+\Lambda N^{[q]}_{J,k}N^{[q+1]}_{J,k}$$
$$+\varepsilon^2\left(\frac{\Phi^{[q]}_{J,k+1}-\Phi^{[q]}_{J,k-1}}{4h^2}\right)(N^{[q+1]}_{J,k+1}-N^{[q+1]}_{J,k-1})$$
$$-\varepsilon^2\left(\frac{N^{[q+1]}_{J,k+1}+N^{[q+1]}_{J,k-1}-2N^{[q+1]}_{J,k}}{h^2}\right)=0, \tag{II.14}$$

for $k=1,...J$, where we need expressions for $N^{[q+1]}_{J+1,k}$ and $\Phi^{[q]}_{J+1,k}$. We then use (II.2) to get $\Phi_{J+1,k}$ as

$$\frac{\Phi^{[q]}_{J+1,k}+\Phi^{[q]}_{J-1,k}-2\Phi^{[q]}_{J,k}}{h^2}+\varepsilon^2\left(\frac{\Phi^{[q]}_{J,k+1}+\Phi^{[q]}_{J,k-1}-2\Phi^{[q]}_{J,k}}{h^2}\right)=\Lambda N^{[q]}_{J,k} \tag{II.15}$$

$$\Rightarrow\ \Phi^{[q]}_{J+1,k}=\Lambda h^2 N^{[q]}_{J,k}-\Phi^{[q]}_{J-1,k}, \tag{II.16}$$

where we have used (II.5) in the last line. We also use (II.13) to get $N^{[q+1]}_{J+1,k}$ as

$$\left(\frac{\Phi^{[q]}_{J+1,k}-\Phi_{J-1,k}}{2h}\right)N^{[q]}_{J,k}-\frac{N^{[q+1]}_{J+1,k}-N^{[q]}_{J-1,k}}{2h}=S_{dk}G-\delta(1-S_{dk})((N^{[q]}_{J,k})^2-1) \tag{II.17}$$

$$\Rightarrow\ N^{[q+1]}_{J+1,k}=N^{[q+1]}_{J-1,k}+\left((\Lambda h^2-2h\delta(1-S_{dk}))N^{[q]}_{J,k}-2\Phi_{J-1,k}\right)N^{[q+1]}_{J,k}+C_k, \tag{II.18}$$

where we write $S_{dk}=S_d(x_k)$ and $C_k=2h[\delta(1-S_{dk})+S_{dk}\hat{G}]$ and use the expression for $\Phi^{[q]}_{J+1,k}$ found earlier. Finally, on the interface, we impose

$$\left[\left(\frac{\Lambda h^2 N^{[q]}_{J,k}-2\Phi^{[q]}_{J-1,k}-4}{4h^2}\right)\left([\Lambda h^2-2h\delta(1-S_{dk})]N^{[q]}_{J,k}-2\Phi^{[q]}_{J-1,k}\right)\right.$$
$$\left.+\frac{\Lambda C_k}{4}+\Lambda N^{[q]}_{J,k}+\frac{2}{h^2}(1+\varepsilon^2)\right]N^{[q+1]}_{J,k}-\frac{2}{h^2}N^{[q+1]}_{J-1,k}$$
$$-\frac{\varepsilon^2}{h^2}N^{[q+1]}_{J,k+1}+-\frac{\varepsilon^2}{h^2}N^{[q+1]}_{J,k-1}=C_k\left(\frac{\Phi^{[q]}_{J-1,k}}{2h}+\frac{1}{h^2}\right), \tag{II.19}$$

for $k=2,...,J-1$. Then, for the corners (0,0) and (0,1) we use the Neumann boundary condition for n. At (0,0) we get

$$\left[\left(\frac{\Lambda h^2 N_{J,1}^{[q]} - 2\Phi_{J-1,1}^{[q]} - 4}{4h^2}\right)\left([\Lambda h^2 - 2h\delta(1-S_{d1})]N_{J,1}^{[q]} - 2\Phi_{J-1,1}^{[q]}\right)\right.$$
$$\left.+\frac{\Lambda C_1}{4} + \Lambda N_{J,1}^{[q]} + \frac{2}{h^2}(1+\varepsilon^2)\right] N_{J,1}^{[q+1]} - \frac{2}{h^2}N_{J-1,1}^{[q+1]}$$
$$-\frac{2\varepsilon^2}{h^2}N_{J,2}^{[q+1]} = C_1\left(\frac{\Phi_{J-1,1}^{[q]}}{2h} + \frac{1}{h^2}\right). \tag{II.20}$$

At (0,1) we get

$$\left[\left(\frac{\Lambda h^2 N_{J,J}^{[q]} - 2\Phi_{J-1,J}^{[q]} - 4}{4h^2}\right)\left([\Lambda h^2 - 2h\delta(1-S_{d(J)})]N_{J,J}^{[q]} - 2\Phi_{J-1,J}^{[q]}\right)\right.$$
$$\left.+\frac{\Lambda C_J}{4} + \Lambda N_{J,J}^{[q]} + \frac{2}{h^2}(1+\varepsilon^2)\right] N_{J,J}^{[q+1]} - \frac{2}{h^2}N_{J-1,J}^{[q+1]}$$
$$-\frac{2\varepsilon^2}{h^2}N_{J,J-1}^{[q+1]} = C_J\left(\frac{\Phi_{J-1,J}^{[q]}}{2h} + \frac{1}{h^2}\right). \tag{II.21}$$

The matrix systems for $\mathbf{\Phi}$ and $\mathbf{N}$, then, read

$$A_\phi \mathbf{\Phi}^{[q+1]} = \Lambda \mathbf{N}^{[q]} + \mathbf{b}_\phi, \tag{II.22}$$
$$A_n(\mathbf{\Phi}^{[q+1]}, \mathbf{N}^{[q]})\mathbf{N}^{[q+1]} = \mathbf{b}_n, \tag{II.23}$$

where A_ϕ and A_n are the matrices of coefficients and $\mathbf{b}_\phi$ and $\mathbf{b}_n$ are vectors, described by the relations in (II.2)-(II.21). A_ϕ has constant entries, while A_n depends on Φ and N. We iterate according to q based on a simple Jacobi iteration method. We stop the iteration when

$$\|\mathbf{\Phi}^{[q+1]} - \mathbf{\Phi}^{[q]}\| < tol \quad \text{and} \quad \|\mathbf{N}^{[q+1]} - \mathbf{N}^{[q]}\| < tol, \tag{II.24}$$

for some tolerance value, tol.

Error Analysis

As there is no analytical exact solution, we use a numerical solution with a very fine grid as a reference to analyse the numerical error and accuracy. We numerically solve (4.135)-(4.147) with $N_b = 1$, $\hat{\omega} = 0.5$ and $\varepsilon = 1$. We get $\bar{\Phi}(z_j, x_k)$ and $\bar{N}(z_j, x_k)$

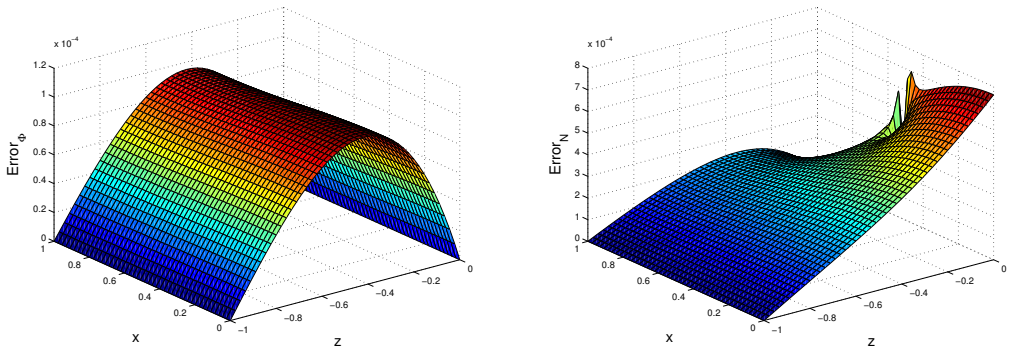

(a) (b)

Figure II.3: Plot of the errors, (a) E_Φ and E_N, generated numerically for the bilayer thin film problem. [Parameters: $\varepsilon = 1$, $S = 0$, $N_b = 1$, $\hat{\omega} = 0.5$, $\delta = 1$, $\hat{V} = 1$, $\Lambda = 1$ and $\hat{N}^- = 1$]

on the reference grid and we use a coarser grid to find $\Phi(z_j, x_k)$ and $N(z_j, x_k)$. We then define the error matrices between the two solutions (evaluated on the common points)

$$E_{\Phi_{j,k}} = |\Phi_{j,k} - \bar{\Phi}(z_j, x_k)|, \quad E_{N_{j,k}} = |N_{j,k} - \bar{N}(z_j, x_k)|. \tag{II.25}$$

In Figure II.3 we show the errors $E_{\mathbf{\Phi}}$ and E_N, for a sample case, to be of significantly small order.

Appendix III - for Chapter 5

The contents of this appendix are relevant to Section 5.3 and we include a detailed description of the numerical scheme used for solving the ordered nanostructured mixed-layer problem. The numerical code produces the distribution of ϕ, n and p throughout the whole cell, allowing the user to vary the parameters: ε_ω, δ, V, $\hat{\epsilon}_p$, $\hat{N}^-$ and $\hat{P}^+$.

The scheme uses the *finite volume method* (FVM) [63]. According to the finite volume method, we introduce a volume element, $\tilde{V}$, (in this case a two dimensional square) around the point of the grid we want to discretise about. If the point is given by (z_j, x_k), then the corners of the square are at $(z_{j\pm\frac{1}{2}}, x_{k\pm\frac{1}{2}})$. We then integrate our equation across this volume element, using the divergence theorem to reduce to a surface integral over the surface of the volume, S, and discretise. In the bulk, the scheme is identical to a finite differences scheme, but it allows for a better discretisation along the interface. We then formulate the problem as a matrix system and the solution is obtained via iteration until reaching an acceptable tolerance level.

The Grid

The domain, $[0,1] \times [0,1]$, is discretised into the uniform grid shown in Figure III.1. To apply the finite volumes scheme we discretise the domain into a piecewise uniform grid with a total of J steps. We introduce $z_j = hj$ and $x_k = hk$, and define the grid by the nodes (z_j, x_k), where $j, k = 0, ..., J$. We let $h = \frac{1}{J}$ be the grid step size. We then let $\Phi_{j,k}$, $N_{j,k}$ and $P_{j,k}$ be the numerical solutions for ϕ, n and p at the node (z_j, x_k). We will define j_a, j_b, k_c and k_d so that $(z_{j_a}, x_{k_c}) = (a, c)$, $(z_{j_a}, x_{k_d}) = (a, d)$, $(z_{j_b}, x_{k_c}) = (b, c)$ and $(z_{j_b}, x_{k_d}) = (b, d)$, respectively.

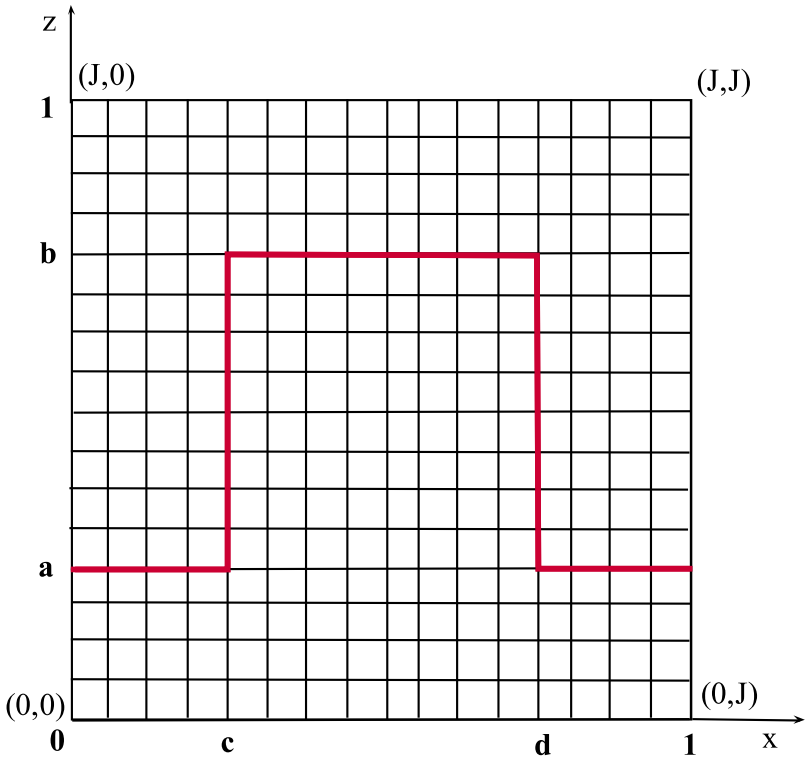

Figure III.1: The numerical domain for one stem.

Discretisation (Bulk regions)

The finite volume method reduces to the centred finite differences method in the bulk regions of the electron acceptor and donor. Note that N is zero in the electron donor region and P is zero in the electron acceptor region. We present the discretisation in each region separately, for clarity.

Electron Acceptor Region

For $[\{j = 1, .., j_{a-1}\} \cap [\{k = 1, .., J-1\}]$ and for $[\{j = j_a, ..., j_{b-1}\} \cap \{k = k_{c+1}, ..., k_{d-1}\}]$:

$$\varepsilon_\omega^2 \Phi_{j-1,k} + \Phi_{j+1,k} - 2\Phi_{j,k} + (\Phi_{j,k-1} + \Phi_{j,k+1} - 2\Phi_{j,k}) = \varepsilon_\omega^2 \Lambda h^2 N_{j,k}, \tag{III.1}$$

$$\varepsilon_\omega^2 \left[\left(\frac{N_{j+1,k} - N_{j-1,k}}{2h} \right) \left(\frac{\Phi_{j+1,k} - \Phi_{j-1,k}}{2h} \right) - \left(\frac{N_{j+1,k} + N_{j-1,k} - 2N_{j,k}}{h^2} \right) \right] + \varepsilon_\omega^2 \Lambda N_{j,k}^2$$
$$+ \left(\frac{N_{j,k+1} - N_{j,k-1}}{2h} \right) \left(\frac{\Phi_{j,k+1} - \Phi_{j,k-1}}{2h} \right) - \left(\frac{N_{j,k+1} + N_{j,k-1} - 2N_{j,k}}{h^2} \right) = 0, \tag{III.2}$$

$$P_{j,k} = 0. \tag{III.3}$$

The Dirichlet boundary conditions on $z = 0$ are imposed for $k = 0, J$

$$\Phi_{0,k} = 0, \tag{III.4}$$
$$N_{0,k} = \hat{N}^{-}, \tag{III.5}$$
$$P_{0,k} = 0, \tag{III.6}$$

for $j = 0$. The periodic boundary conditions on the x-boundaries are for Φ, for $j = 0, J$, are discretised as

$$\Phi_{j,0} = \Phi_{j,J}, \tag{III.7}$$
$$\Phi_{j,1} = -\Phi_{j,J-1}, \tag{III.8}$$

and then we get, by substituting (III.7)-(III.8) into (III.1),

$$\varepsilon_\omega^2 \left(\Phi_{j-1,J} + \Phi_{j+1,J} - 2\Phi_{j,J}\right) + \left(\Phi_{j,J-1} + \Phi_{j,1} - 2\Phi_{j,J}\right) = \varepsilon_\omega^2 \Lambda h^2 N_{j,J}. \tag{III.9}$$

for $j = 0, .., J-1$. Similarly, for N we impose the periodic conditions

$$N_{j,0} = N_{j,J}, \tag{III.10}$$
$$N_{j,1} = -N_{j,J-1}, \tag{III.11}$$

on $j = 0, J$ to get

$$\begin{aligned}\varepsilon_\omega^2 \left[\left(\frac{N_{j+1,J} - N_{j-1,J}}{2h}\right)\left(\frac{\Phi_{j+1,J} - \Phi_{j-1,J}}{2h}\right) - \left(\frac{N_{j+1,J} + N_{j-1,J} - 2N_{j,J}}{h^2}\right)\right] \\ + \varepsilon_\omega^2 \Lambda N_{j,J}^2 + \left(\frac{N_{j,1} - N_{1,J-1}}{2h}\right)\left(\frac{\Phi_{j,1} - \Phi_{j,J-1}}{2h}\right) - \left(\frac{N_{j,1} + N_{j,J-1} - 2N_{j,J}}{h^2}\right) = 0,\end{aligned} \tag{III.12}$$

for $j = 0, .., J-1$.

Electron Donor Region

Similarly to the discretisation for the EA region, in $[\{j = j_{a+1}, ...J-1\} \cap \{k = 1, ..., k_c - 1\}]$, $[\{j = j_{a+1}, ...J-1\} \cap \{k = k_{d+1}, ..., J-1\}]$ and $[\{j = j_{b+1}, ..., J-1\} \cap \{k =$

$k_c, ..., k_d\}]$ we have discretised as

$$\varepsilon_\omega^2 \left(\Phi_{j-1,k} + \Phi_{j+1,k} - 2\Phi_{j,k}\right) + \left(\Phi_{j,k-1} + \Phi_{j,k+1} - 2\Phi_{j,k}\right) = -\varepsilon_\omega^2 \frac{\Lambda}{\hat{\epsilon}_p} h^2 P_{j,k}, \tag{III.13}$$

$$\varepsilon_\omega^2 \left[\left(\frac{P_{j+1,k} - P_{j-1,k}}{2h}\right)\left(\frac{\Phi_{j+1,k} - \Phi_{j-1,k}}{2h}\right) + \left(\frac{P_{j+1,k} + P_{j-1,k} - 2P_{j,k}}{h^2}\right)\right] - \varepsilon_\omega^2 \frac{\Lambda}{\epsilon_p} P_{j,k}^2$$
$$+ \left(\frac{P_{j,k+1} - P_{j,k-1}}{2h}\right)\left(\frac{\Phi_{j,k+1} - \Phi_{j,k-1}}{2h}\right) + \left(\frac{P_{j,k+1} + P_{j,k-1} - 2P_{j,k}}{h^2}\right) = 0, \tag{III.14}$$

and we impose $N_{j,k} = 0$. The Dirichlet boundary conditions on $z = 1$ are imposed by

$$\Phi_{J,k} = \hat{V}, \tag{III.15}$$

$$N_{J,k} = 0, \tag{III.16}$$

$$P_{J,k} = \hat{P}^+, \tag{III.17}$$

for $k = 0, ..., J$. Using the periodic boundary conditions on the x-boundaries (III.7)-(III.8) we get the discretised equation for Φ to be

$$\varepsilon_\omega^2 \left(\Phi_{j-1,J} + \Phi_{j+1,J} - 2\Phi_{j,J}\right) + \left(\Phi_{j,J} + \Phi_{j,1} - 2\Phi_{j,J}\right) = -\varepsilon_\omega^2 \frac{\Lambda}{\hat{\epsilon}_p} h^2 P_{j,J}, \tag{III.18}$$

for $j = 0, .., J-1$. Similarly, we use the discretised periodic conditions

$$P_{j,0} = P_{j,J}, \tag{III.19}$$

$$P_{j,1} = -P_{j,J-1}, \tag{III.20}$$

to obtain the discretised scheme for N to be

$$\varepsilon_\omega^2 \left[\left(\frac{P_{j+1,J} - P_{j-1,J}}{2h}\right)\left(\frac{\Phi_{j+1,J} - \Phi_{j-1,J}}{2h}\right) + \left(\frac{P_{j+1,J} + P_{j-1,J+1} - 2P_{j,J}}{h^2}\right)\right]$$
$$- \varepsilon_\omega^2 \frac{\Lambda}{\hat{\epsilon}_p} P_{j,J}^2 + \left(\frac{P_{j,1} - P_{j,J-1}}{2h}\right)\left(\frac{\Phi_{j,1} - \Phi_{j,J-1}}{2h}\right) + \left(\frac{P_{j,1} + P_{j,J-1} - 2P_{j,J}}{h^2}\right) = 0, \tag{III.21}$$

for $j = 0, .., J-1$.

Discretisation (Interface)

We present the discretisation for each dependent variable separately along the interface using the finite volume method. The dye interface is described by the points

(z_j, x_k), where $[\{j = j_a\} \cap \{k = 0, ..., c\}]$, $[\{j = j_a, ..j_b\} \cap \{k = k_c\}]$, $[\{j = j_b\} \cap \{k = k_c, ..., k_d\}]$, $[\{j = j_a, ..., j_b\} \cap \{k = k_d\}]$ and $[\{j = j_a\} \cap \{k = k_d, ..., J\}]$, as shown in Figure 4.13. In what follows we present the discretised problem for each variable separately.

For Φ

We define the controlled 'volume' (here area) $\bar{\Upsilon}$, being a rectangle with length h and centred at each node; we let $\partial\bar{\Upsilon}$ to denote the perimeter. Then, the scheme for Φ along the interface is derived as follows:

$$\iint_{\bar{\Upsilon}} \nabla \cdot (\epsilon_i \nabla\phi)\, d\tilde{V} = \iint_{\Omega_a} \Lambda n d\Omega_a - \iint_{\Omega_d} \Lambda p d\Omega_d \tag{III.22}$$

$$\Rightarrow \int_{\partial\bar{\Upsilon}} \epsilon_i \nabla\phi \cdot \hat{\mathbf{n}} dS = \iint_{\Omega_a} \Lambda n d\Omega_a - \iint_{\Omega_d} \Lambda p d\Omega_d, \tag{III.23}$$

with Ω_a and Ω_d representing the area of the controlled volume which lies in the EA and ED region, respectively, as shown in Figure III.2. We have used the divergence theorem to reduce to a surface integral. The numerical approximation differs on each point along the interface, thus we break it down in vertical and horizontal interface lines and corner points.

Consider any point along the horizontal lines of the interface, i.e. any point (z_j, x_k), where $[\{j = j_a\} \cap \{k = 0, ..., k_c\}]$, $[\{j = j_a\} \cap [\{k = k_d, ..., J\}]$ and $[\{j = j_b\} \cap \{k = k_c, ..., k_d\}]$, as shown in Figure III.2.

We will show an example of how we discretise along the interface first, and then present the remaining scheme only, as the derivation is the same to the example. Therefore, we discretise along the interface line $[\{j = j_a\} \cap \{k = k = 0, ..., k_{c-a}\}]$, i.e. the line shown in Figure 2(a). We integrate numerically the left-hand side of (III.23) along the surface of the specified controlled area, to find that

$$\int_{\partial\bar{\Upsilon}} \epsilon_i \nabla\phi \cdot \underline{\hat{n}} dS = \underbrace{\Delta z \left(\frac{\Phi_{j,k-1} - \Phi_{j,k}}{\Delta x} \right)}_{surface\ (1)} + \underbrace{\Delta x \left(\frac{\Phi_{j-1,k} - \Phi_{j,k}}{\Delta z} \right)}_{surface\ 2} \tag{III.24}$$

$$+ \underbrace{\Delta z \left(\frac{\Phi_{j,k+1} - \Phi_{j,k}}{\Delta x} \right)}_{surface\ 3} + \underbrace{\Delta x \left(\frac{\Phi_{j+1,k} - \Phi_{j,k}}{\Delta z} \right)}_{surface\ 4}, \tag{III.25}$$

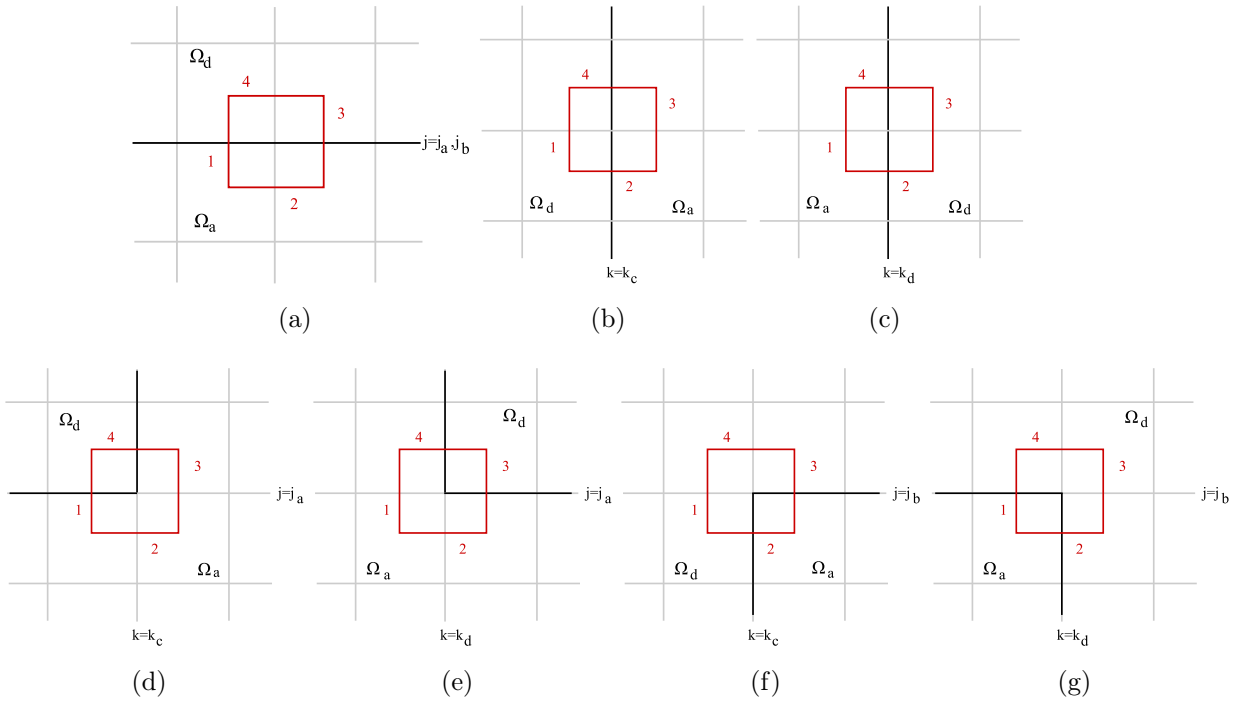

Figure III.2: Controlled volume elements used in the numerical scheme for generating the discretised equations for Φ.

where the surfaces are shown in Figure 2(a). We discretise the right-hand side of (III.23) by

$$\iint_{\Omega_a} \Lambda n d\Omega_a - \iint_{\Omega_d} \Lambda p d\Omega_d = \frac{\Lambda h^2}{2} \left(N_{j,k} - P_{j,k}\right). \tag{III.26}$$

Therefore, on ny point (z_j, x_k), where $[\{j = j_a\} \cap \{k = 0, ..., k_c\}]$, $[\{j = j_a\} \cap [\{k = k_d, ..., J\}]$ and $[\{j = j_b\} \cap \{k = k_c, ..., k_d\}]$, we impose

The

$$\varepsilon_\omega^2 \left(\hat{\epsilon}_p \Phi_{j+1,k} + \Phi_{j-1,k} - (1 + \hat{\epsilon}_p)\Phi_{j,k}\right) + \left(\frac{1 + \hat{\epsilon}_p}{2}\right) \left(\Phi_{j,k-1} + \Phi_{j,k+1} - 2\Phi_{j,k}\right)$$
$$= \varepsilon_\omega^2 \frac{\Lambda h^2}{2} \left(N_{j,k} - P_{j,k}\right). \tag{III.27}$$

In the same horizontal lines of the interface, we impose the periodic boundary conditions on $k = 0, J$, i.e.

$$\Phi_{j,0} = \Phi_{j,J}, \tag{III.28}$$

to get

$$\varepsilon_\omega^2 \left(\hat{\epsilon}_p \Phi_{j+1,J} + \Phi_{j-1,J} - (1+\hat{\epsilon}_p)\Phi_{j,J}\right) + \left(\frac{1+\hat{\epsilon}_p}{2}\right)\left(\Phi_{j,J-1} + \Phi_{j,1} - 2\Phi_{j,J}\right)$$
$$= \varepsilon_\omega^2 \frac{\Lambda h^2}{2}\left(N_{j,J} - P_{j,J}\right). \tag{III.29}$$

We then turn to the vertical line of the interface, i.e. $[\{j = j_{a+1}, ..., j_{b-1}\} \cap \{k = k_c\}]$, as seen in Figure 2(b)), were we impose

$$\varepsilon_\omega^2 \left(\frac{1+\hat{\epsilon}_p}{2}\right)\left(\Phi_{j-1,k} + \Phi_{j+1,k} - 2\Phi_{j,k}\right) + \left(\hat{\epsilon}_p \Phi_{j,k-1} + \Phi_{j,k+1} - (1+\hat{\epsilon}_p)\Phi_{j,k}\right)$$
$$= \varepsilon_\omega^2 \frac{\Lambda h^2}{2}\left(N_{j,k} - P_{j,k}\right). \tag{III.30}$$

Similarly, for the other vertical line of the interface, i.e. $[\{j = j_{a+1}, ..., j_{b-1}\} \cap \{k = k_d\}]$ (see Figure 2(c)), the scheme is

$$\varepsilon_\omega^2 \left(\frac{1+\hat{\epsilon}_p}{2}\right)\left(\Phi_{j-1,k} + \Phi_{j+1,k} - 2\Phi_{j,k}\right) + \left(\Phi_{j,k-1} + \hat{\epsilon}_p \Phi_{j,k+1} - (1+\hat{\epsilon}_p)\Phi_{j,k}\right)$$
$$= \varepsilon_\omega^2 \frac{\Lambda h^2}{2}\left(N_{j,k} - P_{j,k}\right). \tag{III.31}$$

For the corner point (z_{j_a}, x_{k_c}) (see Figure 2(d)), we discretise in a similar manner. The local scheme is

$$\varepsilon_\omega^2 \left(\Phi_{j-1,k} + \left(\frac{1+\hat{\epsilon}_p}{2}\right)\Phi_{j+1,k} - \left(\frac{3+\hat{\epsilon}_p}{2}\right)\Phi_{j,k}\right)$$
$$+ \left(\left(\frac{1+\hat{\epsilon}_p}{2}\right)\Phi_{j,k-1} + \Phi_{j,k+1} - \left(\frac{3+\hat{\epsilon}_p}{2}\right)\Phi_{j,k}\right) = \varepsilon_\omega^2 \frac{\Lambda h^2}{4}\left(3N_{j,k} - P_{j,k}\right). \tag{III.32}$$

For the corner point (z_{j_a}, x_{k_d}), (see Figure 2(e)) the scheme is

$$\varepsilon_\omega^2 \left(\Phi_{j-1,k} + \left(\frac{1+\hat{\epsilon}_p}{2}\right)\Phi_{j+1,k} - \left(\frac{3+\hat{\epsilon}_p}{2}\right)\Phi_{j,k}\right)$$
$$+ \left(\Phi_{j,k-1} + \left(\frac{1+\hat{\epsilon}_p}{2}\right)\Phi_{j,k+1} - \left(\frac{3+\hat{\epsilon}_p}{2}\right)\Phi_{j,k}\right) = \varepsilon_\omega^2 \frac{\Lambda h^2}{4}\left(3N_{j,k} - P_{j,k}\right). \tag{III.33}$$

For the corner point (z_{j_b}, x_{k_c}) (see Figure 2(f)) the scheme is

$$\varepsilon_\omega^2 \left(\left(\frac{1+\hat{\epsilon}_p}{2} \right) \Phi_{j-1,k} + \hat{\epsilon}_p \Phi_{j+1,k} - \left(\frac{1+3\hat{\epsilon}_p}{2} \right) \Phi_{j,k} \right) + \left(\hat{\epsilon}_p \Phi_{j,k-1} + \left(\frac{1+\hat{\epsilon}_p}{2} \right) \Phi_{j,k+1} - \left(\frac{1+3\hat{\epsilon}_p}{2} \right) \Phi_{j,k} \right) = \varepsilon_\omega^2 \frac{\Lambda h^2}{4} \left(N_{j,k} - 3P_{j,k} \right). \tag{III.34}$$

For the corner point (z_{j_b}, x_{k_d}) (see Figure 2(g)) the scheme is:

$$\varepsilon_\omega^2 \left(\left(\frac{1+\hat{\epsilon}_p}{2} \right) \Phi_{j-1,k} + \hat{\epsilon}_p \Phi_{j+1,k} - \left(\frac{1+3\hat{\epsilon}_p}{2} \right) \Phi_{j,k} \right) + \left(\left(\frac{1+\hat{\epsilon}_p}{2} \right) \Phi_{j,k-1} + \hat{\epsilon}_p \Phi_{j,k+1} - \left(\frac{1+3\hat{\epsilon}_p}{2} \right) \Phi_{j,k} \right) = \varepsilon_\omega^2 \frac{\Lambda h^2}{4} \left(N_{j,k} - 3P_{j,k} \right). \tag{III.35}$$

For N

For N on any point of the interface we use the following

$$\iint_{\bar{\Upsilon}} \nabla \cdot \mathbf{F}_n d\bar{\Upsilon} = \int_{\partial\Upsilon} \mathbf{F}_n \cdot \hat{\mathbf{n}} dS = 0, \tag{III.36}$$

where $\bar{\Upsilon}$ is the volume unit and $\partial\bar{\Upsilon}$ is the surface of the volume in which we integrate. However, N is only defined in the EA region, i.e. in only one side of the interface, thus we must restrict the volume elements used to just the side where N is defined, as shown in Figure III.3.

For the horizontal lines of the interface $[\{j = j_a\} \cap \{k = 1, .., k_{c-1}\}]$, $[\{j = j_a\} \cap \{k = k_{d+1}, ..., J\}]$, and $[\{j = j_b\} \cap \{k = k_{c+1}, ..., k_{d-1}\}]$ (see Figure 3(a)) the scheme is derived as follows

$$\int_{\partial\bar{\Upsilon}} \mathbf{F}_n \cdot \hat{\underline{n}} dS = \int_1 \frac{1}{\varepsilon_\omega} \left(n \frac{\partial \phi}{\partial x} - \frac{\partial n}{\partial x} \right) dz + \int_2 \varepsilon_\omega \left(n \frac{\partial \phi}{\partial z} - \frac{\partial n}{\partial z} \right) dx + \int_3 \frac{1}{\varepsilon_\omega} \left(n \frac{\partial \phi}{\partial x} - \frac{\partial n}{\partial x} \right) dz - \int_4 \varepsilon_\omega \left(S\hat{G} - \delta(1-S)(np-1) \right) dx, \tag{III.37}$$

where the notations $1, 2, 3, 4$ in the integrals correspond to the surfaces of the con-

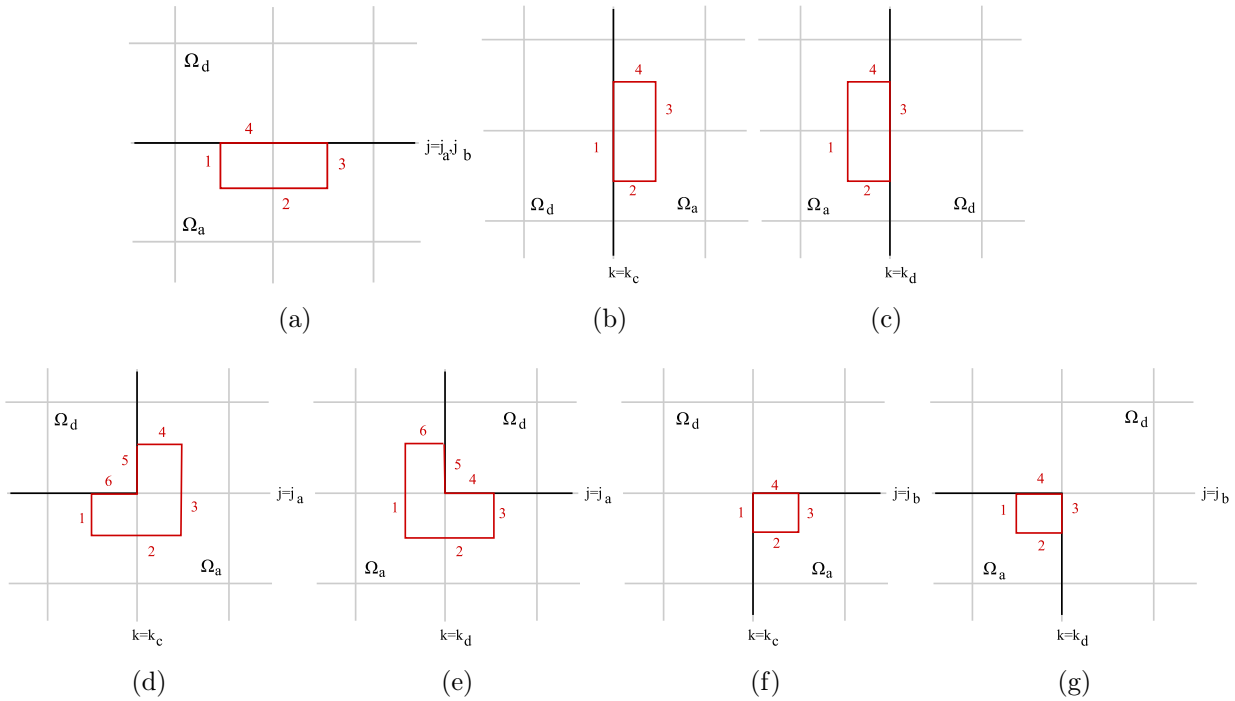

Figure III.3: Controlled volume elements used in the numerical scheme for generating the discretised equations for N.

trolled area, as shown in Figure **??**. The scheme, then, can be written as

$$\begin{aligned}
&\left[\left(\frac{N_{j,k-1}+N_{j,k}}{2}\right)(\Phi_{j,k-1}-\Phi_{j,k})-(N_{j,k-1}-N_{j,k})\right]\frac{1}{2\varepsilon_\omega}\\
&+\left[\left(\frac{N_{j-1,k}+N_{j,k}}{2}\right)(\Phi_{j-1,k}-\Phi_{j,k})-(N_{j-1,k}-N_{j,k})\right]\varepsilon_\omega\\
&+\left[\left(\frac{N_{j,k+1}+N_{j,k}}{2}\right)(\Phi_{j,k+1}-\Phi_{j,k})-(N_{j,k+1}-N_{j,k})\right]\frac{1}{2\varepsilon_\omega}\\
&-\left[S_{j,k}\hat{G}-\delta(1-S_{j,k})\,(N_{j,k}P_{j,k}-1)\right]h\varepsilon_\omega=0,
\end{aligned}\tag{III.38}$$

where $S_{j,k}=S_d(z_j,x_k)$ from now on. At the x-boundaries, i.e. for $k=0,J$, the

scheme is:

$$N_{j,0} = N_{j,J}, \tag{III.39}$$

$$\begin{aligned}
&\left[\left(\frac{N_{j,J-1}+N_{j,J}}{2}\right)(\Phi_{j,J-1}-\Phi_{j,J})-(N_{j,J-1}-N_{j,J})\right]\frac{1}{2\varepsilon_\omega}\\
&+\left[\left(\frac{N_{j-1,J}+N_{j,J}}{2}\right)(\Phi_{j-1,J}-\Phi_{j,J})-(N_{j-1,J}-N_{j,J})\right]\varepsilon_\omega\\
&+\left[\left(\frac{N_{j,1}+N_{j,J}}{2}\right)(\Phi_{j,1}-\Phi_{j,J})-(N_{j,1}-N_{j,J})\right]\frac{1}{2\varepsilon_\omega}\\
&-\left[S_{j,J}\hat{G}-\delta(1-S_{j,J})\left(N_{j,J}P_{j,J}-1\right)\right]h\varepsilon_\omega=0.
\end{aligned} \tag{III.40}$$

On the vertical line of the interface along $[\{j=j_{a+1},...,j_{b-1}\}\cap\{k=k_c\}]$, the scheme is:

$$\begin{aligned}
&-h\left[S_{j,k}\hat{G}-\delta(1-S_{j,k})(N_{j,k}P_{j,k}-1)\right]\\
&+\frac{\varepsilon_\omega}{2}\left[\left(\frac{N_{j-1,k}+N_{j,k}}{2}\right)(\Phi_{j-1,k}-\Phi_{j,k})-(N_{j-1,k}-N_{j,k})\right]\\
&+\frac{1}{\varepsilon_\omega}\left[\left(\frac{N_{j,k+1}+N_{j,k}}{2}\right)(\Phi_{j,k+1}-\Phi_{j,k})-(N_{j,k+1}-N_{j,k})\right]\\
&+\frac{\varepsilon_\omega}{2}\left[\left(\frac{N_{j+1,k}+N_{j,k}}{2}\right)(\Phi_{j+1,k}-\Phi_{j,k})-(N_{j+1,k}-N_{j,k})\right]=0.
\end{aligned} \tag{III.41}$$

On the vertical line on the interface along $[\{j=j_{a+1},...,j_{b-1}\}\cap\{k=k_d\}]$, the scheme is:

$$\begin{aligned}
&\frac{1}{\varepsilon_\omega}\left[\left(\frac{N_{j,k-1}+N_{j,k}}{2}\right)(\Phi_{j,k-1}-\Phi_{j,k})-(N_{j,k-1}-N_{j,k})\right]\\
&+\frac{\varepsilon_\omega}{2}\left[\left(\frac{N_{j-1,k}+N_{j,k}}{2}\right)(\Phi_{j-1,k}-\Phi_{j,k})-(N_{j-1,k}-N_{j,k})\right]\\
&-h\left[S_{j,k}\hat{G}-\delta(1-S_{j,k})(N_{j,k}P_{j,k}-1)\right]\\
&+\frac{\varepsilon_\omega}{2}\left[\left(\frac{N_{j+1,k}+N_{j,k}}{2}\right)(\Phi_{j+1,k}-\Phi_{j,k})-(N_{j+1,k}-N_{j,k})\right]=0.
\end{aligned} \tag{III.42}$$

Similarly, for the corner (z_{j_a}, x_{k_c}) (see Figure 3(d)) the scheme is:

$$\begin{aligned}
&\left[\left(\frac{N_{j,k-1}+N_{j,k}}{2}\right)(\Phi_{j,k-1}-\Phi_{j,k})-(N_{j,k-1}-N_{j,k})\right]\frac{1}{2\varepsilon_\omega}\\
&+\left[\left(\frac{N_{j-1,k}+N_{j,k}}{2}\right)(\Phi_{j-1,k}-\Phi_{j,k})-(N_{j-1,k}-N_{j,k})\right]\varepsilon_\omega\\
&+\left[\left(\frac{N_{j,k+1}+N_{j,k}}{2}\right)(\Phi_{j,k+1}-\Phi_{j,k})-(N_{j,k+1}-N_{j,k})\right]\frac{1}{\varepsilon_\omega}\\
&+\left[\left(\frac{N_{j+1,k}+N_{j,k}}{2}\right)(\Phi_{j+1,k}-\Phi_{j,k})-(N_{j+1,k}-N_{j,k})\right]\frac{\varepsilon_\omega}{2}\\
&-\left[S_{j,k}\hat{G}-\delta(1-S_{j,k})\left(N_{j,k}P_{j,k}-1\right)\right]h\left(\frac{\varepsilon_\omega+1}{2}\right)=0.
\end{aligned}\tag{III.43}$$

For the corner (z_{j_a}, x_{k_d}) (see Figure 3(e)) the scheme is:

$$\begin{aligned}
&\frac{1}{\varepsilon_\omega}\left[\left(\frac{N_{j,k-1}+N_{j,k}}{2}\right)(\Phi_{j,k-1}-\Phi_{j,k})-(N_{j,k-1}-N_{j,k})\right]\\
&+\varepsilon_\omega\left[\left(\frac{N_{j-1,k}+N_{j,k}}{2}\right)(\Phi_{j-1,k}-\Phi_{j,k})-(N_{j-1,k}-N_{j,k})\right]\\
&+\frac{1}{2\varepsilon_\omega}\left[\left(\frac{N_{j,k+1}+N_{j,k}}{2}\right)(\Phi_{j,k+1}-\Phi_{j,k})-(N_{j,k+1}-N_{j,k})\right]\\
&-\left(\frac{\varepsilon_\omega+1}{2}\right)h\left[S_{j,k}\hat{G}-\delta(1-S_{j,k})(N_{j,k}P_{j,k}-1)\right]\\
&+\frac{\varepsilon_\omega}{2}\left[\left(\frac{N_{j+1,k}+N_{j,k}}{2}\right)(\Phi_{j+1,k}-\Phi_{j,k})-(N_{j+1,k}-N_{j,k})\right]=0.
\end{aligned}\tag{III.44}$$

For the corner (z_{j_b}, x_{k_c}) (see Figure 3(f)) the scheme is:

$$\begin{aligned}
&+\frac{\varepsilon_\omega}{2}\left[\left(\frac{N_{j-1,k}+N_{j,k}}{2}\right)(\Phi_{j-1,k}-\Phi_{j,k})-(N_{j-1,k}-N_{j,k})\right]\\
&+\frac{1}{2\varepsilon_\omega}\left[\left(\frac{N_{j,k+1}+N_{j,k}}{2}\right)(\Phi_{j,k+1}-\Phi_{j,k})-(N_{j,k+1}-N_{j,k})\right]\\
&-\left(\frac{\varepsilon_\omega+1}{2}\right)h\left[S_{j,k}\hat{G}-\delta(1-S_{j,k})(N_{j,k}P_{j,k}-1)\right]=0.
\end{aligned}\tag{III.45}$$

For the corner (z_{j_b}, x_{k_d}) (see Figure 3(g)) the scheme is:

$$\frac{1}{2\varepsilon_\omega}\left[\left(\frac{N_{j,k-1}+N_{j,k}}{2}\right)(\Phi_{j,k-1}-\Phi_{j,k})-(N_{j,k-1}-N_{j,k})\right]$$
$$+\frac{\varepsilon_\omega}{2}\left[\left(\frac{N_{j-1,k}+N_{j,k}}{2}\right)(\Phi_{j-1,k}-\Phi_{j,k})-(N_{j-1,k}-N_{j,k})\right]$$
$$-\left(\frac{\varepsilon_\omega+1}{2}\right)h\left[S_{j,k}\hat{G}-\delta(1-S_{j,k})(N_{j,k}P_{j,k}-1)\right]=0. \tag{III.46}$$

For P

Similarly to the derivation of the numerical scheme for N, for P on any point of the interface we use

$$\iint_{\bar{\Upsilon}} \nabla\cdot\mathbf{F}_p d\bar{\Upsilon} = \int_{\partial\bar{\Upsilon}} \mathbf{F}_p\cdot\hat{\mathbf{n}} dS = 0. \tag{III.47}$$

Since this variable is, again, only defined on one side of the interface, we restrict the volume elements to the side where P is defined, as shown in Figure III.4.

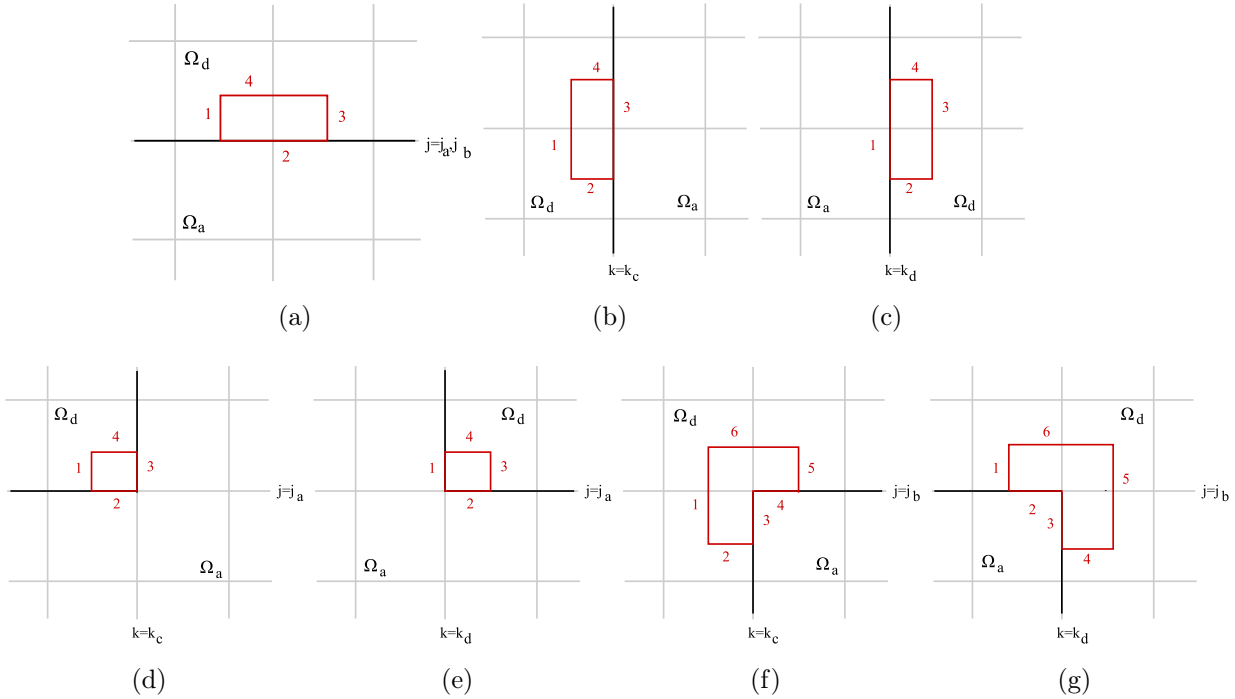

Figure III.4: Controlled volume elements used in the numerical scheme for generating the discretised equations for P.

On the horizontal lines of the interface along $j = j_a$, and $k = 0, ..., k_c$ and $k = k_d, ..., J$,and $j = j_b$ and $k = k_c, ..., k_d$ (see Figure 4(a)) the scheme is

$$\begin{aligned}
&\frac{1}{2\varepsilon_\omega}\left[\left(\frac{P_{j,k-1}+P_{j,k}}{2}\right)(\Phi_{j,k-1}-\Phi_{j,k})+(P_{j,k-1}-P_{j,k})\right]\\
&+\varepsilon_\omega h\left[S_{j,k}\hat{G}-\delta(1-S_{j,k})(N_{j,k}P_{j,k}-1)\right]\\
&+\frac{1}{2\varepsilon_\omega}\left[\left(\frac{P_{j,k+1}+P_{j,k}}{2}\right)(\Phi_{j,k+1}-\Phi_{j,k})+(P_{j,k+1}-P_{j,k})\right]\\
&+\varepsilon_\omega\left[\left(\frac{P_{j+1,k}+P_{j,k}}{2}\right)(\Phi_{j+1,k}-\Phi_{j,k})+(P_{j+1,k}-P_{j,k})\right]=0. \qquad \text{(III.48)}
\end{aligned}$$

On the x-boundaries, i.e. at (z_{j_a}, x_0) and (z_{j_a}, x_J), the periodic conditions are imposed by

$$\begin{aligned}
&P_{j,0}=P_{j,J}, \qquad \text{(III.49)}\\
&\frac{\varepsilon}{2}\left[\left(\frac{P_{j,J-1}+P_{j,J}}{2}\right)(\Phi_{j,J-1}-\Phi_{j,J})+(P_{j,J-1}-P_{j,J})\right]\\
&+\frac{h}{\varepsilon}\left[S_{j,J}\hat{G}-\delta(1-S_{j,J})(N_{j,J}P_{j,J}-1)\right]\\
&+\frac{\varepsilon}{2}\left[\left(\frac{P_{j,1}+P_{j,J}}{2}\right)(\Phi_{j,1}-\Phi_{j,J})+(P_{j,1}-P_{j,J})\right]\\
&+\frac{1}{\varepsilon}\left[\left(\frac{P_{j+1,J}+P_{j,J}}{2}\right)(\Phi_{j+1,J}-\Phi_{j,J})+(P_{j+1,J}-P_{j,J})\right]=0. \qquad \text{(III.50)}
\end{aligned}$$

On the vertical line of the interface along $k = k_c$ and $j = j_a + 1, ..., j_b - 1$, the scheme is

$$\begin{aligned}
&\frac{1}{\varepsilon_\omega}\left[\left(\frac{P_{j,k-1}+P_{j,k}}{2}\right)(\Phi_{j,k-1}-\Phi_{j,k})+(P_{j,k-1}-P_{j,k})\right]\\
&+\frac{\varepsilon_\omega}{2}\left[\left(\frac{P_{j-1,k}+P_{j,k}}{2}\right)(\Phi_{j-1,k}-\Phi_{j,k})+(P_{j-1,k}-P_{j,k})\right]\\
&+h\left[S_{j,k}\hat{G}-\delta(1-S_{j,k})(N_{j,k}P_{j,k}-1)\right]\\
&+\frac{\varepsilon_\omega}{2}\left[\left(\frac{P_{j+1,k}+P_{j,k}}{2}\right)(\Phi_{j+1,k}-\Phi_{j,k})+(P_{j+1,k}-P_{j,k})\right]=0. \qquad \text{(III.51)}
\end{aligned}$$

On the vertical line of the interface along $k = k_d$ and $j = j_a + 1, ..., j_b - 1$, the scheme

is

$$
\begin{aligned}
&h\left[S_{j,k}\hat{G} - \delta(1-S_{j,k})(N_{j,k}P_{j,k}-1)\right] \\
&+\frac{\varepsilon_\omega}{2}\left[\left(\frac{P_{j-1,k}+P_{j,k}}{2}\right)(\Phi_{j-1,k}-\Phi_{j,k}) + (P_{j-1,k}-P_{j,k})\right] \\
&+\frac{1}{\varepsilon_\omega}\left[\left(\frac{P_{j,k+1}+P_{j,k}}{2}\right)(\Phi_{j,k+1}-\Phi_{j,k}) + (P_{j,k+1}-P_{j,k})\right] \\
&+\frac{\varepsilon_\omega}{2}\left[\left(\frac{P_{j+1,k}+P_{j,k}}{2}\right)(\Phi_{j+1,k}-\Phi_{j,k}) + (P_{j+1,k}-P_{j,k})\right] = 0. \qquad \text{(III.52)}
\end{aligned}
$$

For the corner point (z_{j_a}, x_{j_c}) (see Figure 4(d)) the scheme is

$$
\begin{aligned}
&\frac{1}{2\varepsilon_\omega}\left[\left(\frac{P_{j,k-1}+P_{j,k}}{2}\right)(\Phi_{j,k-1}-\Phi_{j,k}) + (P_{j,k-1}-P_{j,k})\right] \\
&+\frac{(\varepsilon_\omega+1)}{2}h\left[S_{j,k}\hat{G} - \delta(1-S_{j,k})(N_{j,k}P_{j,k}-1)\right] \\
&+\frac{\varepsilon_\omega}{2}\left[\left(\frac{P_{j+1,k}+P_{j,k}}{2}\right)(\Phi_{j+1,k}-\Phi_{j,k}) + (P_{j+1,k}-P_{j,k})\right] = 0. \qquad \text{(III.53)}
\end{aligned}
$$

For the corner point (z_{j_a}, x_{k_d}) (see Figure 4(e)) the scheme is

$$
\begin{aligned}
&\frac{(\varepsilon_\omega+1)}{2}h\left[S_{j,k}\hat{G} - \delta(1-S_{j,k})(N_{j,k}P_{j,k}-1)\right] \\
&+\frac{1}{2\varepsilon_\omega}\left[\left(\frac{P_{j,k+1}+P_{j,k}}{2}\right)(\Phi_{j,k+1}-\Phi_{j,k}) + (P_{j,k+1}-P_{j,k})\right] \\
&+\frac{\varepsilon_\omega}{2}\left[\left(\frac{P_{j+1,k}+P_{j,k}}{2}\right)(\Phi_{j+1,k}-\Phi_{j,k}) + (P_{j+1,k}-P_{j,k})\right] = 0. \qquad \text{(III.54)}
\end{aligned}
$$

For the corner point (z_{j_b}, x_{k_c}) (see Figure 4(f)) the scheme is

$$
\begin{aligned}
&\frac{1}{\varepsilon_\omega}\left[\left(\frac{P_{j,k-1}+P_{j,k}}{2}\right)(\Phi_{j,k-1}-\Phi_{j,k}) + (P_{j,k-1}-P_{j,k})\right] \\
&+\frac{\varepsilon_\omega}{2}\left[\left(\frac{P_{j-1,k}+P_{j,k}}{2}\right)(\Phi_{j-1,k}-\Phi_{j,k}) + (P_{j-1,k}-P_{j,k})\right] \\
&+\frac{(\varepsilon_\omega+1)}{2}h\left[S_{j,k}\hat{G} - \delta(1-S_{j,k})(N_{j,k}P_{j,k}-1)\right] \\
&+\frac{1}{2\varepsilon_\omega}\left[\left(\frac{P_{j,k+1}+P_{j,k}}{2}\right)(\Phi_{j,k+1}-\Phi_{j,k}) + (P_{j,k+1}-P_{j,k})\right] \\
&+\varepsilon_\omega\left[\left(\frac{P_{j+1,k}+P_{j,k}}{2}\right)(\Phi_{j+1,k}-\Phi_{j,k}) + (P_{j+1,k}-P_{j,k})\right] = 0. \qquad \text{(III.55)}
\end{aligned}
$$

For the corner point (z_{j_b}, x_{k_c}) (see Figure 4(g)) the scheme is

$$\begin{aligned}
&\frac{1}{2\varepsilon_\omega}\left[\left(\frac{P_{j,k-1}+P_{j,k}}{2}\right)(\Phi_{j,k-1}-\Phi_{j,k})+(P_{j,k-1}-P_{j,k})\right]\\
&-\frac{(\varepsilon_\omega+1)}{2}h\left[S_{j,k}\hat{G}-\delta(1-S_{j,k})(N_{j,k}P_{j,k}-1)\right]\\
&+\frac{\varepsilon_\omega}{2}\left[\left(\frac{P_{j-1,k}+P_{j,k}}{2}\right)(\Phi_{j-1,k}-\Phi_{j,k})+(P_{j-1,k}-P_{j,k})\right]\\
&+\frac{1}{\varepsilon_\omega}\left[\left(\frac{P_{j,k+1}+P_{j,k}}{2}\right)(\Phi_{j,k+1}-\Phi_{j,k})+(P_{j,k+1}-P_{j,k})\right]\\
&+\varepsilon_\omega\left[\left(\frac{P_{j+1,k}+P_{j,k}}{2}\right)(\Phi_{j+1,k}-\Phi_{j,k})+(P_{j+1,k}-P_{j,k})\right]=0. \qquad \text{(III.56)}
\end{aligned}$$

Error Analysis

As we have no analytical solution for reference, we calculate the solution to the problem with a fixed set of parameters using a very fine grid. We let $\bar{\Phi}_{j,k}$, $\bar{N}_{j,k}$ and $\bar{P}_{j,k}$ be the numerical solutions on the finer grid and $\Phi j,k$, $N_{j,k}$ and $P_{j,k}$ be the solutions at the coarser grid, and define the error matrices for each variable by

$$E_{\Phi_{j,k}}=|\bar{\Phi}_{j,k}-\Phi_{j,k}|,\quad E_{N_{j,k}}=|\bar{N}_{j,k}-N_{j,k}|,\quad E_{P_{j,k}}=|\bar{P}_{j,k}-P_{j,k}|. \qquad \text{(III.57)}$$

We note that similar analysis can be done on either ϕ or p, as well, but we only demonstrate the case of n here. The results that follow are similar in any of the cases, expect for ϕ where the error is smaller everywhere. In Figure III.5, we illustrate the errors, E_ϕ, E_n and E_p, for a uniform grid with step size $h = 0.0078$. We observe that the error increases up to $O(10^{-5})$ in the mixed layer.

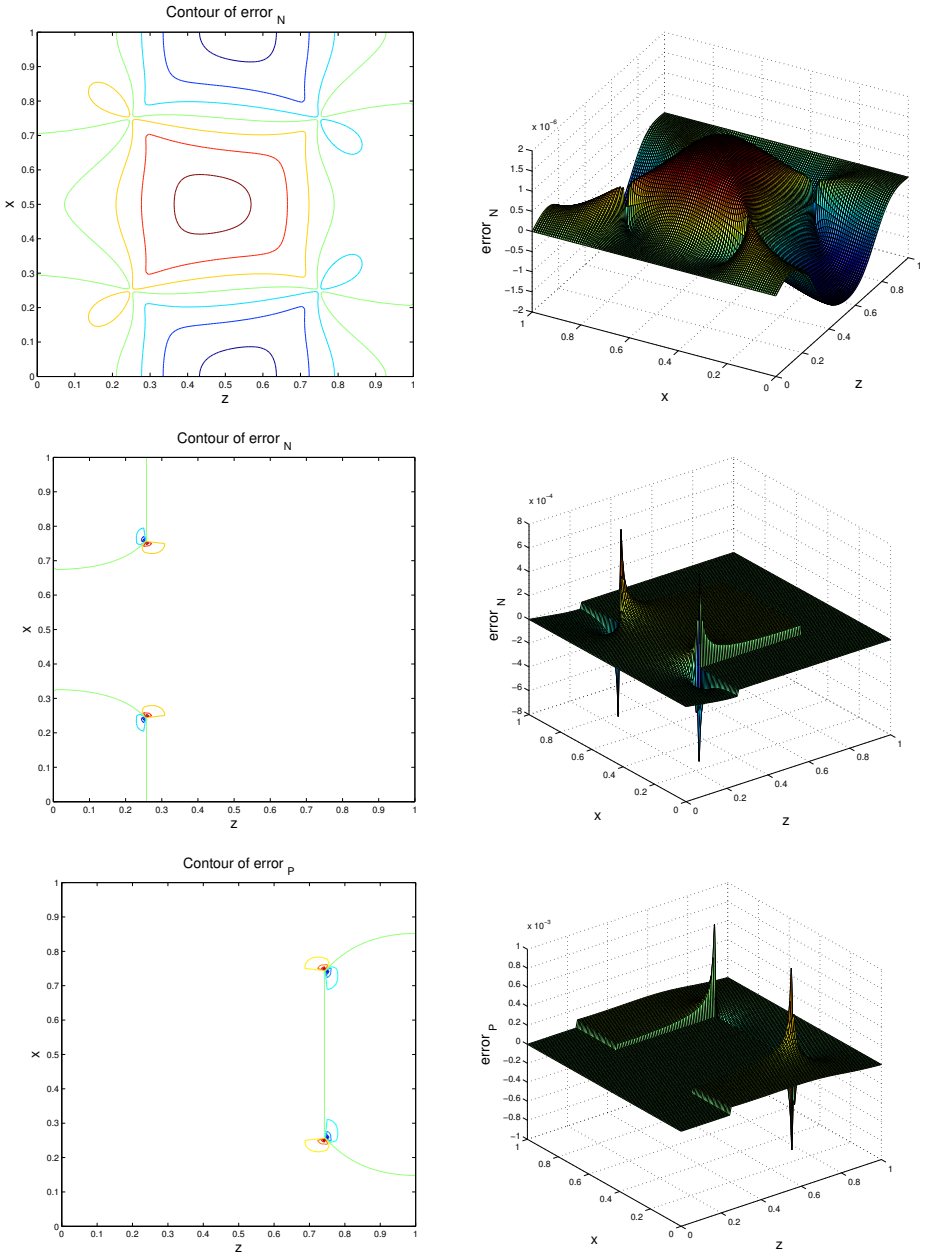

Figure III.5: (a) Contour plot and (b) surface plot of the error, E_n, generated by the numerical scheme used for solving the bilayer thin film problem. [Parameters: $\varepsilon_\omega = 1$, $S = 0$, $\delta = 1$, $\hat{\epsilon}_p$, $V = 1$, $\Lambda = 1$, $\hat{N}^- = 1$, $\hat{P}^+ = 1$]

Bibliography

[1] BP. Bp statistical review of world energy. June 2017.

[2] EUFORES. Repap 2020 - renewable energy policy action paving the way towards 2020. *European Forum for Renewabe Energy Sources (EUFORES)*, 2011.

[3] M. Grätzel. Photoelectrochemical cells. *Nature*, 414:338–344, 2001.

[4] W. Shockley and H. J. Queisser. Detailed balance limit of efficiency of p-n junction solar cells. *Journal of Applied Physics*, 32(3):510–519, 1961.

[5] R. Ohl. Light-sensitive electric device : Patent us2402662, 06 1946.

[6] J. H. Burroughes, D. D. C. Bradley, A. R. Brown, R. N. Marks, K. Mackay, R. H. Friend, P. L. Burns, and A. B. Holmes. Light-emitting diodes based on conjugated polymers. *Nature*, 347:539–541, 1990.

[7] M. Fox. *Optical properties of solids*. Oxford University Press, New York, 2001.

[8] B. O'Regan and M. Grätzel. A low-cost, high-efficiency solar cell based on dye-sensitised colloidal TiO_2 films. *Nature*, 353:737–740, 1991.

[9] P. Wang, S. K. Zakeeruddin, J. E. Moser, M. K. Nazeeruddin, T. Sekiguchi, and M. Grätzel. A stable quasi-solid-state dye-sensitised solar cell with an amphiphilic ruthenium and polymer gel electrolyte. *Nature Materials*, 2:402–407, 2003.

[10] U. Bach, D. Lupo, P. Comté, J. E. Moser, F. Weissortel, J. Salbeck, H. Spreitzer, and M. Grätzel. Solid-state dye-sensitised mesoporous TiO_2 solar cells with high photon-to-electron conversion efficiencies. *Nature*, 395:583–585, 1998.

[11] H.J. Snaith. Perovskites: The emergence of a new era for low-cost, high- efficiency solar cells. *The journal of physical chemistry letters*, 4:3623–3630, 2013.

[12] L. Etgar, P. Gao, Z. Xue, Q. Peng, A. K. Chandiran, B. Liu, Md. K. Nazeeruddin, and M. Graetzel. Mesoscopic $CH_3NH_3PbI_3/TiO_2$ heterojunction solar cells. *Journal of the American Chemical Society*, 134:17396–17399, 2012.

[13] M. Liu, M.B. Johnston, and H.J. Snaith. Efficient planar heterojunction perovskite solar cells by vapour deposition. *Nature Letters*, 501:395–398, 2013.

[14] B.E. Hardin, H.J. Snaith, and M.D. McGehee. The renaissance of dye-sensitized solar cells. *Journal of Applied Physics*, 6:162–169, 2012.

[15] M.A. Green, A. Ho-Baillie, and H.J. Snaith. The emergence of perovskite solar cells. *Nature Photonics*, 8:506–514, 2014.

[16] G. Richardson, S.E.J. O'Kane, R.G. Niemann, T.A. Peltola, J.M. Foster, P.J. Cameron, and A.B. Walker. Can slow-moving ions explain hysteresis in the current–voltage curves of perovskite solar cells? *Energy and environmental science*, 9:1476–1485, 2016.

[17] K. Domanski, B. Roose, T. Matsui, M. Saliba, S. Turren-Cruz, J. Correa-Baena, C.R. Carmona, G. Richardson, J.M. Foster, F. De Angelis, J. Ball, A. Petrozza, N. Mine, M. Nazeeruddin, W. Tress, M. Grätzel, U. Steiner, A. Hagfeldtd, and A. Abate. Migration of cations induces reversible performance losses over day/night cycling in perovskite solar cells. *Energy and environmental science*, 10:604–613, 2017.

[18] H.J. Snaith, A. Abate, J.M. Ball, G.E. Eperon, T. Leijtens, N.K. Noel, S.D. Stranks, J.T. Wang, K. Wojciechowski, and W. Zhang. Anomalous hysteresis in perovskite solar cells. *The journal of physical chemistry*, 5:1511?1515, 2014.

[19] J. M. Foster, H. J. Snaith, T. Leitjens, and G. Richardson. A model for the operation of perovskite based hybrid solar cells: Formulation, analysis and comparison to experiment. *SIAM Journal of Applied Mathematics*, 74 (6):1935–1966, 2012.

[20] S. Guarnera, A. Abate, W. Zhang, J.M. Foster, G. Richardson, A. Petrozza, and H.J. Snaith. Improving the long-term stability of perovskite solar cells with a porous Al_2O_3 buffer layer. *Journal of Physical Chemistry Letters*, 6:432–437, 2015.

[21] G.E. Eperon, V.M. Burlakov, P. Docampo, A. Goriely, and H.J. Snaith. Morphological control for high performance, solution-processed planar heterojunction perovskite solar cells. *Advances functional materials*, 24:151–157, 2014.

[22] D. A. Fraser. *The physics of semiconductor devices*. Clarendon Press Oxford, New York, 1979.

[23] C. Gueymard. The sun's total and spectral irradiance for solar energy applications and solar radiation models. *Solar Energy*, 76:423–453, 2004.

[24] M. Fliggea, S. Solankib, J. Papc, C. Frohlichd, and C. Wehrlid. Variations of solar spectral irradiance from near uv to the infrared—measurements and results. *Journal of Atmospheric and Solar-Terrestrial Physics*, 63:1479–1478, 2001.

[25] E. Schrodinger. An undulatory theory of the mechanics of atoms and molecules. *The Physical Review*, 28 (6):1049–1070, 1926.

[26] M. Grätzel. Dye-sensitized solar cells. *Journal of Photochemistry and Photobiology C: Photochemistry Reviews*, 4:145–153, 2003.

[27] H. J. Snaith and L. Schmidt-Mende. Advances in liquid-electrolyte and solid-state dye-sensitized solar cells. *Advanced Materials*, 19:3187–3200, 2007.

[28] P. Docampo and M. Lee. The art of making solid state dscs. *Private Communication*, 2010.

[29] U. Bach, Y. Tachibana, J. Moser, S. A. Haque, A. R. Durrant, M. Grätzel, and D. R. Klug. Charge separation in solid-state dye-sensitised heterojunction solar cells. *Journal of the American Chemistry Society*, 121:7445–7446, 1999.

[30] L. Kavan and M. Grätzel. Highly efficient semiconducting TiO_2 photoelectrodes prepared by aerosol pyrolysis. *Electrochim. Acta*, 40:643–652, 1995.

[31] C. J. Barbe, F. Arendse, P. Comté, M. Jirousek, F. Lenzmann, V. Shklover, and M Grätzel. Nanocrystalline titanium oxide electrodes for photovoltaic applications. *Journal of the American Ceramic society*, 80(12):3157–3171, 1997.

[32] H. J. Snaith, R. Humphry-Baker, P. Chen, I. Cesar, S. M. Zakeeruddin, and M. Grätzel. Charge collection and pore filling in solid-state dye-sensitised solar cells. *Nanotechnology*, 19, 2008.

[33] H. J. Snaith, S. M. Zakeeruddin, L. Schmidt-Mende, C. Klein, and M. Grätzel. Ion-coordinating sensitizer in solid-state hybrid solar cells. *Angewandte Chemie*, 44:6413–6417, 2005.

[34] M. Filipic, M. Berginc, F. Smole, and M. Topic. Analysis of electron recombination in dye-sensitised solar cell. *Current Applied Physics*, 12:238–246, 2012.

[35] A. Hagfeldt and M. Grätzel. Light-induced redox reactions in nanocrystalline systems. *Chemistry Review*, 95:49–68, 1995.

[36] P. Tiwana, P. Docampo, M. B. Johnston, H. J. Snaith, and L. M. Herz. Electron mobility and injection dynamics in mesoporous ZnO, SnO_2, and TiO_2 films used in dye-sensitized solar cells. *American Chemical Society Nano*, 5(6):5158–5166, 2011.

[37] J. Ferber and J. Luther. Modeling of photovoltage and photocurrent in dye-sensitized titanium dioxide solar cells. *Journal of Physical Chemistry*, 105:4895–4903, 2001.

[38] W. Shockley. Semiconductor amplifier : Patent us2502488, 04 1950.

[39] W. Shockley. Circuit element utilizing semiconductive material : Patent us2569347, 09 1951.

[40] W. Shockley. *Electrons and holes in semiconductors*. D. Van Nostrand Company, London, 1950.

[41] C. Please. *Some mathematical problems of semiconductor devices*. PhD thesis, University of Oxford, 1978.

[42] M. Penny. *Mathematical Modelling of dye-sensitised solar cells*. PhD thesis, Queensland University of Technology, 2006.

[43] G. Richardson, C. P. Please, and J. Kirkpatrick. Asymptotic solution of a model for bilayer organic diodes and solar cells. *SIAM Journal on Applied Mathematics*, 72 (6):1792–1817, 2012.

[44] J.M. Foster, S.J. Snaith, T. Leitjens, and G. Richardson. Model for the operation of perovskite based hybrid solar cells: Formulation, analysis, and comparison to experiment. *SIAM Journal of applied mathematics*, 74 (6):1935–1966, 2014.

[45] S.D. Stranks, V. Burlakov, T. Leijtens, J. Ball, A. Goriely, and H.J. Snaith. Recombination kinetics in organic-inorganic perovskites: Excitons, free charge, and subgap states. *Physical review applied*, 2:034007:1–8, 2014.

[46] P. Docampo, M. Stefik, S. Guldin, R. Gunning, N. A. Yufa, N. Cai, P. Wang, U. Steiner, U. Wiesner, and H. J. Snaith. Triblock-terpolymer-directed self-assembly of mesoporous TiO_2: high performance photo anodes for solid-state dye-sensitised solar cells. *Advanced Energy Materials*, 2:676–682, 2012.

[47] H. J. Snaith. Solid-state dye-sensitized solar cells: device operation, optimization, charge generation, mechanism and novel electrodes structured from diblock copolymers. *Proceedings of: Workshop on nanoscience for solar energy conversion*, 2008.

[48] H. J. Snaith and M. Grätzel. Electron and hole transport through mesoporous TiO_2 infiltrated with spiro−MeOTAD. *Advanced materials*, 19:3643–3647, 2007.

[49] F. Sauvage, D. Chen, P. Comté, F. Huang, L. Heininger, Y. Cheng, R. A. Caruso, and M. Grätzel. Dye-sensitised solar cells employing a single film of mesoporous TiO_2 beads achieve power conversion efficiencies over 10%. *American Chemical Society Nano*, 4 (8):4420–4425, 2010.

[50] T. Krishnamoorthy, V. Thavasi, M. Subodh, and S. Ramakrishna. A first report on the fabrication of vertically aligned anatase TiO_2 nanowires by electrospinning: preferred architecture for nano structured solar cells. *Energy Environmental Science*, 4:2807–2812, 2011.

[51] W. Yang, J. Li, Y. Wang, F. Zhu, W. Shi, F. Wan, and D. Xu. A facile synthesis of anatase TiO_2 nanosheets-based hierarchical spheres with over 90% {001} facets for dye-sensitised solar cells. *Chemical Communications*, 47:1809–1811, 2011.

[52] K. Fan, W. Zhang, T. Peng, J. Chen, and F. Yang. Application of TiO_2 fusiform nanorods for dye-sensitised solar cells with significantly improved efficiency. *Journal of Physical Chemistry*, 115 (34):17213–17219, 2011.

[53] I. C. Flores, J. N. de Freitas, C. Longo, M. De Paoli, H. Winnischofer, and A. F. Nogueira. Dye-sensitised solar cells based on TiO_2 nanotubes and a solid-state electrolyte. *Journal of Photochemistry and Photobiology A: Chemistry*, 189:153–160, 2007.

[54] P. Docampo, A. Ivaturi, R. Gunning, S. Diefenbach, J. Kirkpatrick, C. M. Palumbiny, V. Sivaram, H. Geany, L. Schmidt-Mende, M. E. Welland, and H. J. Snaith. The influence of 1 D, meso- and crystal structures on charge transport and recombination in solid-state dye-sensitised solar cells. *Journal of Materials Chemistry A*, 1:12088–12095, 2013.

[55] S. H. Ahn, D. J. Kim, W. S. Chi, and J. H. Kim. One-dimensional hierarchical nano structures of TiO_2 nano sheets on SnO_2 nanotubes for high efficiency solid-state dye-sensitised solar cells. *Advanced Materials*, 25:4893–4897, 2013.

[56] D. K. Roh, W. S. Chi, H. Jeon, S. J. Kim, and J. H. Kim. High efficiency solid-state dye-sensitised solar cells assembled with hierarchical anatase pine tree-like TiO_2 nanotubes. *Advanced Functional Materials*, 24:379–386, 2014.

[57] M. Law, L. E. Greene, J. C. Johnson, R. Saykally, and P. Yang. Nanowire dye-sensitised solar cells. *Nature Materials*, 4:455–459, 2005.

[58] X. Feng, K. Shankar, O. K. Varghese, M. Paulose, T. J. Latempa, and C. A. Grimes. Vertically aligned single crystal TiO_2 nanowire arrays grown directly on transparent conducting oxide coated glass: synthesis details and applications. *Nano Letters*, 8 (11):3781–3786, 2008.

[59] P. Tiwana, P. Docampo, M.B. Johnston, H.J. Snaith, and L.M. Herz. Electron mobility and injection dynamics in mesoporous ZnO, SnO_2, and TiO_2 films used in dye-sensitized solar cells. *American Chemical Society Nano*, 5(6):5158–5166, 2011.

[60] A. Abate, T. Leijtens, A. Pathak, J. Teuscher, R. Avolio, M.e. Errico, J. Kirkpatrik, J.M. Ball, P. Docampo, I. McPhersonc, and H.J. Snaith. Lithium salts as "redox active" p-type dopants for organic semiconductors and their impact in solid-state dye-sensitized solar cells. *Physical chemistry Chemical physics*, 15:2572–2579, 2013.

[61] A. Abate, R. Perez-Tejada, K. Wojciechowski, J. Foster, A. Sandhanala, U. Steiner, H. Snaith, S. Franco, and J. Orduna. Phosphonic anchoring groups in organic dyes for solid-state solar cells. *Phys Chem Chem Phys*, 2015.

[62] M. C. K. Sellers and E. G. Seebauer. Measurement method for carrier concentration in TiO_2 via the Mott−Schottky approach. *Thin Solid Films*, 519:2103–2110, 2011.

[63] R. LeVeque. *Numerical Methods for conservation laws*. Birkhäuser Verlag, Berlin, 1992.

[64] G. Richardson, C.P. Please, and V. Styles. Derivation and solution of effective medium equations for bulk heterojunction organic solar cells. *European Journal of Applied Mathematics*, pages 1–42, 2017.

[65] C. Sahin, C. Tozlu, K. Ocakoglu, C. Zafer, C. Varlikli, and S. Icli. Synthesis of an amphiphilic ruthenium complex with swallow-tail bipyridyl ligand and its application in ss-dsc. *Inorganica Chimica Acta*, 361:671–676, 2007.

[66] K. Fredin, K. F. Anderson, N. W. Duffy, G. J. Wilson, C. J. Fell, D. P. Hagberg, L. Sun, U. Bach, and S. Lindquist. Effect on cell efficiency following thermal degradation of dye-sensitised mesoporous electrodes using n719 and d5 sensitisers. *Journal of Physical Chemistry*, 113:18902–18906, 2009.

[67] S. M. Sze. *Physics of semiconductor devices.* John Wiley & Sons, New York, 1981.

[68] S. Wegner. *Strategies to optimising dye-sensitised solar cells: organic sensitisers, tandem device structures, and numerical device modelling.* PhD thesis, École Polytechnique Fédérale de Lausanne, 2010.

[69] H. Tang, H. Berger, P. Schmid, and F. Levy. Optical properties of anatase tio2. *Solid state Communications*, 92 (3):267–271, 1994.

[70] C. Chen, S. Hsiao, C. Chen, H. Kang, Z. Huang, and H. Lin. Optical properties of organometal halide perovskite thin films and general device structure design rules for perovskite single and tandem solar cells. *Journal of Material Chemistry A.*, 3:9152–9159, 2015.

[71] M. Born and E. Wolf. *Principles of Optics: Electromagnetic Theory of Propagation, Interference and Diffraction of Light.* Cambridge University Press, Cambridge, UK, 1959.

[72] A. K. Jonscher. Dielectric relaxation in solids. *Journal of Applied Physics*, 32:R57, 1999.

[73] A. M. Saslow and G. Wilkinson. Expulsion of free electronic charge from the interior of a metal. *Am. Journal of Physics*, 39:1244, 1971.

[74] N. Ashby. Relaxation of charge imbalances in conductors. *Am. Journal of Physics*, 43:553, 1975.

[75] H. C. Ohanian. On the approach to electro- and magneto-static equilibrium. *Am. Journal of Physics*, 51:1020, 1983.

[76] A. Sommerfeld. *Optics.* Academic Press, Inc., USA, 1949.

[77] J.M. Foster, J. Kirkpatrick, and G. Richardson. Asymptotic and numerical prediction of current-voltage curves for an organic bilayer solar cell under varying illumination and comparison to the shockley equivalent circuit. *Journal of Applied Physics*, 114:104501:1–15, 2013.

[78] J. Krüger, R. Plass, L. Cevey, M. Piccirelli, M. Grätzel, and *et al.* High efficiency solid-state photovoltaic device due to inhibition of interface charge recombination. *Applied Physics Letters*, 79:2085–2087, 2001.

[79] I. Sobey. *Introduction to interactive boundary layer theory*. Oxford University Press, Oxford, UK, 2010.